MULTI-CRITERIA ASSESSMENT OF WAVE AND TIDAL POWER ALONG THE ATLANTIC COAST OF THE SOUTHEASTERN USA

A Dissertation
Presented to
The Academic Faculty

by

Zafer Defne

In Partial Fulfillment
of the Requirements for the Degree
Doctor of Philosophy in the
School of Civil and Environmental Engineering

Georgia Institute of Technology
May 2010

MULTI-CRITERIA ASSESSMENT OF WAVE AND TIDAL POWER ALONG THE ATLANTIC COAST OF THE SOUTHEASTERN USA

Approved by:

Dr. Kevin Haas, Committee Chair
School of Civil and Environmental Engineering
Georgia Institute of Technology

Dr. Hermann Fritz, Committee Co-Chair
School of Civil and Environmental Engineering
Georgia Institute of Technology

Dr. Paul Work
School of Civil and Environmental Engineering
Georgia Institute of Technology

Dr. Emanuele Di Lorenzo
School of Earth and Atmospheric Sciences
Georgia Institute of Technology

Dr. Dirk Schaefer
School of Mechanical Engineering
Georgia Institute of Technology

Date Approved: January 5, 2010

ACKNOWLEDGMENTS

I would like to express my immense gratitude to my advisors Dr. Kevin Haas and Dr. Hermann Fritz for giving me the opportunity to do this research, and for their guidance throughout the entire study. Their invaluable comments are much appreciated. I am deeply thankful to Dr. Haas for his contributions in developing the fundamentals of this study and for his patience during our long discussions.

I would like to extend my thanks to Dr. Paul Work, Dr. Emanuele Di Lorenzo and Dr. Dirk Schaefer for serving as the committee members. Their time, effort, and comments are greatly appreciated. A special thanks goes to Dr. John Warner for helping me with my questions on ROMS modeling and my colleague Dr. Lide Jiang for the exchange of ideas.

I would like to thank all my friends and my past and present roommates, Mesut Turel, Huseyin Demir, Ayse Erdolen and especially to Kemal Cambazoglu, who was also a great officemate for many years, for sharing all the good and bad times together. Most of all, I would like to thank Elza Bystrom for always being there and for bringing with her all the joy and happiness, and the best of the Asian cuisine.

Last but not least, many thanks to my parents Ahmet and Gulcan Defne for their love and support, and putting the love in our hearts. We may be oceans away, but we are never apart.

This research was a part of the InfinitEnergy partnership between colleges, universities, state and local governments, and commercial entities to promote the use of alternative energy technologies. This work was supported by the National Science

Foundation, Division of Industrial Innovation and Partnerships (IIP) under the Partnerships for Innovation Program Grant No. 0332613. Funding was also provided by the Strategic Energy Institute at Georgia Institute of Technology via a Creating Energy Options grant and the 104B Georgia Water Resources Institute Funding Program, and also by the Department of Energy, Wind and Hydropower Technologies Program award number DE-FG36-08GO18174 and by the state of Georgia.

TABLE OF CONTENTS

LIST OF TABLES

LIST OF FIGURES

SUMMARY

The increasing demand for energy and the increased depletion rate of nonrenewable energy resources call for research on renewable alternatives. Mapping the availability of marine resources is an important step towards development of ocean power conversion projects. For this purpose, the wave power potential along the Atlantic coast of the southeastern USA, and the tidal stream power along the coast of Georgia are investigated in this study. The effect of tidal stream power conversion on the tidal regime is studied at the estuary scale. A multi-criteria method for tidal power conversion schemes to select favorable locations and to rank them according to their suitability is developed and applied to the Georgia coast.

Wave power potential is studied in an area bounded by latitudes 27ºN and 38ºN and longitudes 82ºW and 72ºW (i.e. North Carolina, South Carolina, Georgia, and northern Florida). The available data from National Data Buoy Center wave stations in the study area are examined. Temporal trends of the wave heights, wave periods and the wave power are analyzed for seasonal variations with a time scale of weeks. The time series from the wave stations are downsampled with a 15-day moving average filter with near 50% overlapping to study the seasonal trends. Power calculated from hourly significant wave heights and average wave periods is compared to power calculated using spectral wave energy density. It is found that a factor of 0.61 needs to be applied to the wave power calculated from hourly significant wave heights and average periods in order get the same results with the power calculated from spectral wave density. The mean

power within 50 km of the shore is determined to be ~9 kW/m, whereas higher power (~15 kW/m) is available further offshore beyond the 3500 m contour line.

The tidal stream power potential along the coast of the state of Georgia is evaluated based on the available data and numerical modeling of the currents. This region has low (<0.5 m/s) to moderate (<0.8 m/s) average tidal currents along most of the coast, but with the possibility of relatively very strong (>1.0 m/s) local currents within its complex network of tidal rivers and inlets between barrier islands. The limited number of tidal current prediction locations is not sufficient to resolve the temporal and spatial changes in the current speeds and patterns. Therefore, the currents are modeled with the Regional Ocean Modeling System (ROMS) to determine the locations with high tidal stream power potential. The results from the model are validated against measurements and a sensitivity analysis is provided for various parameters such as the computational cell size, offshore extent of the grids, inclusion of wetlands and bathymetry smoothing. The modeling results show that the areas with the highest tidal power density on the Georgia coast are a part of the Intercoastal Waterway between the Altamaha and Doboy Sounds and a part of the Canoochee River. The tidal power densities based on one-month simulations at these locations are computed to be on the level of 1600 W/m^2, 1400 W/m^2 and 1100 W/m^2, respectively. The Savannah River is also found to have areas with high tidal power density in the region. One-year time series are generated by harmonic analysis of model results, and used to calculate the annual average power and energy at selected locations in the Savannah, Ogeechee and Altamaha Rivers. Annual average power at these locations are found to be respectively, 1.3 MW, 3.0 MW and 1.9 MW, which corresponds to annual energy of 112 GWh/year, 258 GWh/year, and 162

GWh/year. The distribution of tidal current magnitudes and tidal power densities in a year is provided with histograms for each location.

The effect of power extraction on estuarine hydrodynamics is simulated by implementing an additional retarding force in the governing momentum equations in ROMS. Two different power extraction schemes are simulated in the Ogeechee River. The first scheme involves power extraction across the entire cross-section of the river, and causes considerable changes in the original currents, water levels and original undisturbed tidal power. The second extraction scheme, where power is extracted from a part of the cross-section is found to have substantially lower impact on the original flow than the first scheme, but extracts higher power from the flow despite having a smaller area to capture power. This is attributed to the recovery in the flow momentum on the unconstructed part of the river cross-section in the second scheme.

A multi-criteria assessment methodology that accounts for the physical, environmental and socioeconomic constraints is proposed to select the most suitable locations for tidal stream power converters. For this purpose, the model results are incorporated into a Geographical Information System (GIS) database together with many other datasets that are related to different aspects of the site selection methodology. The proposed method is applied to the Georgia coast to find and rank the best locations for power conversion. The suitable areas are narrowed down to a subset of the high power density areas that satisfy the constraints of power conversion. A demonstrative ranking procedure shows that Medway River has one of the best locations for tidal power conversion on the coast of Georgia. This methodology is also applicable to other sites where sufficient geospatial data are available.

CHAPTER I

INTRODUCTION

The continuously increasing world population and the changing life styles have been steadily increasing the demand for energy, rapidly depleting the limited nonrenewable resources and putting a lot of strain on the environment. Today's modern civilizations need to face big challenges to provide energy to the community through sustainable solutions that require fulfillment of energy demand while preserving the ecological quality. The rapidly rising global energy demand keeps escalating the competition over the available resources and increasing prices. The nonrenewable resources cannot naturally replenish and conventional resources have the tendency to deteriorate the ecological quality by releasing excessive amount of carbon dioxide (CO_2) and pollutants into the atmosphere. On the other hand, renewable energy sources such as solar, wind, biomass, ocean thermal and ocean mechanical energy (i.e. waves, tides and currents) are emergent alternatives that can meet a part of the growing energy demand and environmental constraints while helping maintain a diversified energy supply portfolio. Having diverse energy sources is important for it minimizes the dependence on a single energy source. The risk of blackouts and brownouts are reduced and energy security is increased this way. With the use of alternative sources the price security also increases since the reliance on the conventional energy sources, hence the price fluctuations, diminish.

The alternative sources of energy have been more costly than depleting conventional energy sources and therefore historically have been unattractive for investors, but this trend is changing. For example, by 2004 the cost of wind power conversion had dropped by 80% over a time span of 30 years and the installed wind power capacity had been increased significantly (The National Commission on Energy Policy, 2004). Although it could have had the same fate with the wind power today, neither the wave power nor the tidal power could get a similar attention and they still remain a part of novel technologies to be explored (Brown et al., 2006). Countries that push ahead with the research on ocean power conversion include United Kingdom, France, Sweden, Norway Netherlands, Denmark, Sweden, Ireland, Portugal, Spain, Canada, Russian Federation, China, India, Korea, Australia, and Japan (WEC, 2004; 2007). The United States has been a part in this competition with promising attempts such as the Hydrokinetic and Wave Energy Technologies Technical and Environmental Issues Workshop funded by the Wind and Hydropower Technologies Program of the Department of Energy (Schwartz, 2006), the research and publications by Mineral Management Service (MMS), Electrical Power Research Institute (EPRI), with contributions from the private sector and academia.

In the past two centuries, the energy consumption per capita increased by a factor of 20, in excess of the 6-fold increase in the world population. More than 80% of this energy is supplied by fossil fuels around the globe and similarly in the United States. At the present time only 13.5% of the global primary energy is met by renewable resources although they are capable of meeting many times the present global demand (Asif and Muneer, 2007). The coasts are among the world's fastest growing settings with the

population pressure straining water supplies. At a regional scale the picture is not very different. More than half the population of the United States lives within 80 km of coastlines near ocean energy resources (EPA, 2005). The growing population in the states along the southeast coast (North Carolina, South Carolina, Georgia and Florida) demands more energy supply every year while putting the strain on the environment. The total CO_2 emission from fossil fuel combustion in Georgia increased by 35% over the years from 1990 to 2003. In the same epoch, CO_2 emission from electric power generation also increased by 42%. In the other three states the increase due to fossil fuel combustion is about 35% to 45% whereas the increase due to electric power generation is even higher, about 42% to 73%.

Given the current and projected global energy demand, any alternative energy source deserves to be investigated for its feasibility. Being clean and renewable sources of energy that are vastly unexploited, ocean tides and waves are promising areas of research. The regular tide and powerful wave climates in many locations that suffer drinking water supply shortages are ideal for tidal and wave-power generation to power desalination. Similarly, clean hydrogen can be produced with ocean energy directly on shore or offshore. In addition, artificial reefs have been proposed to incorporate ocean energy devices. Both wave energy and in-stream tidal modules have been successfully designed for incorporating into breakwaters, coastal defenses, land reclamation schemes and harbor walls. Recent developments have reduced the environmental impacts by completely submerging the ocean energy devices. Various independent studies have shown that the impact on fish and marine mammals is low due to the slow motion of such devices (Devine Tarbell & Associates Inc., 2006). There are many emerging technologies

around the world to convert the power from these resources to electric power. Eventually, the first stage in conversion of these resources to useful energy is the resource mapping. A comprehensive resource mapping is expected to account for the constraints that determine the availability and accessibility of the power, as well as the level of available power.

The present study aims to assess the tidal and wave power along the Atlantic coast of the southeastern USA and evaluate the siting choices for power conversion schemes based on multiple criteria. The power of the currents are anticipated to be amplified due to the tidal rivers and natural channels that confine and concentrate the flow of water, whereas the wave power is anticipated to diminish more as waves get closer to the shore. Therefore, power potential of the waves in the offshore regime and the tidal currents in the coastal zone are investigated.

First, the related literature is reviewed in Chapter 2. It is followed by assessment of wave power potential for the Atlantic coast of the southeastern USA in Chapter 3, and the assessment of the tidal power potential for the coast of Georgia in Chapter 4. Available wave and tidal data in the region are analyzed and the details of numerical modeling for tidal currents are given in these chapters. Validation of the model with the data and a sensitivity analysis are provided. The algorithm modeling of the effect of tidal power extraction on estuarine hydrodynamics is presented in Chapter 5. The algorithm is demonstrated with two different scenarios for power extraction in one of the estuaries with large tidal power density along the Georgia coast. In Chapter 6, tidal stream power resources are analyzed further in the context of the physical, environmental and social constraints with the help of geographical information system (GIS) tools and a

methodology is created for selecting favorable sites for tidal stream power conversion projects. This methodology is applied to the Georgia coast to determine the most promising locations for tidal power conversion. Finally, the concluding remarks and suggestions for future work are presented in Chapter 7.

CHAPTER II

LITERATURE REVIEW

The literature review is presented in four parts in regards to wave power, tidal stream power, numerical modeling of tidal currents and site selection for tidal stream projects. The wave power section and tidal stream power section are split into two subsections in which power resource and examples of power conversion schemes in the United States and around the globe are reviewed.

2.1. Wave Power

The research on wave power conversion dates back a few decades, yet it still remains a part of novel technologies to be explored for many countries (Brown, 2006). Countries with wave conditions favorable for power conversion have been pursuing ways to further develop this novel technology. In 1978 a program of research and development on wave energy was established by the International Energy Agency (IEA). The program was guided by Ireland, Japan, Norway, Sweden, UK and USA and was discontinued after 1987 because the predominant opinion was that wave energy was a high-cost energy source relative to conventional and other renewable sources (IEA-OES, 2008). Although the development of wave energy continued in many countries after that, it gained more attention with the launching of the Preliminary Research Actions on wave energy by the European Commission in 1991. Today, Ireland (Mollison, 1982), Norway, UK, Denmark and Portugal (Clement et al., 2002), have political and economic governmental support

for the technology. In the United States, Electric Power Research Institute (EPRI) has issued a series of reports on the wave energy potential of selected sites with high wave energy and relatively long measurement records (EPRI, 2006). In 2005 USA Department of Energy sponsored the Hydrokinetic and Wave Energy Technologies Technical and Environmental Issues Workshop as a part of the Wind and Hydropower Technologies program (Schwartz, 2006). Also, the Minerals Management Service (MMS) under the U.S. Department of the Interior was given jurisdiction over Renewable Energy and Alternate Use Program projects in Federal waters with the Energy Policy Act of 2005 (MMS, 2006b).

2.1.1. Wave Power Resource Mapping

The MMS has issued a series of white papers and prepared a programmatic environmental impact statement for wave energy generation on the USA outer continental shelf in 2007. According to these reports, the annual average wave energy along the USA coastline is about 2100 TWh, which is a significant source when compared to the USA total electricity demand of 11,200 TWh. This estimate was made at a water depth of 60 m irrespective of the distance from the shore. Wave power in USA offshore regions range from 2 to 6 kW/m in the mid-Atlantic, 12 to 22 kW/m in regions with trade winds, and 36 to 72 kW/m along the northwestern USA coast. In the last few decades various locations have been investigated for the availability of wave power for power conversion. Studies on wave power potential of the UK (Crisp and Scott, 1981; Salter, 1974; Winter, 1980), Denmark (Kofoed et al., 2006), Belgium (Beels et al., 2007), Portugal (Pontes et al., 2005), Baltic Sea (Bernhoff et al., 2006; Henfridsson et al., 2007),

Hawaii (USA) (Bretschneider and Ertekin, 1989), New England (USA) (Walker et al., 2005), North Carolina (USA) (Hagerman et al., 1989), California (USA) (Beyene and Wilson, 2007; Kim, 1997), India (Baba, 1987; Sivaramakrishnan, 1992), Argentina (Lanfredi et al., 1992), Brazil (Beserra et al., 2007) and Australia (Harries et al., 2006) can be found in the related literature. Developments in New Zealand, Japan, Korea, Norway and Sweden are also cited (Boud, 2003). Based on these regional studies, annual wave power potential in a more regional scale is given for various locations in Table 2.1 (Baba, 1987; Bedard et al., 2005; Beels et al., 2007; Beyene and Wilson, 2007; Boud, 2003; Bretschneider and Ertekin, 1989; Clement et al., 2002; Cornett, 2006; Hagerman et al., 1989; Pontes et al., 2005; Sivaramakrishnan, 1992; Walker et al., 2005; Winter, 1980). On a macro scale the wave energy in the USA, Canada, Japan, and Australia appear to be comparable to each other, whereas around the British Isles it is more than twice as large (Voss, 1979). The wave power potential along the Atlantic coast of the southeastern USA has not been assessed in detail until now.

Table 2.1. Annual wave power for various locations in the world.

Location	Estimated wave power (kW/m)	Reference
Belgium	10	Beels et al., 2007
Canada	33	Cornett, 2006
Denmark	7 ~ 24	Kofoed et al., 2006
France, Atlantic Ocean	40	Clement et al., 2002
France, Mediterranean	4 ~ 5	Clement et al., 2002
Greece	2 ~ 4	Clement et al., 2002
India	10 ~ 32	Baba, 1987; Sivaramakrishnan, 1992
Ireland	57 ~ 77	Mollison, 1982
Italy	10 ~ 5	Clement et al., 2002
Japan	6 ~ 7	Boud, 2003
Norway	20 ~ 40	Boud, 2003
Portugal	30 ~ 40	Pontes et al., 2005
United Kingdom	45 ~ 75	Crisp and Scott, 1981; Salter, 1974; Winter, 1980
USA, California	10 ~ 32	Beyene and Wilson, 2007; Kim, 1997
USA, Hawaii	15	Bretschneider and Ertekin, 1989
USA, Maine	14	Hagerman et. al, 1989
USA, New England	4 ~ 22	Walker et al., 2005
USA, North Carolina	5 ~ 15	Hagerman et. al, 1989
USA, Massachusetts	5	Hagerman et. al, 1989
USA, Oregon	21	Hagerman et. al, 1989

2.1.2. Wave Power Conversion Devices

Offshore wave power conversion technology is developing with new concepts and designs every year. On the other hand, the most common offshore wave power converters can be grouped into four categories according to their working principles. These are attenuators, overtopping devices, terminators and point absorbers (MMS, 2006b). Attenuators are floating converters that are oriented parallel to the travel direction of the waves. This type of devices is known to have high survivability under extreme wave conditions. Pelamis by Pelamis Wave Power (Figure 2.1.a) and Anaconda by Checkmate Sea Energy (Figure 2.1.b) are examples of this technology. Pelamis is a 750 kW machine, 120 m long and 3.5 m in diameter. Three of these devices have been installed and are operational off the Atlantic coast of Portugal (Pelamis Wave Power, 2008). The

Anaconda is in laboratory testing stage (Anaconda, 2008; CSE, 2008). Overtopping devices have turbines driven by the water from their reservoirs that are filled by waves breaking at levels higher than the surrounding water level. Wave Dragon, 1:4.5 scale prototype was the world's first offshore grid-connected wave power conversion device when it was deployed off the coast of Denmark in 2003. Wave Dragon's full scale 300 m wide wave collector concentrates waves toward its 10 MW rated low-head turbines (Wave Dragon, 2003; 2008). Terminator devices, such as oscillating water columns (OWC) align perpendicular to the dominant direction of waves. The waves that are captured in a chamber act like a piston that forces the trapped air above it in and out of a turbine. Mighty Whale, tested in open-sea offshore Japan between years 1998 and 2002 (JAMSTEC, 2003; 2008), and Oceanlinx OWC (Oceanlinx, 2008) deployed off the Australia coast are examples of this type converter (Figure 2.2).

(a) (b) (c)

Figure 2.1. Offshore wave power converter examples. Attenuator types (a) Pelamis, (b) Anaconda, and overtopping type (c) Wave Dragon (Photo credits: Project websites).

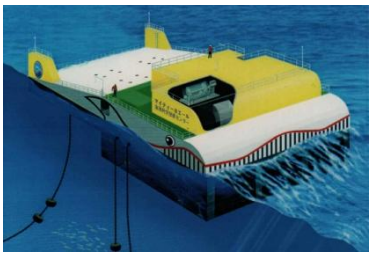

(a)

(b)

Figure 2.2. Examples of terminator type offshore wave power converters: (a) Mighty Whale (JANSTEC), (b) Oceanlinx (Photo credits: Project websites).

Point absorbers have a small horizontal to vertical dimension ratio and they move along the vertical axis with the wave action. There are many examples of offshore point absorbers with varying sizes under development around the world (Independent Natural Resources Inc., 2007). Some examples that have accomplished their laboratory scale or prototype tests are WaveBob in Ireland (Wavebob, 2008), AquaBuoy in Canada (Finavera, 2008), Archimedes Wave Swing in the Netherlands (AWS, 2008), PowerBuoy in New Jersey (OPT, 2008), MWEC in California (SARA, 2008), Aegir Dynamo in UK (ON, 2008), and Sperboy in UK (Sperboy, 2008). Some of these are as shown in Figure 2.3.

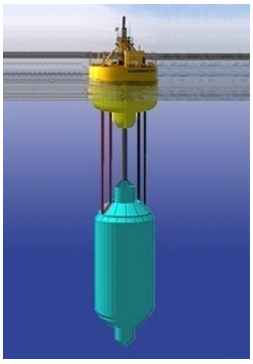

(a)

(b)

(c)

(d)

Figure 2.3. Examples of point absorber type wave power converters: (a) Wavebob, (b) AquaBuoy, (c) AWS, (d) PowerBuoy (Photo credits: Project websites).

2.2. Tidal Stream Power

Tides are controlled by the relative motion of the earth, the moon and the sun. They do not depend on the weather, or the daylight. Therefore, the tidal sea levels and the tidal currents can be analyzed to determine the amount and the distribution of the available power. This makes tidal power predictable and dependable. Tidal power conversion is one of the fastest growing emerging technologies in the renewable energy sector and can make a strong contribution to carbon free energy generation with the benefit of creating new sources of jobs and expanding the local industry.

2.2.1. Tidal Stream Power Resource Mapping

There are many locations with strong tidal currents around world: the Aleutian Islands (USA), the straits of Alaska (USA) and British Columbia (Canada), Pentland Firth (Scotland), between the islands of North and West Scotland, the Severn estuary (UK), the English Channel (UK), the fjords of Norway, the straits of Messina (Italy), the Bosporus (Turkey), and Magellan, Taiwan, Indonesia, Philippines and many other locations (Bryden and Melville, 2004; Charlier, 2003). In 2005, EPRI evaluated a few selected sites within the United States including Knik Arm, AK; Tacoma Narrows, WA; Golden Gate, CA; Muskeget Channel, MA; Western Passage, ME without mapping the resources (Bedard et al., 2006a). Additional favorable sites exist in Puget Sound, WA; Cook Inlet and the Aleutian Islands, AK; Southeast Alaska, New York, and Connecticut among others. The findings show that besides large scale power conversion, tidal streams may serve as local and reliable energy sources for remote and dispersed coastal communities and islands. Although the extractable resource is not completely known,

assuming extracting 15% of the available power, EPRI has documented tidal stream power levels up to 240 MW in Alaska, 166 MW in Nova Scotia, 30 MW in New Brunswick, 7.1 MW in Maine, and 2 MW in Massachusetts (Hagerman and Bedard, 2006a; b; Hagerman et al., 2006a; Hagerman et al., 2006b; Polagye and Bedard, 2006). Although there are locations with very large average tidal power densities (e.g. more than 7 kW/m^2 at Chatham Strait, AK and at Petit Passage, NS), these locations do not necessarily have the largest power. This is due to the fact that the tidal power density is a function of velocity and it corresponds to the power per unit cross sectional area. The available power on the other hand is given by the multiplication of the power density by the available cross section. Nevertheless, the tidal power density is a very important criterion in measuring the quality of a tidal stream source. A higher power density means more energy can be converted per unit area of flow. Tidal power density distribution based on the predictions for maximum tidal currents at various locations by NOAA along the coast of the United States is given in Figure 2.4.

Figure 2.4. Tidal stream power density along the USA mainland coast based on NOAA maximum current predictions (not an indicator of the offshore extent of the resource).

2.2.2. Tidal Stream Power Conversion Devices

There are two types of power conversion from tides: utilizing the head difference by building a tidal barrage across an estuary and placing turbines directly in the tidal flow to harvest the kinetic energy from the free flow. The La Rance tidal barrage in France (Lebarbier, 1975), Jiangxia Station in China, and the Annapolis Royal Generating Station in Nova Scotia, Canada are notable examples of tidal barrages (Hammons, 1993). Although these tidal barrages have large installed capacities (240 MW, 3.2 MW, 17.8 MW, respectively) compared to tidal stream power converters, there are only a few viable locations around the world for tidal barrages. In general tidal barrages usually suffer from high infrastructure cost and environmental issues. Flooding and mortality of fish migrating downstream are known environmental issues related with tidal barrages. Thus harvesting the tidal kinetic energy without any dam structure has gained popularity as a more environmentally friendly energy source.

The upper limit that can be converted to usable power from an ideal wind turbine was defined by a German scientist named Betz in 1920, and exclusively by a British scientist, Lanchester (Bergey, 1979) and a Russian scientist, Joukowsky within the same decade (Kuik, 2007). Therefore this limit was proposed to be called Lanchester-Betz-Joukowsky limit formally and Betz limit in short. This limit was derived by applying conservation of mass, momentum and energy to the volume of the flow passing through the turbine. The work done by the change in kinetic energy is set equal to the work done on the turbine to solve for the flow speed through the turbine, hence the mass flux. Then these are back-substituted into work done on the turbine and differentiated with respect to the wake velocity to determine the optimal ratio of the wake velocity to the undisturbed

velocity. Finally the maximum amount of work done by the turbine and its ratio to the power of undisturbed flow are calculated. This way the upper limit for the kinetic energy that can be converted from a stream tube having the same area as the disc area is 16/27 or 59.3%. In deriving this limit the fluid flow that passes through the turbine was considered to be rectilinear with a uniform pressure distribution, therefore overestimating the force applied to the turbine and the resulting turbine power. Using a model that accounts for the curvilinear streams yields a maximum efficiency of 30.1% for a horizontal axis turbine (Gorban et al., 2001).

Although tidal stream power conversion is not a brand new idea for human civilization and has real life examples from as early as the 10^{th} century (Del Rosario et al., 2006; Spain, 2008), a commercial scale energy production using the same idea has emerged only very recently (Sanford, 2003). Given its earlier development and its analogies with the tidal current power conversion, the theory and practice of wind power conversion is often revisited in the literature. The findings and experience from the wind energy industry are frequently referenced.

A variety of conversion devices are currently proposed or are under active development, from a water turbine similar to a wind turbine, driving a generator via a gearbox, to an oscillating hydrofoil which drives a hydraulic motor. Efficiency of tidal power converters are reported to be between 16% and 50% (Elghali et al., 2007; Gorban et al., 2001). Common generic types are shown in Figure 2.5. Horizontal axis turbines are usually constructed with allowance for pitching of the turbine blades in order to increase their efficiency. Pitching of the blades is also used to permit the turbine to work under a bidirectional flow condition. Alternatively, most of the horizontal axis turbines are free to

yaw to face against the tidal currents. On the other hand vertical axis turbines can rotate unidirectionally under a bidirectional flow condition. A pitching mechanism can also be integrated to the system to increase its efficiency. Earlier vertical axis turbines are known to have low starting torque, torque ripple due to pulsating during rotation, and lower efficiency. However, recent prototypes are designed so that these issues are minimized or totally resolved (Antheaume et al., 2008; Gorban et al., 2001).

In order to increase the power capture, a concentrator (also called augmentation channel, duct, shroud, diffuser, nozzle or concentrator) can be integrated to tidal turbines to increase and regulate the flow velocity around the rotor by creating a large pressure difference between two ends. Depending on the geometry of the turbine and the flow conditions different shapes are used for this purpose (HydroVolts, 2008).

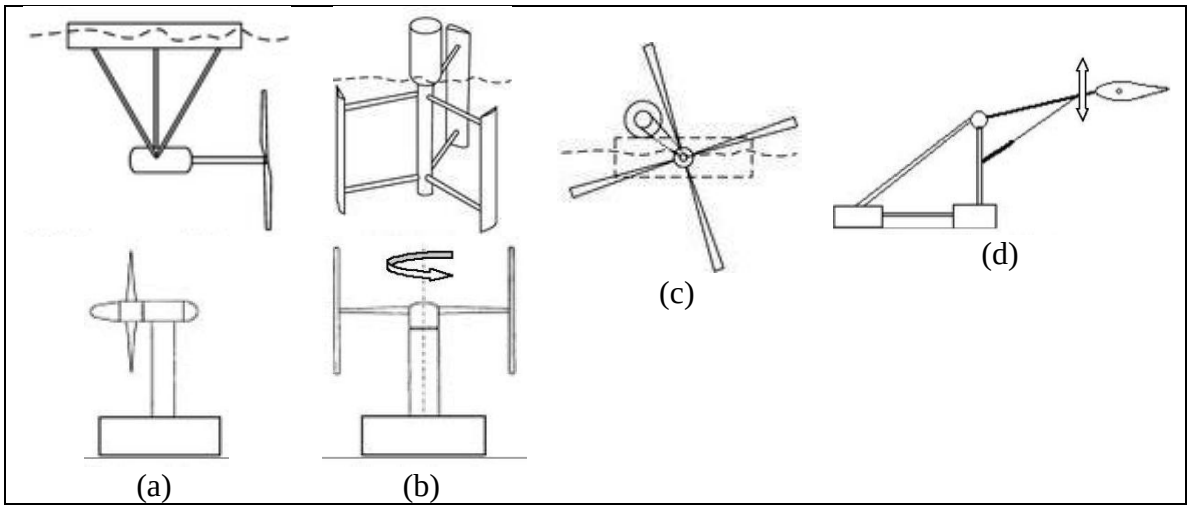

Figure 2.5. Common generic types of tidal kinetic power converters: (a) Horizontal axis (floating and rigid mooring), (b) Vertical axis (floating and rigid mooring), (c) In-plane axis (floating water wheel), (d) Hydrofoil (HydroVolts, 2008).

Many companies and organizations claim that they have a tidal power conversion system under development. Although there are many conceptual designs, the examples of

tidal power converters provided here are kept limited to the ones that have been documented in the recent literature having model or prototype studies. Marine Current Turbines (MCT), a UK based firm, developed and deployed the world's first full-scale offshore tidal turbine, 11 m in diameter with rated power of 300 kW, off the Devon Coast, UK in 2003 (Sanford, 2003). The total cost of the Seaflow project was approximately £3.5 million and was subsidized partially by the UK government, European Commission, the German government and MCT Ltd (Figure 2.6.a) (Fraenkel, 2006). Subsequently the company developed the commercial scale turbine with a pair of rotors each rated around 600 kW (Figure 2.6.b) for their second project, Seagen. A single unit has been deployed at Strangford Narrows in Northern Ireland and is generating electricity for approximately 1000 homes. It is planned to have an array of seven units by 2011. Both the Seaflow and the Seagen rotors can be raised above the water surface for relatively easier maintenance. A Norwegian company, Hammerfest Strom AS (Hammerfest Strom, 2008) deployed a 15 m diameter 300 kW prototype off Kvalsund, Northern Norway (Figure 2.6.c). In the United States, Verdant Power deployed an array of six turbines of approximately 5 m diameters each in New York City's East River (Figure 2.6.d). The company aims to generate up to 10 MW of electricity by deploying an array of 300 units in place (Verdant Power, 2008). HydroHelix, a French company has developed the Sabella tidal turbine to harvest the tidal stream power in the English Channel. The company claims that the rim that connects the tip of the blades in this design increases the robustness of the turbine (HydroHelix, 2008). A 3 m diameter prototype was deployed at Odet estuary in 2008 (Figure 2.6.e). An example of floating horizontal axis turbine type is the TidEl project by the UK based firm, SMD Hydrovision.

It consists of a pair of contra-rotating 15 m diameter, 500 kW turbines mounted on a buoyant crossbeam that is tethered to the seabed by mooring chains (Figure 2.6.f). Another British firm, Tidal Stream, has developed a similar concept, in which 20 m rotors are attached to a swing arm that is hinged to a rigid anchorage as shown in Figure 2.6.g (Tidal Stream, 2008). Both systems are designed to freely align with the prevailing tidal currents to maximize the power captured from them.

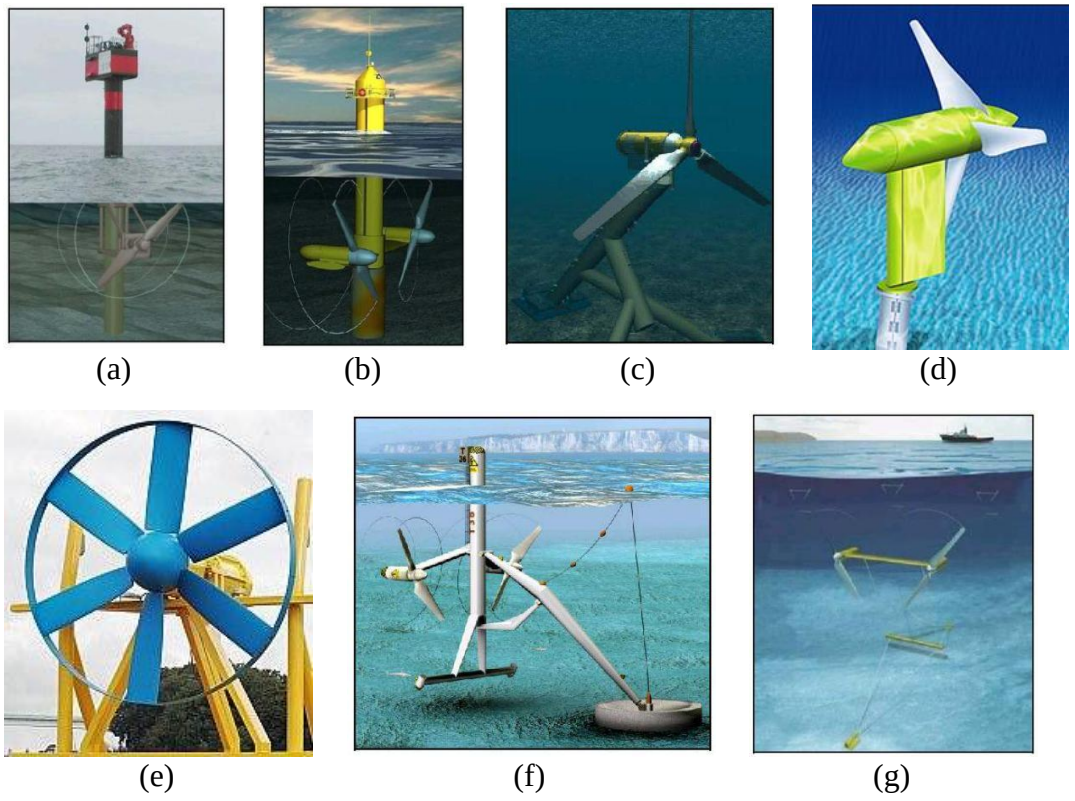

Figure 2.6. (a) Seaflow (MCT), (b) Seagen (MCT), (c) E-tide (Hammerfest Strom AS), (d) Verdant Power, (e) Sabella (HydroHelix), (f) TidEL (SMD Hydrovision), (g) Tidal Stream (Photo credits: Project websites).

In order to increase their efficiency some systems have a ducted or shrouded turbine design. Lunar Energy (UK) turbines allow an offset of 40 degrees between the tidal flow and the axis of the duct without any change in the performance (Figure 2.7.a).

Additionally, the design of the blades allows a bidirectional power capture without any yawing or pitching mechanism. The rotor can be inserted in and ejected as a cassette into the duct reducing the maintenance efforts. A model was tested in 2004 and a 300 MW tidal farm is planned to be built in South Korea by 2015 (Lunar Energy, 2008).

Underwater Electric Kite was established in 1981 in Maryland, USA. The UEK unit is positively buoyant and attached to the seabed with a single anchorage system. Each UEK prototype is capable of producing 100 kW (Figure 2.7.b). The models were tested at Chesapeake Bay and Caqueta River (UEK Systems, 2008). In 2006 Clean Current Power Systems Incorporated (Canada) installed a demonstration tidal turbine at Race Rocks Ecological Reserve in Canada for about six months, replacing two diesel generators Figure 2.7.c. A large hole at the center of the turbine is intended for providing a passage for fish and marine life (Clean Current, 2008). Based in Ireland, OpenHydro adopted an open center turbine design, which is anticipated to meet the simplicity and robustness required for underwater turbines with its slow-moving rotor and lubricant-free operation minimizing risk to marine life (Figure 2.7.d). The turbine is a solid state permenant magnet generator encapsulated within the outer rim and has only one moving part (OpenHydro, 2008). The prototypes were tested at the European Marine Energy Centre (EMEC) based in Orkney, UK. EMEC was set up in 2003 to provide developers of wave and tidal energy devices with the world's first purpose built performance testing facility. The designers can install their devices at EMEC facilities to test in open sea conditions with a grid connection and also to evaluate their environmental impact (EMEC, 2008).

(a) (b) (c) (d)

Figure 2.7. Examples of shrouded and cased turbines: (a) Lunar Energy, (b) Underwater Electric Kite, (c) Clean Current, (d) OpenHydro (Photo credits: Project websites).

The concept of a vertical axis (also named cross flow) turbine was first developed by Georges Darrieus in 1931 as a wind turbine that has a number of airfoils vertically mounted on a rotor. Since then variations of this design were used in wind and tidal power conversion industry. A Canadian firm, Blue Energy (formerly Nova Energy Ltd.), has tested four prototypes of different sizes (4, 5 ,20 and 100 kW) of their Davis Hydro Turbine since 1980s in Nova Scotia, Ontario and Florida (Blue Energy, 2008). The Enermar Project by Ponte di Archimede International (Italy) is another example of a vertical axis tidal turbine. The Kobold turbine shown in Figure 2.8.b has a very high torque making it able to start spontaneously and it rotates independent of the direction of the current. In 2006, a 25 kW prototype with a swept area of 30 m^2 was tested in the Strait of Messina, Italy (Ponte Di Archimede International 2008). More lately the Gorlov turbine and the Achard turbine (Figure 2.8.c and 2.9.d) solved the pulsating behavior of a Darrieus Turbine. The efficiency of each design is 35% and 29%, respectively, and was shown to increase by favorable configuration of separate units (Antheaume et al., 2008; GCK, 2008; Gorban et al., 2001).

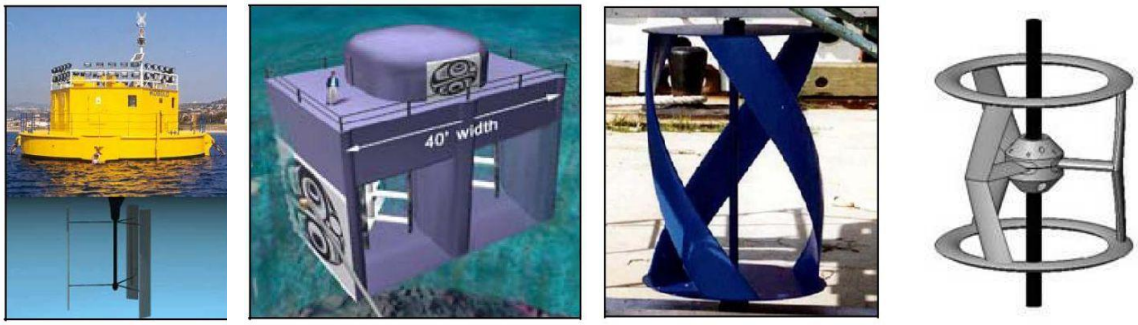

(a) (b) (c) (d)

Figure 2.8. Examples of vertical axis turbines: (a) Enermar Project (Ponte Di Archimede), (b) Blue Energy, (c) Gorlov Turbine (GCK Technology), (d) Achard Turbine (Tharvest) (Photo credits: Project websites).

Stingray by Engineering Business (UK) and Sea Snail by Robert Gordon University (UK) (Figure 2.9.a and 2.9.b) are two examples of hydrofoil type tidal power converters. The oscillatory movement of the wings pushes hydraulic cylinders to pressurize oil in order to drive the generators. Both prototypes were tested in real sea conditions in UK.

(a) (b)

Figure 2.9. Examples of Hydrofoil type tidal power converters: (a) Stingray (Engineering Business), (b) Sea Snail (Photo credits: Project websites).

The converters are usually scalable up or down within a certain limit. Some of the designers follow a modular approach in which comparatively smaller units are planned to be used in the form of a tidal farm or a tidal fence to increase the power capture. Additionally, there are also small scale projects such as Garman turbines by Thropton Energy Service which provide 2 kW water current turbines that can operate flow speeds as low as 0.5 m/s and at depths 1.75 m or more. The application areas include pumping water for irrigation, producing electricity in countries like Somalia, Sudan and Egypt (Thorpton Energy Services, 2008).

Since the tidal energy sources fluctuate by nature, it is preferred to have a system that can handle the part load and overloads. Traditionally a gearbox is used to handle this issue. However, since moving parts require frequent maintenance and the maintenance cost increases more once the device is placed underwater it is desired to keep the number of moving parts minimal for tidal stream power converters. Therefore, using a direct drive generator and permanent magnets in the rotor simplifies the overall system. A high-speed generator coupled with a gearbox is more efficient at the rated speed, but the direct drive generator is capable of working efficiently over a wide range of speeds under both part and overloads. Although the power output is not regulated when a permanent magnetized generator is used, it can be regulated for connection to the grid with the use of rectifiers. Consequently, direct power conversion systems are argued to be more robust than systems with input power regulators or gearboxes (Leijon and Nilsson, 2007).

2.3. Numerical Modeling of Tidal Currents and Effect of Tidal Stream Power Converters on Tidal Flow Regime

Tidal currents can be idealized into five generic cases considering their hydromechanics (Couch and Bryden, 2006). These are (i) offshore deep ocean, (ii) unbounded near-shore coastal region, (iii) tidal streaming through a restricted channel, (iv) hydraulic current between two water bodies that are out of phase, and (v) resonant systems. In the case of offshore deep ocean the depths are very large and the velocities are inconsiderable for power conversion. In unbounded near-shore coastal regions tidal currents are bounded mainly with a coastline in only one direction and the increase in flow velocity is due to shallowing. Although these two cases are prevalent around the world, they are not very feasible sources for power conversion considering the cut in speeds (0.5 to 1.0 m/s) of the converters. The tidal streaming case occurs when the flow is forced through a constriction or over a sill causing the local velocities to increase. A good example for this case is Strangford Lough Narrows in Northern Ireland, where the flow velocities reach up to 3.5 m/s. When two water bodies that are out of phase are connected with a channel the flow velocities increase due to the pressure head between the two ends of the channel. Naruto Strait in Japan, where there is a 5 hour phase difference causes a head difference of 1 m and flow velocities up to 5 m/s, is a good example for this case. The resonant systems occur when incoming and reflected tidal waves interfere constructively forming a standing tidal wave. Bay of Fundy and Bristol Channel are two examples of resonant systems. In nature, the tides usually occur as a mixture of the mechanisms in these different cases rather than isolated examples for each case. In order for a location to be an energetic and persistent resource it requires a unique

geography that significantly enhances one of these mechanisms or allows a favorable combination of them. Because of its complex geometry the Georgia coast is anticipated to have potential for amplified local tidal currents and detailed modeling is required to investigate this potential.

Modeling the effects of the tidal power conversion on the flow regime is important since the converters alter the tidal regime, which may result in a beneficial or an unfavorable effect on the local ecosystem (Pearce, 2005; Scott, 2007). These effects can be felt kilometers away from the converters and therefore modeling of the tidal currents at an estuary scale is warranted. Additionally, the estimates for available power only based on undisturbed flows turn out to overestimate the real available power when there is extraction (Bryden et al., 2004). Two dimensional numerical models that solve the shallow water equations such as MIKE21 (DHI, 2008), TELEMAC (TELEMAC, 2008), DIVAST (CU, 2008), TIDE2D (Sutherland et al., 2007; Triton Consultants Ltd., 2002) can be used for modeling tidal currents, but they are not suitable to model flow around the converters and three-dimensional full Navier-Stokes solvers are numerically too expensive to model at an estuary scale. For this reason, the energy extraction process is introduced as a momentum sink in the governing momentum equations (Bryden and Melville, 2004; Bryden and Couch, 2006; Garrett and Cummins, 2004) or an additional loss in the governing energy equation (Couch and Bryden, 2007). For one-dimensional, simple channel models, the momentum sink or the energy loss is introduced uniformly across the channel, whereas for two-dimensional models it can be introduced within each desired computational cell. In the case of simple channel models, the amount of extractable power has been estimated with one-dimensional numerical and analytical

solutions (Blanchfield et al., 2008; Karsten et al., 2008; Kowalik, 2004; Polagye et al., 2008) by ignoring the time-dependent effects and modeling steady-state flows (Bryden and Melville, 2004; Bryden and Couch, 2006; 2007; Bryden et al., 2007), and also flows driven by the phase lag between two large water bodies (Blanchfield et al., 2008b; Garrett and Cummins, 2005; Polagye et al., 2008; Sutherland et al., 2007). In numerical models where a simple channel is used to model the tidal currents the major flaw is the assumption of the constraining walls, which lead to a larger change in the water level and larger loss in the kinetic energy compared to a sea inlet (Bryden and Melville, 2004; Bryden and Couch, 2007). Although it was suggested to keep the level of energy extraction limited to 15% by EPRI disregarding the underlying hydrodynamics (Hagerman et al., 2006c), it has been proposed that even a 25 to 30% of energy extraction would have a small change in the flow speed, and may be environmentally acceptable for a tidal inlet that is energetic enough (Bryden and Melville, 2004; Couch and Bryden, 2006; Hagerman et al., 2006; Polagye et al., 2008).

In this study, Regional Ocean Modeling System (ROMS) is used to model the tidal currents. ROMS uses hydrostatic and Boussinesq approximations to solve the Reynolds-averaged Navier-Stokes equations. It is a three dimensional, free-surface, terrain-following, numerical model that has been used for various purposes in marine modeling systems across a variety of space and time scales (Haidvogel et al., 2008; Shchepetkin and McWilliams, 2005) as well as tidal simulations (Haidvogel et al., 2008; Robertson, 2006; Xiaochun et al., 2006).

2.4. Site Selection for Tidal Stream Power Conversion Projects

The choice of location for a tidal stream power converter farm depends on assessment of a number of criteria. These include the available extractable power, site characteristics, and environmental, economical and social impacts of the planned project. The available power is determined by the speed and volume of water passing through the site and together with the site characteristics such as bathymetry, water depth and the geology of the seabed, constitute part of the physical constraints of the problem. Converting tidal stream power is a developing field of research and the comprehensive evaluation of the available resource is limited. Although it is anticipated to be an environmentally benign means of energy supply, the amount of research and experience is not sufficient to derive comprehensive conclusions. Economical considerations are also based on estimations of the lifetime of the devices and strongly depend on the developments in the tidal power conversion industry and related industries. Therefore the environmental, economical and social constraints are not easy to measure. Recently, the International Electrotechnical Commission (IEC) is preparing the international standards for marine power conversion systems, TC 114 Marine Energy – Wave and Tidal Energy Converters, which addresses the evaluation and mitigation of environmental impacts, resource assignment requirements, performance measurement of converters and other related issues (IEC, 2008). Since there is not an international standard yet, usually the experience from other marine renewables and wind power conversion projects has been used in selecting the locations for conversion projects so far. The available literature also supports the idea that the constraints that affect the site selection criteria for a tidal power demonstration scheme depend on the energy output, construction methods, and

environmental, social and economic impacts of it (Devine Tarbell & Associates Inc., 2006; Fraenkel, 2006; Michel et al., 2007; MMS, 2006a; Pearce, 2005; Triton Consultants Ltd., 2002; Young, 1995). The environmental impacts of converters can be grouped as the physical impacts, such as changes in the flow patterns and water quality, and related ecological impacts on the aquatic and terrestrial life. The converters also have economical and social impact due to their energy supply for the region and their effects on the marine and land use. Commercial activities such as shipping and fishing, and recreational and touristic activities need to share or compete against each other for the space use rights.

The most important effects of converters on the environment can be listed as the effects on the water quality, aquatic life and terrestrial life, marine use and land use. The aesthetical concerns and the effects on the cultural and historic sites are additional aspects to be considered when evaluating the environmental effects (Devine Tarbell & Associates Inc., 2006). The effects on each of these have to be evaluated for different stages of the project such as installation, operations and maintenance and decommissioning. The effect on water quality during installation mainly consists of disturbance to the sediment, which results in suspension of sediment and increased turbidity. This is of more concern if the bottom sediment has contamination. However, this disturbance is expected to be less than that associated with one tidal cycle. During operation, converters alter the tidal energy flow hence the sedimentation patterns and suspension as well as the vertical mixing. Scour and loss of soft sediments might occur near the structures.

In order to avoid the adverse impact on aquatic life, habitats for endangered, protected or sensitive species should be clearly identified and avoided if possible.

Because during installation, suspension of fine sediment due to construction may have impact on the immediate surroundings, fish spawning or nursery areas and also benthic habitat. Anchor sweep and the frequency of anchor lift of the vessels used in the construction and open trenching to bury the cable where it is required causes most of the sediment redistribution. The impact of opening trenches can be reduced by plowing instead of air jetting and can be completely avoided by horizontal directional drilling, which provides installation of cables through a conduit drilled under the seabed. Noise and vibration during construction might disturb the aquatic life especially during breeding nesting and migration. However, it can be minimized by careful site selection and timing for the project. The sound levels higher than 145 dB are determined to have an effect on the behaviors of whales and sounds levels higher than 180 dB are determined to be harmful to marine mammals and sea turtles (Michel et al., 2007). The effect of noise and vibration during operation is a continuing research for the ongoing projects.

The mechanical and flow related injuries of the aquatic life from conventional hydropower facilities include impingement with screens and contact with the blades, and abnormal change in pressure gradients and water velocities. Although converters with unenclosed turbines look similar to boat propellers or hydroelectric power turbines, they operate at much lower speeds and much lower pressures than those traditional devices. The blades are usually slender and the percentage of area swept by the rotor is much smaller. This reduces the probability of fish passing through to contact with the blades. Lack of a screen or a shroud prevents injury from impingement, abrasion, pinching and grinding. The installation stage may also require permanent removal of some terrestrial habitat to construct the shore station, access roads and right of way for the transmission

lines. The disturbance to the wetlands should be kept at minimum and temporary level as much as possible and permanent changes to the hydrology of the wetlands should be avoided.

Land and marine activities in the vicinity of the project area needs to be restricted during the installation of converters. At the operation stage, fishing exclusion zones and restricted areas for recreational boats may need to be introduced. If navigation or commercial shipping cannot be avoided, enough navigation clearance should be left between the rotor blade and the devices at lowest astronomic tides.

As far as the decommissioning effects considered, disturbance due to noise and vibration, suspension of sediments due to removal of transmission lines and anchoring of vessels are all temporary. Disposal of removed structures and loss of benthic habitat may have longer term consequences.

On the other hand, some positive environmental impact may also be expected from the converters. Establishing fishing exclusion zones around converters may help increasing the amount of aquatic life by providing shelter for marine life. Project structures, such as transmission cable may serve as suitable structures for invertebrates and macro algae developing an artificial reef for the aquatic community (Devine Tarbell & Associates Inc., 2006).

Evaluation of these criteria to match the needs in a way that the consumption of material and energy is minimized requires integration of a significant amount of information, which makes utilizing computers and GIS tools extremely beneficial (Yapa, 1991). For the last 20 years GIS applications has been successfully used to assess the environmental and economical constraints, and to select suitable sites for energy projects

(Amador and Domínguez, 2005; Baban and Parry, 2001; Biberacher, 2008; Brody et al., 2006; Carrion et al., 2007; Cowen et al., 1995; Kaijuka, 2007; Larsen and Madsen, 2000; Moller, 2006; Muselli et al., 1999; Otawa, 1980; Prest et al., 2007; Ramachandra and Shruthi, 2007; Ramirez-Rosado et al., 2008; Rodman and Meentemeyer, 2006; Voivontas et al., 1998; Yue and Yang, 2007; Yue and Wang, 2006). The suitability of GIS to serve for this purpose was proposed earlier (Yapa, 1991), with its performance and shortcomings having been evaluated more recently (Domínguez and Amador, 2007).

A system for decision support for siting of wind power conversion projects was first defined in 1980 (Otawa, 1980). The system involved resource analysis, quantifying the proximities to areas of interest or special importance and excluding the restricted areas. The results were ranked and synthesized in a matrix in order to identify the most suitable locations (Figure 2.10). Through the years there has not been any significant change in the methodology and in 2000, a GIS-based approach with a similar methodology was used to evaluate sites for wind farms in the UK (Baban and Parry, 2001). Although there are significant differences between them (Herbert et al., 2007; Pearce, 2005; Turner and Owen, 2007), the essentials of wind power conversion and tidal stream power conversion are similar. Thus a similar workflow can be created to assess the suitability of locations for tidal stream power conversion projects.

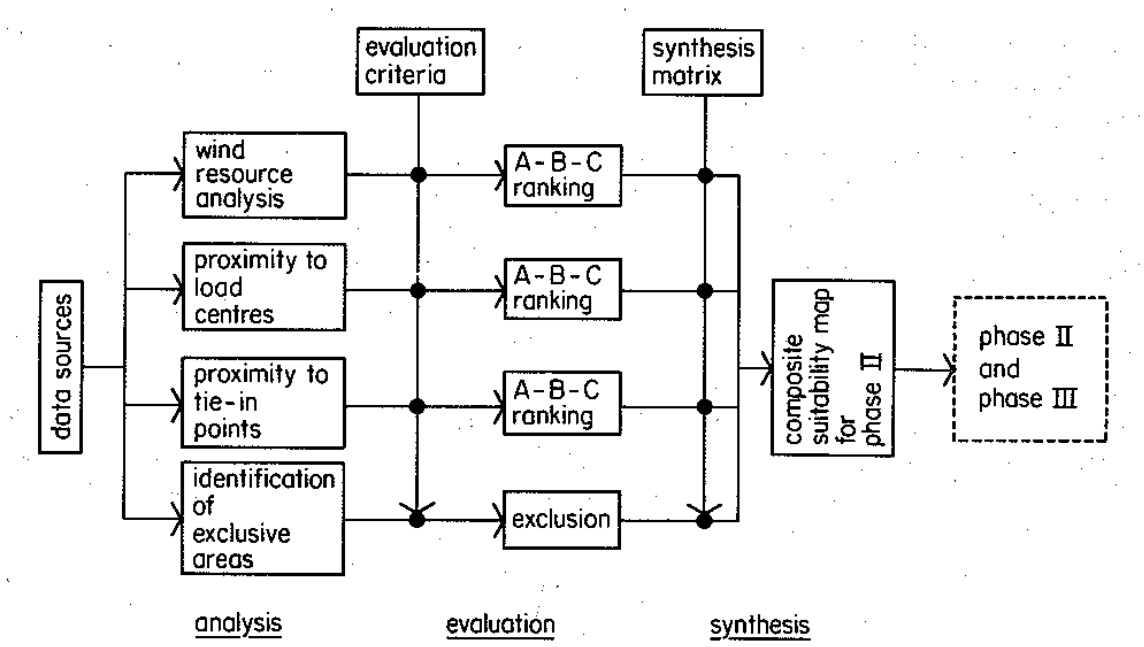

Figure 2.1. Example system of site selection for wind power development (Otawa, 1980).

There are no comprehensive guidelines on how to determine acceptable limits for changes to the wave, current, or sediment transport climates caused by current energy extraction devices. EPRI's reports on assessing the tidal power potential of North America focusing on a few specific regions with high potential to identify the environmental impacts and economical constraints and assess the available technologies for suitability, and other related studies can be used as a guide for determining the related parameters (EPRI, 2008; MMS, 2006a; Schwartz, 2006). Although they are mainly prepared for oil and chemical spill response purposes, Environmental Sensitivity Index maps also provide some essential data that can be used with the site selection methodology (NOAA, 2008c).

CHAPTER III

ASSESSMENT OF WAVE POWER ALONG THE ATLANTIC COAST OF THE SOUTHEAST USA

The wave power potential is assessed based on the data from the wave stations in the study area. First the spatial and temporal coverage, and the quality of the data are introduced. This is followed by the wave power computation and the assessment of seasonal variations in the wave climate. Finally average and maximum annual wave power maps are provided.

3.1. Wave Data

The region evaluated for offshore wave power potential is bounded by the 28ºN - 37 ºN latitudes and 82ºW - 72ºW longitudes off the coast of northern Florida, Georgia, South and North Carolina as shown in Figure 3.1. The datasets used for the wave analysis are acquired from the National Oceanic and Atmospheric Administration (NOAA)'s National Data Buoy Center (NDBC). There are more than 30 stations along the Atlantic coast of the United States that are scattered sparsely and mostly over the continental shelf. Historical wave data for varying time periods up to 30 years are available from these stations. However, only a limited number of them provide wave height and period or spectral wave data necessary to calculate the power. These are some of the Coastal-Marine Automated Network (C-MAN) and Skidaway Institute of Oceanography (SKIO) stations and NDBC moored buoys. The locations of these stations are shown in Figure

3.1. The information about data formats is available from National Oceanographic Data Center (NODC) and NDBC (NDBC, 2008; NOAA, 2008a). NDBC provides two types of data sets with regards to wave properties; standard meteorological data (SMD) and spectral wave density data (SWD). These two datasets differ in format and availability, and usually the SMD has longer data coverage starting with earlier years than the SWD. The time series of the available wave data in the region and the dataset that is used out of that available set are shown in Table 3.1. The availability of SMD, the actual availability of the wave height and period data, and the availability of the SWD are marked in the table.

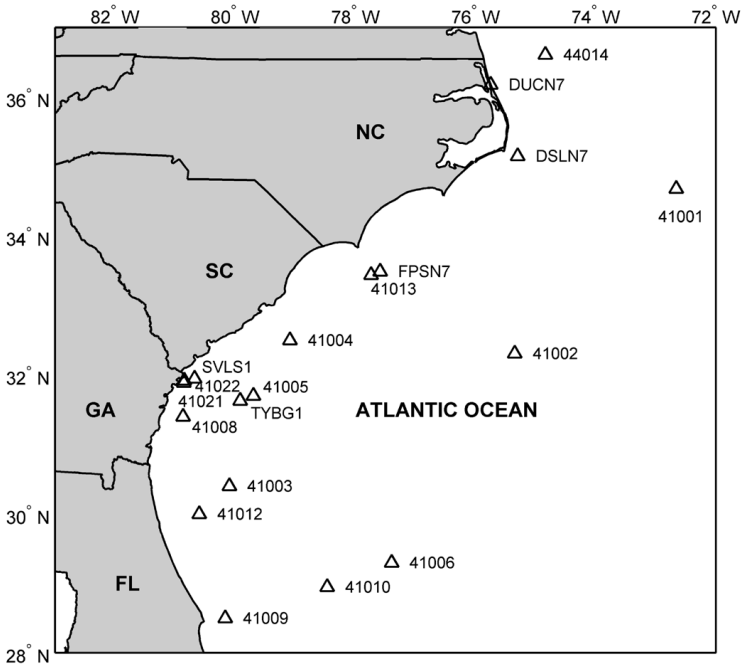

Figure 3.1. Locations and names of the wave measurement stations along Atlantic coast of the southeastern USA.

The wave heights provided with the SMD are in terms of significant wave height H_s, which are calculated as the average of the highest one-third of all of the wave heights

during the 20-minute sampling period. Similarly, the wave periods, T_m, are average wave periods of all waves during the 20-minute period (NDBC, 2008). Spectral wave data is not provided at every station. For spectral wave data, the energy in m^2/Hz, for each frequency bin (typically from 0.03 Hz to 0.40 Hz) is given. Example for SMD and SWD are given in Tables 3.2 and 3.3.

Table 3.1. List of available buoys and the datasets according to years. Availability of the SMD (light shade), wave heights and periods (dark shade), and SWD ("s") are shown.

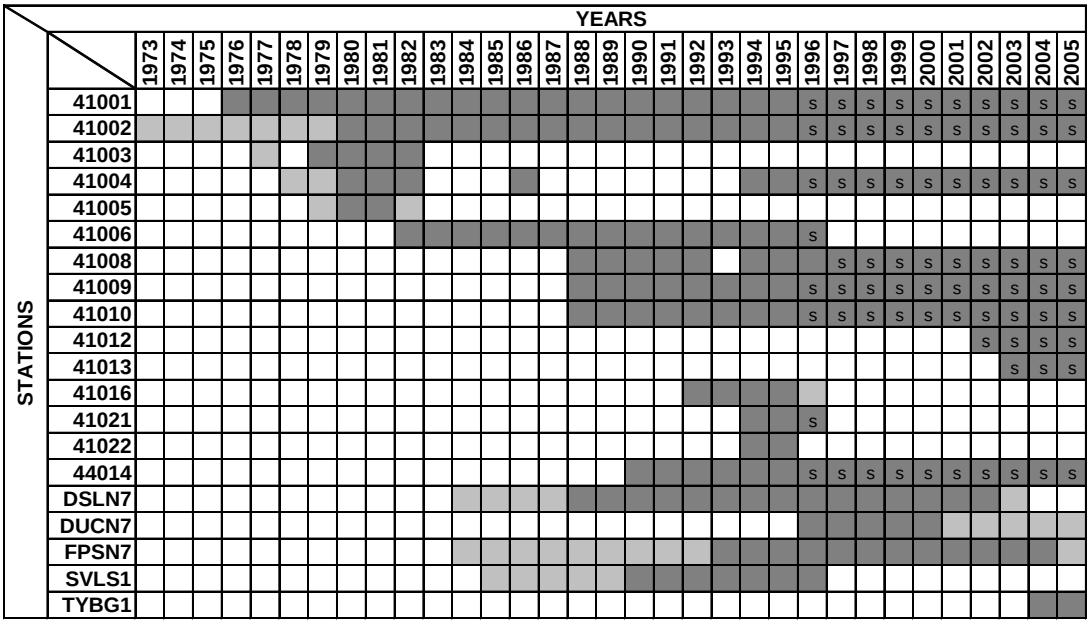

Table 3.2. Example of standard meteorological data (SMD) from the NDBC wave station 41002 for the first 12 hours of the year 2004.

YYYY	MM	DD	hh	WD	WSPD	GST	WVHT	DPD	APD	MWD	BAR	ATMP	WTMP	DEWP	VIS	TIDE
2004	1	1	0	99	1.4	2.9	1.27	6.67	5.8	999	1026.8	19	23	10.5	99	99
2004	1	1	1	124	0.5	1.2	1.25	6.25	5.68	999	1027.3	19	23	10.5	99	99
2004	1	1	2	220	4.5	5.9	1.16	6.67	5.69	999	1027.3	19.6	23.3	8.5	99	99
2004	1	1	3	247	3.4	5.2	1.25	5.88	5.88	999	1027.4	19.4	23.4	7.8	99	99
2004	1	1	4	263	3.8	4.8	1.22	7.14	5.91	999	1026.9	19.4	23.4	9.3	99	99
2004	1	1	5	287	4.1	5.8	1.29	7.69	6.08	999	1026.3	19.4	23.4	8.9	99	99
2004	1	1	6	264	2.9	4.1	1.25	7.69	6.03	999	1026	19.3	23.4	9.6	99	99
2004	1	1	7	249	2.8	3.8	1.21	7.14	6.2	999	1026	19.3	23.3	10.6	99	99
2004	1	1	8	253	3.3	5.3	1.05	7.69	6.05	999	1026	19.4	23.3	11.5	99	99
2004	1	1	9	253	4.7	6.2	1.08	7.14	6.12	999	1025.5	19.8	23.3	12.9	99	99
2004	1	1	10	283	6.4	9.8	99	99	99	999	1025.7	20	23.3	14	99	99
2004	1	1	11	283	8.5	11.3	1.13	8.33	5.47	999	1026.4	19.8	23.3	13.4	99	99
2004	1	1	12	284	7.9	9.8	1.31	8.33	5.38	999	1026.9	19.5	23.3	13	99	99

Table 3.3. Example of spectral wave data (SWD) from the NDBC wave station 41002 for the first 12 hours of the year 2004 (The table is transposed for display).

YYYY	2004	2004	2004	2004	2004	2004	2004	2004	2004	2004	2004	2004	2004	2004	2004	2004	2004	2004	2004	2004
MM	1	1	1	1	1	1	1	1	1	1	1	1	1	1	1	1	1	1	1	1
DD	1	1	1	1	1	1	1	1	1	1	1	1	1	1	1	1	1	1	1	1
hh	0	1	2	3	4	5	6	7	8	9	11	12	13	14	15	16	17	18	20	
0.03	0	0	0	0	0	0	0	0	0	0	0	0	0	0	0	0	0	0	0	
0.04	0	0	0	0	0	0	0	0	0	0	0	0	0	0	0	0	0	0	0	
0.05	0	0	0	0	0	0	0	0	0	0	0	0	0	0	0	0	0	0	0	
0.06	0	0	0	0	0	0	0	0	0	0	0	0	0	0	0	0	0	0	0	
0.07	0.07	0.04	0.05	0.06	0.03	0.06	0.06	0.05	0.04	0.05	0.04	0.04	0.01	0.06	0.02	0.03	0.02	0.02	0.04	
0.08	0.31	0.53	0.22	0.33	0.23	0.18	0.25	0.23	0.15	0.12	0.13	0.12	0.11	0.13	0.09	0.11	0.11	0.09	0.09	
0.09	0.68	0.93	0.31	0.61	0.49	0.35	0.47	0.62	0.33	0.29	0.26	0.36	0.32	0.23	0.22	0.19	0.28	0.1	0.12	
0.1	0.72	0.48	0.31	0.44	0.44	0.43	0.6	0.61	0.47	0.43	0.4	0.68	0.67	0.45	0.57	0.31	0.41	0.12	0.19	
0.11	0.41	0.2	0.28	0.58	0.53	0.7	0.57	0.58	0.38	0.6	0.65	0.87	0.74	0.61	0.9	0.37	0.32	0.19	0.29	
0.12	0.32	0.31	0.45	0.54	0.79	1.47	0.99	0.86	0.59	0.77	1.13	0.9	0.84	0.91	0.88	0.49	0.4	0.31	0.28	
0.13	0.42	0.46	0.65	0.62	0.8	1.55	1.24	0.84	0.92	0.77	0.97	0.72	0.91	1.18	0.71	0.51	0.4	0.38	0.24	
0.14	1	0.61	0.77	0.87	0.98	1.02	0.78	0.98	0.7	0.79	0.6	0.39	0.69	0.82	0.63	0.29	0.38	0.38	0.25	
0.15	1	0.56	0.81	0.86	0.67	0.63	0.72	0.87	0.46	0.58	0.33	0.4	0.42	0.73	0.58	0.26	0.39	0.32	0.29	
0.16	0.97	1.06	0.56	0.73	0.52	0.57	0.72	0.7	0.43	0.48	0.22	0.38	0.37	0.92	0.57	0.42	0.31	0.2	0.15	
0.17	0.97	0.78	0.66	0.99	0.57	0.42	0.59	0.5	0.53	0.33	0.33	0.45	0.47	0.87	0.6	0.37	0.39	0.27	0.16	
0.18	0.6	0.74	0.8	0.62	0.75	0.47	0.42	0.49	0.44	0.35	0.28	0.62	0.69	0.6	0.76	0.52	0.53	0.65	0.31	
0.19	0.43	0.69	0.62	0.46	0.56	0.4	0.48	0.32	0.31	0.33	0.21	0.65	0.71	0.7	0.49	0.71	0.55	0.6	0.43	
0.2	0.37	0.39	0.43	0.32	0.4	0.54	0.32	0.22	0.2	0.3	0.19	0.67	0.85	0.61	0.45	0.39	0.63	0.43	0.57	
0.21	0.24	0.23	0.3	0.36	0.33	0.41	0.25	0.23	0.16	0.19	0.2	0.74	0.62	0.49	0.45	0.24	0.44	0.35	0.62	
0.22	0.3	0.28	0.25	0.32	0.23	0.24	0.23	0.23	0.11	0.15	0.19	0.71	0.45	0.27	0.41	0.25	0.24	0.22	0.43	
0.23	0.26	0.23	0.23	0.22	0.16	0.21	0.25	0.23	0.1	0.15	0.2	0.42	0.38	0.2	0.28	0.23	0.14	0.31	0.21	
0.24	0.19	0.26	0.16	0.11	0.17	0.16	0.21	0.11	0.09	0.09	0.21	0.32	0.27	0.28	0.17	0.14	0.14	0.2	0.19	
0.25	0.18	0.16	0.11	0.1	0.11	0.13	0.13	0.11	0.09	0.09	0.25	0.23	0.16	0.23	0.17	0.13	0.14	0.1	0.17	
0.26	0.15	0.12	0.07	0.09	0.09	0.07	0.11	0.07	0.08	0.07	0.21	0.26	0.11	0.16	0.11	0.16	0.14	0.09	0.12	
0.27	0.09	0.12	0.07	0.09	0.06	0.09	0.06	0.05	0.04	0.08	0.21	0.25	0.12	0.09	0.1	0.17	0.11	0.13	0.09	
0.28	0.07	0.1	0.06	0.07	0.05	0.08	0.04	0.05	0.04	0.04	0.15	0.13	0.09	0.05	0.08	0.14	0.07	0.09	0.07	
0.29	0.06	0.08	0.05	0.06	0.07	0.06	0.04	0.04	0.05	0.03	0.1	0.1	0.1	0.06	0.07	0.08	0.08	0.08	0.04	
0.3	0.05	0.05	0.04	0.04	0.05	0.04	0.04	0.02	0.04	0.03	0.08	0.08	0.07	0.06	0.07	0.06	0.06	0.05	0.05	
0.31	0.05	0.05	0.03	0.04	0.03	0.04	0.03	0.03	0.03	0.03	0.06	0.07	0.06	0.06	0.05	0.05	0.04	0.04	0.05	
0.32	0.03	0.05	0.02	0.04	0.03	0.03	0.03	0.03	0.03	0.02	0.07	0.06	0.04	0.04	0.04	0.04	0.03	0.03	0.04	
0.33	0.04	0.04	0.02	0.04	0.02	0.02	0.03	0.02	0.03	0.01	0.07	0.04	0.03	0.03	0.04	0.03	0.04	0.03	0.02	
0.34	0.03	0.03	0.04	0.03	0.03	0.02	0.03	0.02	0.02	0.01	0.04	0.02	0.03	0.03	0.05	0.02	0.04	0.03	0.02	
0.35	0.03	0.03	0.03	0.02	0.02	0.02	0.02	0.02	0.01	0.01	0.02	0.02	0.02	0.03	0.03	0.02	0.04	0.03	0.02	
0.36	0.03	0.02	0.01	0.02	0.02	0.02	0.02	0.02	0.01	0.01	0.03	0.02	0.03	0.02	0.02	0.03	0.03	0.03	0.02	
0.37	0.03	0.02	0.01	0.02	0.02	0.02	0.02	0.01	0.01	0.01	0.03	0.02	0.03	0.02	0.02	0.02	0.03	0.02	0.01	
0.38	0.02	0.02	0.01	0.02	0.02	0.01	0.02	0.01	0.01	0.01	0.02	0.02	0.02	0.02	0.02	0.01	0.02	0.02	0.01	
0.39	0.01	0.02	0.01	0.01	0.01	0.01	0.02	0.01	0.01	0.01	0.02	0.01	0.02	0.02	0.02	0.01	0.01	0.02	0.01	
0.4	0.01	0.02	0.01	0.01	0.01	0.01	0.01	0.01	0.01	0	0.02	0.01	0.01	0.01	0.01	0.01	0.01	0.02	0.01	

Since the SMD is available at more stations and has longer time series, it provides a better spatial and temporal coverage than the SWD. However, the SWD is the measured spectra of the waves and it is more accurate to use for estimating the wave power. For this reason, a methodology is developed to calculate the power directly from the SMD by using the available SWD. Wave power maps are constructed using the data from each of the stations for the annual maximum and mean power. Also seasonal wave power distributions are given at each station. The level of wave energy along the southeast coastline of the United States is not anticipated to be attractive and feasible with the existing technology. Therefore, the evaluation of wave power is limited to power resource mapping only. The highlights of the wave power analysis given here are available in a published manuscript (Defne et al., 2009). The list of stations used in this study and some of their properties are given in Table 3.4. The availability of standard meteorological data (SMD) and spectral wave data (SWD), and wave height and period statistics through 2005 are shown in Table 3.5. Overall, the SMD provides a better temporal and spatial coverage with 1,419,203 hourly measurements, whereas the SWD provides only 365,825.

Table 3.4. List of stations with wave measurements within latitudes 27ºN - 38ºN and longitudes 82ºW - 72ºW (N/A: Not Available).

Station ID	Station Name	Latitude (deg)	Longitude (deg)	Distance to coastline (km)	Water depth (m)
41001	150 NM East of Cape Hatteras	34.68	72.66	323	4389
41002	S Hatteras, 250 NM East of Charleston, SC	31.33	75.44	285	3786
41003	N/A	30.4	80.1	140	39
41004	Edisto, 41 NM Southeast of Charleston, SC	32.51	79.10	64	38
41005	N/A	31.7	79.7	106	67
41006	N/A	29.3	77.3	360	1006
41008	Grays Reef, 40 NM Southeast of Savannah, GA	30.7	81.1	36	18
41009	Canaveral, 20 NM East of Cape Canaveral, FL	28.50	80.18	40	42
41010	Canaveral East, 120NM East of Cape Canaveral	28.90	78.55	235	841
41012	St Augustine, 40NM ENE of St Augustine, FL	30.04	80.55	75	38
41013	Frying Pan Shoals, NC	33.44	77.74	52	24
41021	Olympic Northeast	31.92	80.85	5	9
44014	Virginia Beach 64 NM East of Virginia Beach, VA	36.58	74.83	110	48
DSLN7	Diamond Shls Lt., NC	35.15	75.3	26	16
DUCN7	Duck Pier, NC	36.18	75.75	0	10
FPSN7	Frying Pan Shoals, NC	33.49	77.59	57	14
SVLS1	Savannah Light, GA	31.95	80.68	18	15
TYBG1	U.S. Navy Tower R8, GA	31.63	79.92	98	45

Table 3.5. Summary of data used from stations within latitudes 27ºN - 38ºN and longitudes 82ºW - 72ºW (N/A: Not Available).

Station ID	Wave data interval (yr)	Spectral wave density data interval (yr)	Sampling rate (hr)	Duration of wave acquisition (min)	Mean H_s (m)	Standard deviation of H_s (m)	Mean T_m (s)	Standard deviation of T_m (s)
41001	75 - 05	96 - 05	1	20	2.02	1.12	5.84	1.01
41002	80 - 05	96 - 05	1	20	1.83	0.99	5.72	1.01
41003	79 - 82	N/A	1	N/A	1.27	0.67	4.59	0.93
41004	80 - 82, 86, 94 - 05	96 - 05	1	20	1.32	0.70	5.12	0.90
41005	80, 81	N/A	1	N/A	1.32	0.74	4.58	1.03
41006	82 - 96	96	1	N/A	1.68	0.88	5.57	1.01
41008	88 - 92,97 - 05	97 - 05	1	20	0.98	0.48	5.01	0.99
41009	88 - 99,00 - 05	96 - 05	0.5, 1	20	1.17	0.66	5.39	1.14
41010	88 - 99,00 - 05	96 - 05	0.5, 1	20	1.55	0.83	5.70	1.07
41012	02 - 05	02 - 05	1	20	1.10	0.65	4.98	1.07
41013	03 - 05	03 - 05	1	20	1.32	0.64	5.28	0.86
41021	94 - 96	96	1	N/A	0.68	0.31	4.70	1.02
44014	95 - 05	96 - 05	1	40	1.43	0.85	5.52	1.04
DSLN7	88 - 02	96 - 02	1	N/A	1.48	0.80	5.53	0.93
DUCN7	96 - 00	96 - 99	1	N/A	0.83	0.49	5.69	1.04
FPSN7	93 - 04	96 - 04	1	20	1.36	0.68	5.23	0.78
SVLS1	90 - 96	96	1	N/A	0.88	0.42	4.78	0.77
TYBG1	04, 05	N/A	1	N/A	1.49	0.94	N/A	N/A

3.2. Wave Power Computation

Since the SMD are available at more stations than the SWD and they cover longer time periods, it is preferred to use them in calculating the wave power. However, using only a single wave height and a single average period to represent a spectrum of waves introduces errors in calculating the power. In order to have larger temporal and spatial coverage and space and to account for the error introduced by using the SMD the following method is used. The wave power per unit crest for a monochromatic wave can be calculated by

$$P(H,T) = \frac{1}{8} \cdot \rho \cdot g \cdot H^2 \cdot C_g \tag{3.1}$$

where $P(H,T)$ is power calculated using a single wave height and a single period, ρ is the density of water, g is the gravitational acceleration, H is the wave height and C_g is the speed of the wave group or the speed of the energy, which is given by

$$C_g = \frac{1}{2}\frac{\omega}{k}\left(1 + \frac{2 \cdot k \cdot h}{sinh(2 \cdot k \cdot h)}\right) \tag{3.2}$$

where ω is the angular frequency, k is the wave number, and h is the water depth. The power of irregular waves in a real sea state can be described by superposition of infinite number of regular waves with different heights and frequencies (Cornett, 2006; Smith et al., 2004; Tucker, 2001). Hence the frequency spectrum can be used to define power as

$$P_{spectral} = \rho \cdot g \cdot \int_{f=0}^{\infty} S(f) \cdot C_g(f) \cdot df \tag{3.3}$$

where $P_{spectral}$ is power calculated using the wave spectrum and f is the wave frequency. In practice the wave records are finite in length and constructed with discrete sampling intervals. Similarly the frequency spectrum is also constructed with a finite number of different frequency components, which yields

$$P_{spectral} = \rho \cdot g \cdot \sum_{i=1}^{N} \Delta S(i) \cdot C_g(i) \quad (3.4)$$

where N is the number of frequency components (N = 38 for each hourly spectrum in the NDBC spectral dataset), $\Delta S(i)$ is spectral energy for each frequency component and $C_g(i)$ is the wave group speed for that component. Equation (3.4) can also be approximated in terms of Equation (3.1) as

$$P_{spectral} \approx \alpha \cdot P(H_s, T_m) = \frac{\alpha}{8} \rho \cdot g \cdot H_s^2 \cdot C_g(f_m) \quad (3.5)$$

where α is a coefficient whose value depends on the shape of the frequency spectrum that is used to define the sea state, H_s is the significant wave height and f_m is the average frequency, which corresponds to the average period of the spectrum (i.e. $f_m = 1/T_m$). For a Rayleigh wave distribution, α would have a value of 0.5. However, in order to account for the realistic spectral shapes observed for the study area, a regression analysis of the relationship between Equation (3.4) and Equation (3.5) is done using the hourly data for the measured frequency spectra and the corresponding measured significant wave heights and average periods. In order to estimate the wave power more accurately the wave group speed is calculated without the deep water assumption ($C_g = \frac{1}{2} \cdot \frac{\omega}{k}$) in contrast to some of the references in the literature. (Hagerman et al., 2006c; MMS, 2006b; Shepherd, 1999; Tucker, 2001).

The result of the regression analysis of 365,825 spectral data measurements is shown in Figure 3.2. α is found to be equal to 0.61 with R^2 = 0.81. Therefore, this empirical coefficient of 0.61, which is somewhat larger than the theoretical value of 0.5, is applied to the power calculated using the significant wave height and average period to obtain

$$P_{corrected} = 0.61 \cdot P(H_s, T_m) \tag{3.6}$$

where $P_{corrected}$ is the corrected value of the power.

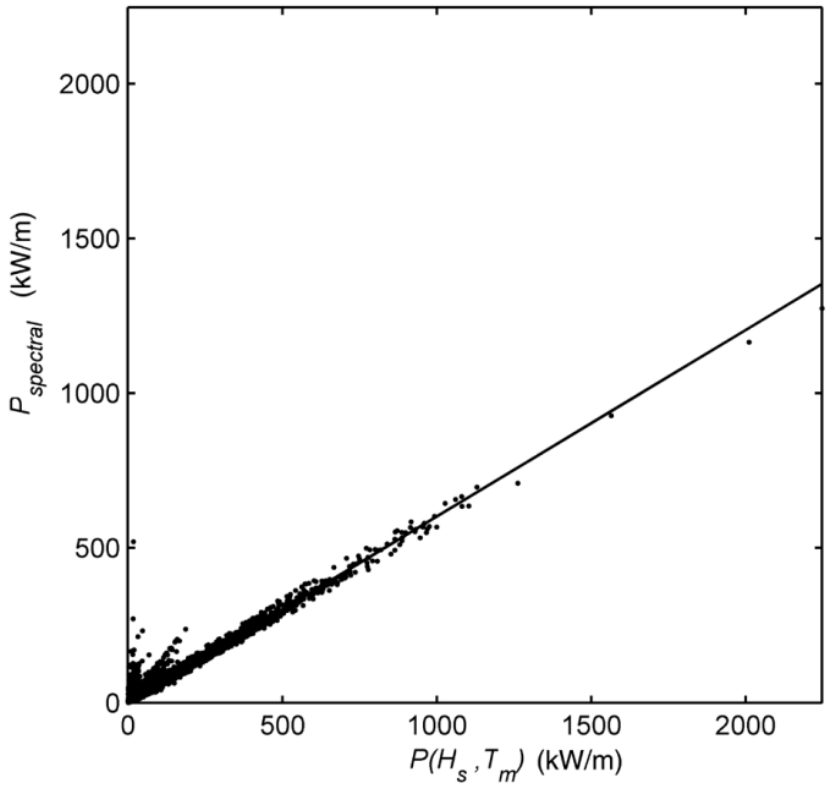

Figure 3.2. Linear regression analysis of $P_{spectral}$ vs. $P_{H,T}$ from raw data with best line fit constrained to pass through the origin. Regression coefficient is 0.61 with R^2 = 0.81.

3.3. Seasonal Variations and Annual Average Wave Power

In order to analyze the slow time variations (weeks and months) of the wave height and wave power, a moving average filter is applied by using

$$H_{filtered}, T_{filtered}(i,k) = \frac{1}{m} \cdot \sum_{j=k-\frac{m}{2}}^{k+\frac{m}{2}} H, T(i,j) \tag{3.7}$$

and

$$P_{filtered}(i,k) = \frac{1}{m} \cdot \sum_{j=k-\frac{m}{2}}^{k+\frac{m}{2}} P_{corrected}(i,j) \tag{3.8}$$

where *i* is the year, *j* is the hour of the year, *m* is the window size in hours and *k* is the resultant hour of the filter given by

$$k = n \cdot 24 \cdot (1,2,3,\dots,\frac{365}{n} - 1) \tag{3.9}$$

where *n* is increment of the filter window in days. Different combinations of the window size and the moving rate (m/n) are tested in order to remove the extreme events from the data. The window sizes used in the analysis ranges from *m* = 2 days to *m* = 30 days, with moving rates of *n* = 1 to *n* = 30 days with combinations of 2/1, 3/2, 7/1, 7/4, 15/4, 15/8, 30/1, 30/5, 30/15, 30/30. An example of filtering is shown in Figure 3.3 with filters 3/2, 7/4, 15/8 and 30/15 applied at Station 41002. Although 30/15 filter can be used for very coarse averages for the seasonal changes, 15/8 filter is observed to provide more details than 30/15 filter and still smoother results than 7/4 or 3/ 2 filters. The 15/8 filter is chosen to be used in further analyses.

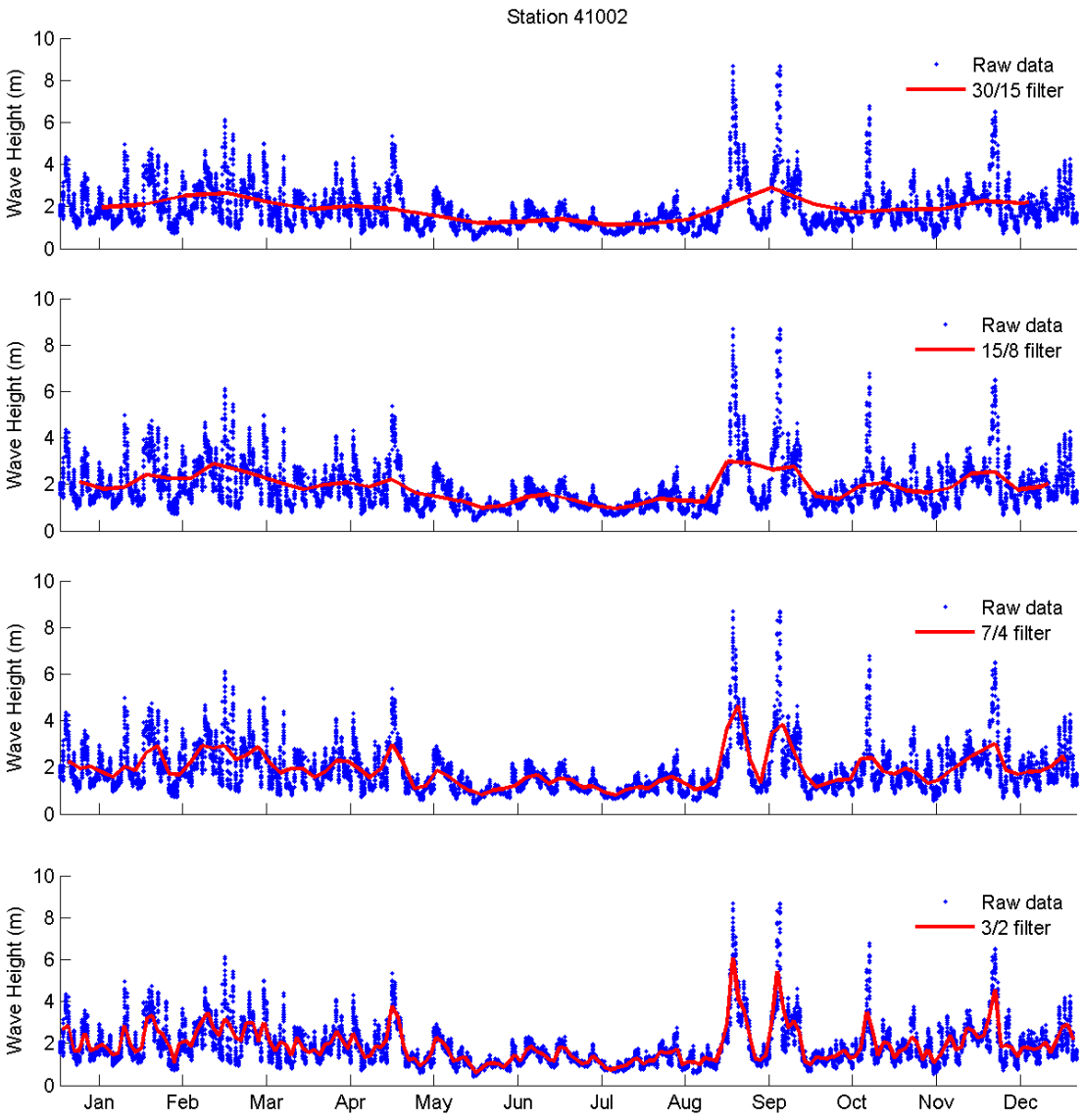

Figure 3.3. Filters (m/n) with various window sizes (m) and the moving rates (n) applied at Station 41002.

The data are also averaged over years in order to get the typical variation of wave properties in a year by

$$H_{averaged}, T_{averaged}(k) = \frac{1}{M} \cdot \sum_{i=1}^{M} H_{filtered}, T_{filtered}(i,k) \tag{3.10}$$

$$P_{averaged}(k) = \frac{1}{M} \cdot \sum_{i=1}^{M} P_{filtered}(i,k) \tag{3.11}$$

where M is the number of years of available data. The mean power at a station is estimated by calculating the mean of the averaged wave power, $P_{averaged}$. Similarly the maximum wave power for a typical year is estimated by calculating the maximum of $P_{averaged}$. Without the application of the filter, the maximum power would simply give the maximum observed power for a single extreme event rather than the power available for energy extraction.

Station 41002 is an offshore buoy (~250 km) in deep water (3786 m). This station is one of the stations with the longest continuous time series, which is convenient to assess the change in seasonal variations over the years. The variation of the significant wave height filtered by Equation (3.7) is shown in Figure 3.4. A well-defined seasonal trend in the wave heights can be seen in the figure, generally higher in the winter season (~3 m) when compared to the summer season (~1 m). The waves are usually higher than 2 m starting from October until the end of April. The isolated peaks in the figure represent isolated extreme conditions.

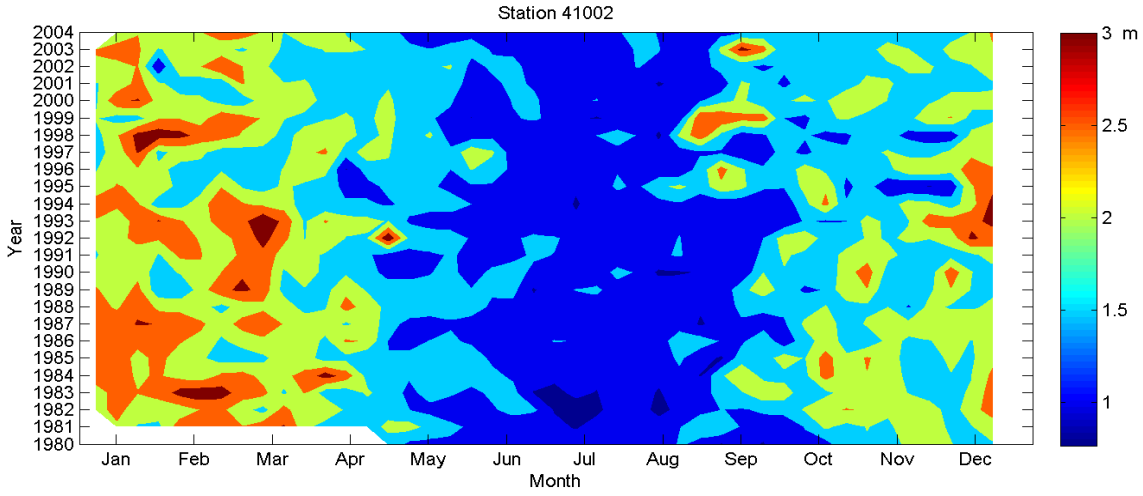

Figure 3.4. Contour plot of the average wave domain in time at buoy station 41002.

$H_{averaged}$, $T_{averaged}$ and $P_{averaged}$ for station 41002, which are calculated by Equation (3.10) and (3.11), are shown in Figure 3.5. It is seen that the average period increases with the increasing mean wave height. The cross-correlation between wave heights and periods is a known fact and its effect on wave power calculations has been studied in the past (Ozger et al., 2004; Smith et al., 2006). Since the power is proportional to the wave height squared times the period, the variation of power also follows the similar trend with the wave height and period variation. However, the effect of changes in wave height on wave power is much more significant since power is proportional to the square of the wave height.

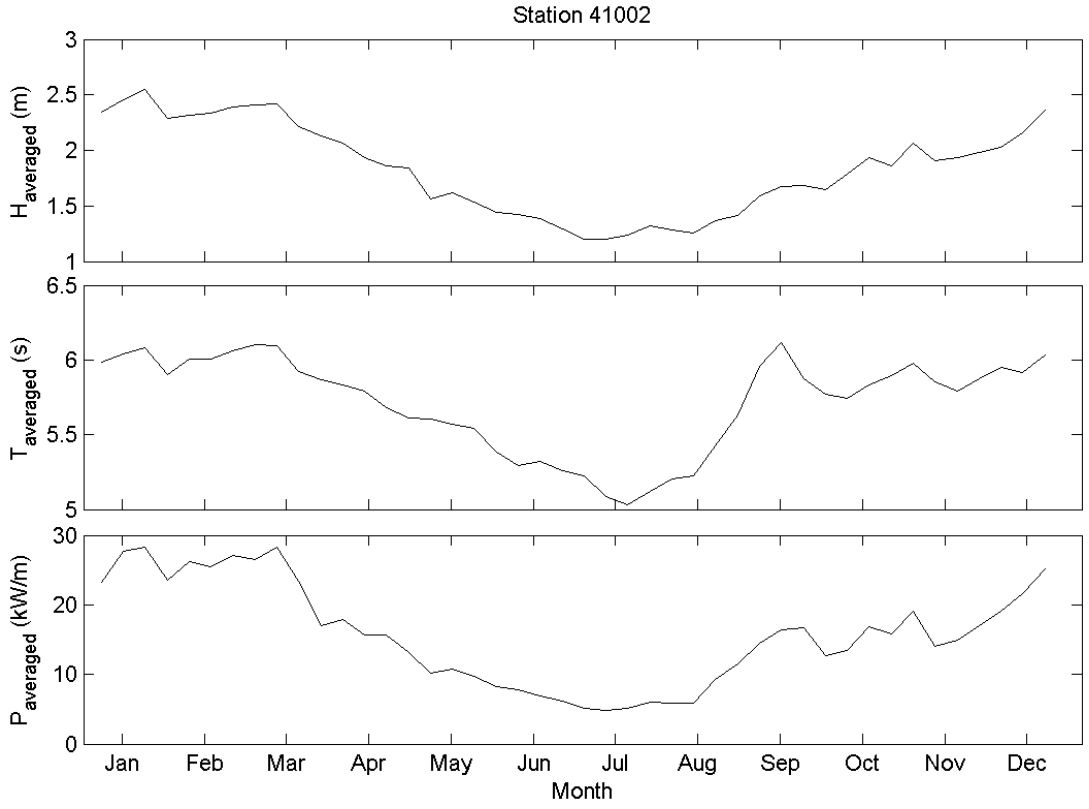

Figure 3.5. Wave height, mean wave period and power, averaged over the years, for the waves observed at buoy station 41002.

Station FPSN7 is located closer to the shore (~50 km) at shallower depth (14 m). This buoy also has a long continuous time series of the wave heights. A seasonal pattern is also seen in wave heights at this station (Figure 3.6). The low season for the wave heights is again the summer season (~1 m). However, this time the waves in winter season are not as big as they are at station 41002, below 1.5 m. The extreme conditions occurring around September seem to have a regular pattern of every 3 to 4 years, most likely due to tropical weather systems. Clearly wave heights have seasonal dependency, being higher in winter and fall season whereas less in summer season. This seasonal trend is observed at all stations and it is in correlation with the wind speeds in the region (Stewart, 2007).

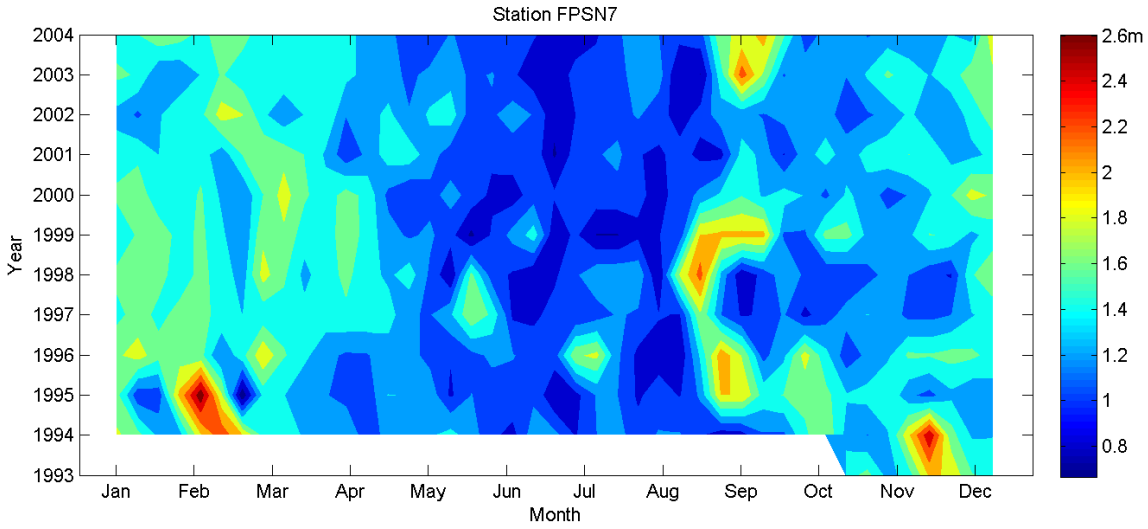

Figure 3.6. Contour plot of the average wave domain in time at buoy station FPSN7.

The maximum and mean wave heights for station FPSN7 (Figure 3.7) are smaller when compared to the wave heights at the station 41002. The maximum average wave height drops from 2.5 m at 41002 to 1.75 m at FPSN7. Similarly the range of the average

period drops from the limits 6.5 ~ 5 seconds to 5 ~ 4.5 seconds. Consequently, the available power is also decreased, but has a similar pattern to power at 41002; smaller in the summer season and increasing in the fall season towards the winter and decreasing in the spring again. A difference in this trend is observed for the station FPSN7 in the fall, where extreme conditions are observed sporadically. Although the wave power is larger at 41002 than FPSN7, the minimum mean power is not drastically different, from ~12 kW/m to ~7 kW/m, when compared to the change in the distance to the shore from ~250 km to ~50 km. Comparing Figures 3.5 and 3.7, the drop in the range of power is seen to be from 21 ~ 4 kW/m to 11 ~ 3 kW/m.

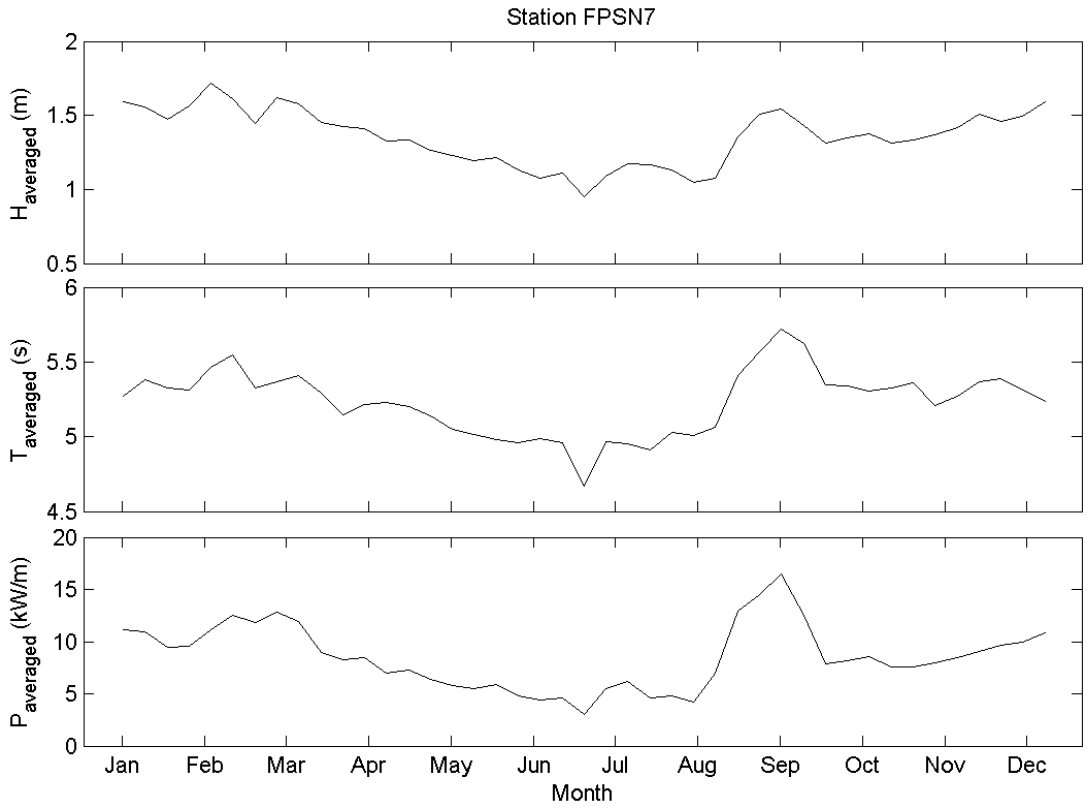

Figure 3.7. Wave height, mean wave period and power, averaged over the years, for the waves observed at buoy station FPSN7.

The maximum, mean and minimum power along with the depth at each station are given in Table 3.6. The spatial distribution of the wave power is shown in Figure 3.8. The diameters of the circles in the figure represent the amount of wave power computed for each station. The larger outer circle represents the maximum, and the smaller inner circle represents the mean wave power for that location. These values are determined by calculating the maximum and mean of $P_{averaged}$, respectively. The wave power at station TYBG1 cannot be calculated since it was found out that only wave heights, but no wave periods were available at this station. Also wave power at station 41013 is not shown in Figure 3.8 since it is located very close to station FPSN7. The offshore waves have more power than the waves closer to the shore as expected. The stations 41001, 41002, 41006 and 41010 are far offshore, which makes these locations less attractive to provide energy to the land, even though the waves contain more power.

Table 3.6. Maximum and mean wave power estimates at each station within latitudes 27ºN - 38ºN and longitudes 82ºW - 72ºW.

Station	Depth (m)	Distance to coastline (km)	Estimated maximum power (kW/m)	Estimated mean power (kW/m)
41001	4389	323	35.6	17.5
41002	3786	285	28.3	15.6
41003	39	140	13.1	5.0
41004	38	64	11.0	6.9
41005	67	106	24.9	5.4
41006	1006	360	22.9	12.4
41008	18	36	5.9	3.8
41009	42	40	12.3	6.3
41010	841	235	25.6	12.1
41012	38	75	15.6	5.0
41013	24	52	17.1	7.2
41021	9	5	3.4	1.2
44014	48	110	19.0	10.2
DSLN7	16	26	14.9	8.9
DUCN7	10	0	10.3	3.8
FPSN7	14	57	14.6	7.6
SVLS1	15	18	4.3	2.6

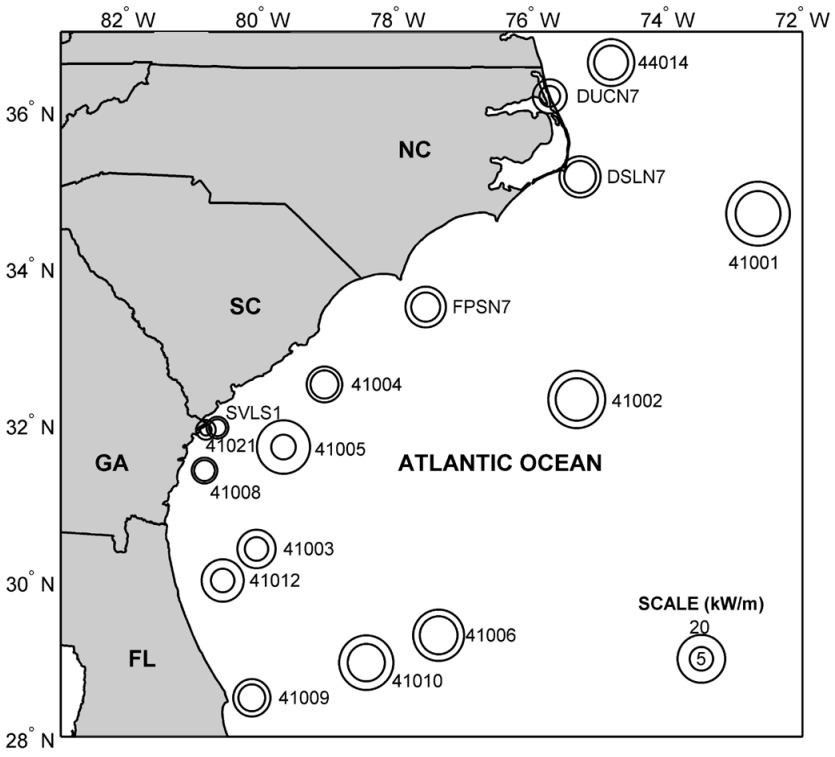

Figure 3.8. Estimated wave power, $P_{averaged}$, along Atlantic coast of the southeastern USA (outer circle: maximum, inner circle: mean).

A contour plot of the wave power based on the available data from the stations is shown in Figure 3.9.a. The power contours are seen to follow the underlying bathymetry contours shown in Figure 3.9.b. There are several possible reasons for this. First, as the waves propagate they lose energy due to dissipation. The dissipation of the energy is due to viscous effects on the seafloor and breaking of the waves. Because of the broad continental shelf in the southeast coast of the United States considerable energy is lost due the effects of the sea bed such as bottom friction. Second, the fetch length in the open ocean is primarily bound by the atmospheric conditions. Closer to shore the curvature of the coast provides sheltering to significantly reduce the fetch length for winds from the North or West. Therefore, the waves generated offshore are larger.

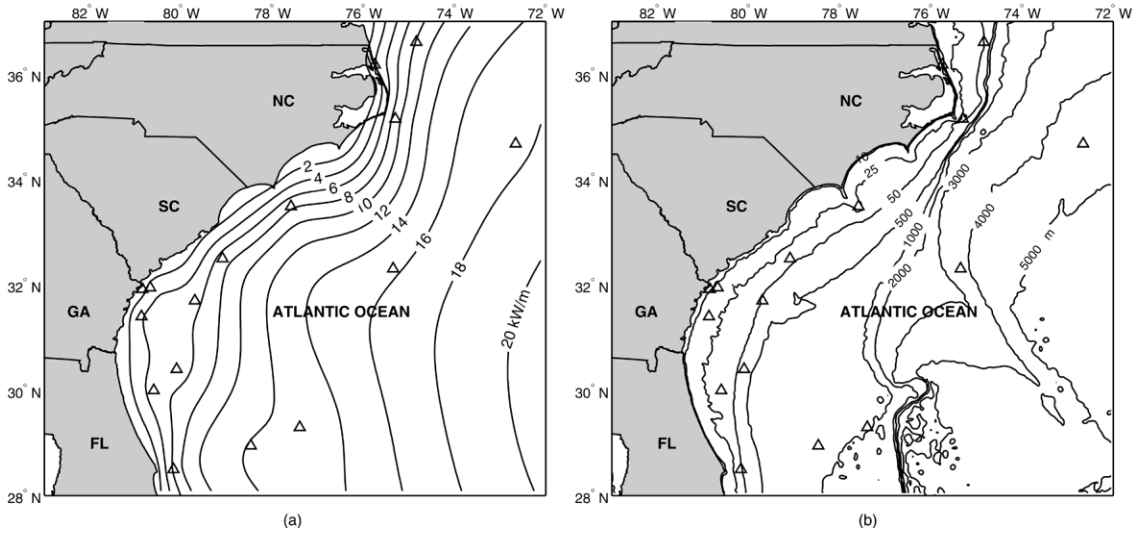

Figure 3.9. Contour lines of (a) the estimated mean wave power and (b) the bathymetry along Atlantic coast of the southeastern USA.

The accessible wave power is small when compared to conventional sources of energy. However, the wave power estimates are for a unit length of wave crest. When integrated along a certain length of shoreline or along an array of generators, the available power increases significantly. Although the efficiency of the power extraction depends on the type of the device, it is possible to come up with a rough estimation for the wave power output since the efficiency of most devices centers around 20% (Thorburn et al., 2004; Tsenga, 2000). For example the mean power for station FPSN7 is given as 7.6 kW/m. If a power converter like a point absorber type can extract energy from 5 m of a wave with 20% efficiency, then converted power from a single device would be 7.6 kW. A rough estimate neglecting the interactions between devices, a farm with 20 of these converters would convert 152 kW of power and an array of 20 by 20 of these devices would produce 3.04 MW of total power. Such a system would provide 2.19 GWh of energy in a month. The average monthly electricity consumption for a residential

unit in Georgia is by year 2007 is reported as 1.2 MWh (USEIA, 2009). The average monthly consumption for commercial and industrial sectors in Georgia is given as 7.3 MWh and 193 MWh, respectively. Therefore, the energy converted from waves 50 km offshore can be considered to be on the order of electricity consumption by more than 1800 residential units or 300 commercial units or 11 industrial units in the state of Georgia.

CHAPTER IV

ASSESSMENT OF TIDAL STREAM POWER ALONG THE COAST OF GEORGIA

The tidal power along the Georgia coast has been evaluated using the available data and numerical modeling. The tidal stream power is evaluated by computing the power density from the tidal current speeds using

$$P = \frac{1}{2} \cdot \rho \cdot V^3 \tag{4.1}$$

where P is the tidal stream power per unit area of flow, i.e. tidal stream power density, ρ is the density of seawater and V is the current speed. The tidal current magnitudes are computed from the available data from tidal current stations in the region and from the modeling output. The available data with regards to the tidal currents and elevations in the region are reviewed in the next subsection. It is followed by a subsection containing details of the modeling of the tidal stream flows and validation of the results. The remaining subsections present respectively the annual tidal power density, the effective power, and finally the additional power density from river discharge.

4.1. Tidal Power Density Computation from Tidal Current Data

The information about the tidal currents acquired from NOOA's Center for Operational Oceanographic Products and Services (CO-OPS) includes tidal stations in the region that provide data describing water elevations, harmonic constituents, datum values, benchmarks and some meteorological observations (NOAA, 2008d). Three of

these stations are within or near the borders of Georgia. In addition to these, there are more than 130 locations in Georgia where tidal current predictions are provided. The tidal stations and tidal current prediction locations are shown in Figure 4.1.a and Figure 4.1.b.

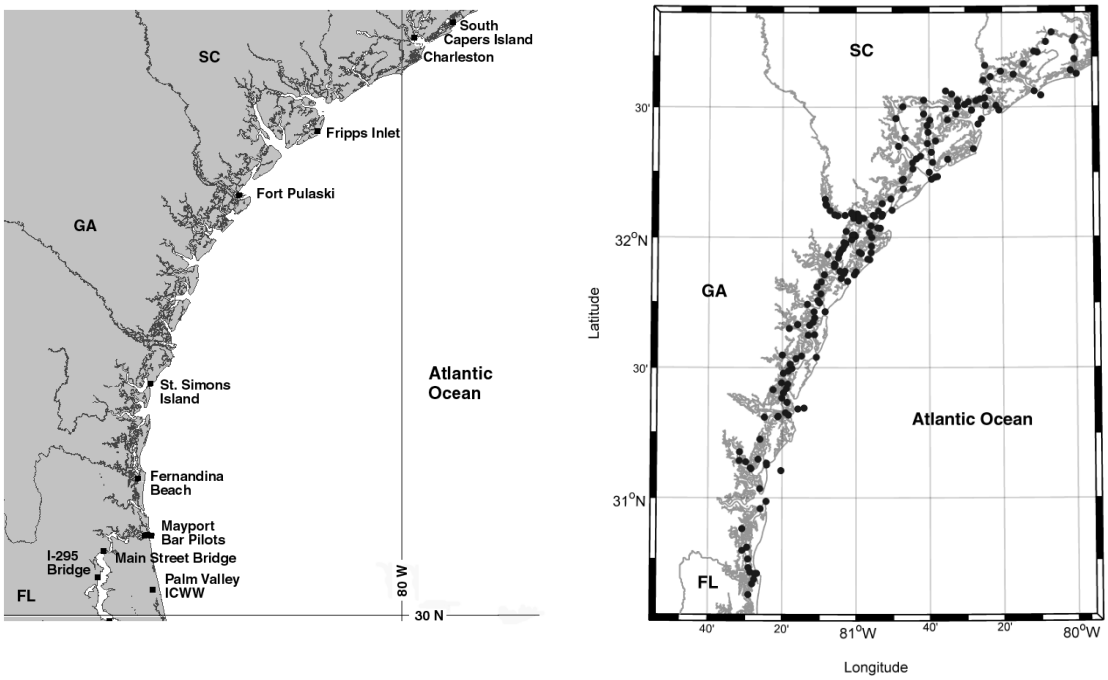

Figure 4.1. (a) Tidal stations between 30ºN - 32º30'N and (b) tidal current prediction stations between 30º30'N - 33ºN along the SE Atlantic coast of USA.

Tides can be decomposed into harmonic terms that are called tidal constituents which are periodic oscillations driven by the celestial forces. Mathematical approximation of the astronomical tides is given as

$$H = a_0 + \sum_{i=1}^{N} a_i \cdot \cos(\sigma_i \cdot t + \delta_i) \qquad (4.2)$$

where H is the astronomical tide at time t since the start of the tidal epoch, a_0 is the vertical offset, a_i, σ_i, δ_i are the amplitude, angular frequency and phase angle of the i^{th} tidal constituent (Zevenbergen et al., 2004). More than 30 constituents are applied by NOAA to calculate the tidal water levels. The tidal constituents used to calculate the

water level at the Fort Pulaski station are given in Table 4.1 as an example. The name of constituents, related amplitudes, phases and phase speeds are shown in the table. The amplitude is defined as half of the range of a tidal constituent, and phase is defined as the phase lag between the observed and the equilibrium tide. Speed is defined as the rate of change in the phase of a constituent, which is equal to 360 degrees divided by the constituent period in hours.

Table 4.1. Example of tidal constituents that are computed by NOAA CO-OPS tidal stations; Fort Pulaski station, GA.

Constituent Number	Name	Amplitude (m)	Phase (deg)	Speed (deg/hr)
1	M2	1.013	17.9	28.9841042
2	S2	0.158	45.8	30
3	N2	0.219	2.2	28.4397295
4	K1	0.11	200.7	15.0410686
5	M4	0.042	248.1	57.9682084
6	O1	0.079	206.5	13.9430356
7	M6	0.006	60.4	86.9523127
8	MK3	0.009	33.1	44.0251729
9	S4	0.007	49.4	60
10	MN4	0.02	241.9	57.4238337
11	NU2	0.044	355.4	28.5125831
12	S6	0	0	90
13	MU2	0.032	50.2	27.9682084
14	2N2	0.028	349.1	27.8953548
15	OO1	0.005	213.3	16.1391017
16	LAM2	0.018	5.6	29.4556253
17	S1	0.019	168.1	15
18	M1	0.006	249.2	14.4966939
19	J1	0.006	228	15.5854433
20	MM	0	0	0.5443747
21	SSA	0.06	51.8	0.0821373
22	SA	0.084	176	0.0410686
23	MSF	0	0	1.0158958
24	MF	0	0	1.0980331
25	RHO	0.003	204.7	13.4715145
26	Q1	0.017	198.9	13.3986609
27	T2	0.019	30.7	29.9589333
28	R2	0.011	285.6	30.0410667
29	2Q1	0.002	212.2	12.8542862
30	P1	0.039	199.8	14.9589314
31	2SM2	0.003	122.4	31.0158958
32	M3	0.024	152.1	43.4761563
33	L2	0.044	12.2	29.5284789
34	2MK3	0.005	77	42.9271398
35	K2	0.041	45.9	30.0821373
36	M8	0	0	115.9364166
37	MS4	0.023	274.4	58.9841042

The tidal prediction locations are sparsely distributed in the inlets, rivers and channels in the region, and are often named for the channel, river, or bay in which they are located or for a nearby navigational reference point. A limited number of these locations are categorized by CO-OPS as reference stations and full daily predictions for the maximum values are published for them. No current time series are available at the prediction locations. The remaining locations are categorized as subordinate stations. Specific differences are applied to the times and speeds of the predicted tidal currents at the specified reference stations to calculate the predictions for subordinate stations (NOAA, 2008d). These locations are shown in Figure 4.1.b and an example of tidal predictions computed by CO-OPS for the Savannah River area for year 2007 is given in Table 4.2.

Table 4.2. Example of tidal predictions computed by CO-OPS for Savannah River area for year 2007.

				Average Speed and Direction							
				Min Before Flood		Flood		Min Before Ebb		Ebb	
Station	Depth	Latitude	Longitude	Spd	Dir	Spd	Dir	Spd	Dir	Spd	Dir
SAVANNAH RIVER ENT. (between jetties)	11	32º 2.14'	80º 53.42'	- -	- -	2	286	- -	- -	2	110
Fort Pulaski		32º 2.2'	80º 54.1'	- -	- -	1.8	283	- -	- -	3.1	98
Fort Pulaski, 1.8 miles above		32º 2.7'	80º 55.9'	- -	- -	2.2	316	- -	- -	2.8	140
Fort Pulaski, 4.8 miles above		32º 4.5'	80º 58.6'	- -	- -	2.1	296	- -	- -	3	116
McQueen Island Cut	10	32º 3.9'	80º 59.2'	- -	- -	0.7	251	- -	- -	1.2	69
Elba Island Cut, NE of, Savannah River	10	32º 4.4'	80º 57.9'	0.1	202	1.4	288	0.1	183	2.6	104
Elba Island, NE of, Savannah River	10	32º 5.4'	80º 59.6'	- -	- -	1.1	329	- -	- -	2.5	149
Elba Island, west of, Savannah River	10	32º 5.7'	81º 1.2'	- -	- -	0.9	219	- -	- -	1.6	40
Fig Island, north of, Back River		32º 5.1'	81º 3'	- -	- -	1	280	- -	- -	1.5	94
South Channel, western end		32º 5.3'	81º 1'	- -	- -	1	300	- -	- -	1.5	122
Wilmington R. ent., south channel		32º 4.6'	81º 0.1'	- -	- -	1	32	- -	- -	1.6	206
Savannah, southeast of highway bridge	10	32º 5.2'	81º 5.8'	- -	- -	1.1	319	- -	- -	2.6	146
Savannah		32º 5'	81º 5'	- -	- -	1.6	279	- -	- -	2.2	106
Kings Island Channel, Savannah River	10	32º 7.6'	81º 8.2'	- -	- -	1.5	339	- -	- -	2.1	152
Seaboard Coast Line Railroad		32º 6.2'	81º 7.1'	- -	- -	2.4	320	- -	- -	3.5	150
King Island, west of		32º 7.4'	81º 8.1'	- -	- -	1.4	337	- -	- -	2	160
Port Wentworth, 0.2 mile above		32º 8.8'	81º 8.4'	- -	- -	0.9	22	- -	- -	1.5	210
Wassaw Island, N of E end, Wassaw Sound	10	31º 54.9'	80º 56.3'	0.1	15	1.4	292	- -	- -	2.1	108

All speeds are in knots, depths are in feet, directions are in degrees from true north.

Following the guidelines in the EPRI report for estimating tidal current energy resources (Hagerman et al., 2006c), preliminary investigations of the tidal currents can be conducted based on the tidal current predictions provided by 133 tidal current stations. The information on maximum flood and ebb flow magnitudes and their directions are provided at these stations. The maximum tidal power densities calculated using these data along the Georgia coast are shown in Figure 4.2. As seen in the figure, the tidal currents can have significant spatial variability; therefore, predictions of currents at one location are generally a poor indicator of conditions at another location, even nearby. The majority of the data is available along the navigation channels, with sparse data within the rest of the tidal area. EPRI (Hagerman et al., 2006c) suggests a methodology using continuity and the Bernoulli equation for determining the flow in different sections of a channel. This is a reasonable approach for flow along a geometrically simple channel, but is not applicable for the flow in the complex network of rivers and creeks along much of the Georgia coastline. These tidal currents can have significant spatial and temporal variability; therefore, predictions at one location are generally a poor indicator of conditions at another location. The model and the measurements used in computing the predictions are not transparent, therefore, the quality of the predictions is questionable (Rear, 2009; Zevenbergen et al., 2004). Consequently, a state-of-the-art numerical model, ROMS, is applied for simulating the tidal flows along the coast of Georgia.

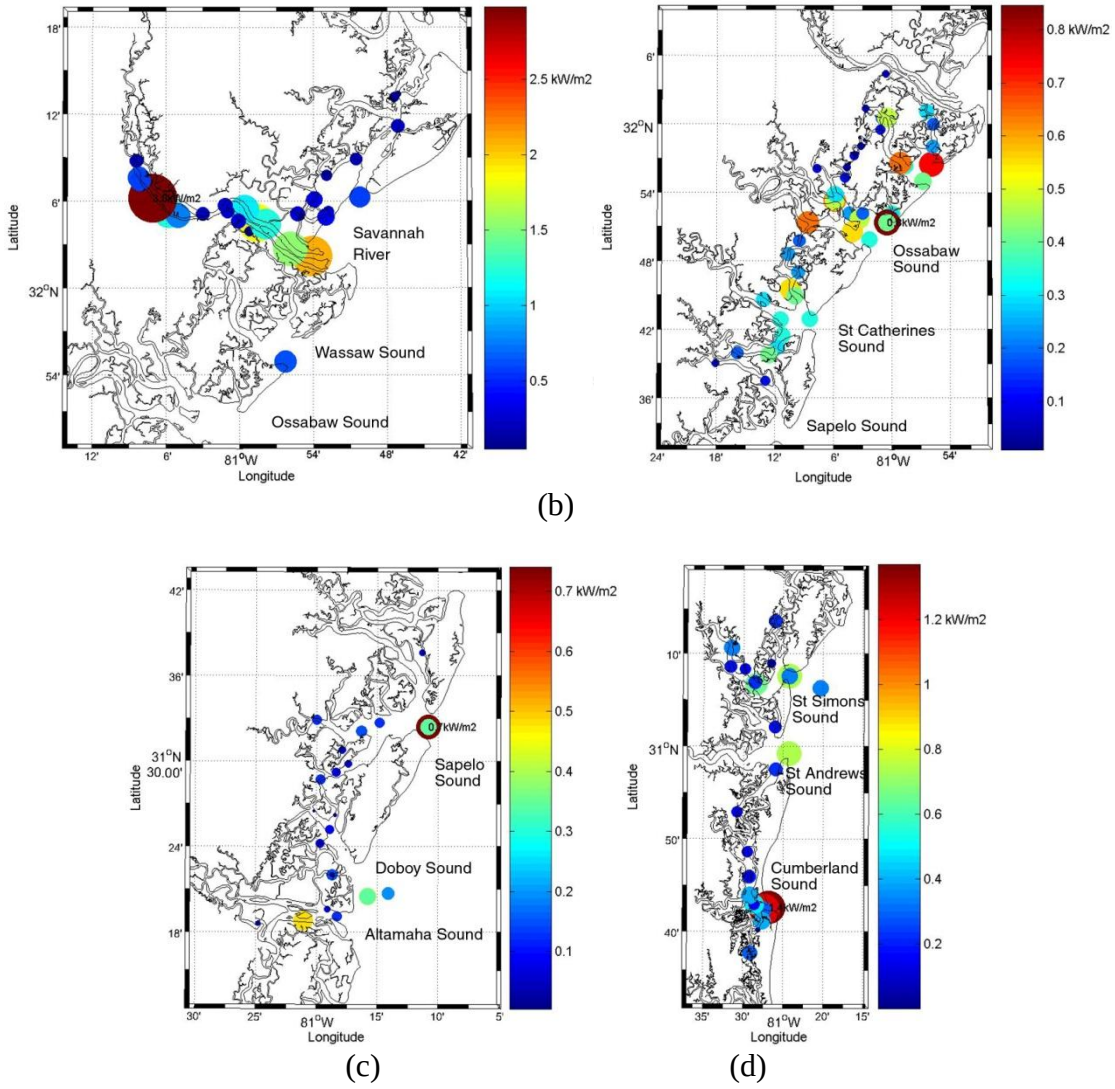

Figure 4.2. Maximum available power per unit area based on NOAA tidal current predictions along the Georgia coast.

4.2. Numerical Modeling of Tidal Currents

Although the tidal currents are a result of gravitational force of the celestial bodies on the earth, which makes them highly predictable, their magnitudes might change significantly due to the geography of the coastline. Therefore, the number of tidal stations is not enough for a comprehensive assessment of tidal power in the region. The spatial variation of tidal power should be investigated in detail by modeling hydrodynamics in the entire domain. For this purpose The Regional Ocean Modeling System (ROMS) is used. ROMS is a member of a general class of three-dimensional, free surface, terrain-following numerical models that solve the three-dimensional Reynolds-averaged Navier-Stokes equations (RANS) using the hydrostatic and Boussinesq assumptions (Haidvogel et al., 2008). ROMS uses finite-difference approximations on a horizontal curvilinear Arakawa C grid (Duran, 1999) and vertical stretched terrain-following coordinates. Momentum and scalar advection and diffusive processes are solved using transport equations and the density field that accounts for temperature, salinity, and suspended-sediment concentrations are computed with an equation of state. The modeling system provides a flexible framework that allows multiple choices for many of the model components such as several options for advection schemes (second-order, third-order, fourth-order, and positive definite), turbulence models, lateral boundary conditions, bottom- and surface-boundary layer submodels, air-sea fluxes, surface drifters, a nutrient-phytoplankton-zooplankton model, and a fully developed adjoint model for computing model inverses and data assimilation. The model also includes a wetting and drying boundary condition, which can be used for a more realistic simulation of tidal flows. The code is written in Fortran90 and runs in serial mode or on multiple processors using

either shared- or distributed-memory architectures (Open Multi-Processing or Message Passing Interface).

4.2.1. Model Properties

The preliminary grids used in this study are smaller than the final grids and can run on a desktop computer with dual processors. The later models are run on a Linux cluster computer with 10 nodes. Each node has 3942 MB RAM and 4 Intel(R) Xeon(TM) CPU 3.20GHz processors. A 32 day simulation on a grid with 400x800 computational nodes, and half a second fast time step takes about 6 days to complete using 24 processors on 6 nodes.

Tidal Forcing

In order to produce simulations of the tidal currents, the model requires tidal forcing along the boundaries of the computational domain. This forcing can be derived from a variety of sources including measurements, model simulations or the harmonic constituents provided by the NOAA CO-OPS. In this study the tidal forcing comes from the tidal database created based on the data from the numerical model ADCIRC for the Western North Atlantic Ocean (Mukai et al., 2002). The extent of the database near the Georgia coast is shown in Figure 4.3. This database includes the M2, S2, N2, K2, O1, K1, P1, Q1, M4, M6 and STEADY tidal constituents. The constituents are extracted from the tidal database and applied at the open boundary of the computational grids to force the ROMS simulations of the tidal currents.

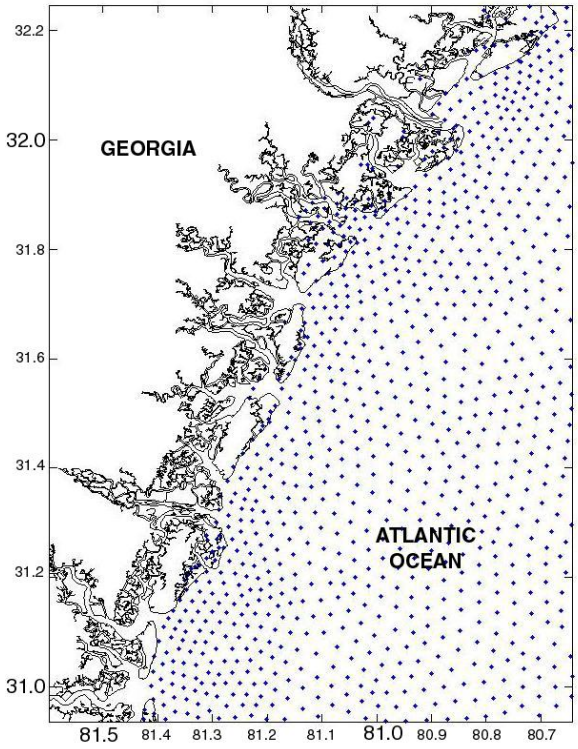

Figure 4.3. Extent of ADCIRC tidal data base near the Georgia coast based on (Mukai et al., 2002).

Coastline, Bathymetry and Topography Information

To produce accurate simulations of tidal currents, the model requires detailed bathymetric data for the generation of the computational grid. The coastline and bathymetry information is obtained from the National Geophysical Data Center (NGDC). NOAA's medium resolution shoreline (1/70,000) dataset is used for the coastline information. The medium resolution shoreline provides sufficient detail to be used to mask the grids (Figure 4.4.a). The coastline dataset is extracted using the coastline extractor available at the NGDC website (NGDC, 2008). The digital sounding data from NGDC bathymetric maps is used for the bathymetry (NOS, 2008). The digital sounding data provides detailed coverage of the bathymetry of the coastal zone as shown in Figure

4.4.b. The bathymetry measurements are with reference to the Mean Lower Low Water (MLLW), whereas ROMS uses mean sea level as the reference for depths. Therefore, the vertical datum for the bathymetry data is adjusted using MLLW and MTL values reported by NOAA at local tidal stations.

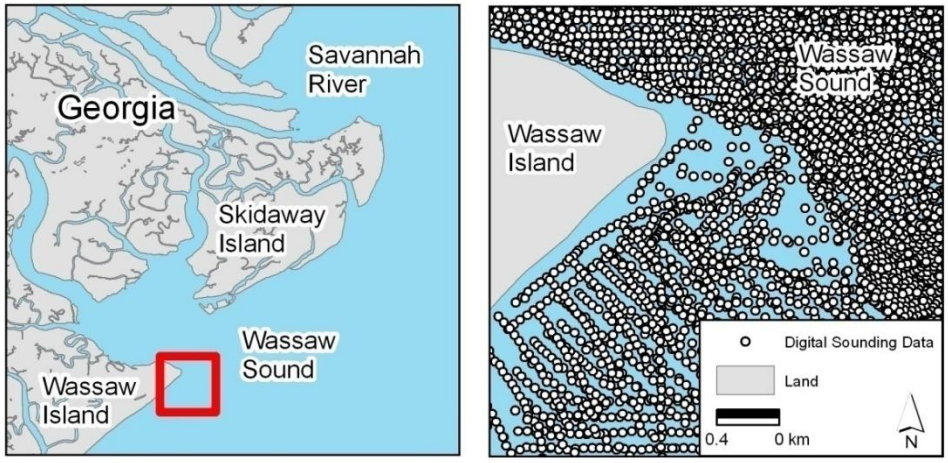

(a) (b)

Figure 4.4. Example of (a) the coastline and (b) the details of bathymetry coverage for the extent of the red rectangle shown on the left.

The wetland topography is obtained from the National Wetlands Inventory (NWI) of the U.S. Fish and Wildlife Service. The vertical datum for the wetland topography is NAVD88 and needs to be converted to the MTL for the model runs. A vertical datum conversion utility called VDatum that can generate tidal-to-geodetic offsets for most coastal locations in the USA is being developed by a joint project between the National Geodetic Survey (NGS) and NOAA's National Ocean Service (NOS, 2008). Although this utility provides coverage for the most of the USA coasts it is not available for the Atlantic coast of the southeastern USA. Therefore, the vertical datum conversion is based on the measurements available from the SouthEast U.S. Atlantic Coastal Ocean

Observing System stations (SEACOOS, 2008). The arithmetic mean of the offset between NAVD 88 and MSL at these stations (-0.15 m) is used (Figure 4.5).

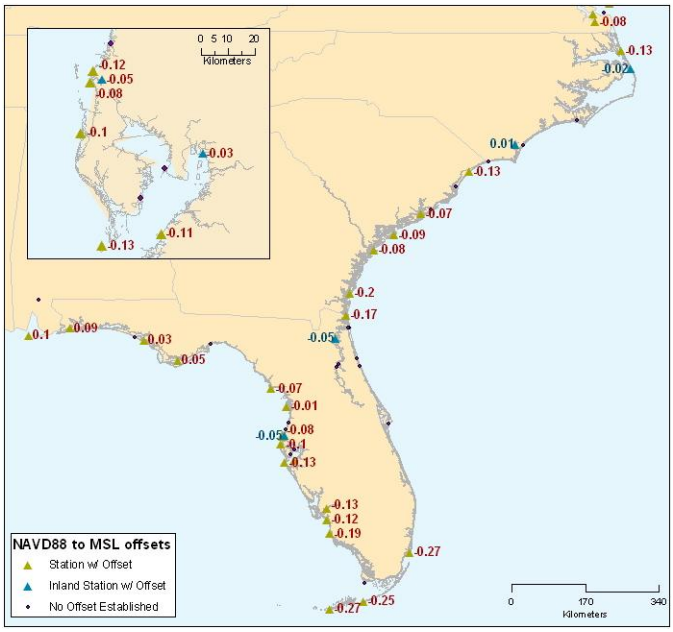

Figure 4.5. Map of the vertical difference between NAVD 88 and MSL at water level stations in the SEACOOS region (SEACOOS, 2008). Offsets indicate moving from NAVD 88 zero level to MSL zero level in meters.

Computational Grids

The computational grids are generated using SeaGrid, which is a toolbox developed for Matlab to prepare an orthogonal grid within a curved perimeter, suitable for oceanographic modeling (Denham, 2008). The bathymetric data, which is measured positive downwards from the MSL, is used to generate depths for each grid point. Grid points within the computational domain which remain permanently "dry" are determined and marked by using a masking feature utilizing the coastline data. The boundary between land and water is a solid wall boundary with free slip condition. Each grid that is created needs to be examined manually to ensure that all computational points are

interconnected with at least two other points in order for the model to run correctly. Finally, the vertical datum for each grid needs to be adjusted to the MTL before running the models. In order to simulate the tidal flows inside the estuaries, rivers, inlets and bays in more detail numerical grid resolution needs to be kept small enough to have at least a few grid cells across the narrowest channels in the model. For this reason, to keep the computational domain to a manageable size, the coast is broken up into subgrids, each to be used for separate simulations. Wherever possible, natural barriers are selected as boundaries between the different grids; and estuaries or bays are contained in their entirety within a single computational domain. The neighboring grids contain overlaps of several kilometers to ensure seamless coverage. As an example of the grids that are created, a part of the computational grid for the St. Andrews Sound is shown in Figure 4.6 with the land masking differentiating the "wet" cells from the "dry" cells.

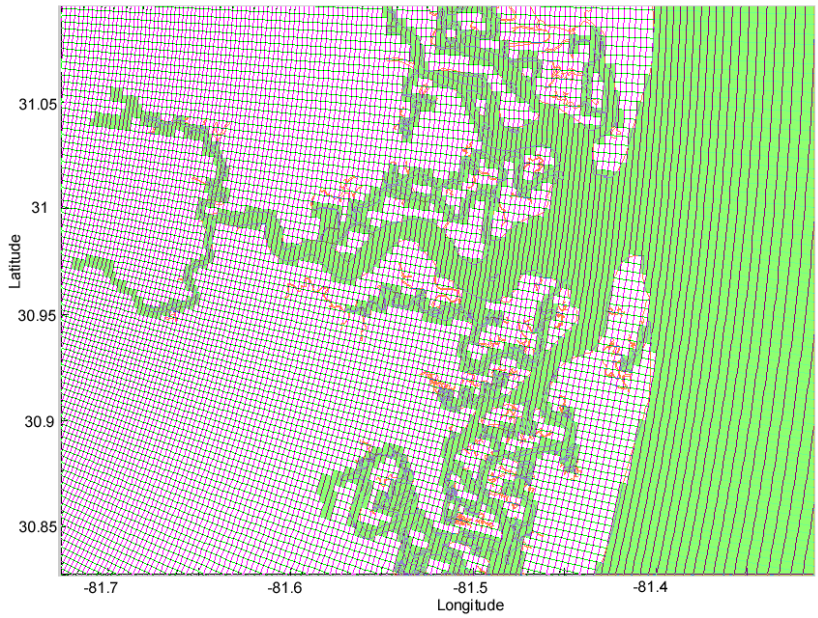

Figure 4.6. An example of computational grid and land masking from the St. Andrews Sound excluding wetlands. White cells are the dry cells and green cells are the wet cells.

A minimum clipping depth is required for the model runs to keep the "wet" cells always wet, whereas dry cells always stay dry. The wetting and drying option in ROMS allows the initially masked land cells to become wet or dry depending on the depth of the flow in that cell. For this purpose it is required to specify a minimum critical depth value under which a cell becomes dry and transport out of it is prevented. On the other hand, water is always permitted to flow into any cell. This makes it possible to account for the changes in the surface area of the water which affects computation of the tidal prism. Additionally it provides means to include the wetlands in the modeled area in the model simulations. Wetlands are neither considered to have high tidal currents nor are they suitable for placing a power converter on them, yet they might contain significant amount of water in them that moves in and out with the tides. Therefore, they are included in the model to observe their effect on the flow characteristics. The wetting and drying routine of ROMS has been used by the ocean modeling community for the last few years and the routine has been continuously evolving with changes and updates to the algorithm. The latest version of the routine at the time of this study (April 2009) is used during modeling efforts. Although this routine can be used by many researchers at the time of the study it is a relatively new routine in ROMS with some stability issues. The experience with different model grids in this study shows that the stability of the model strongly depends on the critical depth value that is used by the routine to determine if a cell is wet or dry. The overhead of the wetting and drying option is an increase in the model simulation times, which can sometimes be on the order of two depending on the ratio of wetlands to wet points within the modeled area.

In order to simulate the tidal flows inside the estuaries, rivers, inlets and bays in more detail, numerical grid resolution is kept on the order of a hundred meters. The coast of Georgia has been separated into three different grids *ga31*, *ga32*, *ga33* as shown in Figure 4.7. The northern and southern grids (i.e. *ga31*, *ga33*) have negligible overlap at their boundaries, and the middle grid (*ga32*) overlaps sufficiently with both of the grids to ensure full coverage. For each computational domain, the model is run to simulate 32 days, encompassing an entire lunar cycle starting from an arbitrarily selected date, November 1st, 2005. The constituents from the model are computed while neglecting the first 2 days to eliminate startup effects in the model.

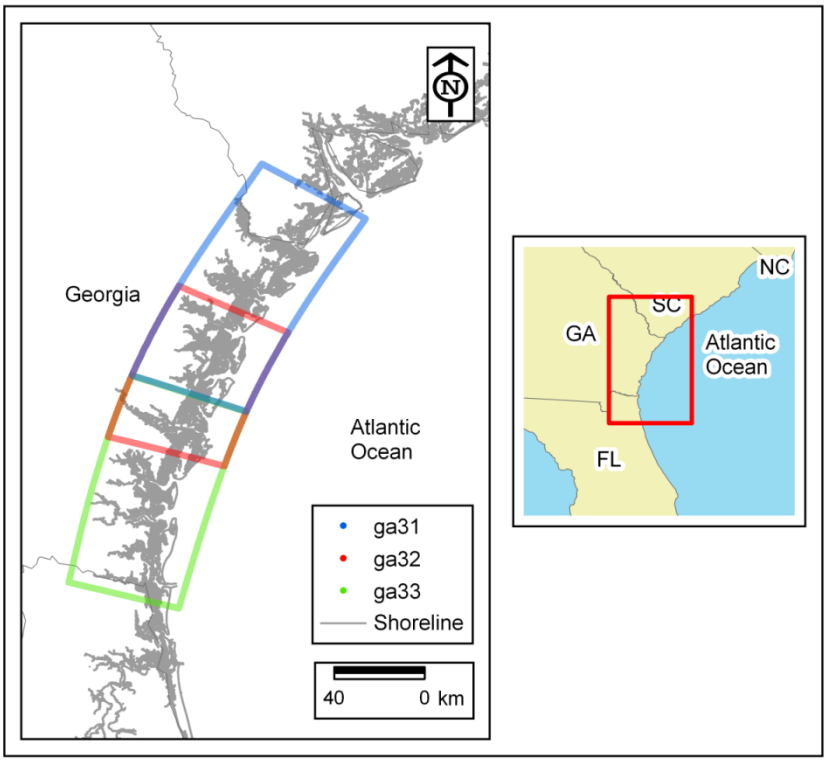

Figure 4.7. The computational grids used for ROMS simulations of the tidal currents along the Georgia coast.

4.2.2. Model Results and Validation

The model results are validated against measurements and predictions where available. The field data from different sources are used as the primary control data for this purpose. Along the coast of Georgia there are six tidal gauge stations that provide observed and predicted tidal elevation time series and harmonic constituents of tidal elevation. There are two locations where ADCP measurements by NOAA are available through NOAA's Currents Measurements for the Study of Tides (C-MIST). There are also several other locations where tidal current measurements were done (Blanton et al., 2003). The predictions of high/low tide water levels and maximum currents by NOAA are used as the secondary control data since they are predictions by a model based on measurements of unknown quality in the past. They do not provide time series, but only the maxima values, and are less reliable than the primary data, which are actual measurements.

In analyzing the model results, a set of key validation parameters are defined to compare the model results to each other and to the available data for validation purposes. The types of data that are compared are maximum currents, high/low tide elevations and harmonic constituents of tidal elevation. The validation parameters are categorized into groups according to these types and explained below in detail.

Parameters Used for Validating the Predicted Maximum Currents

a. Mean Current Magnitude Ratio of Maximum Currents (*cmgrt*)

The average ratio of the maximum current magnitudes from the model, including flood and ebb flows to the magnitude of the corresponding maximum current values from the validation data, given by

$$cmgrt = \frac{\sum_{i=1}^{N} \frac{|(cur_m)_i|}{|(cur_v)_i|}}{N} \tag{4.3}$$

where cur_m is the maximum current magnitude from the model and cur_v is the maximum current value from the validation data. i and N are the i^{th} occurrence and total number of occurrences of maximum and minimum during the simulation duration, respectively.

b. Root-Mean-Square Difference of Maximum Currents (*crms*, *fcrms* and *ecrms*)

The root-mean-square of the difference between the maximum current values output by the model and maximum current values from the data. It is an estimate for the error of the model prediction in terms of tidal current given by

$$crms = \sqrt{\frac{\sum_{i=1}^{N} \{(cur_m)_i - (cur_v)_i\}^2}{N}} \tag{4.4}$$

Current root-mean-square differences for maximum flood and ebb currents (*fcrms* and *ecrms*) are calculated using the same equation with Equation (4.4), but only the maximum of the flood (or ebb) tides are used to compare.

c. Mean Difference in Maximum Flood (or Ebb) Currents (*fcmd* and *ecmd*)

The mean difference in maximum flood current between the model output and the validation data shows whether the model produced larger flood current (*fcmd* > 0) or smaller flood current (*fcmd* < 0) than the validation data. It is given by

$$fcmd = \frac{\sum_{i=1}^{N}\left\{\left(cur_m^f\right)_i - \left(cur_v^f\right)_i\right\}}{N} \tag{4.5}$$

where cur_m^f and cur_v^f are maximum flood currents from the model and from data, respectively. Similarly, the difference in maximum ebb current between the model output and the validation data is computed by

$$ecmd = \frac{\sum_{i=1}^{N}\{(cur_m^e)_i - (cur_v^e)_i\}}{N} \tag{4.6}$$

where cur_m^e and cur_v^e are maximum flood currents from the model and from data, respectively. *fcmd* and *ecmd* are used to evaluate ability of the model to simulate the flood or ebb dominant tidal regimes.

d. Phase Difference between Maximum Currents (*cpd, fcpd* and *ecpd*)

The mean phase difference for maximum currents and the mean phase difference for maximum flood and ebb currents are given by

$$cpd = \frac{\sum_{i=1}^{N}\{(t_m)_i - (t_v)_i\}}{N} \tag{4.7}$$

$$fcpd = \frac{\sum_{i=1}^{N}\left\{\left(t_m^f\right)_i - \left(t_v^f\right)_i\right\}}{N} \tag{4.8}$$

$$ecpd = \frac{\sum_{i=1}^{N}\{(t_m^e)_i - (t_v^e)_i\}}{N} \tag{4.9}$$

where t_m and t_v are the times that correspond to the maximum tidal current occurrences in the model output and the validation data, respectively. The superscripts *f* and *e* denotes

flood and ebb, respectively. Current phase difference is an estimate to how much phase the model output lags (*cpd, fcpd, ecpd* > 0) or leads (*cpd, fcpd, ecpd* < 0) the validation data.

Parameters Used for Validating the Predicted High/Low Tides

a. Standard Deviation Ratio of High/Low Tides (*stdrt*)

It is the ratio between standard deviation of the high/low tide computed with the model and given in the data. It is an estimate of how much the model underpredicts (*stdrt* < 1) or overpredicts (*stdrt* > 1) the tidal range.

$$stdrt = \frac{\sqrt{\frac{\sum_{i=1}^{N}\{(elv_m)_i - \overline{elv_m}\}^2}{N}}}{\sqrt{\frac{\sum_{i=1}^{N}\{(elv_v)_i - \overline{elv_v}\}^2}{N}}} \tag{4.10}$$

where elv_m and elv_v are the high/low tide time series from the model and the data.

b. Root-Mean-Square Difference of High/Low Tides (*rms*, *hirms* and *lorms*)

Root mean square difference between the model output and the data for high/low tides is an estimate for the error of the model prediction in predicting the tidal elevation. It is given by

$$rms = \sqrt{\frac{\sum_{i=1}^{N}\{(elv_m)_i - (elv_v)_i\}^2}{N}} \tag{4.11}$$

The root-mean-square difference between the model output and the data for the high tides only (*hirms*) and low tides only (*lorms*) are also calculated with Equation

(4.11), but using only the water surface levels for high (or low) tides only. It estimates the error of the model in predicting the high (or low) tides.

c. Phase Difference between High/Low Tide (*phd*, *hiphd* and *lophd*)

These terms estimate how much the model output lags (*phd*, *hiphd*, *lophd* > 0) or leads (*phd*, *hiphd*, *lophd* < 0) the change in the water surface level during tides. It is calculated with the same equations for currents by substituting the high and low tide times for time.

Parameters Used for Validating the Harmonic Constituents

a. Amplitude Difference for Modeled Harmonic Constituents (*amd*)

This parameter shows how much the model underpredicts (*amd* < 0) or overpredicts (*amd* > 0) the amplitude of the k^{th} harmonic constituent.

$$amd_k = (amp_m)_k - (amp_v)_k \tag{4.12}$$

where $(amp_m)_k$ and $(amp_v)_k$ are the amplitudes of the k^{th} harmonic constituent computed by the model output and given in data, respectively.

b. Percentage Amplitude Difference for Modeled Harmonic Constituents (*amdp*)

$$amdp_k = \frac{(amp_m)_k - (amp_v)_k}{(amp_v)_k} \cdot 100 \tag{4.13}$$

This is a dimensionless parameter that gives the percent underprediction (*amdp* < 0) or overprediction (*amd* > 0) of the amplitude of the k^{th} harmonic constituent.

c. Phase Difference for Modeled Harmonic Constituents (*phd*)

This parameter indicates how much the model output lags (*phd* > 0) or leads (*phd* < 0) the given data for each of the modeled harmonic constituent for water surface level.

$$phd_k = (pha_m)_k - (pha_v)_k \tag{4.14}$$

where $(pha_m)_k$ and $(pha_v)_k$ are the phases of the k^{th} harmonic constituent computed by the model output and given in data, respectively, in minutes.

4.2.2.1. Validation with NOAA Computed Constituents

There are three tidal stations in Georgia where NOAA continuously measures the water surface elevations and provides the tidal constituents for the water levels. The data from these stations are compared to the constituents computed from the 30-day model simulations. The locations of these stations are shown in Figure 4.8. The Figures 4.9 – 4.11 show the amplitude and phase of each tidal constituent computed by the model and given by NOAA at the measurement locations. Tables 4.3 – 4.5 provide more detailed and quantitative results from the comparison between the model results and the data. The period of each constituent is given in hours. The terms amp_{NOAA} (or pha_{NOAA}) and amp_{model} (or pha_{model}) stand for the amplitudes (or phases) for each constituent given by NOAA and computed by the model, respectively. The terms *amdp*, *amd* and *phd* are used for a quantitative comparison as described in the section on validation parameters.

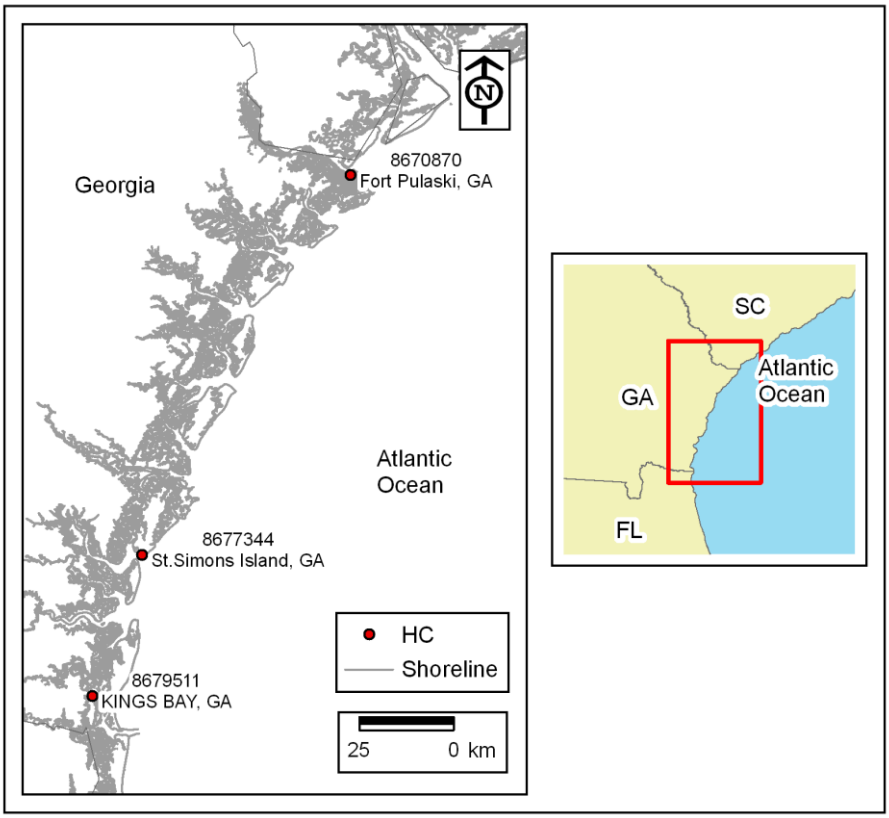

Figure 4.8. NOAA harmonic constituent computation locations.

The results for stations 870870 show that the model underpredicts the most energetic constituent M2 by 10 cm, which corresponds to a 10% error in its magnitude, and does a much better job in predicting the magnitude of the other 8 constituents modeled. An error on the order of 10 cm for M2 s considered to be within the acceptable limits since it is not more than 10%. The error in computing the phase is below 50 minutes except M4. The M4 and M6, called the overtides of M2, are generated because of the non-linearities from the bottom friction and continuity constraints due to channel morphology (Blanton et al., 2002). They become important when tidal amplitude to bottom depth ratio gets larger and cause the maximum ebb and flood to shift closer to high or low water, distorting the M2 component. Their amplitudes in this case, however,

are very small, hence their impact is minimal. Although the percent amplitude difference *amdp* is very high for the overtides the absolute difference *amd* is negligible.

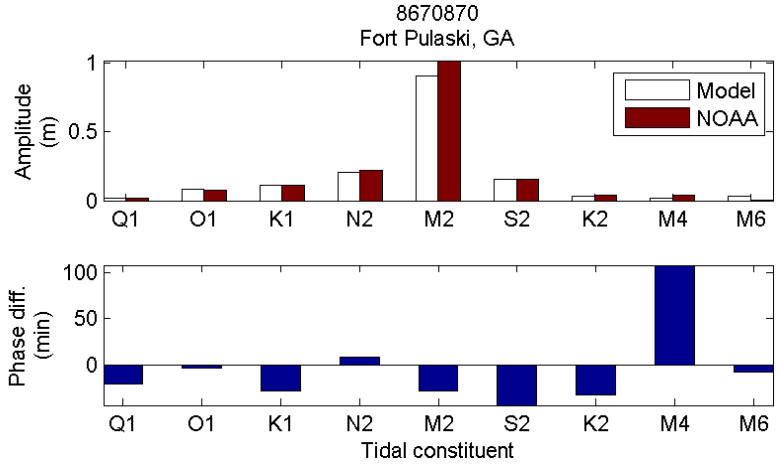

Figure 4.9. Modeled and measured tidal constituents from the NOAA data at stations 8670870, Fort Pulaski, GA.

Table 4.3. Validation parameters of the tidal constituents from the NOAA station at Fort Pulaski, GA

Name	Period (hrs)	amp_{NOAA} (m)	amp_{model} (m)	amdp (%)	amd (m)	pha_{NOAA} (min)	pha_{model} (min)	phd (min)
M2	12.42	1.013	0.906	-10.5	-0.107	37	9	-28
N2	12.66	0.219	0.203	-7.3	-0.016	5	745	9
S2	12.00	0.158	0.158	0.2	0.000	92	49	-43
K1	23.93	0.110	0.111	1.2	0.001	801	773	-27
O1	25.82	0.079	0.082	3.5	0.003	889	885	-3
M4	6.21	0.042	0.021	-49.7	-0.021	257	364	108
K2	11.97	0.041	0.035	-15.5	-0.006	92	60	-32
Q1	26.87	0.017	0.015	-12.3	-0.002	891	870	-20
M6	4.14	0.006	0.030	407.7	0.024	42	34	-7

The comparison of the model results to the data from stations 8677344 and 8679511 show that the model can successfully predict the tidal constituents for those locations that it can resolve (Figures 4.10 and 4.11). The error in the amplitude of M2 is less than 5 cm, and on the order of a centimeter for other amplitudes at these stations

(Tables 4.4 and 4.5). The phase difference is less than 20 minutes for M2 and below 50 minutes for all other constituents with the exception of M4 at station 8677344, for which the phase difference is more than 2 hours. Although it is larger than the phase difference of the other constituents, its overall effect on the predicted water levels is not a major issue since the amplitude for this constituent is on the order of a few centimeters. In conclusion, the tidal constituents of water level computed by the model are generally consistent with the NOAA measurements. The amplitude of the major constituents (i.e. M2, N2, and S2) along with the other constituents used to force the model agrees with the measurements. The difference between the measured and computed phases is found to be small, except for M4, which has relatively small amplitude and a minimal effect on the computed water level.

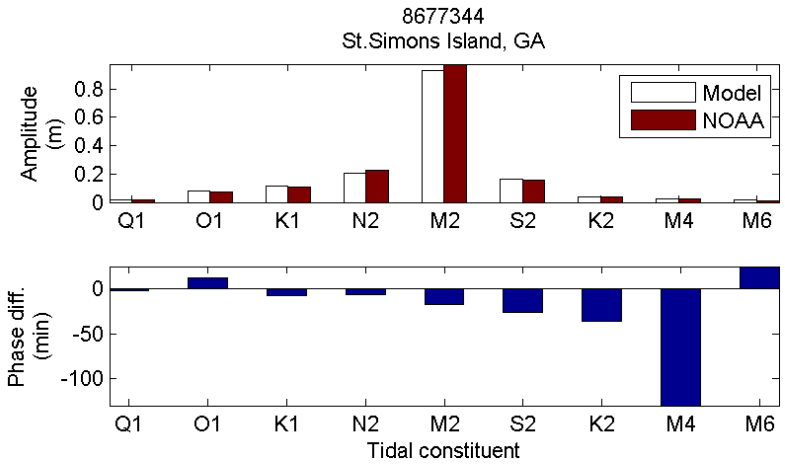

Figure 4.10. Modeled and measured tidal constituents from the NOAA data at station 8677344, St. Simons Island, GA.

Table 4.4. Validation parameters of the tidal constituents from the NOAA station at St. Simons Island, GA.

Name	Period (hrs)	amp_{NOAA} (m)	amp_{model} (m)	amdp (%)	amd (m)	pha_{NOAA} (min)	pha_{model} (min)	phd (min)
M2	12.42	0.976	0.931	-4.6	-0.045	48	31	-17
N2	12.66	0.226	0.207	-8.4	-0.019	17	11	-7
S2	12.00	0.160	0.166	3.6	0.006	102	76	-26
K1	23.93	0.107	0.112	5.1	0.005	803	795	-8
O1	25.82	0.076	0.082	7.7	0.006	895	907	12
K2	11.97	0.041	0.038	-7.7	-0.003	106	70	-36
M4	6.21	0.027	0.022	-20.2	-0.005	314	184	-130
Q1	26.87	0.017	0.015	-13.6	-0.002	903	901	-2
M6	4.14	0.007	0.019	171.1	0.012	133	157	25

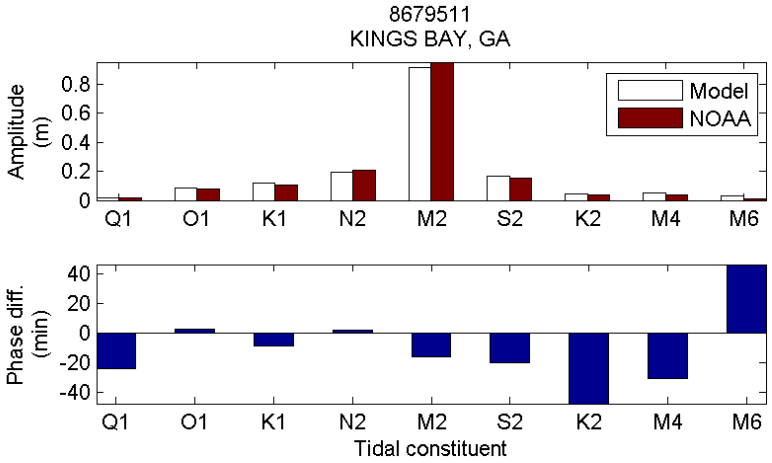

Figure 4.11. Modeled and measured tidal constituents from the NOAA data at station 8679511, Kings Bay, GA.

Table 4.5. Validation parameters of the tidal constituents from the NOAA station at Kings Bay, GA.

Name	Period (hrs)	amp_{NOAA} (m)	amp_{model} (m)	amdp (%)	amd (m)	pha_{NOAA} (min)	pha_{model} (min)	phd (min)
M2	12.42	0.950	0.912	-4.0	-0.038	75	59	-16
N2	12.66	0.207	0.196	-5.5	-0.011	42	44	2
S2	12.00	0.155	0.169	8.8	0.014	135	115	-20
K1	23.93	0.106	0.117	10.4	0.011	836	827	-9
O1	25.82	0.080	0.086	7.0	0.006	938	941	3
K2	11.97	0.040	0.047	17.7	0.007	132	84	-48
M4	6.21	0.040	0.048	19.3	0.008	215	184	-31
Q1	26.87	0.018	0.015	-14.5	-0.003	973	948	-24
M6	4.14	0.010	0.029	188.5	0.019	114	161	47

4.2.2.2. Validation with ADCP Current Measurements

The current measurements come from a variety of data sources. In order to compare the tidal currents, the constituents are calculated at the end of a 30-day model simulation, and the time series for the corresponding period of the measurements are generated from these constituents. The time series for the water surface elevations are also compared if data is available at the same location along with the current measurements. The locations of the available current measurements along the coast are shown in Figure 4.12.

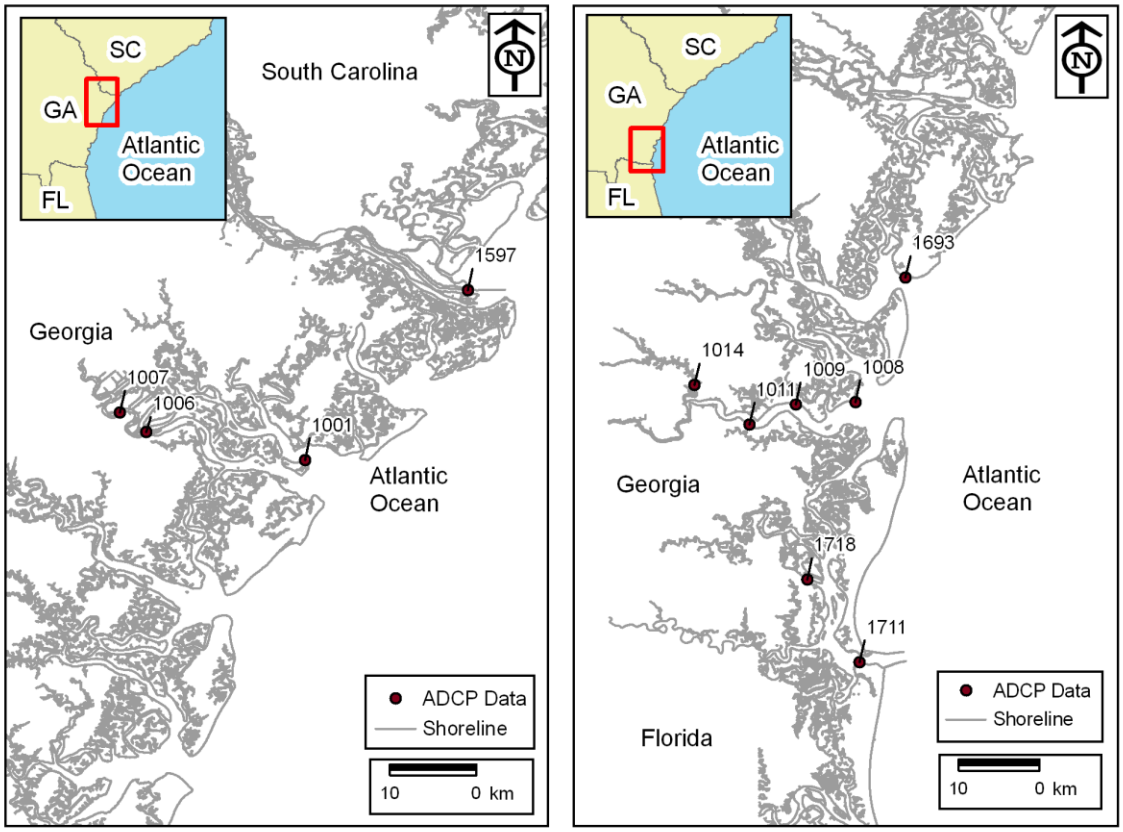

Figure 4.12. ADCP current measurement locations along the Georgia coast.

The ADCP measurements near Fort Pulaski (1597) are obtained from NOAA C-MIST for a time span of July-August 1997. There are only current measurements but no water level measurements available from this dataset. The comparison with the data near Fort Pulaski with the model is shown in Figure 4.13. It is seen that the model predictions agree well with the ADCP measurements on predicting the maximum tidal currents. Although the mean velocity component in each direction is removed from the measurements, the measured current magnitude almost never goes below 0.2 m/s whereas the model predicts current magnitudes that reach to zero at slack water times. This can be due to the fluctuations in the flow from the Savannah River as opposed to the model which is only forced with the tides.

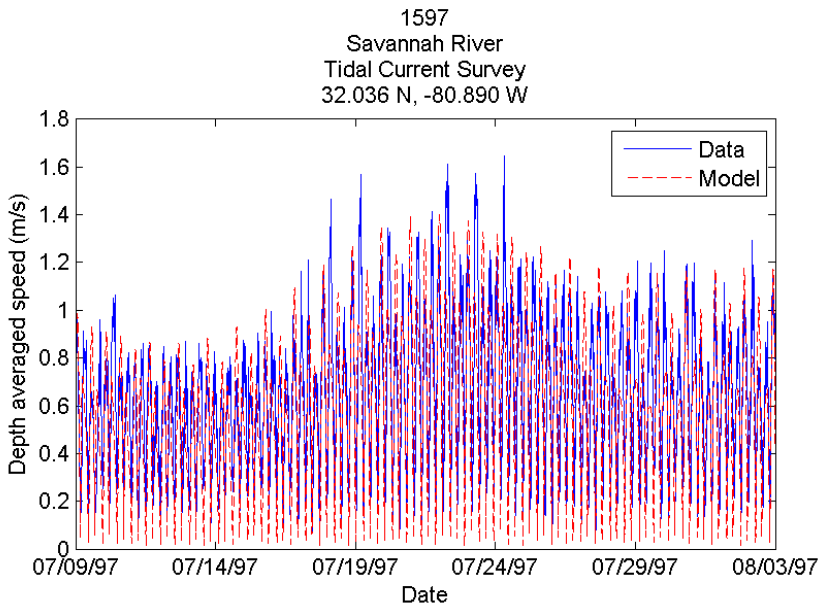

Figure 4.13. Depth averaged tidal current magnitude predicted by the model and from NOAA ADCP measurements at location 1597, Savannah River, GA.

Quantitative comparisons of the maximum currents and high/low predictions for all of the measurement locations are given in Tables 4.6 and 4.7, respectively. The water depths at the computational cells that correspond to the measurement locations are also shown in the table. The measurements show that the average of the maximum current magnitudes at 1597, is on the order of 0.9 m/s (*cmg* = 0.88 m/s). The model satisfactorily predicts the maximum tidal currents with a 10% relative difference (*cmgrt* = 1.07) and a 20 cm/s absolute difference (*crms* = 19 cm/s). Although the *cmgrt* shows a very good match, the *crms* is larger than expected. A detailed look at the time series plot reveals that the model is actually doing a good job in predicting flood dominated tides at this location, with the stronger flood and weaker ebb tides at the location. However, there are time intervals where the ebb flow increases significantly and the flood decreases. This can only be explained by the atmospheric or the natural events that might occur during the time of measurements. For instance an upstream flood or increase in the surface flow due to excessive rainfall might cause such a change in the pattern of the tidal currents. The phase for the flood matches better with the measured phases (*fphd* < 30 minutes) than the phase for the ebb does with the measurements (*ephd* > 60 minutes). However, when combined the phase from the model leads the phase measured by the ADCP with less than 30 minutes.

Table 4.6. Validation parameters for maximum tidal currents at the NOAA and USACE ADCP measurement locations.

Location	Depth (m)	cmg (m/s)	cmgrt (-)	fcrms (m/s)	ecrms (m/s)	crms (m/s)	fcmd (m/s)	ecmd (m/s)	fcpd (min)	ecpd (min)	cpd (min)
1597	9.1	0.88	1.07	0.22	0.17	0.19	0.19	0	24	-72	-24
1693	10.9	0.74	1.08	0.11	0.14	0.13	-0.05	0	-24	-13	-19
1710	18.7	1.07	1.08	0.03	0.14	0.10	0.03	0	6	-33	-13
1711	13.7	0.97	1.00	0.07	0.04	0.05	-0.07	0	7	-13	-6

Table 4.7. Validation parameters for high/low tides at the NOAA and USACE ADCP measurement locations.

Location	Depth (m)	meanhi (m)	meanlo (m)	strdt (-)	rms (m)	hirms (m)	lorms (m)	phd (min)	hiphd (min)	lophd (min)
1693	10.9	0.99	-1.03	1.01	0.12	0.14	0.11	-26	-18	-34
1711	13.7	0.95	-0.74	0.92	0.12	0.15	0.08	-23	-20	-25
1718	10.0	1.06	-0.87	0.89	0.16	0.20	0.11	-6	-4	-8

The second location for ADCP measurements given by C-MIST is station 1693 at St. Simons Sound. The measurements were taken between the end of August and the start of October in 1997. The current measurement and water surface elevation comparisons for this location are shown in Figures 4.14.a and 4.14.b, respectively. The model predicts a smaller difference between the magnitudes of neap tide currents and the spring tide currents than the given by the measurement. This is also true for the high/low tide elevations. The model predictions for tidal currents are validated at this location with *cmgrt* = 1.1, *crms* = 13 cm/s, and *cpd* = 19 minutes (Table 4.6). The predictions by the model for the water surface elevations for this location have values of *stdrt* = 1.01 and *rms* = 12 cm. The high and low tides predicted by the model leads the phase of the measured high/low tides by 26 minutes (Table 4.7).

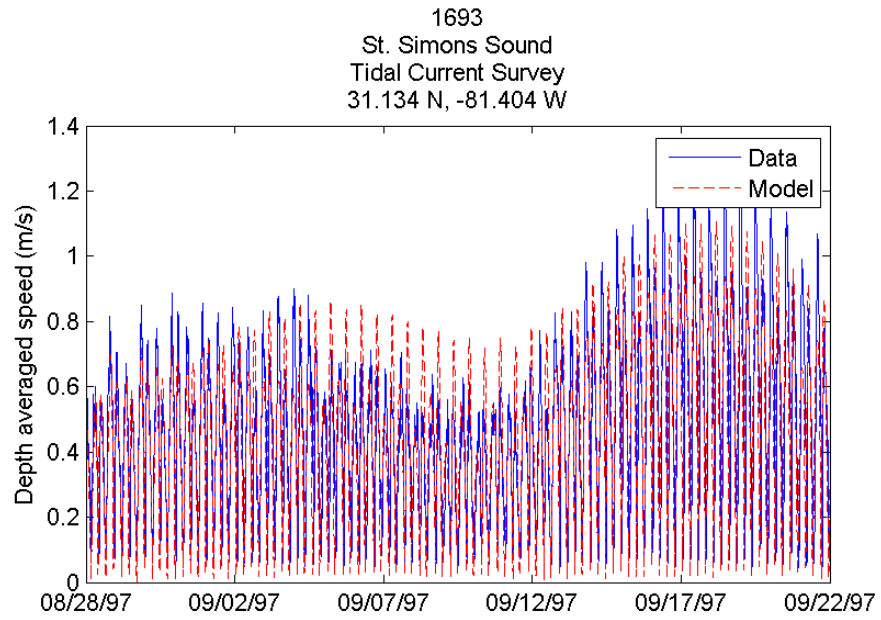

(a)

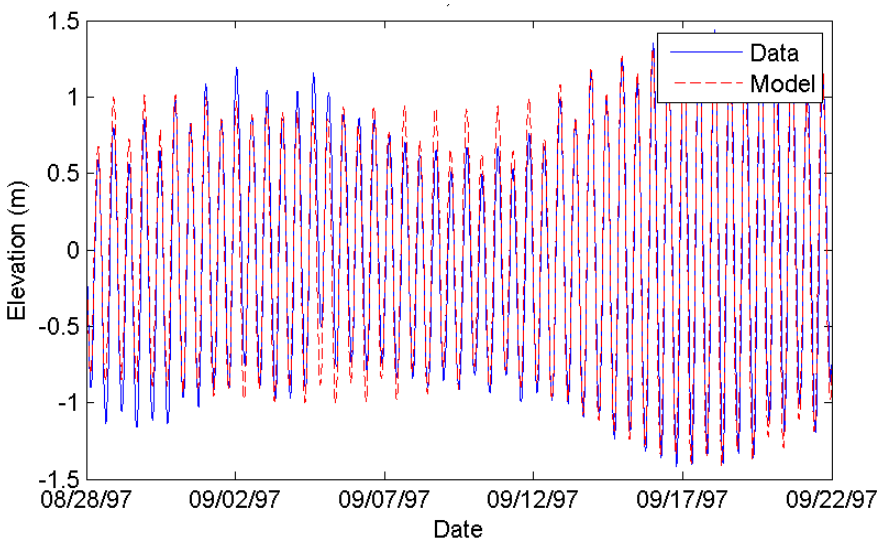

(b)

Figure 4.14. (a) Depth averaged tidal current magnitude and (b) water surface elevation predicted by the model and from NOAA ADCP measurements at 1693, St. Simons Sound, GA.

The ADCP data for the entrance of the Cumberland Sound comes from Hydrodynamic Data Collection USACE Waterways Experiment Station Hydraulics Laboratory (Fagerburg et al., 1992). The measurements were performed in May, 1990. The current measurement data at the entrance to Cumberland Sound are shorter than a day (Figure 4.15) and the high/low tide water level measurements span about two days (Figure 4.16). The model current predictions agree very well with the measurements from both locations Cumberland Sound entrance at locations 1710 and 1711. Quantitative comparison show that the current predictions from the model for these locations have the best results within the group of comparison with the measurements, with *cmgrt* =1.08 and 1.00, *crms* = 10 cm/s and 5 cm/s, *cpd* = -13 and -6 minutes (Table 4.6). For the water surface elevation, there are only high/low tide measurements available. The validation of model predictions for the high/low tides at points 1711 and 1718 are also satisfactory with *stdrt* = 0.92 and 0.89 *rms* = 12 cm and 16 cm. At both of these locations the model predictions lead measurements for the high/low tides with 23 and 6 minutes, respectively.

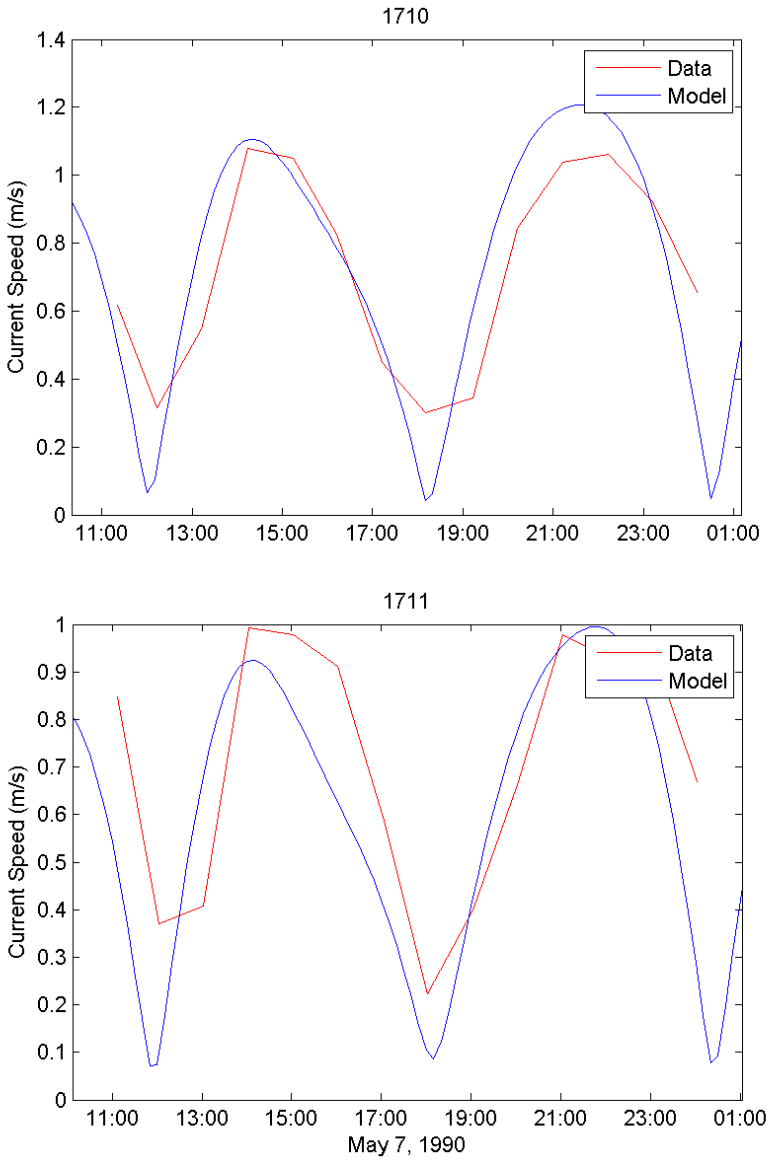

Figure 4.15. Current magnitude data from ADCP measurements (Fagerburg et al., 1992) and model predictions at locations 1710 and 1711.

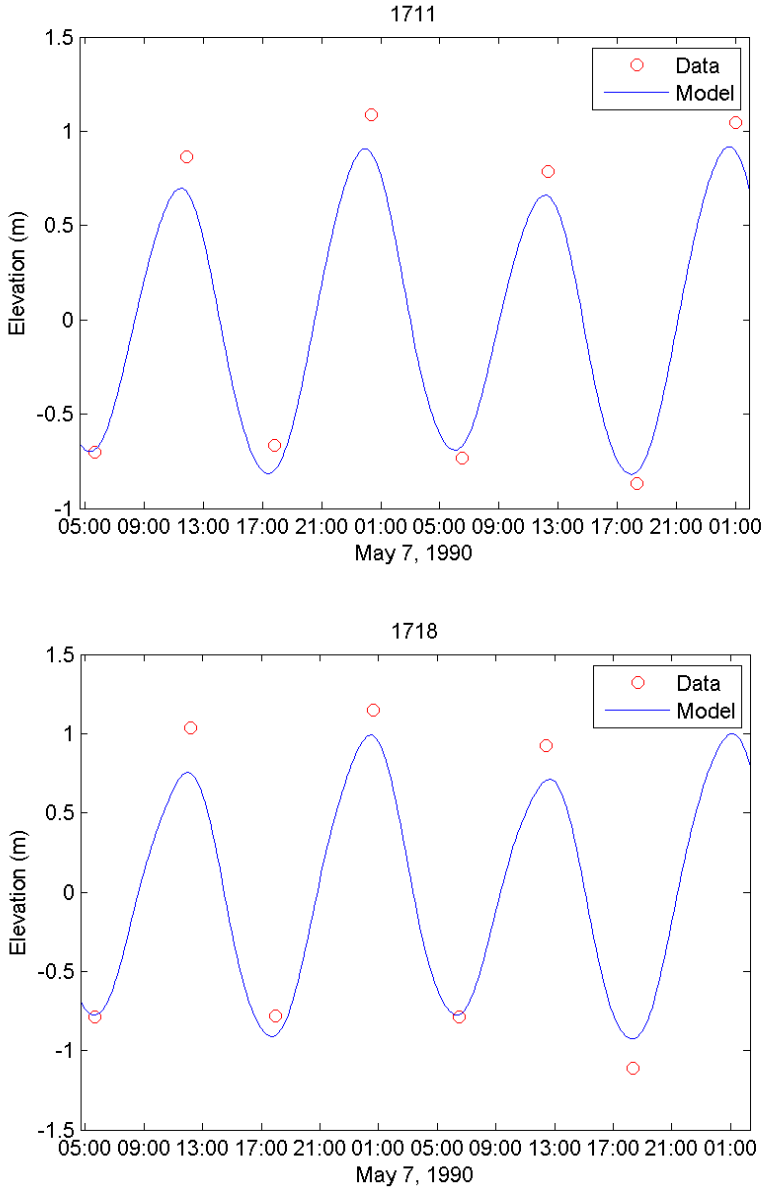

Figure 4.16. Water surface elevation from ADCP measurements (Fagerburg et al., 1992) and model predictions at locations 1711 and 1718.

The ADCP measurements from several locations on the Ogeechee and Satilla Rivers (Blanton et al., 1999; Seim et al., 2009; Seim et al., 2002) are used to validate the model predictions. The measurements on the Ogeechee River from October 11 to November 26, 2001 provide current magnitude at locations 1001, 1006 and 1007. The

points range from river the mouth to upstream Ogeechee River and further inland moving from 1001 to 1007. The spring and neap tide pattern is clearly seen to match the measurements at these points, but the predictions are observed to deviate from the measurements moving towards inland where the river becomes narrower (Figures 4.17. and 4.18).

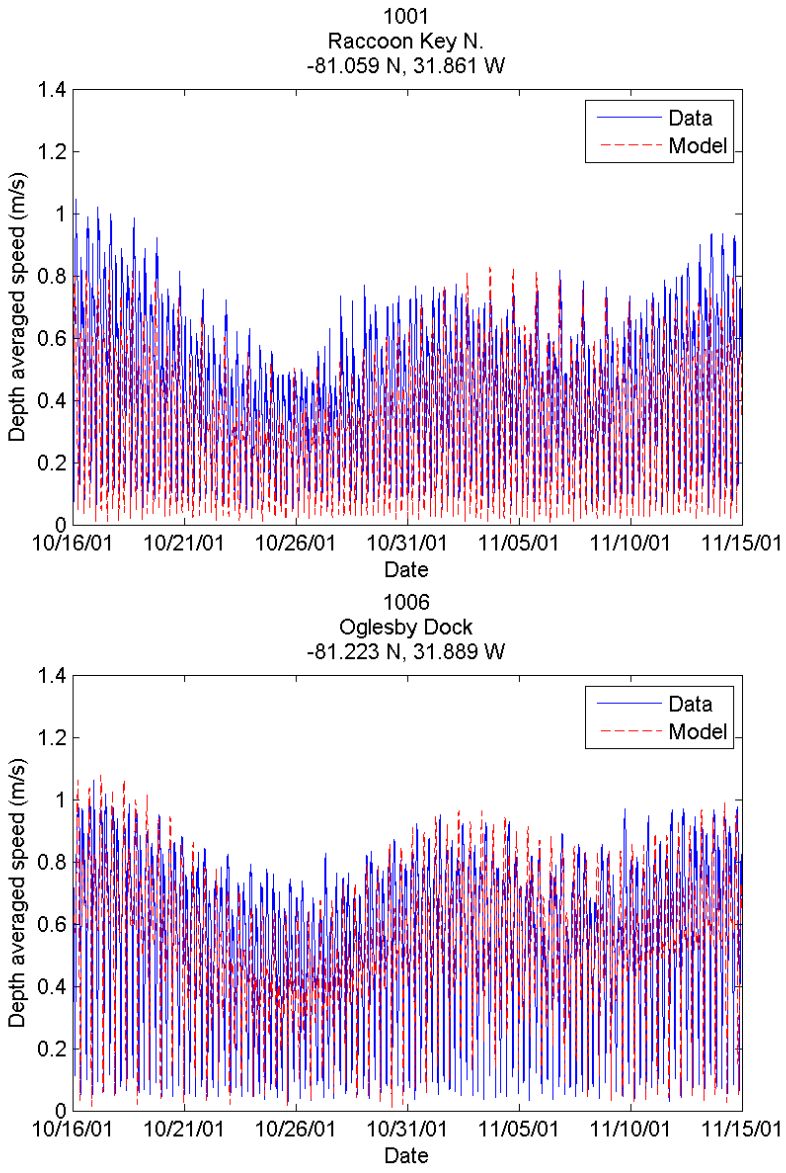

Figure 4.17. Depth averaged tidal current magnitude from model predictions and measurement data on Ogeechee River at locations 1001 and 1006.

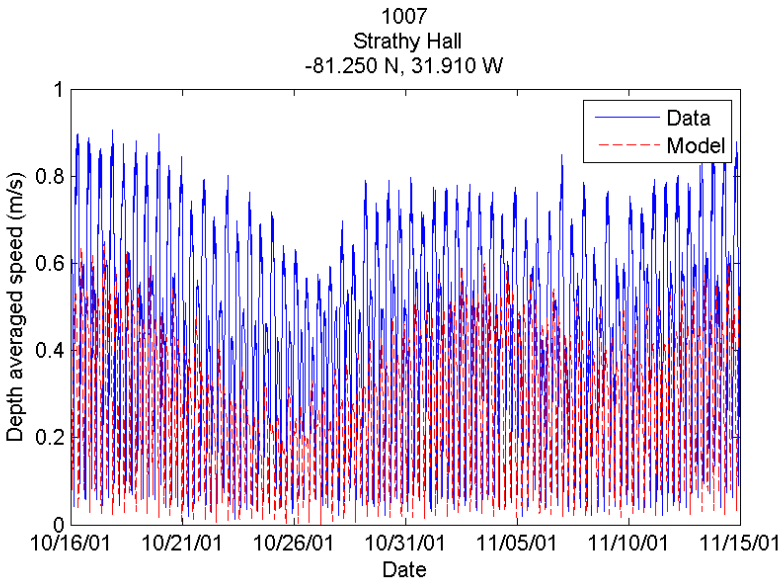

Figure 4.18. Depth averaged tidal current magnitude from measurement predictions and measurement data on Ogeechee River at location 1007.

The current predictions are validated satisfactorily at 1001 and 1006 with *cmgrt* = 0.85 and 0.92 and *crms* = 12 and 16 cm/s, respectively, but fall short in satisfying the measurements at 1007 with *cmgrt* = 0.73 and *crms* = 23 cm/s (Table 4.8). This is also true for the phase difference between the model predictions and the data, where 1001 and 1006 have phase differences less than 40 minutes whereas 1007 is more than 75 minutes. The results are similar for the high/low water predictions with 1001 and 1006 having *stdrt* number closer to 1.0 (0.99 and 1.03, respectively) while for 1007 it is 1.23. The *rms* for the high/low tides also increase going from 1001 to 1007 i.e. 0.14, 0.19, 0.30 cm, although *phd* is the same for all of them, about half an hour (Table 4.9).

Table 4.8. Validation parameters for maximum tidal currents at the ADCP measurement locations on Ogeechee and Satilla Rivers.

Location	Depth (m)	cmg (m/s)	cmgrt (-)	fcrms (m/s)	ecrms (m/s)	crms (m/s)	fcmd (m/s)	ecmd (m/s)	fcpd (min)	ecpd (min)	cpd (min)
1001	9.3	0.62	0.85	0.14	0.09	0.12	-0.13	-0.03	-22	-64	-40
1006	6.2	0.78	0.92	0.18	0.12	0.16	-0.15	0.04	8	3	6
1007	5.8	0.60	0.73	0.10	0.32	0.23	-0.05	-0.31	-56	-97	-76
1008	6.7	0.42	1.69	0.35	0.21	0.28	0.32	0.19	-29	-53	-41
1009	7.1	0.48	1.30	0.18	0.14	0.16	0.14	0.12	1	-76	-37
1011	2.3	0.34	0.92	0.12	0.10	0.11	-0.09	0.01	6	-33	-12
1014	6.8	0.52	0.89	0.17	0.09	0.13	-0.15	0.02	-13	-64	-39

Table 4.9. Validation parameters for high/low tides at the ADCP measurement locations on Ogeechee and Satilla Rivers.

Location	Depth (m)	meanhi (m)	meanlo (m)	strdt (-)	rms (m)	hirms (m)	lorms (m)	phd (min)	hiphd (min)	lophd (min)
1001	9.3	0.97	-1.05	0.99	0.14	0.11	0.16	-35	-13	-56
1006	6.2	0.87	-0.96	1.03	0.19	0.15	0.21	-34	-7	-61
1007	5.8	0.69	-0.88	1.23	0.30	0.31	0.28	-32	-43	-20
1008	6.7	0.89	-0.93	1.01	0.14	0.11	0.17	-28	-24	-31
1009	7.1	0.89	-0.97	0.90	0.18	0.13	0.22	-16	-9	-23
1011	2.3	0.88	-0.99	0.92	0.18	0.12	0.22	-11	-2	-20
1014	6.8	0.80	-1.04	1.11	0.22	0.19	0.24	-3	-5	-1

The measurements on Satilla River cover a time span between September – October 1999. Four different locations, 1008, 1009, 1011 and 1014, from these measurements are used to validate the model predictions. The model predictions tend to be less reliable at the upstream reaches of rivers and creeks due to the incapability of model in resolving these features with its limited computational cell size. This is a possible explanation for the model to underpredict the currents more at inland locations (Figures 4.19 and 4.20). The current magnitude ratio, *cmgrt*, drops down from 1.69 to 0.92 and further to 0.89, and *rms* decreases consistently from 21 cm/s to 9cm/s (Table 4.8). On the other hand the *rms* for water level predictions increase from 14 to 22 cm, and

stdrt varies between 1.1 and 0.9 with no clear trend with respect to the changing river width. The measurements show that the magnitude of currents in Satilla River are significantly low for power conversion (<0.5 m/s). The averages of the maximum current speeds are smaller than the other validation locations. This is one possible explanation to the fact that it is not possible to see a consistent trend when the predicted maximum current values are compared to the measurement data. The validations at these points are not strong, but since locations with very small tidal current magnitudes are not important for power conversion they are of secondary importance.

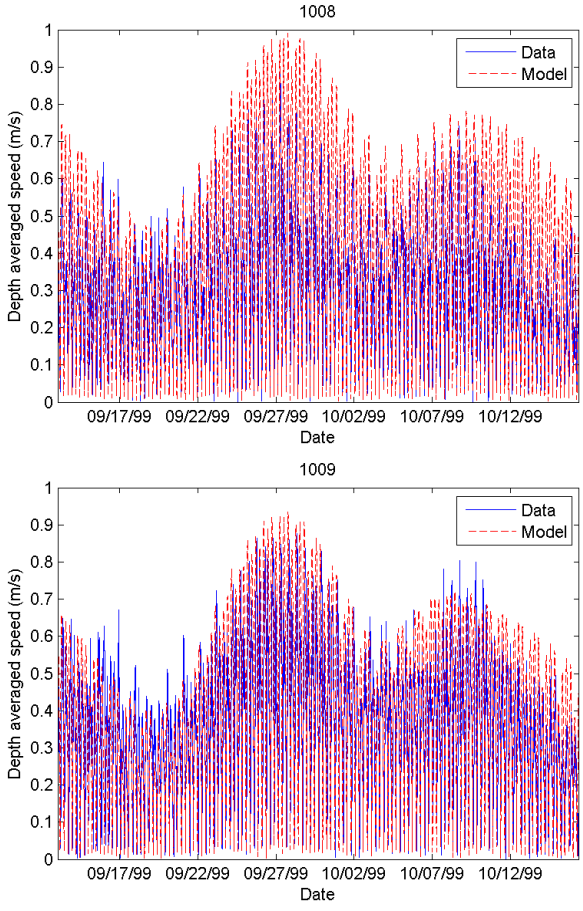

Figure 4.19. Depth averaged tidal current magnitude from model predictions and measurement data on Satilla River at locations 1008 and 1009.

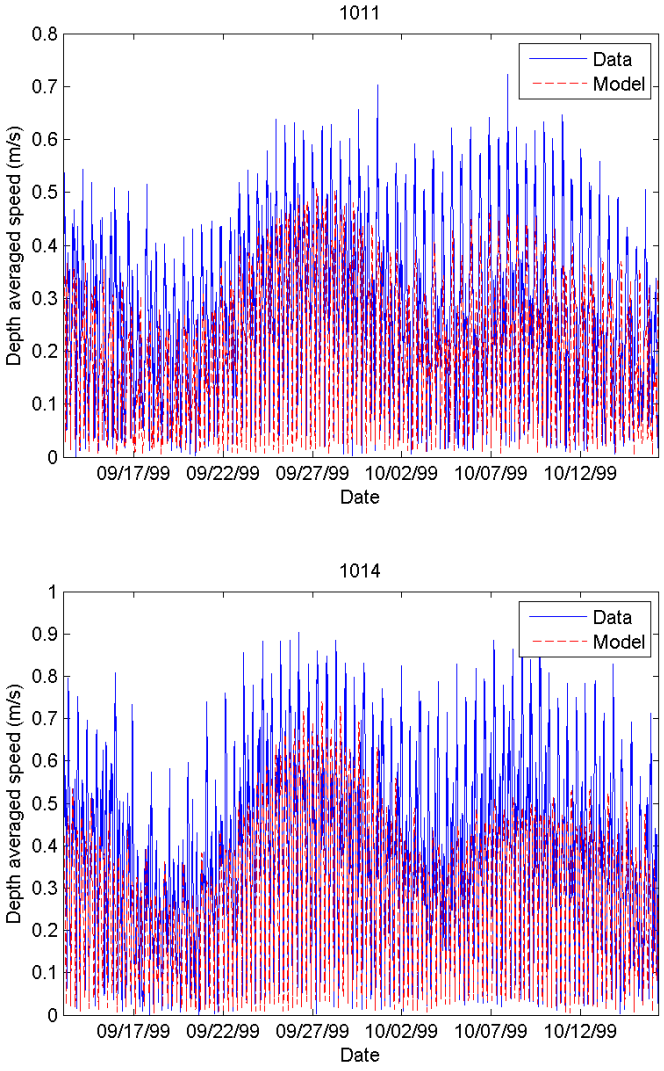

Figure 4.20. Depth averaged tidal current magnitude from predictions and measurements on Satilla River at locations 1011 and 1014.

4.2.2.3. NOAA Water Level Predictions for High and Low Tide

Starting from November 1, 2005, 32 days of tides were simulated with the model, although the first 48 hours are neglected in computing the tidal constituents. Currents and water levels are retained at 1 hour intervals for all points within the domain and at 10 minute intervals for selected locations to allow for harmonic analysis using the T_Tide harmonic analysis toolbox for Matlab (Pawlowicz et al., 2002) of both the water levels and the velocities. Time series of water level and tidal current velocity for the simulation period are regenerated from the computed constituents and compared with the NOAA predictions for high/low tide elevations and maximum current magnitudes.

The locations of NOAA high/low tide predictions that are compared to the model predictions are shown in Figure 4.21. The statistics for the comparison are given in Table 4.10. The mean for high (*meanhi*) and low (*meanlo*) tide elevations are provided jointly with the validation parameters to indicate the mean tidal range for the region. The depth at the prediction location is also given. When compared with the NOAA predictions it is seen that the difference between the phase predicted by the model and given with NOAA predictions is on the order of a minute. The *stdrt* number for the magnitude of the high/low tides usually shows 90% agreement with NOAA predictions. A difference on the order of 0.1 m for *rms* is observed in all of the model runs. The higher values of *rms* are usually observed where measurements locations fall near those computational cells adjacent to river banks and the predictions are interpolated between a wet cell and the neighboring wetland cell. The water levels in the wetland cell are limited by the critical depth (0.2 m or 0.5 m) required for running the wetting and drying routine in ROMS. The water level can go up but never goes below the critical depth at these cells. The results at

those computational cells where the depth is modified as a result of bathymetry smoothing, the relative change in the depth is comparable to the original depth. Overall, the difference between the predictions in terms of *rms* is on the order of 0.1 m to 0.2 m, there is minimal phase difference. The model predictions in rivers and main channels agree better with the NOAA predictions than at remote locations.

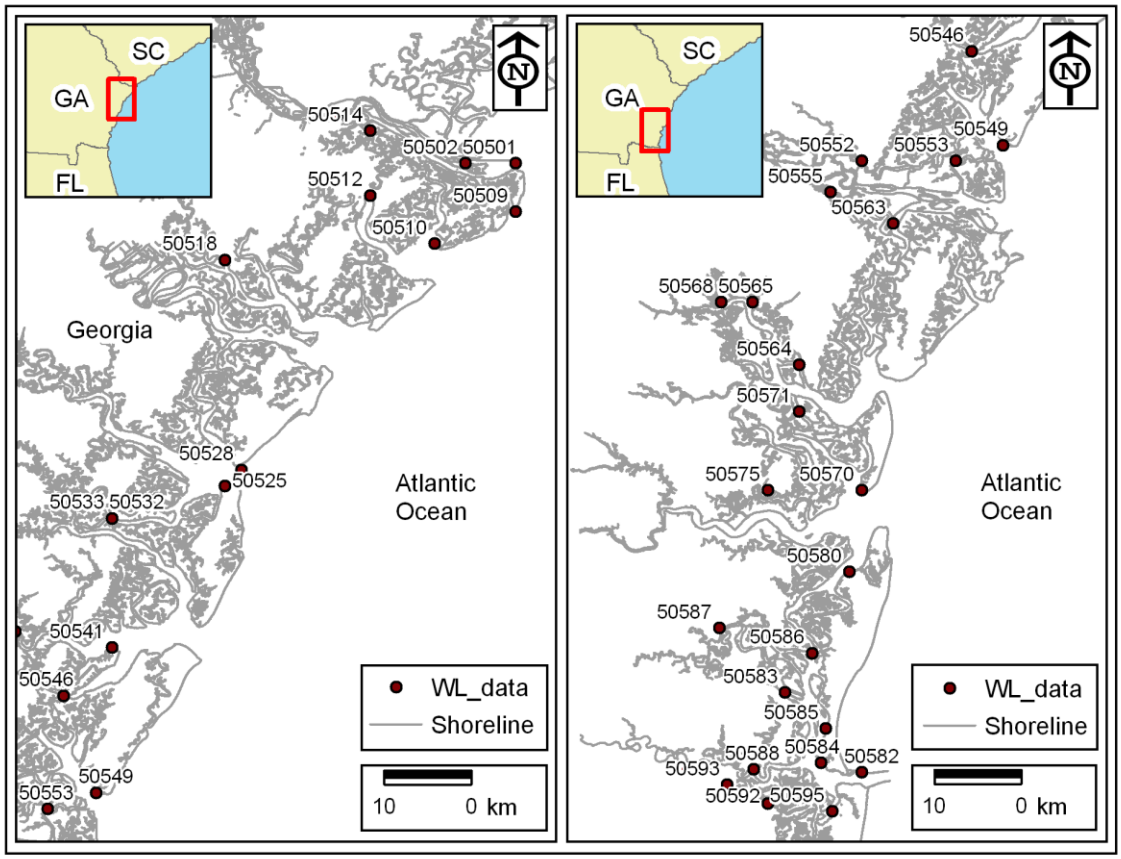

Figure 4.21. Locations of NOAA high/low tide predictions used to compare the model predictions.

Table 4.10. Validation parameters for NOAA high/low tide predictions on the Georgia coast.

SID	Name	Depth (m)	meanhi (m)	meanlo (m)	strdt (-)	rms (m)	hirms (m)	lorms (m)	phd (min)	hiphd (min)	lophd (min)
50501	Tybee Light	5.2	1.1	-0.9	0.9	0.1	0.2	0.1	-1	-2	0
50502	SAVANNAH RIVER ENTRANCE, FORT PULASKI	10.4	1.1	-0.9	0.9	0.1	0.2	0.1	0	-1	0
50503	Fort Jackson	9.7	1.1	-1.0	0.8	0.2	0.3	0.2	-1	-1	0
50509	Tybee Creek entrance	1.5	1.1	-0.9	0.8	0.2	0.2	0.1	0	0	1
50510	Beach Hammock	8.4	1.1	-0.9	0.9	0.1	0.2	0.1	0	-1	1
50512	Wilmington River, Savannah Sheraton	9.8	1.2	-1.1	0.8	0.2	0.2	0.2	0	-1	1
50514	Wilmington River, North entrance	1.5	1.2	-1.0	0.7	0.3	0.3	0.3	-1	-2	1
50518	Coffee Bluff, Forest River	5.6	1.2	-1.0	0.8	0.2	0.2	0.2	-1	-3	0
50525	Walburg Creek entrance	7.9	1.1	-1.0	0.9	0.2	0.2	0.1	-1	-2	-1
50528	Bear River Entrance	8.9	1.1	-0.9	0.9	0.2	0.2	0.1	0	0	0
50532	North Newport River	5.5	1.2	-1.0	0.9	0.2	0.2	0.1	-1	-3	1
50533	South Newport Cut, N. Newport River	5.5	1.1	-1.0	0.9	0.2	0.1	0.2	0	-1	1
50541	Dog Hammock, Sapelo River	3.2	1.1	-1.0	0.9	0.1	0.2	0.1	-1	-1	0
50543	Pine Harbor, Sapelo River	3.6	1.1	-1.0	0.8	0.2	0.2	0.2	-1	-3	1
50546	Mud River, at Old Teakettle Creek	2.7	1.2	-1.0	0.9	0.2	0.2	0.1	-1	-2	0
50549	Old Tower, Sapelo Island	3.7	1.1	-0.9	0.9	0.2	0.2	0.1	0	-1	1
50552	Darien, Darien River	6.5	1.1	-0.9	0.8	0.3	0.3	0.3	0	-1	1
50553	Rockdedundy River (Daymark 185)	3.0	1.1	-0.9	0.9	0.2	0.2	0.1	-1	-2	0
50555	Champney Island, South Altamaha River	8.0	0.8	-0.7	1.1	0.1	0.1	0.1	1	1	1
50563	Mackay River (ICWW)	3.6	1.1	-0.9	0.9	0.2	0.2	0.1	-1	-2	0
50564	Brunswick, East River	5.6	1.1	-0.9	0.9	0.2	0.2	0.1	-2	-3	-1
50565	Turtle River, Crispen Island	3.3	1.2	-1.1	0.8	0.3	0.4	0.1	1	1	1
50568	Turtle River, Buffalo River entrance	2.3	1.2	-1.1	0.9	0.3	0.4	0.1	0	-1	0
50570	Jekyll Point, Jekyll Sound	3.5	1.0	-1.0	0.9	0.1	0.1	0.1	-1	-2	0
50571	Jointer Island, Jointer Creek	3.5	1.0	-1.1	0.9	0.1	0.2	0.1	-1	-3	0
50575	Dover Bluff, Dover Creek	1.4	1.0	-1.0	0.7	0.3	0.3	0.3	-1	-2	0
50580	Cumberland Wharf, Cumberland River	2.3	1.0	-1.0	0.9	0.1	0.1	0.1	-1	-2	0
50582	St. Marys Entrance, North Jetty	2.4	0.8	-0.9	0.9	0.1	0.1	0.1	-1	-3	1
50583	Kings Bay, Navy Base	2.4	0.9	-1.0	0.9	0.1	0.1	0.1	-2	-3	0
50584	Beach Creek ent., Cumberland Island	2.4	0.8	-0.9	0.9	0.1	0.1	0.1	-1	-3	1
50585	Seacamp Dock, Cumberland Island	2.7	0.9	-0.9	0.9	0.1	0.1	0.1	-1	-3	0
50586	Crooked River, Cumberland Dividings	4.0	0.9	-1.0	0.9	0.2	0.2	0.2	2	3	1
50587	Harrietts Bluff, Crooked River	3.4	0.9	-0.9	0.9	0.1	0.1	0.1	2	1	2
50588	St. Marys River, St. Marys	7.9	0.8	-0.9	0.9	0.1	0.2	0.1	1	1	0
50589	St. Marys River, Crandall	5.9	0.7	-0.7	1.2	0.2	0.2	0.2	1	0	3
50592	Chester, Bells River	2.4	0.9	-0.9	0.9	0.1	0.1	0.1	-1	-2	1
50593	Roses Bluff, Bells River	2.9	0.9	-0.9	0.9	0.2	0.1	0.2	1	1	1
50595	FERNANDINA BEACH, Amelia River	8.1	0.9	-0.9	0.9	0.1	0.1	0.1	-1	-2	0

4.2.2.4. NOAA Maximum Current Predictions

Because of the large number of prediction locations, the current predictions from the model are validated against the NOAA maximum current predictions in two parts. The first part covers the northern part of the Georgia coast and includes stations 1592-

1672. The second part is the southern half of the Georgia coast, which contains stations 1681-1721. The locations are shown in Figure 4.22, and the results are given in Tables 4.11 and 4.12. In addition to the validation parameters defined earlier, the average of the predicted maximum current magnitudes (*cmg*) is also included in the Tables. Although the NOAA current predictions are less reliable than the current measurements, the *cmg* is still considered as a measure for the level of current magnitude at a location. The locations with larger current magnitudes (*cmg* > 0.7 m/s) are more important than those with smaller magnitudes (*cmg* < 0.7 m/s) from power extraction point of view, and they are more critical to match. The comparison of the model predictions with the NOAA predictions for locations 1597 and 1598 on Savannah River is an example for this. As shown in the previous section, the model predictions agree well (*cmgrt* = 1.1, *crms* = 0.2 m/s) with the NOAA ADCP measurements at location 1597, Savannah River entrance. On the contrary, comparison with the NOAA predictions produces a very low match (*cmgrt* = 0.7, *crms* = 0.5 m/s) between the two predictions. In this case, even if the data and the model used in calculating the NOAA predictions were known, they still would not constitute a more reliable source for validation than the measurement itself. In light of these considerations, a *cmgrt* number between 0.8 and 1.2 or a *crms* value less than 0.2 m/s when compared to the NOAA predictions is assumed to be a satisfactory validation of the results in simulating the tidal currents. Some of the locations have *cmgrt* values out of this range, some of which are narrow channels or creeks (e.g. 1607 and 1660) not well resolved by the model. The phase difference between the model and NOAA predictions are usually less than an hour, with the exception of locations 1592, 1607, 1610, 1664, 1694, 1703 and 1706. Amongst these, 1592 is not on the Georgia coast, and close to the

computational grid boundary; and 1607 is in a narrow channel difficult for the model to resolve.

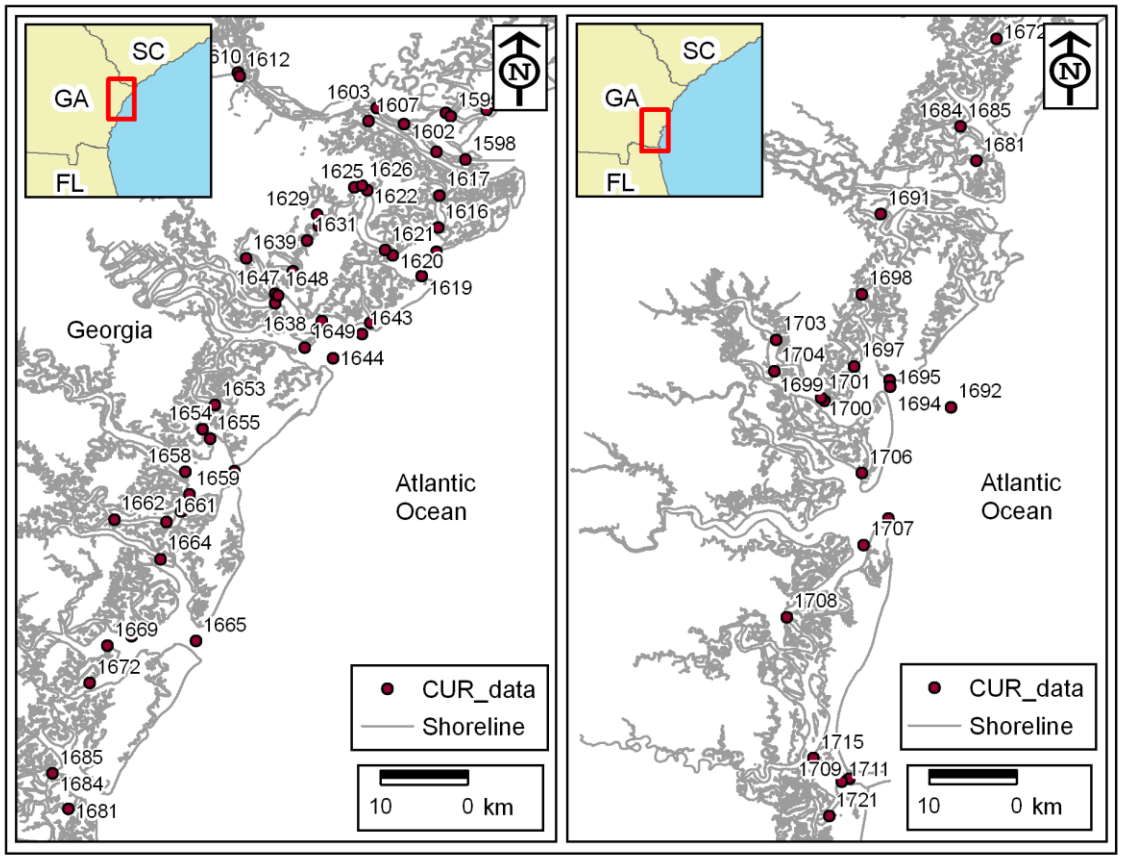

Figure 4.22. Locations of NOAA maximum current predictions used to compare the model predictions

Table 4.11. Validation parameters for the NOAA predictions of maximum currents for the northern part of the Georgia coast (November, 2005).

SID	Name	Depth (m)	cmg (m/s)	cmgrt (-)	fcrms (m/s)	ecrms (m/s)	crms (m/s)	fcmd (m/s)	ecmd (m/s)	fcpd (min)	ecpd (min)	cpd (min)
1592	Bloody Pt., 0.5 mile north of, New River	2.4	0.6	0.8	0.1	0.1	0.1	-0.1	-0.1	-9	-103	-79
1594	Wright R., 0.2 mile above Walls Cut	3.6	0.7	0.9	0.2	0.1	0.1	-0.1	0.0	-31	-31	-31
1595	Walls Cut, Turtle Island	4.0	0.5	0.8	0.1	0.1	0.1	-0.1	-0.1	94	-10	16
1598	Fort Pulaski	9.8	1.2	0.7	0.7	0.5	0.5	-0.7	-0.3	-75	-55	-60
1599	Fort Pulaski, 1.8 miles above	8.9	1.2	0.8	0.4	0.3	0.3	-0.4	-0.1	-26	-4	-9
1602	Elba Island Cut, NE of, Savannah River	6.8	1.0	1.0	0.5	0.4	0.4	-0.5	0.0	-23	-3	-8
1603	Elba Island, NE of, Savannah River	7.3	0.9	0.9	0.5	0.3	0.4	-0.5	-0.1	10	2	4
1607	Wilmington R. ent., south channel	2.4	0.6	0.7	0.4	0.2	0.3	-0.3	-0.2	17	86	69
1610	Kings Island Channel, Savannah River	7.1	0.9	0.8	0.2	0.2	0.2	-0.2	-0.1	103	85	89
1612	King Island, west of	4.2	0.8	0.9	0.2	0.2	0.2	-0.2	-0.1	75	66	68
1615	Entrance, off Beach Hammock	9.3	1.0	0.9	0.2	0.1	0.2	-0.2	-0.1	-13	44	30
1616	Wilmington Island, SSE of, Bull River	10.4	0.5	1.2	0.1	0.2	0.2	0.0	0.1	50	4	15
1617	Lazaretto Creek Entrance, N of, Bull River	5.1	0.6	1.0	0.1	0.1	0.1	-0.1	0.0	55	40	44
1619	Entrance, off Wassaw Island	12.0	0.8	0.7	0.3	0.2	0.3	-0.3	-0.2	-26	28	15
1620	Wilmington River ent. off Cabbage Island	10.3	0.7	1.1	0.1	0.1	0.1	0.1	0.1	30	-18	-6
1621	Joes Cut, Wilmington River	8.5	0.8	1.1	0.2	0.2	0.2	-0.1	0.1	12	-12	-6
1622	Wilmington R., 0.5 mi. S of Turners Creek	13.1	0.6	1.0	0.1	0.1	0.1	0.0	0.0	8	38	30
1625	Skidaway River, north entrance	6.1	0.6	0.9	0.2	0.1	0.1	-0.1	-0.1	27	46	41
1626	Skidaway Island, N End, Wilmington River	13.5	0.7	0.9	0.3	0.2	0.2	-0.3	-0.1	1	32	25
1629	Isle of Hope City, Skidaway River	0.5	0.3	0.8	0.1	0.1	0.1	-0.1	-0.1	119	17	43
1630	Burntpot Island, west of, Skidaway River	0.5	0.5	0.9	0.1	0.1	0.1	0.0	-0.1	-16	13	6
1631	Skidaway Narrows	0.1	0.5	0.7	0.2	0.2	0.2	-0.1	-0.2	-93	34	2
1635	Burnside Island, SE of, Burnside River	3.1	0.5	0.9	0.2	0.1	0.1	-0.2	-0.1	60	-7	10
1637	Little Ogeechee River Entrance	9.8	0.8	0.8	0.1	0.2	0.2	-0.1	-0.1	-20	-9	-12
1639	Montgomery, Vernon River	5.1	0.4	1.0	0.2	0.1	0.2	-0.2	0.0	-20	41	26
1640	Odingsell River Entrance	6.8	0.8	0.9	0.3	0.2	0.2	-0.2	-0.1	-3	-29	-22
1642	Wassaw Island, SSW of	10.9	0.9	0.8	0.2	0.2	0.2	-0.2	-0.2	-23	52	33
1644	Bradley Point, NNE of	6.1	0.7	1.1	0.1	0.2	0.2	0.0	0.1	1	-6	-4
1645	Raccoon Key	11.6	0.8	1.0	0.1	0.2	0.2	0.1	0.0	15	39	33
1646	Little Wassaw Island, SW of	10.6	0.8	0.8	0.1	0.3	0.3	0.0	-0.3	-1	32	24
1647	Vernon R., 1.2 miles S of Possum Point	5.5	0.7	1.1	0.2	0.1	0.1	0.1	0.1	-1	45	34
1648	Little Ogeechee River Entrance, north of	6.5	0.7	1.2	0.2	0.2	0.2	0.2	0.1	29	33	32
1649	Raccoon Key & Egg Island Shoal, between	10.8	0.9	1.1	0.1	0.2	0.1	0.1	0.1	-118	-12	-38
1653	North of Big Tom Creek Entrance	7.9	0.6	0.9	0.1	0.1	0.1	-0.1	-0.1	22	51	44
1654	South of Kilkenny Creek Entrance	11.5	0.8	1.1	0.1	0.2	0.1	-0.1	0.1	-16	-26	-23
1655	Northwest of Newell Creek Entrance	9.1	0.7	1.1	0.1	0.1	0.1	0.0	0.1	-23	27	15
1657	St. Catherines Sound Entrance	13.0	0.8	1.2	0.4	0.3	0.3	0.4	0.0	-9	16	10
1658	Medway River, northwest of Cedar Point	10.8	0.7	1.0	0.2	0.2	0.2	0.2	0.0	-94	-17	-36
1659	N. Newport River, NE of Vandyke Creek	9.7	0.7	1.1	0.2	0.1	0.2	0.2	0.0	5	25	20
1660	N. Newport River, above Walburg Creek	4.3	0.7	0.7	0.2	0.2	0.2	-0.2	-0.2	1	-20	-15
1661	N. Newport River, NW of Johnson Creek	4.0	0.7	0.8	0.2	0.2	0.2	-0.2	-0.1	-58	-41	-46
1662	N. Newport River, ESE of S. Newport Cut	4.9	0.6	1.2	0.1	0.1	0.1	0.1	0.1	-78	26	0
1664	S. Newport River, above Swain River Ent	8.2	0.6	1.2	0.4	0.3	0.3	0.4	0.1	-96	-72	-78
1665	Entrance	13.4	1.0	1.1	0.2	0.2	0.2	0.1	0.1	38	29	31
1668	Cedar Hammock, south of	9.1	0.6	1.2	0.2	0.1	0.2	0.2	0.0	-4	55	40
1669	Sapelo River Entrance	7.5	0.6	1.2	0.2	0.1	0.1	0.2	0.1	-89	31	1
1672	New Teakettle Cr., 0.8 mi. N of	1.9	0.4	1.1	0.1	0.1	0.1	0.0	0.1	30	11	15

Table 4.12. Validation parameters for the NOAA predictions of maximum currents for the southern part of the Georgia coast (November, 2005).

SID	Name	Depth (m)	cmg (m/s)	cmgrt (-)	fcrms (m/s)	ecrms (m/s)	crms (m/s)	fcmd (m/s)	ecmd (m/s)	fcpd (min)	ecpd (min)	cpd (min)
1681	South River	4.1	0.6	0.9	0.1	0.1	0.1	-0.1	0.0	-101	-42	-56
1684	Doboy Island (North River)	7.0	0.5	0.8	0.1	0.2	0.1	0.0	-0.1	-94	2	-22
1691	Broughton Island (south)	1.6	0.4	1.0	0.1	0.1	0.1	0.0	0.0	-45	39	18
1692	Bar Channel	6.9	0.6	0.9	0.2	0.2	0.2	-0.2	0.0	-12	-63	-50
1693	Entrance, north of channel	10.9	0.7	1.0	0.2	0.3	0.3	0.2	-0.1	-7	-10	-9
1694	Entrance, south of channel	10.0	0.9	0.9	0.2	0.2	0.2	-0.2	-0.1	-106	-88	-93
1696	Back River entrance	4.9	0.5	0.8	0.1	0.1	0.1	-0.1	-0.1	41	-62	-36
1698	Mackay R., 0.5 mi. N of Troup Creek entrance	3.4	0.6	1.2	0.1	0.2	0.2	0.0	0.1	-12	22	14
1699	Brunswick River, off Quarantine Dock	10.7	0.8	0.8	0.3	0.2	0.2	-0.3	-0.2	-76	-47	-54
1700	Brunswick River Bridge, southeast of	8.6	0.6	1.1	0.1	0.1	0.1	0.0	0.1	21	-25	-13
1703	Turtle River, off Allied Chemical Corp	8.8	0.7	0.7	0.2	0.2	0.2	-0.2	-0.2	-60	-63	-62
1704	Turtle River, off Andrews Island	9.2	0.6	1.1	0.1	0.1	0.1	0.1	0.1	-46	-65	-60
1705	Entrance	21.8	1.1	0.8	0.1	0.2	0.2	-0.1	-0.2	29	-2	6
1706	Jekyll Creek, south entrance	3.5	0.6	0.8	0.3	0.2	0.2	-0.3	-0.1	-49	-93	-82
1707	Cumberland River, north entrance	8.7	0.7	1.0	0.1	0.1	0.1	0.1	0.0	69	-12	8
1708	Cabin Bluff, Cumberland River	5.0	0.6	0.8	0.1	0.2	0.2	0.0	-0.2	-31	-30	-31
1709	Fort Clinch, 0.6 n.mi. NE of	14.7	1.2	1.1	0.1	0.2	0.2	0.0	0.1	-20	-54	-46
1711	Fort Clinch, 0.1 n.mi. N of	13.7	1.1	0.9	0.2	0.2	0.2	-0.2	-0.1	-31	-43	-40
1715	Cumberland Island, Range B Channel	11.6	0.8	1.2	0.1	0.2	0.2	0.0	0.2	-30	-10	-15
1721	Fernandina Beach, Amelia River	5.4	0.4	1.0	0.1	0.1	0.1	0.0	0.0	23	-57	-37

4.2.3. Model Sensitivity Analysis

Over a hundred model runs were performed throughout the study to determine the sensitivity of the numerical model to a range of parameters. Amongst these, a limited number of runs are selected as the milestones for the modeling effort as shown in Table 4.13. The name of each case, total number of computational nodes in *x* and *y* direction (*xi* and *eta*, respectively) are shown in the table. The maximum, minimum and average distances between the computational nodes in *x* and *y* direction (Lm and Ln, respectively), and the representative area for each computational cell are also given. The objective of each grid and the extent of the coastline they cover are explained in the table.

Table 4.13. Summary of computational grids used in milestone model runs

Name	Objective	eta	xi	Lm max / min / ave (m)	Ln max / min / ave (m)	A max / min / ave (km^2)	Coastline Extent
ga41	Preliminary north grid	400	300	329 / 164 / 225	816 / 102 / 348	.166 / .022 / .080	Savannah River, Wassaw, Ossabaw Sounds
ga42	Preliminary mid-north grid	250	300	475 / 63 / 138	297 / 11 / 184	.141 / .012 / .025	St. Cathrines and Sapelo Sounds
ga43	Preliminary mid-south grid	300	300	256 / 90 / 163	356 / 75 / 155	.066 / .009 / .025	Doboy, Altamaha and St. Simons Sound
ga44	Preliminary south grid	125	250	737 / 212 / 349	1022 / 291 / 414	.604 / .063 / .151	St. Andrews and Cumberland Sounds
ga41_t	ga41 grid truncated offshore	330	300	262 / 164 / 217	816 / 102 / 205	.165 / .022 / .045	Savannah River, Wassaw, Ossabaw Sounds
ga44_t	ga44 grid truncated offshore	330	300	607 / 212 / 288	1048 / 291 / 398	.560 / .063 / .117	Savannah River, Wassaw, Ossabaw Sounds
ga31	North grid	424	200	265 / 188 / 228	249 / 207 / 238	.064 / .043 / .054	Savannah River, Wassaw, Ossabaw Sounds
ga31wd	North grid with wetting and drying						
ga32	Center grid	288	200	262 / 188 / 229	248 / 220 / 235	.065 / .043 / .054	Ossabaw, St. Catherines, Sapelo, Doboy and Altamaha Sounds
ga32wd	Center grid with wetting and drying						
ga33	South grid	376	200	269 / 185 / 225	338 / 221 / 245	.090 / .043 / .055	Doboy, Altamaha, St. Simons, St. Andrews and Cumberland Sounds
ga33wd	South grid with wetting and drying						
ga31F	Finer north grid	400	900	205 / 70 / 98	318 / 84 / 100	.032 / .006 / .010	Savannah River, Wassaw, Ossabaw Sounds
ga31Fwd	Finer north grid with wetting and drying						
ga32F	Center finer grid	800	400	140 / 42 / 93	226 / 84 / 107	.021 / .004 / .010	Ossabaw, St. Catherines, Sapelo, Doboy and Altamaha Sounds
ga32Fwd	Finer center grid with wetting and drying						
ga33F	Finer south grid	900	400	202 / 71 / 96	261 / 78 / 105	.021 / .006 / .010	Doboy, Altamaha, St. Simons, St. Andrews and Cumberland Sounds
ga33Fwd	Finer south grid with wetting and drying						

The grids used prior to the final grids are also shown in Figure 4.23. The stations or measurement locations used for validation purposes depend on the extent of each grid. Also for different grids, the number of the stations used for validation purposes may change depending on which of the stations can be resolved by that computational grid. The effect of the parameters on the model runs is assessed through comparison of the output from short term model runs (2-day simulations) with the predicted maximum currents and high/low tide elevations from NOAA. Despite not being as reliable as the measurements, they are still useful as reference values in comparing different model results.

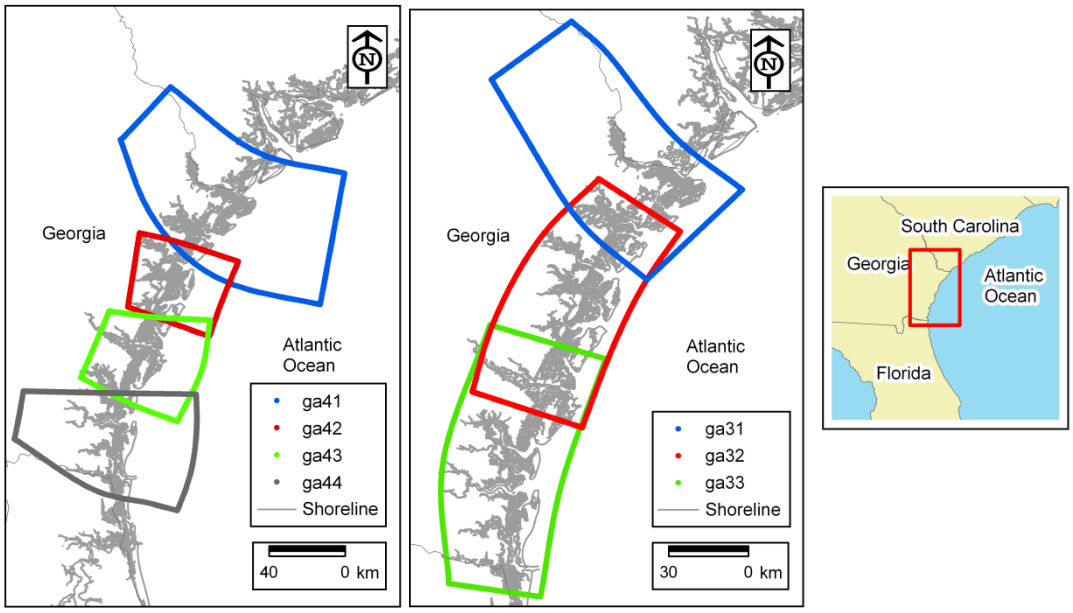

Figure 4.23. Examples of different computational grids that are used for ROMS simulations of the tidal currents along the Georgia coast.

Effect of computational cell size

In order to understand the effect of the resolution of the computational grid on the results, two different cases are discussed here. Case ga31FR is a case that stretches approximately over the northern one third of the Georgia coast. It includes the Savannah River up to Clyo, GA. It is a 400x900 mesh of computational grid points with the average distance between the grid points around 100 meters. Case ga31R is a coarser grid that also covers about the one third of the coast, but stretching inland only about half of the finer grid, ga31FR. It is a 424x200 grid with the average distance between the points about 230 meters. Both cases account for wetting and drying at the unmasked computational cells. The results from the two models are compared on the basis of how well each one agrees with the predictions given by NOAA. When compared to the maximum current predictions from NOAA, neither of the model results matches completely (Figure 4.24). There are over predictions and underpredictions at different locations. The current magnitude ratio (*cmgrt*) ranges between 0.5 and 1.2, but is closer to 1.0 for larger currents. It is seen that the results agree less with the NOAA predictions for locations with small current magnitudes, which are not shown in the figure. Also for locations with large magnitudes one model can give a ratio closer to 1.0 at a location and do worse at another, where as it might be the opposite for the other model. The differences in the phase are usually less than ±60 minutes. The model with the fine grid consistently underpredicts at a number of locations.

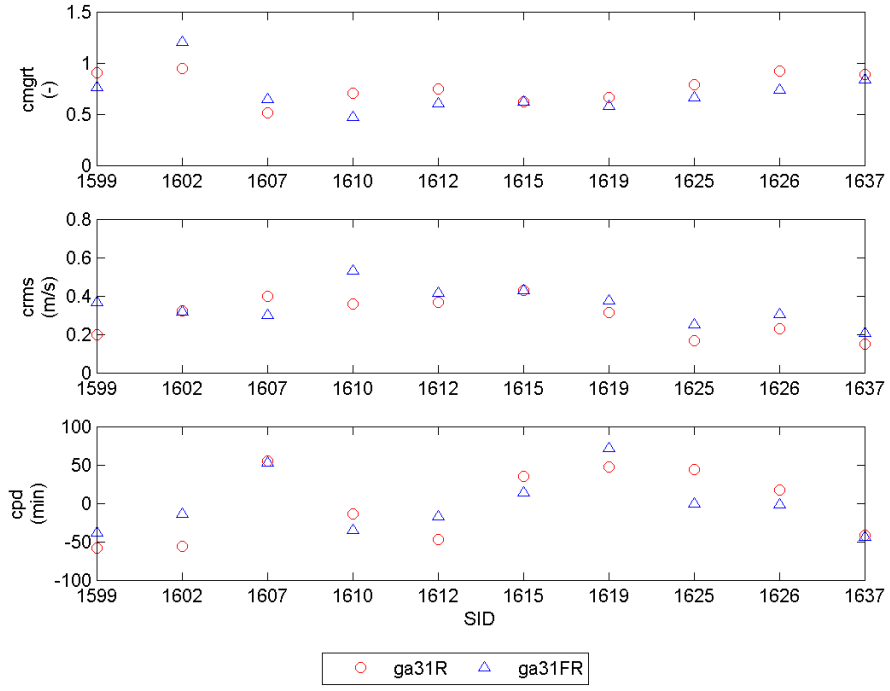

Figure 4.24. North grid (ga31R) and finer north grid (ga31FR) validation parameters for NOAA maximum current predictions at each prediction location SID.

The comparison of the model results with the NOAA high/low predictions show that ga31FR agrees slightly better with the NOAA predictions, yet both of the models do a good job with *srtdt* between 0.9 - 1.05, and *phd* within -40 to +20 minutes usually (Figure 4.25). The same trend is observed between the two center grids, ga32R and ga32FR, and between the two south grids, ga33F and ga33FR. It is usually expected for a finer computational grid to more accurately resolve the details of the coastline hence improve the results. However, once the locations of major interest are resolved by the model, further refining of the grid has a minor effect on the result when compared to the additional computational load.

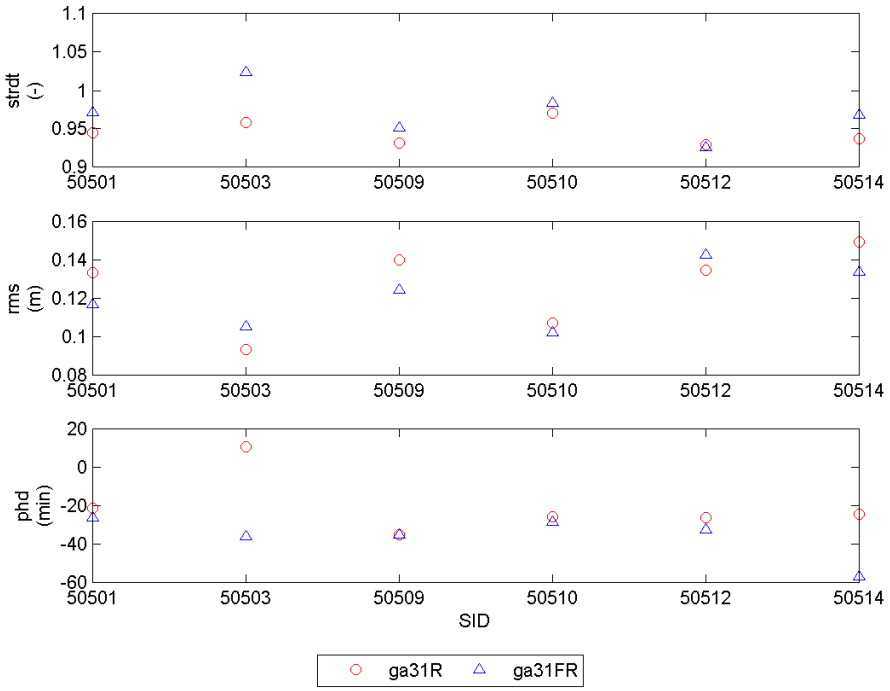

Figure 4.25. North grid (ga31R) and finer north grid (ga31FR) validation parameters for NOAA high/low tide predictions at each prediction location SID.

In the case of models used through this study, reducing the cell size twice showed no significant or consistent change in the results, but significantly increased the computational time required. Since *ga31FR* has computational points that are about 2 times denser spatially than *ga31R*, it is expected to be slower. However, the model run time is much longer (about 16 times longer) than the coarser grid, because the grid with the smaller computational cell size also requires smaller time step for stability. A computational grid that is 2 times finer in both planar directions has about 4 times more computational cells and the time step is also 4 times smaller. In the end, it is concluded that an average cell size of 230 m was sufficient and a finer mesh was not required.

Determining the Offshore Extent of Computational Grids

While modeling it is preferred to reduce the computational time as much as possible by keeping the number of grid points small without degrading the quality of modeling. For this purpose, analysis of the offshore extent of the grid at the open boundary is performed (Figure 4.26). The offshore extent of the original model runs is set along the inner continental shelf boundary (i.e. 20-m isobath). After each successful run, the grid is cropped at the offshore extent and the results from these different models are compared to assess its effect on the modeling. The predicted constituents for tidal water elevation and tidal currents from each case are compared at the grid points that are selected from the offshore boundary of the smaller grid, the river mouths and sound entrances, and away from the open boundary at the upstream reaches of rivers. Two examples from the preliminary models, one from the northern and the other from the southern part as shown in Figure 4.26 are discussed here.

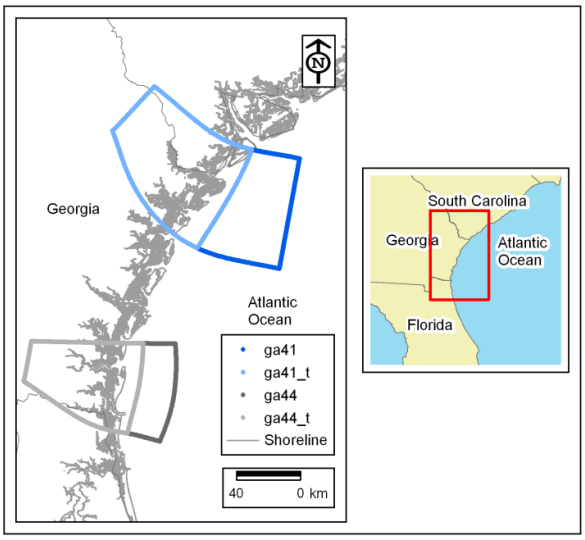

Figure 4.26. The extent of computational grids compared on the Georgia coast for the effect of the location of the open boundary.

The first example is from the northern part of the Georgia coastline, where the results from a model with an offshore extent at the inner continental shelf and a model with a varying distance from the shoreline (0 to 15 km) are compared. The locations of the control points are shown in Figure 4.27. Point 10 is upstream of point 11 along the Savannah River and cannot be seen in the figure. The difference between the results from the original and the truncated models is analyzed by comparing the magnitudes and phases of the M2 constituent for the tidal currents and water surface elevations. The results from the comparisons at the north grid are shown in Table 4.14. The difference between two models is generally under 2 cm/s and 2 cm for the currents and the elevations, respectively. The maximum magnitude difference is found to be 3 cm/s for the currents and 3 cm for the elevations. The phase difference in M2 constituent for the currents and elevations is under 5 minutes at most of the control points. The two models agree well on the magnitude of the M2 constituent for the currents and the water surface elevations at most of the control points. There is a larger difference (12 minutes) in the phase of M2 for the currents at the offshore boundary of the truncated grid.

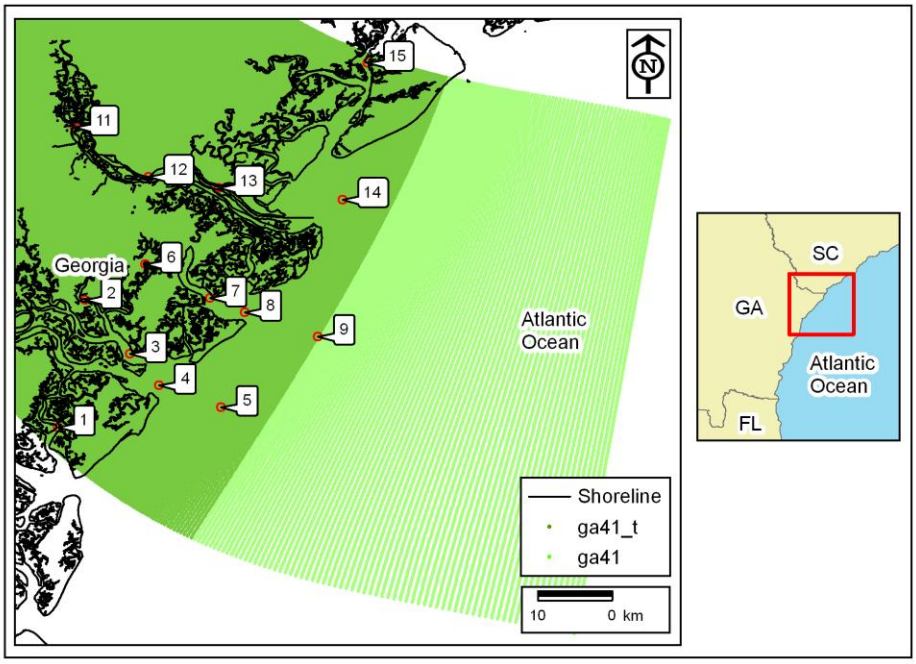

Figure 4.27. The points where results from the preliminary north grid (ga41) and the grid truncated at the offshore boundary (ga41_t) are compared.

Table 4.14. Difference in the M2 constituent of tidal currents and water surface elevations between the original (ga41) and the truncated (ga41_t) north grid.

Point	1	2	3	4	5	6	7	8	9	10	11	12	13	14	15
Current Magnitude Diference (m/s)	.00	.01	.02	.01	.01	.00	.02	.03	.01	.00	.00	.01	.01	.00	.00
Current Phase Difference (min)	4	3	4	4	2	0	1	3	12	4	4	4	6	6	5
Elevation Magnitude Difference (m)	.01	.01	.02	.02	.02	.02	.02	.02	.03	.00	.01	.01	.01	.01	.01
Elevation Phase Difference (min)	4	3	4	5	5	1	2	2	1	4	4	4	4	5	5

The second example is from the southern part of the Georgia coastline. The initial grid has its offshore boundary following the 15-m isobath, and the cropped grid is generated by truncating the offshore extent of the initial grid closer to the shoreline (> 5

km). The locations of the control points are shown in Figure 4.28 and differences in the between the magnitudes and phases of the M2 constituent are given in Table 4.15. The difference between the two model results in terms of the differences between the M2 constituent for current magnitude and water surface level are observed to be smaller for the inland than the offshore boundary locations (e.g. 1 to 3, 4 to 8, and 7 to 11). The difference in the magnitude and phase of M2 is larger closer to the offshore boundary of the truncated grid (e.g. Point 6). However, the differences at the entrances to the sounds and the river mouths (e.g. 2, 3, 10, 12 and 11) are small (< 3cm/s and < 3 cm). Therefore, the offshore extent for the final computational grids is set around the 10-m isobath, not closer than 5 km to the shoreline.

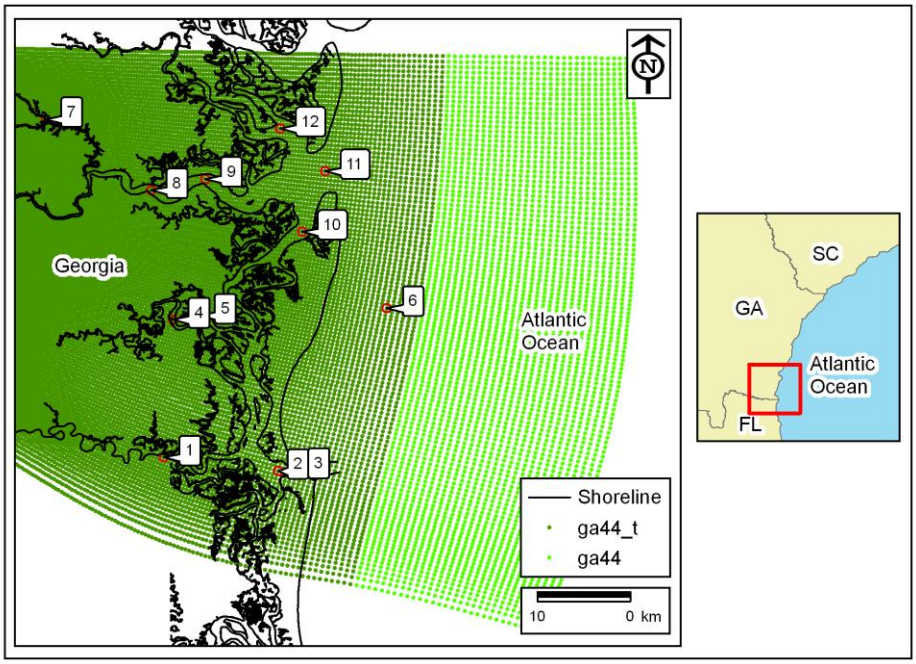

Figure 4.28. The points where results from the preliminary south grid (ga44) and the grid truncated at the offshore boundary (ga44_t) are compared.

Table 4.15. Difference in the M2 constituent of tidal currents and water surface elevations between the original (ga44) and the truncated (ga44_t) south grid.

Point	1	2	3	4	5	6	7	8	9	10	11	12
Current Magnitude Diference (m/s)	.00	.01	.02	.00	.00	.03	.00	.01	.02	.02	.01	.01
Current Phase Difference (min)	2	1	1	1	1	36	1	1	1	1	2	1
Elevation Magnitude Difference (m)	.01	.01	.01	.01	.01	.02	.01	.02	.02	.02	.03	.02
Elevation Phase Difference (min)	1	1	1	1	1	0	1	2	2	2	3	2

Effect of Wetlands

According to the National Wetlands Inventory data and the wetlands constitute 47% of the wet cells in the computational grid used for the Georgia coast (Figure 4.29.a). Although the maximum wetland area is not achieved at every tidal cycle due to the higher locations in the topography, the wetlands still accommodate significant amount of water in each tidal cycle. Although there is virtually no additional wet area introduced due to the wetlands at MTL, it starts to make an impact once the water level rises above the MTL. Additional wet area for water level 0.2 m above MTL is shown in Figure 4.29.b. For every 10 cm increase in the water level, about a hundred square kilometers additional area is inundated with sea water (Table 4.16).

Time series for current magnitudes from Fort Pulaski near the Savannah River entrance on the north and Fort Clinch at Cumberland Sound entrance demonstrate the amplification in the ebb currents when wetlands are incorporated in the model (Figure 4.30). The additional volume of water in the tidal prism added by the wetlands increases

the ebb magnitude, whereas it may sometime increase the flood magnitude as well due to the larger volume of water in the computational grid compared to the original grid without the wetlands.

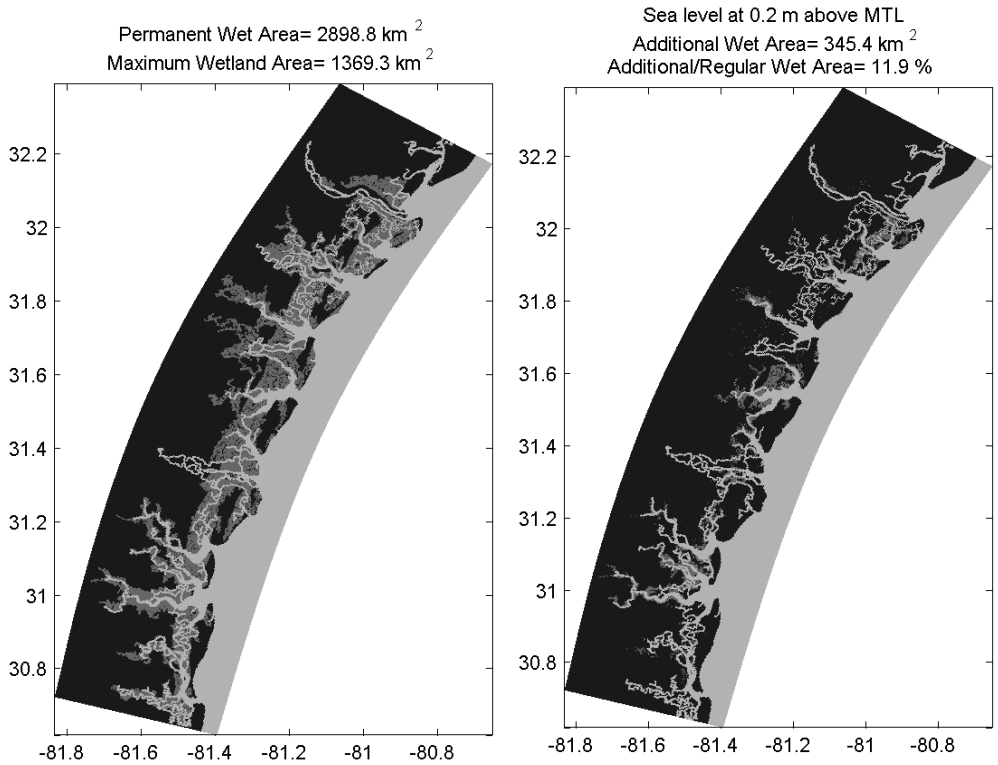

Figure 4.29. (a) Wetland area in the computational domain and (b) additional wet area for water level 0.2 m above MTL. Permanently dry cells (black), permanently wet cells (light gray) wetting drying cells (gray).

Table 4.16. Additional wet area due to wetlands at different tidal stages for the Georgia coast computational domain.

Sea Level above MTL (m)	0	0.1	0.2	0.3	0.4	0.6	0.8	1	1.5	2
Additional Wet Area (km^2)	28	112	345	442	524	657	938	1118	1318	1341

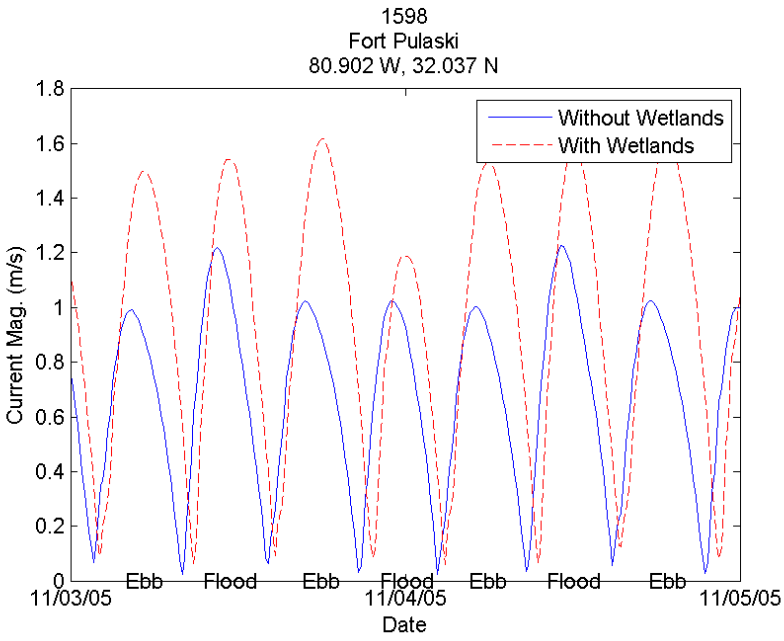

(a)

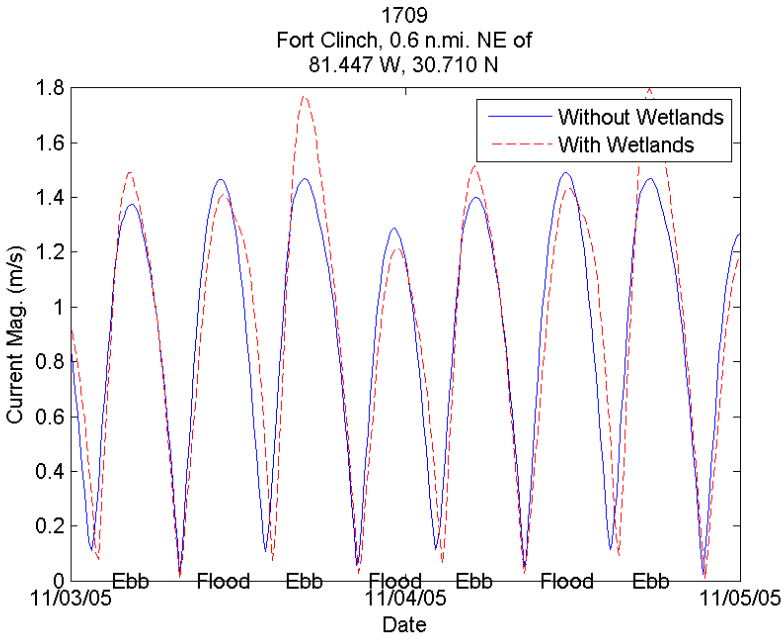

(b)

Figure 4.30. Current magnitudes computed by the model with and without wetlands at (a) Fort Pulaski near Savannah River entrance and (b) Fort Clinch at Cumberland Sound entrance.

In order to show the effect of integrating the wetlands in modeling the tidal currents, the modeling results from the computational grids without the wetlands are compared to the results with the wetlands on the basis of how well the results agree with the predictions given by NOAA. For this purpose, first the north grid without the wetlands (ga31R) is compared to the north grid with the wetlands (ga31wd). Then a comparison between the south grids (ga33wd and ga33R) is given. Figure 4.31 shows the variation of validation parameters for maximum tidal currents at the NOAA prediction locations for results from ga31R and ga31wd. The mean of the modeled current magnitudes are also closer to the predictions by NOAA. i.e. *cmgrt* is closer to 1.0, and the absolute difference between the model and the NOAA predictions are smaller when the wetlands are included (i.e. *crms* is smaller). The comparison between ga31wd and ga31R shows that in general the current magnitudes from the model increase when wetlands are included in modeling the currents. This is due to the fact that the additional wet cells provide additional water mass through a larger tidal prism that increases the rate of flow in the rivers and estuaries.

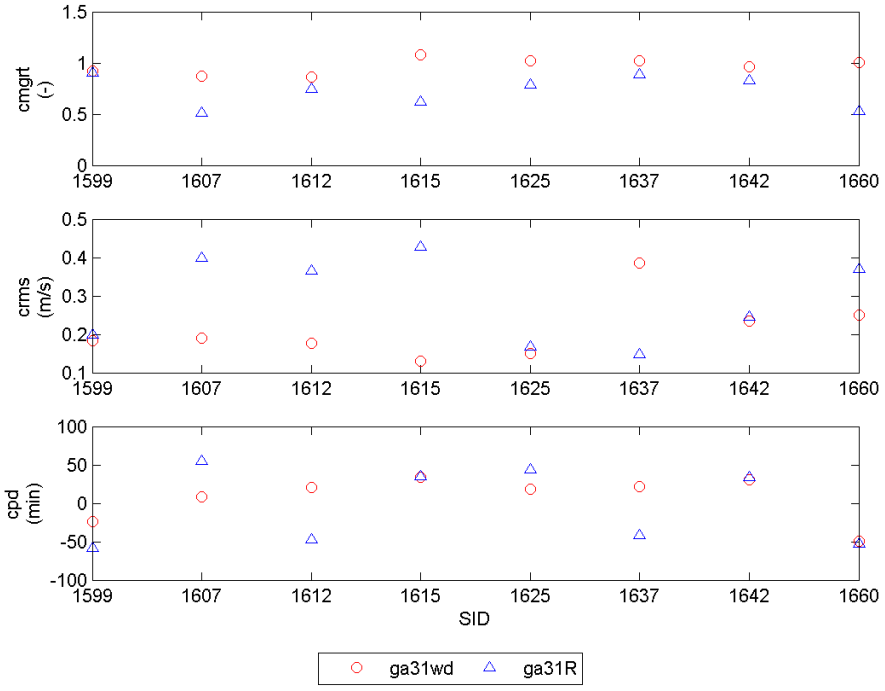

Figure 4.31. Validation parameters for maximum tidal currents at the NOAA prediction locations for north grid (ga31R) and north grid with wetlands (ga31wd).

At location 1637, *crms* is noticeably larger for the model with the wetlands than without the wetlands (Figure 4.31). The *cmgrt* value for this location is 1.03, which means that the model is good in computing the average magnitude of the maximum currents. The *crms* is higher for this location since the model with the wetlands overpredicts the maximum ebb currents and underpredicts the maximum flood currents as shown in Figure 4.32. When compared to the NOAA predictions, the model with wetlands do a slightly better job in computing the phase difference for the tidal currents than the model without the wetlands. There are, however, a few locations where the model with the wetlands is not any better than the regular grid in computing the phase differences. Even for those locations the difference between the phase computed with the

model and the NOAA predictions are less than 50 minutes, and they are not shown in Figure 4.31.

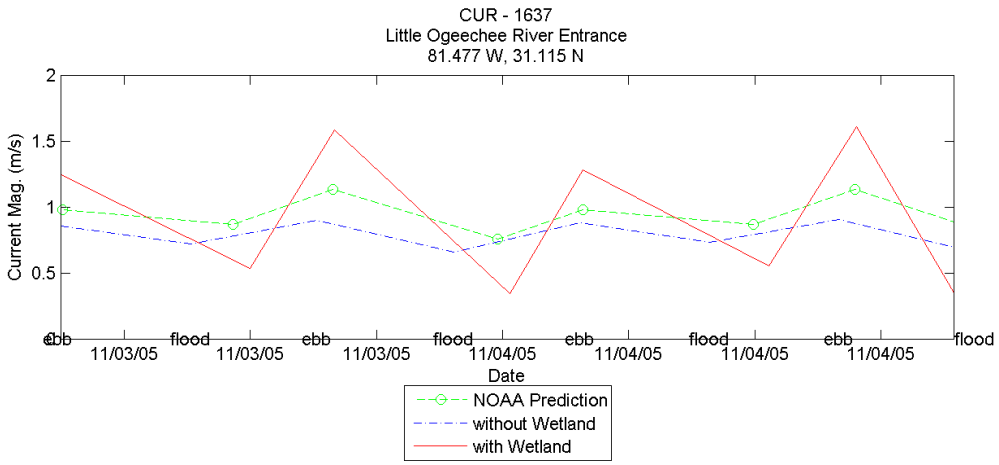

Figure 4.32. Maximum current magnitudes from the NOAA predictions, and computed by the model with wetlands (ga31wd) and without wetlands (ga31R) for location 1637.

The comparison with the high/low tide water surface elevations from NOAA is given in Figure 4.33. At some locations (e.g. 50525 and 50528) the *rms* is for the model without the wetlands is smaller than with the wetlands. However, for other locations the mode l with the wetlands still has the smaller values. The phase computed by the model with wetlands is generally closer to the phase given by NOAA predictions even though the improvement is small (~5 minutes). Including wetlands provides some improvement in computing the high/low tide elevations and phases, but the results from the model without the wetlands are close to NOAA predictions in this case, therefore, the improvement is not as considerable as the improvement in the currents.

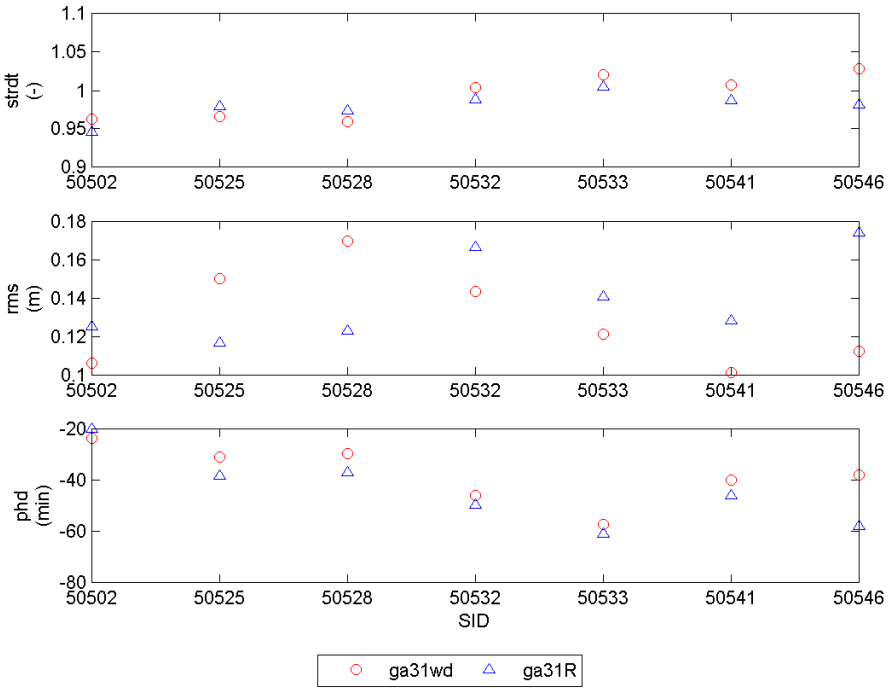

Figure 4.33. Validation parameters for high/low tides at the NOAA prediction locations for north grid (ga31R) and north grid with wetlands (ga31wd).

The validation parameters for maximum tidal currents from the south grids are shown in Figure 4.34. Based on the validation parameters, the *cmgrt* is usually closer to 1.0 with the wetlands than without the wetlands for the south grids. The only exception is at location 1700, where *crms* is larger than the case without the wetlands. However, when the maximum current magnitudes from the two models are compared at the NOAA prediction, the model with the wetlands is observed to follow the variations in ebb and flood magnitudes better at this location (Figure 4.35). On the other hand, the tidal currents from the model without the wetlands have are flood dominated (i.e. flood current has larger magnitude then ebb current) at this location contradicting with the ebb dominated NOAA predictions. Although the ratio of the *crms* at location 1700 is higher than the other locations plotted in Figure 4.34, overpredicting is not a major problem

since the average magnitude of the currents at this location is quite low i.e. on the order of 0.6 m/s. Similarly, the phase difference is around the same level or smaller with wetlands, except point 1696. This is also a location with small tidal currents (~0.5 m/s) and is not of main concern. As a result, when ga33wd and ga33R are compared against the NOAA predictions, it is concluded that the inclusion of wetlands generally yields to a better agreement between the model and the predictions.

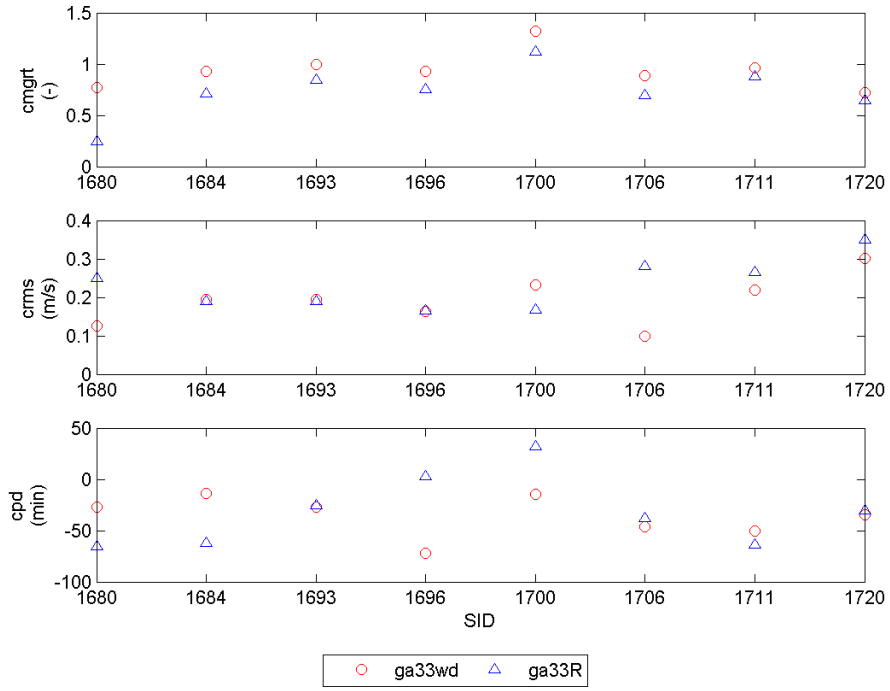

Figure 4.34. Validation parameters for maximum tidal currents at the NOAA prediction locations for south grid (ga33R) and south grid with wetlands (ga33wd).

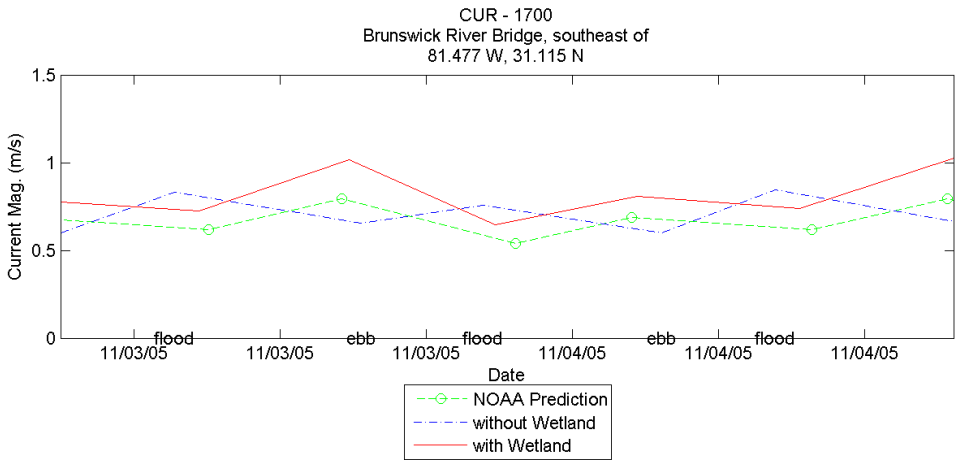

Figure 4.35. Maximum current magnitudes from the NOAA predictions, and computed by the model with wetlands (ga33R) and without wetlands (ga33wd) for location 1700.

The comparison with the high/low tide predictions show that the water surface levels from the model with the wetlands are closer to NOAA predictions (Figure 4.36). The results from the model without the wetlands at locations with significant differences from the predictions (i.e. 50555 and 50587) are substantially improved when the wetlands are included. The *crms* for these locations is reduced about 15-20 cm, and for most of the remaining locations it is below 15 cm. For the southern part of the coast the improvement in the phase difference for the water levels is more pronounced (usually on the order of 40 minutes) than the northern coast when the wetlands are included in the modeling.

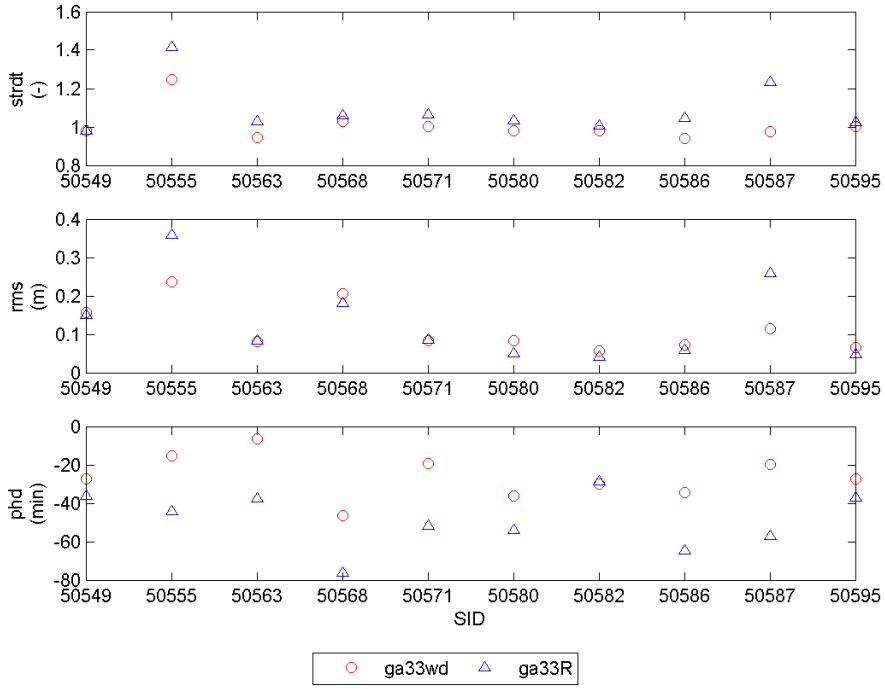

Figure 4.36. Validation parameters for high/low tides at the NOAA prediction locations for north south (ga33R) and south grid with wetlands (ga33wd).

The benefit of the wetting and drying algorithm in the ROMS simulations is that the coastline does not have to be a wall boundary anymore, and the wetlands can be included in the model. This provides a more realistic model, which can capture the asymmetry between the ebb and flood currents. The tidal prism is not confined to the solid boundaries but varies according to the topography of the wetlands. The increased number of wet cells and the change in the tidal prism are found to enhance the tidal current magnitudes. The results from the model runs with wetlands are closer to NOAA predictions in general, and agree better with the measurements than the model runs without wetlands.

Effect of Bathymetry Smoothing

Sigma-coordinate ocean models are prone to have intrinsic error in the horizontal pressure gradient (HPG) term in the presence of strongly varying bathymetry, which presents a problem for the stability of the model solution. One way to solve this problem is to increase the number of grid points in the horizontal and vertical direction, which in return requires smaller time steps for stability purposes thus results in a computationally expensive model. The other way to solve this problem is to smooth the bathymetry. Bathymetry smoothing is required for the computational grids with fine resolution and when the wetland topography is included in the simulations.

Different methods for smoothing can be found in the literature (Martinho and Batteen, 2006; Mellor et al., 1994; Sikiric et al., 2009). Some of these methods are the Shapiro filter, Mellor-Ezer-Oey (MEO), Martinho and Batteen (MB) and linear programming (LP). Amongst these, the MEO and LP methods preserve the features of the bathymetry the most. The Shapiro and MB filters have faster algorithms, but they are not as good in preserving the bathymetry (Sikiric et al., 2009). Although they perform similarly for the range of smoothing applied herein, the LP method is computationally expensive when compared to the MEO method. The MB method smoothes the bathymetry by increasing the depths only, while the MEO method both increases and decreases them in order to preserve the total volume. Both of these methods are set up to use the slope factor (rx_0) and hydraulic inconsistency number (rx_1) to assess the stability of the model related to hydrostatic inconsistency. The slope factor (rx_{0_p}) is given as the ratio of the difference between the depths of adjacent wet cells to the sum of them;

$$rx_{0_p} = \frac{|h_p - h_{padj}|}{h_p + h_{padj}} \tag{4.15}$$

where *h* is the depth, *p* denotes the p^{th} computational cell and *padj* denotes the cells adjacent to the p^{th} computational cell. The hydraulic inconsistency number (rx_{1_p}) is a similar ratio between the vertical layers of the adjacent wet cells;

$$rx_{1_p} = \frac{\left|z_p^k - z_{padj}^k + z_p^{k-1} - z_{padj}^{k-1}\right|}{\left|z_p^k + z_{padj}^k - z_p^{k-1} - z_{padj}^{k-1}\right|} \tag{4.16}$$

where z^k and z^{k-1} are the k^{th} and $(k-1)^{th}$ depth layers that bound parallelepiped for that vertical layer. Based on ROMS modeling community experience it is recommended to satisfy $rx_0 \leq 0.2$ and $rx_1 \leq 6$ for ROMS models. Since the hydraulic inconsistency number is defined based as a function of depth layers and the wetlands lie above the MTL (i.e. topography is negative according to the ROMS sign convention), the hydraulic inconsistency number is not suitable for smoothing. The slope factor is found to be sufficient for the smoothing required in the studied cases and the sensitivity analysis is based on it.

Two different methods are followed in smoothing the bathymetry for the computational grid. In the first method the smoothing is performed on the whole computational grid after merging of the topography of the wetlands and the bathymetry of the wet cells. For the second method the smoothing was applied separately to the wetlands and the wet cells before merging them on the final computational grid. The second method preserves the shoreline better (i.e. less difference between amount of wet area in the computational grid at MTL for the original and smoothed bathymetry), and is used in further analysis of the effect of smoothing. The effect of bathymetry smoothing is evaluated by assessing the amount of change in the water surface area at different tidal

stages. For this purpose the amount of wet area with the original bathymetry and with the smoothed bathymetry are compared for water levels within the tidal range. Using this approach, a comparison between three different smoothing methods, MB with $rx_0 \leq 0.2$, MEO with $rx_0 \leq 0.2$ and $rx_0 \leq 0.8$ is shown in Table 4.17. Considering the first two cases with $rx_0 \leq 0.2$, the overall change in the bathymetry is larger when the original bathymetry is smoothed with the MB method than smoothed with the MEO method. The MEO method conserves the volume by decreasing the depth at one point and increasing in others while satisfying the required rx_0. The change in the volume due to the change in the elevation of a wet cell is compensated by adjusting the elevation of the connected wet cells according to their cell sizes. The additional wet area computed for the second and the third cases (i.e. MEO with $rx_0 \leq 0.2$ and $rx_0 \leq 0.8$) indicates that satisfying a larger slope factor ($rx_0 \leq 0.8$) than the commonly known limit ($rx_0 \leq 0.2$) while smoothing is sufficient to sustain the stability of the model. The additional wet area hence the alteration in the bathymetry is significantly lower than the other two cases. The percent change in the wet area is kept below 1% at all stages between -2 m and 2 m.

Both for the topography of the wetlands (positive sea levels) and the bathymetry of the sea floor (negative sea levels) the MEO method is found to alter the original values less than the MB method. It is important to keep the deviation from the original topography small especially above the MTL, since the change in the tidal prism and the amount of additional water body depends strongly on it. When MEO ($rx_0 \leq 0.8$) is used the change is kept minimal (below 0.1%). Therefore, with the original bathymetry is altered less while avoiding related computational blow-ups.

Table 4.17. Change in wet area of the computational gird due to smoothing of the original bathymetry with different methods (Positive sea level means above MTL).

Sea Level above MTL	Additional Wet Area					
	MP ($rx_0 \leq 0.2$)		MEO ($rx_0 \leq 0.2$)		MEO ($rx_0 \leq 0.8$)	
(m)	(km^2)	(%)	(km^2)	(%)	(km^2)	(%)
-2	165	6.6	111	4.5	0	0
-1.5	119	4.5	92	3.5	0	0
-1	47	1.7	37	1.3	0	0
-0.8	33	1.2	24	0.8	1	0
-0.6	26	0.9	17	0.6	2	0.1
-0.4	25	0.9	18	0.6	3	0.1
-0.3	27	1	19	0.7	4	0.1
-0.2	30	1.1	22	0.8	5	0.2
-0.1	37	1.3	28	1	6	0.2
0	93	3.3	90	3.2	27	0.9
0.1	-100	-3.3	-83	-2.8	-9	-0.3
0.2	-177	-5.4	-111	-3.4	-1	0
0.3	-155	-4.6	-64	-1.9	1	0
0.4	-130	-3.8	-28	-0.8	1	0
0.6	-64	-1.8	38	1.1	2	0.1
0.8	-30	-0.8	34	0.9	1	0
1	-17	-0.4	28	0.7	2	0
1.5	-9	-0.2	3	0.1	1	0
2	-3	-0.1	4	0.1	0	0

4.3. Tidal Power Potential of the Georgia Coast

In this section, the results from the modeling are used to generate tidal power density maps to determine the sites with higher tidal power potential on the Georgia coast. Annual average power for favorable sites is computed from one-year time series and the effect of turbine efficiency on converting the tidal power is discussed. Streamflow from rivers is assessed regarding its effect on the tidal currents and tidal power density.

4.3.1. Tidal Power Density

The concentration of available power density is usually located at the sound entrances, river mouths or narrower reaches of channels between the islands. However, tidal power is also affected by interaction of many other parameters such as the bathymetry, the interconnection of the tidal streams, and geographical shape of the sound. Tidal power maps are useful in identifying these locations, and quantifying their extent. Tidal power density is defined as the power density per unit vertical area that water flows through. Additionally, surface areas of the high power density locations are calculated from the power maps. The surface area does not contribute to power density, but instead provides information on the extent of the area that can be considered for development. A larger area is expected to accommodate more turbines than a smaller area although it is unlikely to have a linear relation between the surface area and the number of turbines due to the downstream effect of energy extraction. Similarly, the width of the surface area across the flow direction is an important parameter.

The average tidal power density computed by the model for the northern coast of Georgia is shown in Figures 4.37. Regions with tidal power density larger than 500 W/m^2 are shown in red color on the map. The surface areas for these regions are also given on the map in terms of square kilometers if they are larger than 0.15 km^2. Starting from the north to south, there are two such regions along the Savannah River; upstream of the final bifurcation before the river reaches the ocean and on the southern branch near Fort Pulaski. The tidal power density upstream of the bifurcation varies from 600 to 1100 W/m^2 whereas along the southern branch of the Savannah River it is between 300 and 800 W/m^2. The width of these areas across the river is about 300 m. Along the northern part of the coast, the Wassaw Sound has the least amount of tidal current power with less than 200 W/m^2 at its entrance. Although the Ossabaw Sound entrance has low tidal power density, there is a relatively larger amount of tidal power density at the mouth of the Ogeechee River and Canoochee River that flows into the Ossabaw Sound. The regions of even larger tidal current power are isolated at upstream of the branches that flow to Ogeechee River, but there are considerably large areas along the Canoochee River (0.15, 0.29, 0.23 and 0.77 km^2). The model results indicate that the Canoochee River is the most energetic feature along the northern Georgia coast for tidal current power. The mean tidal power density is on the order of 800 W/m^2 for 0.29 km^2 and 0.23 km^2, and varies between 750 and 1050 W/m^2 for areas of 0.15 and 0.77 km^2. It is found that the mean power density can be as large as 1400 W/m^2 at certain locations of the 0.23 km^2 areas. The width of these regions across the river is about 250 m, with an exception for the 0.77 km^2 area, which has a maximum width as large as 750 m. St. Catherines Sound entrance has a moderate tidal current power density (200~500 W/m^2), but tidal

current power density in the Medway River that flows into it is relatively larger, 800 W/m^2 with a surface area of 0.68 km^2 and a width between 250 to 500 m across the river. Finally, Sapelo Sound entrance and the Sapelo River accommodate regions of 0.19 and 0.21 km^2, respectively, with tidal power densities on the order of 700 W/m^2. The widths across these areas are ~500 m and ~250 m respectively.

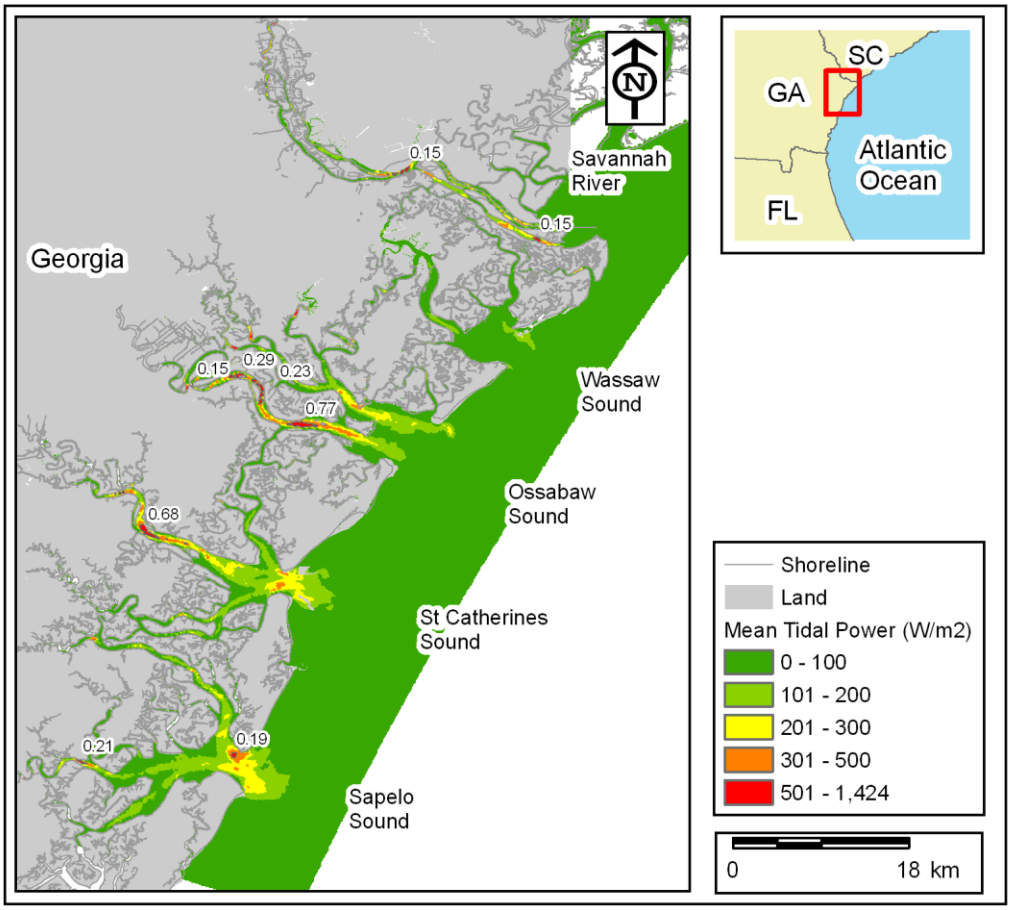

Figure 4.37. Map of the mean power density along the northern coast of Georgia. Numbers show the surface area (km^2) of the sites with high tidal power density (>500 W/m^2).

The southern part of the Georgia coast is generally a more moderate source of tidal current power (Figure 4.38). With mean tidal power densities of < 100 and < 200

kW/m^2 respectively, Doboy and St. Simons Sounds are the least energetic sounds along the southern coast. However, the largest tidal power density on the southern Georgia coast is observed in one of the channels along the Intercoastal Waterway between the Doboy and Altamaha Sounds. The mean tidal power varies from 500 to 1600 W/m^2 within an area of 0.28 km^2. The tidal power density at the entrance of the Altamaha Sound is on the order of 300 – 600 W/ m^2. It increases to 500 W/m^2 and up to 600 - 800 W/m^2 for an area of 0.37 km^2 further upstream of the Altamaha River. Although tidal power density south of this location, along the branch that comes from the Buttermilk Sound is found to be as large as 800 – 1100 W/m^2, it is a narrowly confined area (< 0.15 km^2) not visible in the figure. The northern half of the St. Andrews Sound entrance, downstream of the Little Satilla River, has slightly larger power density than the southern half. However, the Satilla River itself has a larger area of larger tidal power density (200 – 700 W/m^2) than the sound and the Little Satilla River. A total area of 0.16 km^2 with tidal power density larger than 500 W/m^2 is available, but it is split into two smaller areas along the upstream of the river. The Cumberland Sound entrance has the largest contiguous area (2.2 km^2) for a tidal power density level between 300 – 600 W/m^2. The largest tidal power density for this area (~ 700 W/m^2) is observed right at the entrance to the Cumberland Sound. The extent of the total area with power density larger than 500 W/m^2 is about 0.22 km^2, sum of 0.16 km^2 and 0.06 km^2 east of it (not shown on the map). 600 – to 1600 W/m^2. The width of this area across the entrance varies between 250 and 500 m.

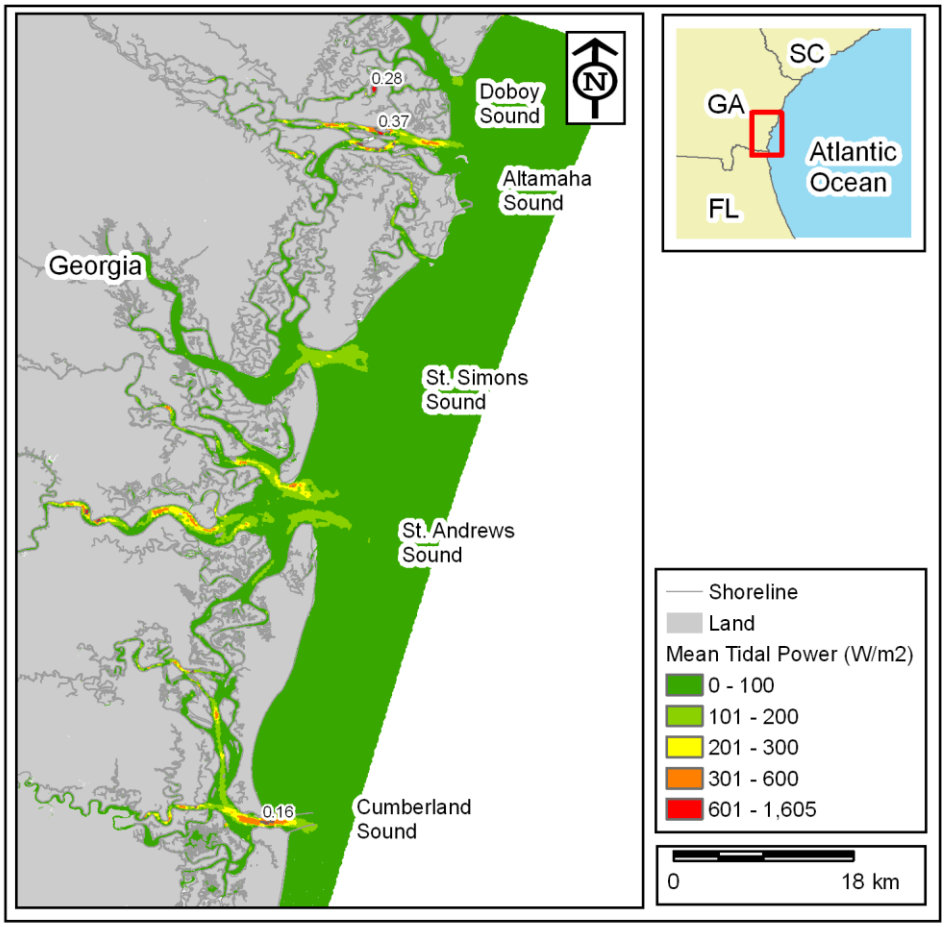

Figure 4.38. Map of the mean power density along the southern coast of Georgia. Numbers show the surface area (km^2) of the sites with high tidal power density (>500 W/m^2).

4.3.2. Annual Average Power

The locations with higher power density and larger surface area determined in the preceding section are analyzed using histograms of the annual distribution of the mean tidal power density. One year of hourly data generated using constituents computed from the 30-day model runs are used to create a histogram of the velocity magnitude and the related power density. This method is applied to selected locations including the Savannah River (Coordinates: 80.907 W, 32.026 N; Surface area: 0.15 km^2), Canoochee

River (Coordinates: 81.125 W, 31.856 N; Surface area: 0.77 km^2), and Altamaha River (Coordinates: 81.343 W, 31.330 N; Surface area: 0.37 km^2). The time series for velocity magnitude for 30 days computed by the model and the time series generated for the whole year with harmonic analysis for those locations are shown in Figure 4.39.

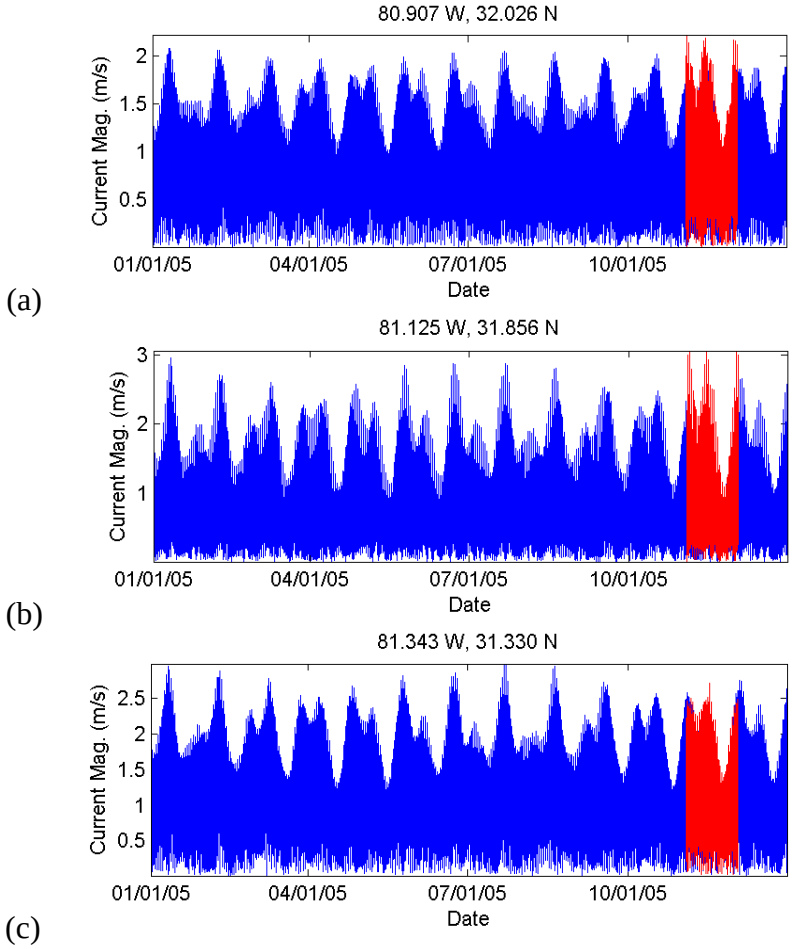

Figure 4.39. Tidal velocity magnitudes computed from velocity constituents from 30-day simulations (red), and constructed 1 year time series (blue) for (a) Upstream of the Savannah River entrance, (b) Canoochee River, (c) Altamaha River.

The histogram for the current magnitude upstream of the Savannah River entrance calculated based on a one-year time series is shown in Figure 4.40. The histogram shows the distribution of the number of hours per year for the range of tidal current magnitudes

at this location. The range of current magnitudes is defined by using a bin size of 0.10 m/s. The dominant current magnitude is between 1.00 and 1.10 m/s for this location with 684 hours (~ 8 days) a year. It is also seen that there is a steady drop in number of hours for current magnitudes that are greater than 1.30 m/s. There is also a smaller drop in the number of hours for current magnitudes less than 1.00 m/s and greater than 0.50 m/s. There is however, significant duration, about 1982 hours (~82 days) where the current magnitude is less than or equal to 0.50 m/s. The histograms of annual tidal current velocity are used to compute a histogram of total available power density. These histograms can be used to compute the annual average available power at all locations.

The histogram for the power density upstream of the Savannah River entrance is shown in Figure 4.40.b. The first bin that corresponds to 100 W/m^2 represents current magnitudes less than ~0.75 m/s and has the largest number of hours per year. More than 3000 hours (125 days) the power density at this location is less than 200 W/m^2. The power density is less than 400 W/m^2 for 4153 hours (~173 days) a year, and greater than or equal to 400 W/m^2 for 4584 hours (~191) days. The annual average for the tidal current magnitude and tidal power density upstream of the Savannah River entrance are computed as 0.93 m/s and 745 W/m^2, respectively. The annual average power is at this location is 1.3 MW and which corresponds to a total energy of 112 GWh/year.

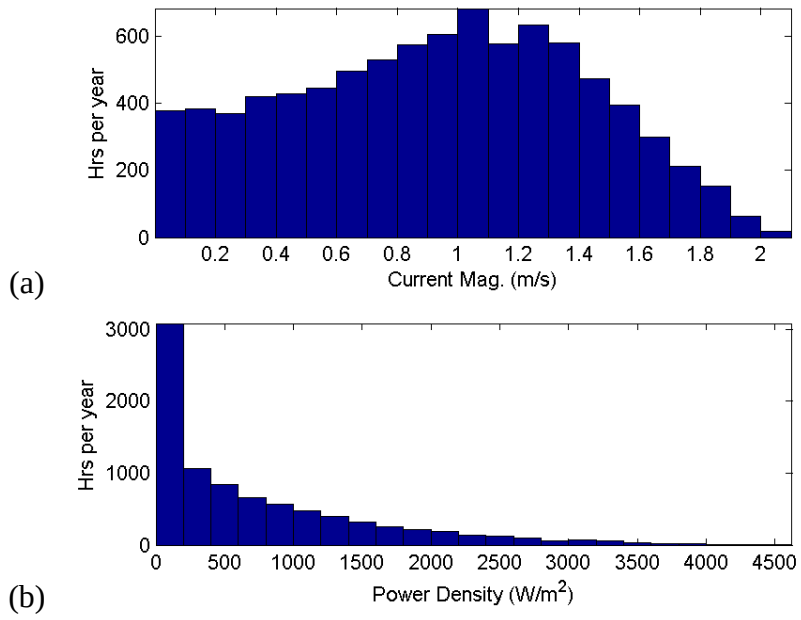

Figure 4.40. Distributions of the number of hours per year: (a) tidal current magnitudes and (b) tidal power densities in Savannah River entrance based on one-year time series.

The current magnitude histogram for the Canoochee River shows that the most frequent current speed, which occurs 590 hours (~25 days) a year is between 1.00 and 1.10 m/s (Figure 4.41). The tidal current magnitude is less than or equal to 0.50 m/s for 2180 hours (~90 days) of a year, and it is greater than or equal to 1.00 m/s for 3750 hours (~156 days) of a year. Although the annual maximum for the mean current magnitude at this location can be as large as 3 m/s the average is 0.93 m/s. This results in a bigger gap between the maximum and the mean of the tidal power density since the power is directly proportional to the cube of the current magnitude shown in Figure 4.41.b. Here the tidal power density is larger than or equal to 400 W/m^2 for 4200 hours (~175 days) a year. The tidal power density is less than 200 W/m^2 for about 3450 hours (~114 days) a year. The annual average for the tidal power density in Canoochee River is computed to be 880

W/m^2, which translates to an annual average power of 3.0 MW and a total energy of 258 GWh/year.

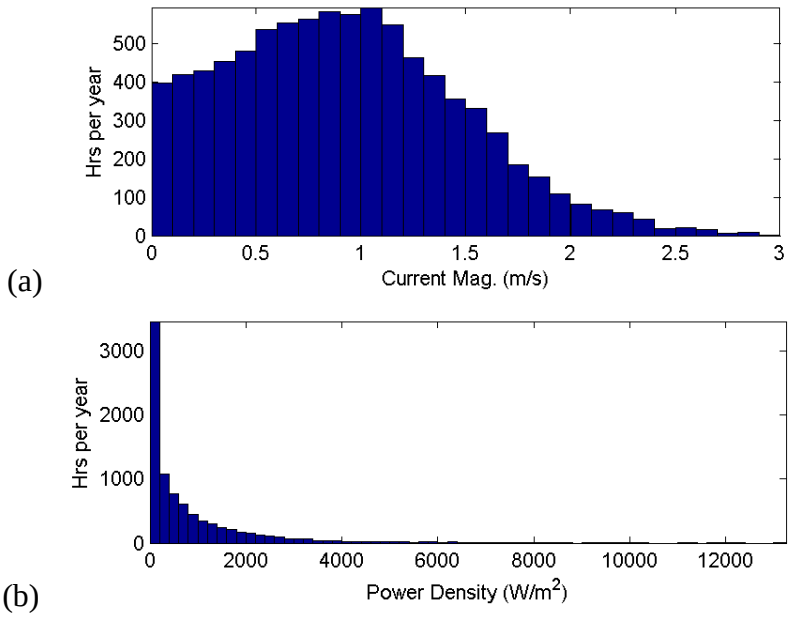

Figure 4.41. Distributions of the number of hours per year: (a) tidal current magnitudes and (b) tidal power densities in Canoochee River based on one-year time series.

Figure 4.42.a. and 4.43.b show the histograms for the tidal current magnitude and power density for the Altamaha River. The tidal current magnitude is between 1.20 and 1.30 m/s for 540 hours of a year at this location. It is less than 0.50 m/s and more than 1.00 m/s for 1395 hours and for 5558 hours (~230 days) a year, respectively. The annual mean tidal power density is less than 200 W/m^2 2138 hours (~90 days), and is more than 400 W/m^2 for 5905 hours (~245 days). The annual average for the tidal current magnitude and tidal power density in Altamaha River are computed as 1.23 m/s and 1735 W/m^2, respectively. The annual average power for Altamaha River is 1.9 MW and the total energy is 162 GWh/year.

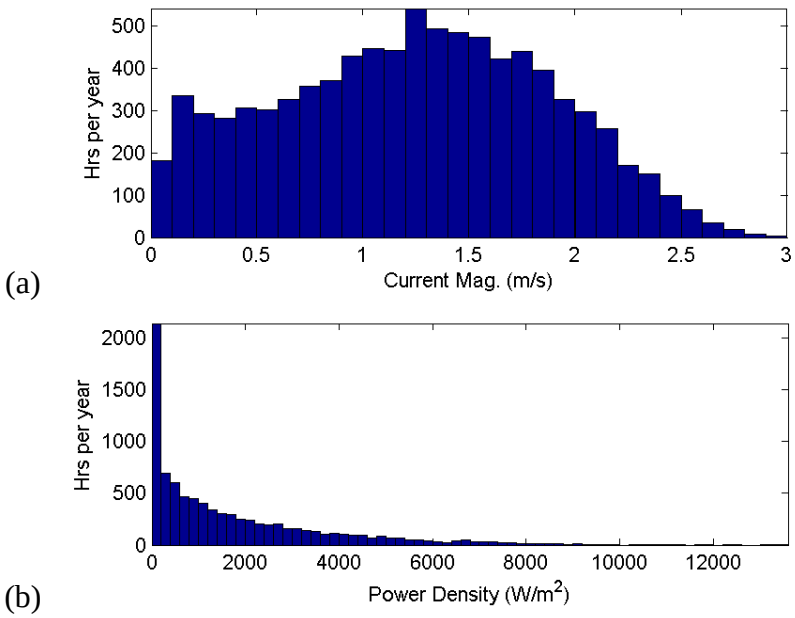

Figure 4.42. Distributions of the number of hours per year: (a) tidal current magnitudes and (b) tidal power densities in Altamaha River based on one-year time series.

4.3.3. Effective Power

Unfortunately turbines are incapable of converting all of the power in the flow field. For any given tidal stream converter the power that is converted to usable power can be estimated by

$$P_{eff} = C_{eff} \cdot \rho \cdot V^3 \tag{4.17}$$

where P_{eff} is the effective power density and C_{eff} is the efficiency of the device in converting the power (Bryden and Melville, 2004; Bryden and Couch, 2006; Garrett and Cummins, 2004). Since the efficiency is a function of the flow speed, an efficiency curve is frequently used for computing the expected turbine output power. A generic efficiency function of velocity that accounts for the losses and maximum turbine speeds (Hagerman et al., 2006c) as shown in Figure 4.43 is used as C_{eff}. for and sane either by orienting themselves with the flow direction or by other means. In effective power calculations it is

assumed that the devices are capable of converting power with the same efficiency independent of the flow direction either by orienting themselves with the flow direction or by other means.

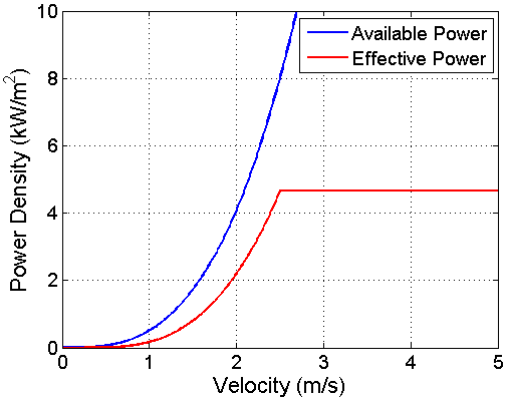

Figure 4.43. Example of an efficiency curve for tidal turbines (Hagerman et al., 2006c) and the ideal available power density.

The effect of efficiency curves on the available tidal power density is highlighted in Figure 4.44. For all of the cases there is a significant reduction in the maximum mean tidal power, a noticeable increase in the number of hours for the first bin of the histogram. Using an efficiency curve for calculating the power density results in a decrease in the output power but provides a more realistic estimate of the practical power potential. Upstream of the Savannah River turbine efficiency reduces the average annual available power density from 745 W/m^2 to 323 W/m^2. Similarly, at Canoochee River the reduction is from 880 W/m^2 to 405 W/m^2 for Canoochee River. The average annual power density of 1735 W/m^2 in Altamaha River converts to 870 W/m^2 of effective power.

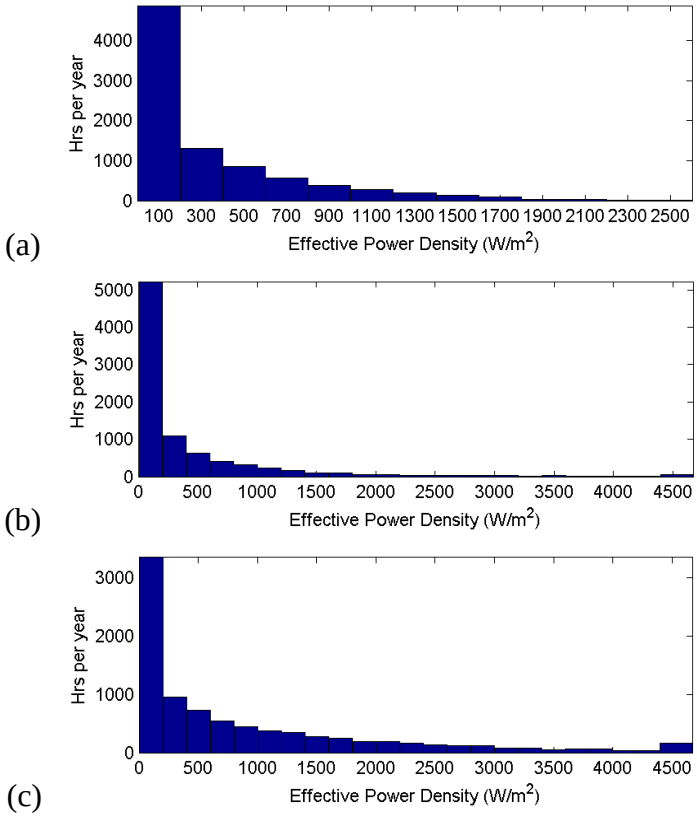

Figure 4.44. Effective power density histograms for (a) Savannah River upstream, (b) Canoochee River, (c) Altamaha River.

The total converted power depends on the total area swept by the turbine blades for horizontal converters and the number of units deployed in a flow. A small turbine with a diameter of 3 m can extract that 2.9 kW from the tidal currents in Canoochee River, and a larger turbine with a 5 m diameter can increase this value up to 8.0 kW. This section of Canoochee River is 9000 m wide, and has a depth of ~9 m for ~250 m of the width, which can accommodate tens of 5m-diameter converters. In a case where 20 converters are deployed the power conversion at this location can be as high as 160 kW. This corresponds to monthly energy of 115.2 MWh, about the monthly electricity consumption by 100 residential units in Georgia. The calculations for power conversion

given here are rough estimates for demonstration purposes only, and determining the real power conversion values requires a much more detailed analysis, which is beyond the scope of this study. In addition to the efficiency of power conversion, physical constraints such as the allowable space in the vertical to place a power converter further constrain available of areas for power conversion. Physical and additional constraints are discussed later in Chapter 6 about the use of GIS tools in selection of the suitable areas for tidal power conversion projects.

4.4. Including River Discharge

For all the previous results, the model is run with the tidal forcing only, and therefore the results are solely based on tidal currents. River flow is subsequently incorporated in order to assess the related amount of current power density by investigating the change in the total power density. For this purpose, a point source needs to be defined on the computational grid at the upstream boundary of a river. USGS National Water Information System (USGS, 2008b) provides information on surface water, which includes water flow in streams. There are many USGS streamflow gages in the region and the ones closest to the shoreline can be used in determining the fresh water fluxes. USGS provides real-time, daily and peak flow data and statistics for daily, monthly and annual periods for each gage. Some of the coastal counties of Georgia and the location of the streamflow gages are shown in Figure 4.45. Different colors of gages represent the real-time streamflow compared to percentiles of historical daily streamflow for the day of the year. Daily mean discharge for streamflow gage at Savannah River near Clyo for a year is also provided as an example.

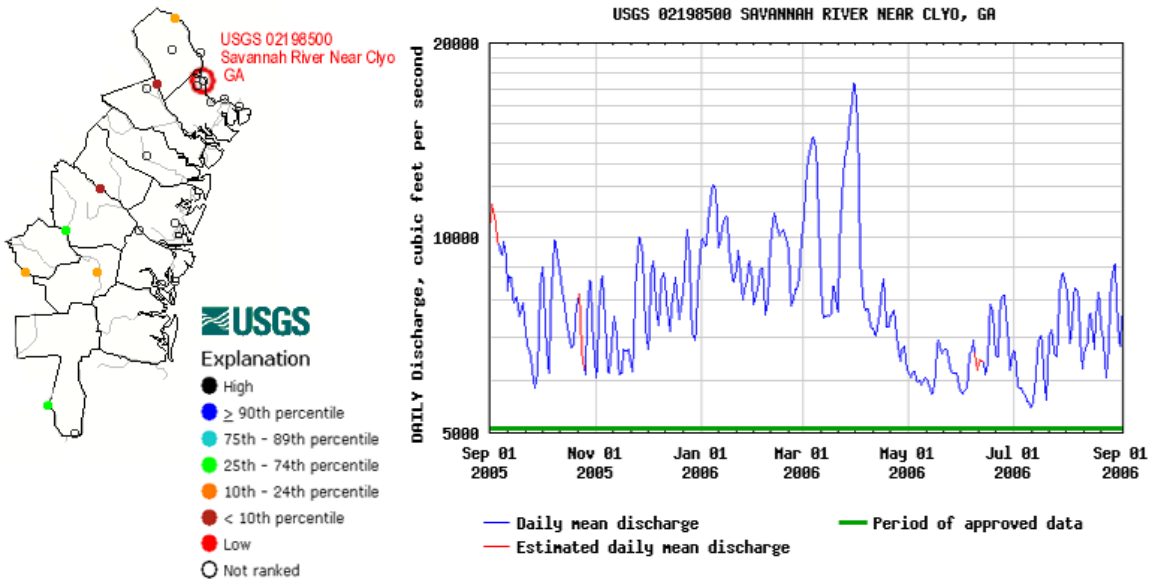

Figure 4.45. Location of streamflow gages in coastal counties of Georgia and daily mean discharge for the Savannah River station near Clyo for a year.

The 20-year mean of the total discharge from the ten rivers along the South Atlantic Bight shows a seasonal low of 1000 m^3/s in autumn and a maximum of 4000 m^3/s in spring. The maximum discharge is over 8000 m^3/s during the high discharge years (Blanton and Atkinson, 1983; Chen, 2000). The streamflow data from the available USGS stations implies that most of the rivers in the modeled area can be considered tidal rivers, since they have small discharges upstream of the intertidal zone compared to the tidal fluxes. The streamflow time series for two of the rivers with the largest discharge are shown in the Figures 4.46. The figures show the availability of the data for the modeled year, 2005, and availability of data in general. The data is smoothed with a 90-day moving average to filter the extreme discharge values and to provide a slow time variation of the discharge in a year, allowing four different average values per year to represent different seasons.

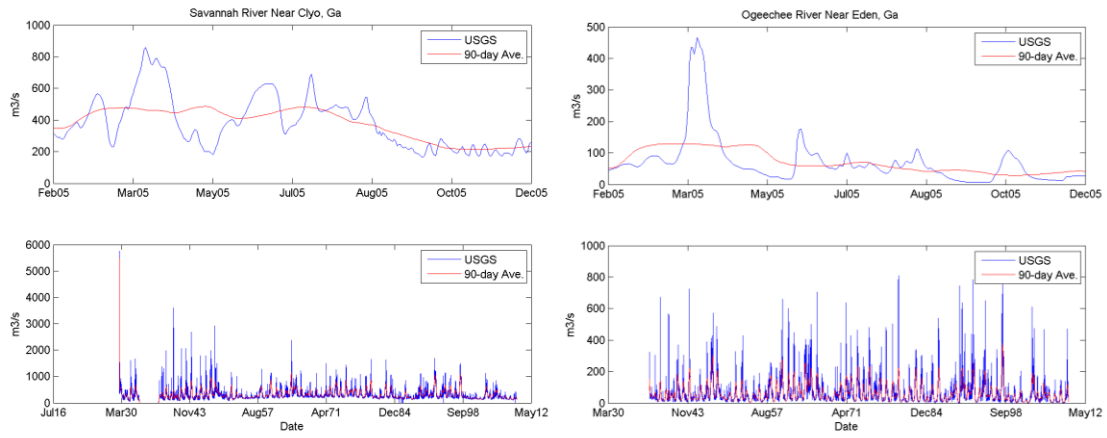

(b)

Figure 4.46. Daily streamflow data and 90-day moving discharge averages for (a) Savannah River and (b) Ogeechee River.

Along the Georgia coast, the Savannah River discharge dominates the other rivers, hence it is suitable to demonstrate the effect of river flow on the model and the additional power density accompanied with it. The data from USGS shows that the mean discharge for the Savannah River at Clyo stations is about 500 m^3/s and the maximum discharge can be as large as 4000 m^3/s. Hence different levels of discharges between 500 m^3/s and 4000 m^3/s are simulated by introducing a point source at the lateral boundary, upstream of the Savannah River. In each case, the discharge is applied at the two computational grid cells located at the boundary with a flow profile uniform in the vertical. Consequently, the results from these cases are compared to the results from the model runs with the tidal forcing only.

The difference in the mean power density in Savannah River between a case with purely tidal forcing and no river flow, and a case with a point source of 500 m^3/s located at the river upstream boundary is shown in Figure 4.47.a. Both of the maps are based on the time series from the 30-day simulations. This is an example for the average discharge

in the Savannah River. The effect of the river inflow is observed as an increase in the power density in comparison to the case without the river flow. The increase in the power density is more noticeable within the first 8 km downstream of the source (not shown in the figure) and at those locations downstream of bifurcation at 81.13° W – 31.14° N and upstream of the merger at 81.13° W – 31.14° N. However, the maximum increase in power density is on the order of 50 to 100 W/m^2, and remains relatively small compared to the tidal current power at these locations (usually larger than 300 W/m^2). The increase is significantly smaller at the river mouth (~25 W/m^2).

The example for a maximum river flow case for a 30-day simulation is shown in Figure 4.47.b. The added power density is much larger in this case, since the river discharge is 8 times larger than the average river flow and the power density is directly proportional to the cube of the velocity. The extreme river discharge can boost the power density as high as 8000 to 10000 W/m^2, especially near the source (not shown in the figure). An overall increase of 200 – 300 W/m^2 is observed in the tidal power density along the Savannah River in this case. The tidal power at the split and the merge is amplified on the order of 2000 – 4000 W/m^2, and about 4000 W/m^2, respectively. The additional power from the maximum flow is not reliable in terms of predictable usable power since this occurs rarely depending on meteorological events. The maximum possible current, however, is an important criterion in the design of any prospective tidal stream power converters from a survivability point of view.

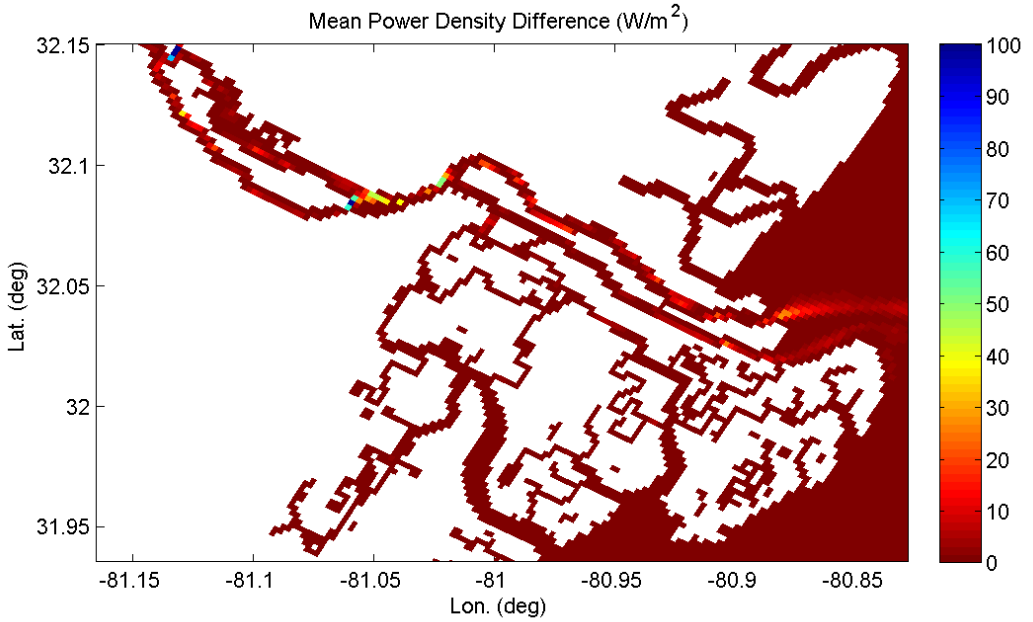

(a)

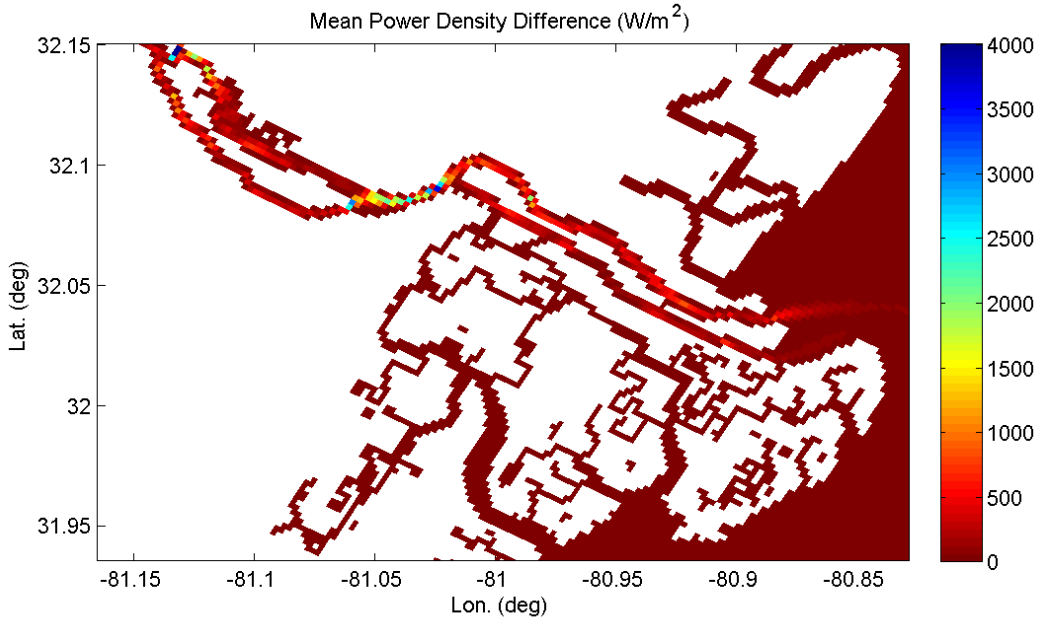

(b)

Figure 4.47. Difference in mean power density for Savannah River between a model with no river flow and a model with (a) 500 m^3/s and (b) 4000 m^3/s river flow at the upstream boundary.

The harmonic constituents computed by two different models; without river discharge and with 4000 m^3/s at the Fort Pulaski station are shown in Figure 4.48. The effect of integrating the river flow into the model has a minor effect on the tidal water level constituents computed by the model. Change in the constituent amplitudes is observed in the form of a slight decrease in the amplitudes of the four major tidal constituents (M2, N2, S2 and K1). However, even the largest reduction is i.e. ~3 cm for M2 is negligible. The additional river flow results in a slight delay in the phase of the all water level constituents, but M4 and M6 are overtides with very small amplitudes hence their computation is less reliable than the other constituents. Nonetheless, the delay is on the order of a few minutes for all constituents. In conclusion, the effect of even a very large river flow on computation of the constituents by the model remains negligibly small. On the other hand, the steady discharge reduces the magnitude of the M2 constituent on the major current axis noticeably. The current magnitude along the major axis is dominant over the minor axis at the river mouth, hence the absolute change in the minor axis is negligible. The change in the phase is less than a 100 minutes and can be either positive or negative.

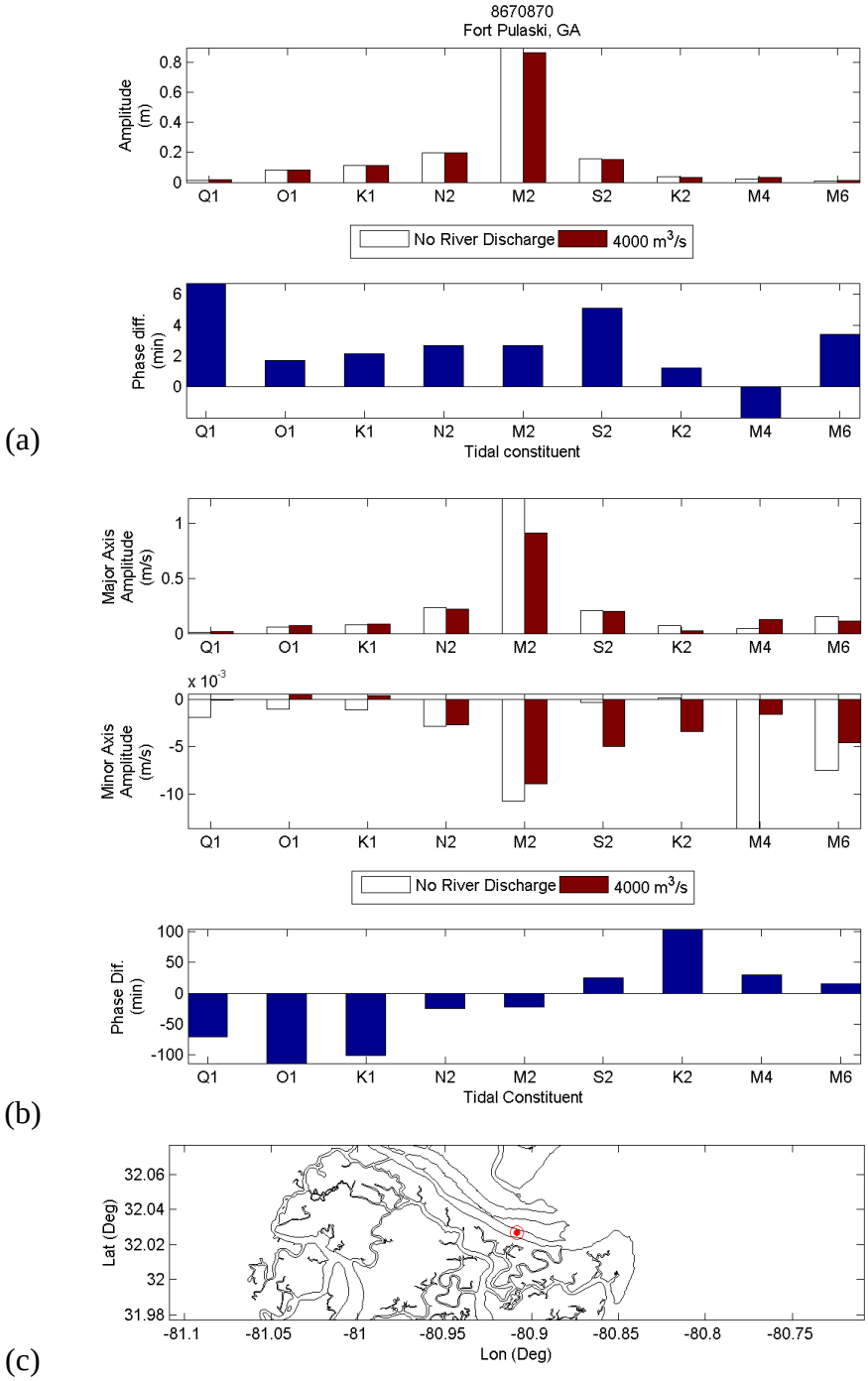

Figure 4.48. Constituents of (a) water levels and (b) tidal currents for cases without river flow and with 4000 m^3/s river flow at (c) Fort Pulaski.

Finally, 2-day time series of current magnitude and power density are compared upstream of the Savannah River entrance for three different cases; 0 m^3/s (no river flow), 500 m^3/s and 4000 m^3/s river flows (Figure 4.50). The comparison of the time series for current magnitudes show that the river flow amplifies with the tidal currents during ebb and diminishes during flood as expected. However, the relation between increase and the decrease is disproportional. For the three tidal cycles shown in the figure, the average decrease in magnitude of the flood currents is about 10 cm/s and 81 cm/s for 500 m^3/s and 4000 m^3/s additional river flow, respectively. This is less than the magnitude of decrease in the current speeds during ebb for the same cases; 7 and 32 cm/s, respectively. As seen in Figure 4.51, the river flow reduces the flood flow magnitude more than it increases the ebb flow. The comparison between the average power densities in these three different cases are emphasizes the average power density increases with increasing river discharge. The average power densities are estimated as ~580 W/m^2, ~595 W/m^2 and ~770 W/m^2, for no river, 500 m^3/s and 4000 m^3/s additional river flow cases. This is attributed to the tidal power density being proportional to the cube of the current magnitude, while the cube of the increased current speed adds more to the power density than the cube of the decreased current speed takes out in this case. The average annual power at this location is computed as 0.9 MW for the no river flow case, and 1 MW and 1.3 MW for 500 m^3/s and 4000 m^3/s cases, respectively.

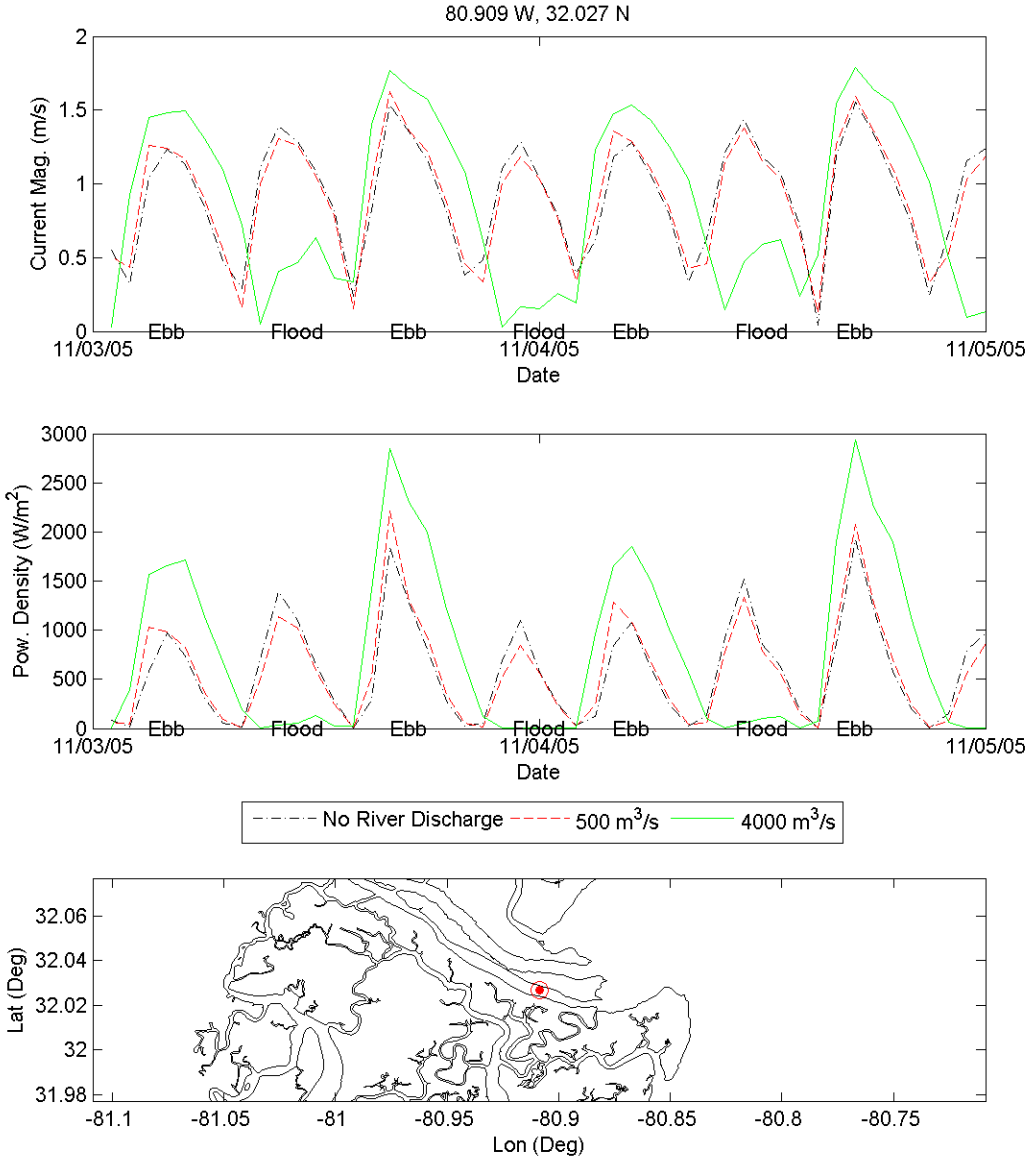

Figure 4.49. 2-day time series for the (a) current magnitude and (b) power density for different river discharge values (c) upstream of the Savannah River Entrance.

CHAPTER V

MODELING THE EFFECT OF TIDAL POWER EXTRACTION ON ESTUARINE HYDRODYNAMICS

Placing a group of power converters in a free stream flow will change the near-field and far-field flow patterns depending on the amount of power removed from the original flow. The power deficiency caused by the converters, referred to as absorbed or extracted power, is usually advised to be limited to 15-30% of the total power in the flow field for practical applications to avoid any major impact on the ecosystem (Bryden et al., 2004; Couch and Bryden, 2006; Hagerman et al., 2006c; Polagye et al., 2008). Modeling of tidal power extraction is discussed in the first part of this chapter. The methodology for simulating the power extraction in the computational model is explained and the model results are analyzed to quantify the extracted power. The consequences of power extraction on the estuarine hydrodynamics are evaluated in the second part in terms of change in the mean tidal power density in the modeled domain. The change in the water levels and tidal current magnitudes are evaluated by analyzing the time series from the model and statistics are provided.

5.1. Modeling Power Extraction

The effect of power extraction on flow can be simulated by a retarding force collinear with the direction of the flow as

$$\vec{F} = -\frac{P_{ext}}{|\vec{V}|} \cdot \frac{\vec{V}}{|\vec{V}|} \tag{5.1}$$

where $\vec{F}$ is the retarding force per unit area, $\vec{V}$ is the flow velocity, $|\vec{V}|$ is the magnitude of the velocity. P_{ext} is the extracted power density given by

$$P_{ext} = C_{ext} \cdot P \tag{5.2}$$

where C_{ext} is the coefficient that denotes the ratio of extraction and P is the power density in the undisturbed flow field. The power extraction is implemented in the computational model by modifying the governing momentum equations at the computational cells that contain power conversion devices. The magnitude of the retarding force depends on the total number of devices in a computational cell, their vertical area in the direction of flow and the efficiency of each conversion device in extracting power. Combining Equation (5.1) for the retarding force with Equation (5.2) for the extracted power, one gets the sink terms that need to be substituted in the general momentum equations in x and y directions, respectively as

$$F_u = -C_{ext} \cdot \frac{1}{2} \cdot \rho \cdot u \cdot |\vec{V}| \tag{5.3}$$

$$F_v = -C_{ext} \cdot \frac{1}{2} \cdot \rho \cdot v \cdot |\vec{V}| \tag{5.4}$$

where ρ is the density, F_u and F_v are the retarding force components per unit area, and u and v are the velocity components in x and y directions, respectively. The sink terms are implemented in ROMS as additional drag along the x and y axes of the computational cells with extraction. Each retarding force is calculated based on depth averaged velocity and a constant extraction coefficient, and applied at every depth layer since the focus here is on the far field effect. The retarding forces are applied uniformly over the entire depth with the assumption that the any devices that might be deployed along the Georgia coast will have heights comparable to the depth of the flow. However, depending on the type of the device or the depth of flow where it is deployed this might change. For example the

sink terms may be applied as a body force at the upper vertical layers starting from the water surface for floating devices, or at the lower vertical layers for devices mounted at the seafloor at deeper water. It is also assumed that the ratio of the power extraction is independent of the flow direction and the flow speed i.e. same C_{ext} in both x and y direction.

The analysis of the model results, where no power extraction is simulated, shows that part of the Canoochee River has considerably larger tidal power density over a large surface area. The Canoochee and the Ogeechee rivers are interconnected with a natural channel a few kilometers upstream of where they both merge to Ossabaw Sound. This whole area, with spots of higher power density and with its geographical complexity constitutes a worthwhile region to study the effect of power extraction in an estuarine scale. For this purpose, power extraction is simulated along the cross section of Canoochee River where the tidal power density is the highest (81.125° W, 31.856° N). Two different layouts for placing of converters are considered. For the first layout, the power converters are assumed to be uniformly distributed along the entire cross-section across the width of the river. In the second layout the flow is partially obstructed with the converters at one side across the width. The average depths for the first and the second layout are computed as 7.0 m and 5.0 m, respectively. The orientations of the two layouts are plotted in Figure 5.1 on the tidal power density map of the baseline case.

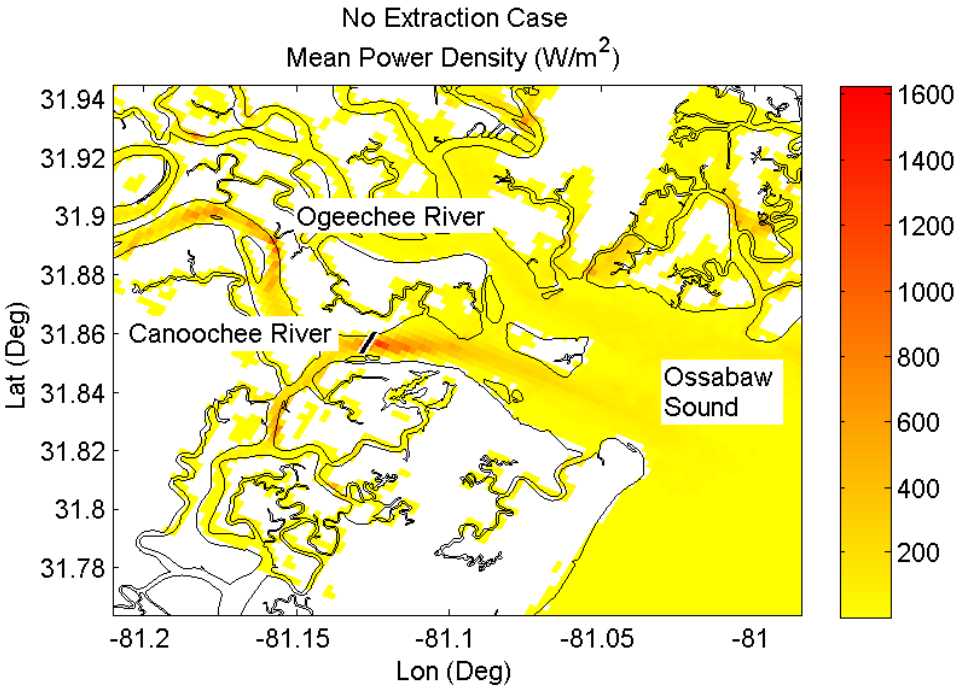

(a)

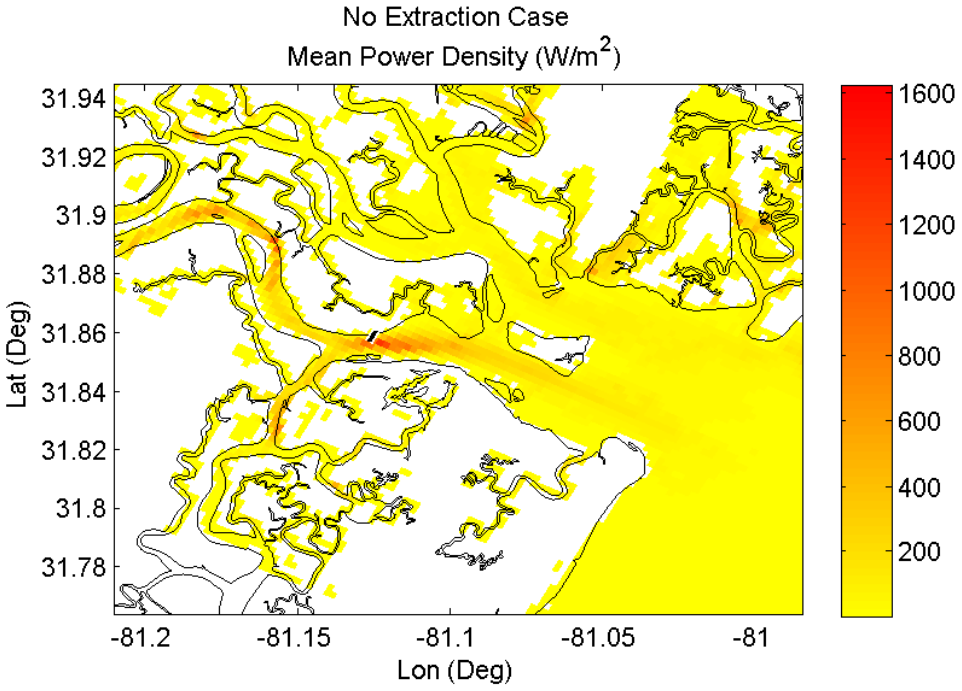

(b)

Figure 5.1. Two different layouts for placing the converters, (a) across the entire width, and (b) a part of the width, are shown on the tidal power density map of the baseline case.

In order to evaluate the effect of power extraction on the far-field flow characteristics various hypothetical cases are considered. Case 1 is a theoretical extreme, where 30% extraction (C_{ext} = 0.30) is simulated with the first layout i.e. across the entire width of the river. For this case the whole cross-section of the river is assumed blocked with a fence of converters each removing 30% percent of the tidal current power, which is at the limit of the suggested value of 15-30% for power extraction. This is a hypothetical case which is simulated to analyze the extreme possible effects of power extraction on the far-field hydrodynamics. For Case 2, the second layout for power extraction (i.e. partially obstructed) is modeled with the same extraction rate (C_{ext} = 0.3) This is also a theoretical case which can be achieved by closing the half of the river cross-section with conversion devices that remove 30% of the original tidal current power in the flow.

The time series of the tidal current magnitude and power for the first 2 days of a one-month simulation after a 2 day spin-up are compared at the extraction location. Figure 5.2 shows the tidal current time series from the baseline case and Case 1. The original power of the flow from the baseline case is provided with the extracted power and the residual power of the flow in Case 1. The maximum extracted power in Case 1 is found to be 16 MW. The total extracted energy per month in this case is computed to be 234 MWh/month, which corresponds to 12.2% of the 1.865 GWh/month total energy in the tidal currents in the baseline case with no power extraction. Although the ratio of extraction in the simulation is 30%, the ratio of the actual extracted energy to the power from the undisturbed flow in the baseline case is much smaller than this. In the case of extraction across the entire cross-section of the river, it is seen that the entire momentum

of the flow is significantly reduced resulting in a less efficiently extracted energy in the end. There is a major difference between the power time series from the case of no extraction and from the residual power in Case 1 as seen in Figure 5.2. The residual power and the extracted power in Case 1 do not add up to the original power in the baseline case, which indicates that a flow reduction occurs in Case 1 due to blocking the entire cross section.

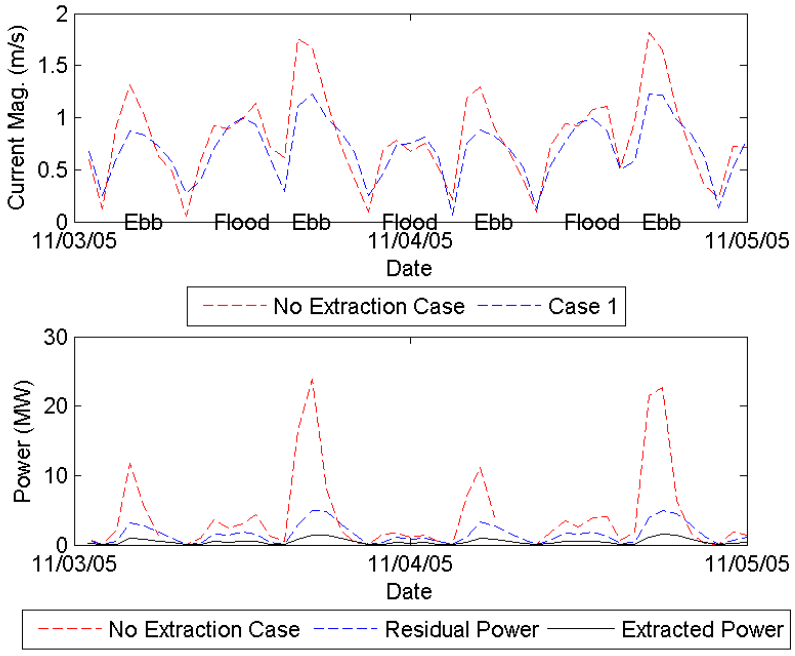

Figure 5.2. 2-day time series of tidal current magnitude, tidal current power and extracted power for the baseline case and Case 1.

In Case 2, when the cross-section is partially obstructed with the same extraction rate (C_{ext} = 0.3), both the ebb and the flood current magnitudes are reduced by comparable amounts in contrast to Case 1 (Figure 5.3). The residual power in this case is found to be closer to the power from the no extraction case. Maximum power extracted during the simulation is 4.1 MW with a mean equal to 429 kW yielding a total extracted

energy in the amount of 309 MWh/month. In Case 2, the coefficient of extraction is the same with Case 1, whereas only the energy from the partially constructed part of the channel is used for extraction. Despite a much smaller area for extracting energy, the overall amount of extracted energy is higher than in Case 1. The sum of the extracted power and the residual power in Case 2 exceeds the original power of flow in the baseline case. This is a counterintuitive finding. It appears that the replenishing of the flow with regards to the non-constricted cross-section works in favor of the power extraction by restoring some of the power removed from the flow. The ratio of the extracted energy in this case to the overall energy in the total cross-section in the baseline case is 16.7%. The energy removed from the original energy of the river is still within the suggested level in this case (Hagerman et al., 2006c).

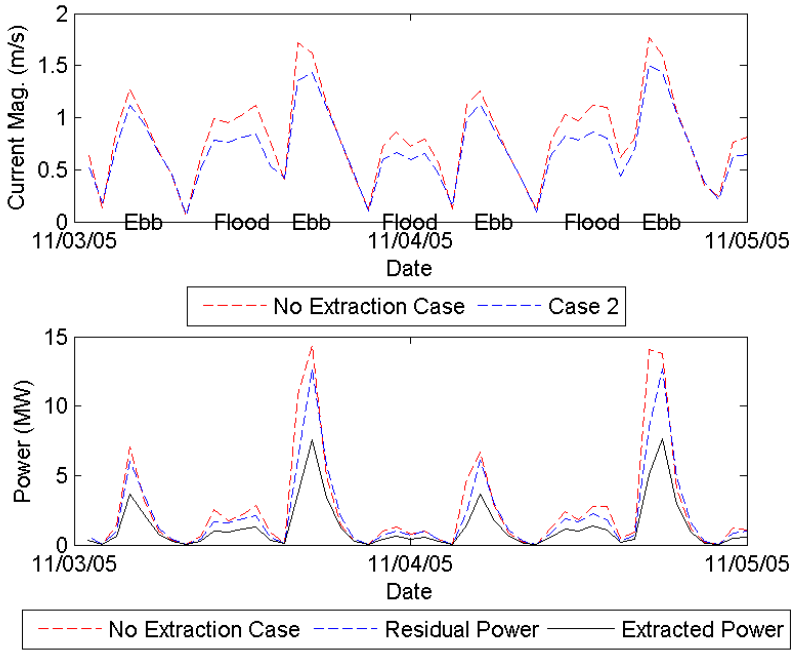

Figure 5.3. 2-day time series of tidal current magnitude, tidal current power and extracted power for the baseline case and Case 2.

5.2. Effect of Power Extraction on the Estuarine Hydrodynamics

The effect of power extraction on the surrounding estuary and rivers is investigated by analyzing the spatial and temporal change in tidal power, water levels, and current speeds for the two hypothetical cases discussed in the previous section. The difference in mean tidal power density between the no extraction case and Case 1 based on a one-month simulation is shown in Figure 5.4. The power extraction over the entire cross-section is discovered to have a severe impact on the original flow, especially in the vicinity of the extraction location. The impact is observed to be particularly significant downstream of the power extraction in the direction of ebb currents (i.e. on the open boundary side of the power extraction site), since the tidal currents in the Canoochee River are ebb dominated. The deficiency in the mean power density at this location can be as high as ~1000 W/m^2, which is comparable to the total mean power density in the baseline case without any extraction. The average reduction in power density in the Canoochee River upstream of the extraction site (i.e. on the closed boundary side of the power site) is computed to be on the order of 120 W/m^2 with areas where the power density is reduced larger than 250 W/m^2. An increase in tidal power density in the amount of 200 W/m^2 is observed in a computational cell adjacent to the extraction cells on the south, indicating increased current magnitude at this location. This is probably due to the increase in the amount of the water that seeps to this cell from the surrounding wetland cells as a result the blocked river flow. The effect of the power extraction on the Ossabaw Sound entrance observed as an average decrease in the mean tidal power density on the order of 15 W/m^2 up to 50 W/m^2 in the sound and 150 W/m^2 at the mouth of the Canoochee River.

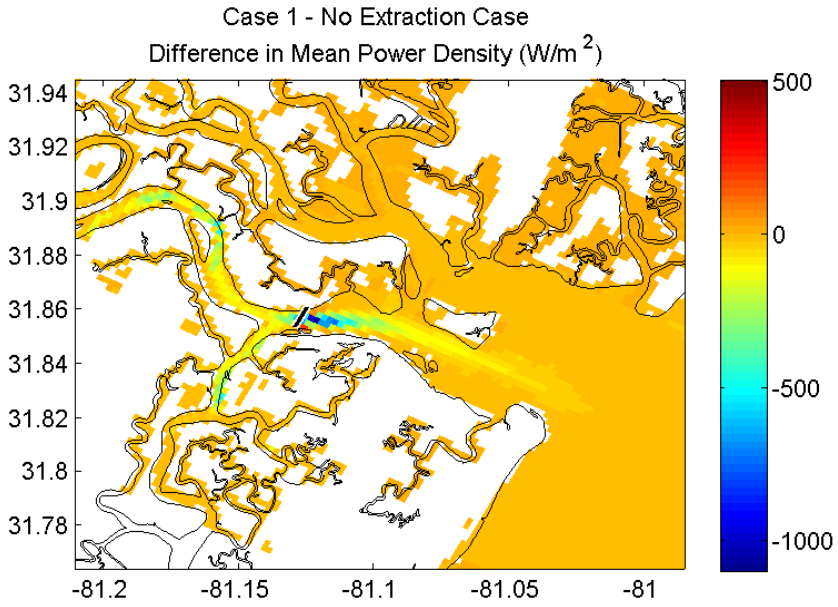

Figure 5.4. Difference in mean tidal power density in Ossabaw Sound between the no extraction case and extraction across the entire cross-section of the Canoochee River with C_{ext} =0.3 (Case 1).

The model results from Case 2 show that partially obstructing the river cross-section results in a considerably milder drop in the power density along the entire Canoochee River and its branches (Figure 5.5). The largest reduction in the mean power upstream of the Canooche River is less than 112 W/m^2, and the overall decrease in the power density upstream of the extraction site is well below 15%, with an average of 13 W/m^2.The deficiency in the power density downstream of the extraction site is more than 250 W/m^2 in a limited number of cells. The average and the maximum for these cells are 337 W/m^2 and 423 W/m^2. On the other hand, there are also a number of cells downstream of the non-constricted half of the cross-section that have larger power density than the case without power extraction. The area that has increased power density is comparable to the area with the power density deficiency, with equivalent average and maximum magnitudes, 295 W/m^2 and 336 W/m^2, respectively. Additionally, the effect of power

extraction on the power density at the entrance of the Ossabaw Sound is reduced in this case.

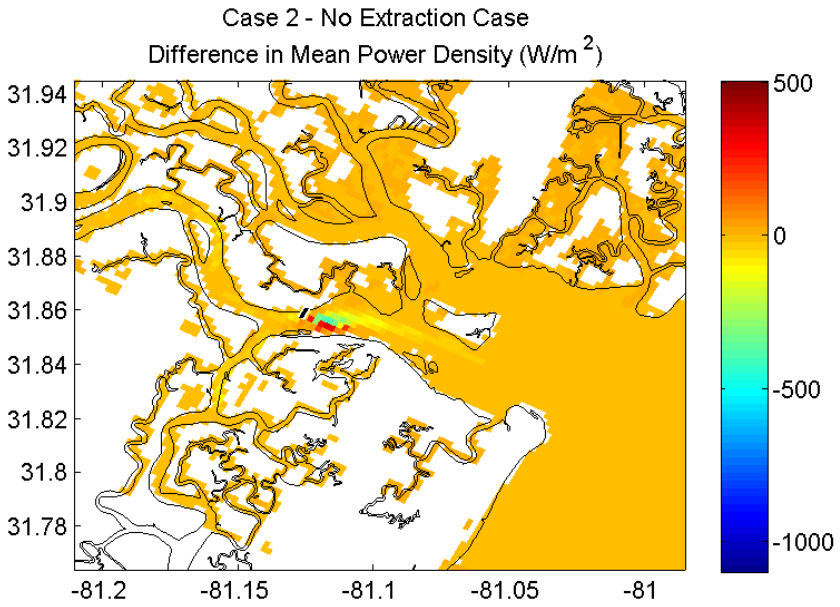

Figure 5.5. Difference in mean tidal power density in Ossabaw Sound between the no extraction case and partial extraction across the cross-section of the Canoochee River with C_{ext} =0.3 (Case 2).

The effect of power extraction on the hydrodynamics of the modeled region is demonstrated using snapshots of various parameters around the maximum ebb and flood tide in the remaining part of this section. The difference in current magnitudes between Case 1 and the case without power extraction near the maximum ebb current time is shown in Figure 5.6. The time series for the *u* component of the velocity for a point downstream (Point 1) and a point upstream (Point 2) of the extraction site are also provided in the same figure. The *u* component of the velocity is nearly along the axis of flow in the river, and thus is the dominant velocity component for this domain. Figure 5.6 is the snapshot for the instance where the strongest currents occur. There is a significant reduction (~30 cm/s) in the current magnitude in the Canoochee River in its entirety and

its southern branch, with the maximum decrease occurring downstream of the extraction location, near Point 1. The current magnitude is reduced by 1.42 m/s at Point 1. Although it is not observed at Point 2, at this time step, the drop in the current magnitude around this point is observed to be about 50 cm/s on the map and from the time series plot. The current in the channel connecting the Canooche River to the Ogeeche River is amplified by 50 cm/s. The modification to the current pattern at the Ossabaw Sound entrance is clearly noticeable during the maximum ebb currents for Case 1, in the form of a decrease (~40 cm/s) in the current magnitude on the Canoochee River side and a slight increase (~25 cm/s) at the middle of the entrance.

The map of water level difference between the baseline case and Case 1 for the maximum high tide is in a month is shown in Figure 5.7 along with the water level time series from Points 1 and 2 for 12 hours. There is no significant influence on the water elevation downstream of the extraction location including Point 1 due to power extraction. On the other hand, a relatively substantial decrease on the order of 5 to 30 cm is observed in the upstream water elevation (Figure 5.7.a). There is also a delay observed in the water level change. The time of high tide in Case 1 lags the time of high tide in the no extraction case by almost an hour. This delay is noticeable in the time series plot for Point 2 in Figure 5.7.c. The domain on the open boundary side of the power extraction appears to restore to the water levels as opposed to the domain on the closed boundary side. The difference in the water levels at Point 1 and Point 2 in this case are 3 cm and 12 cm, respectively

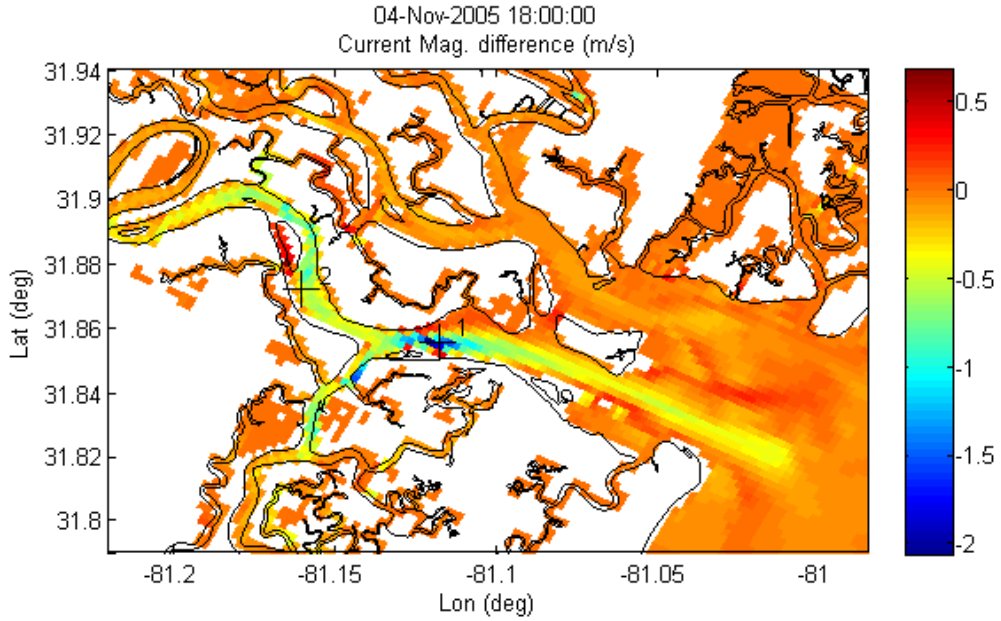

(a)

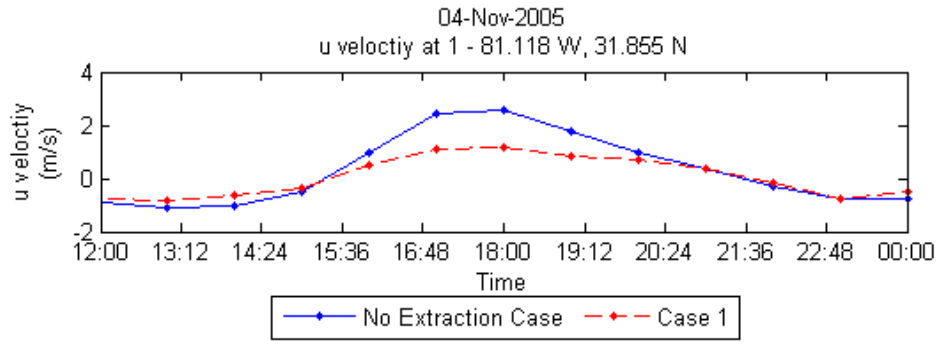

(b)

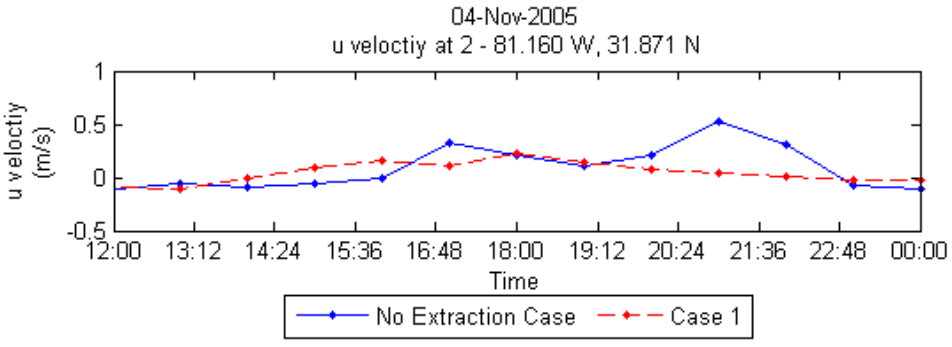

(c)

Figure 5.6. (a) Difference in the current magnitude in the computational domain between the case with no extraction and extraction across the entire cross-section, and time series for velocity from points (b) upstream and (c) downstream of the extraction for the ebb tide on November 4th, 2005.

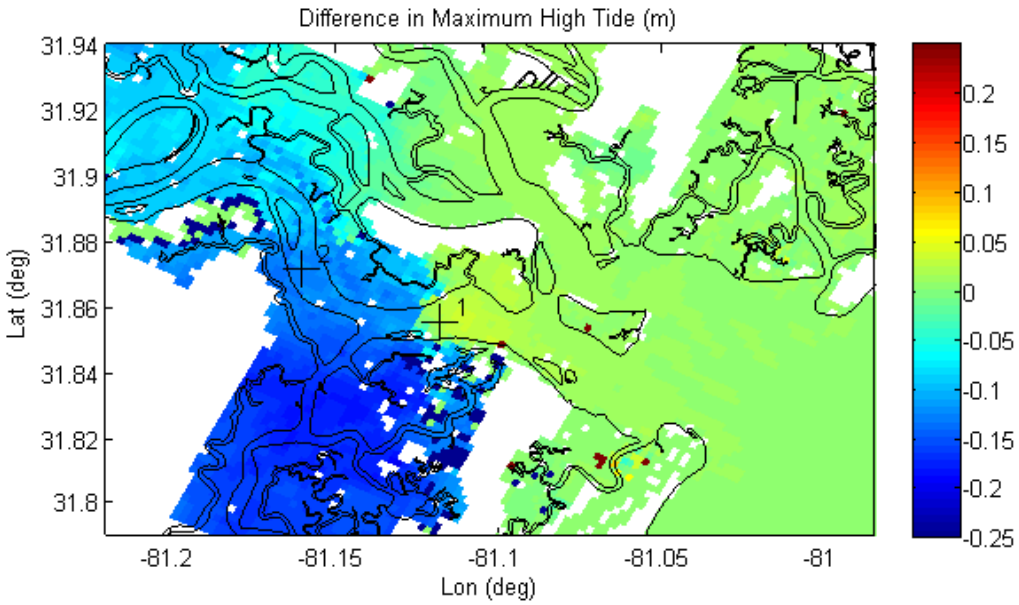

(a)

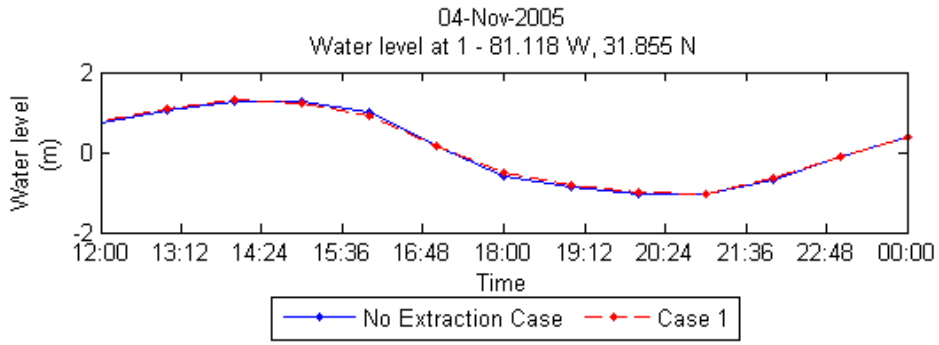

(b)

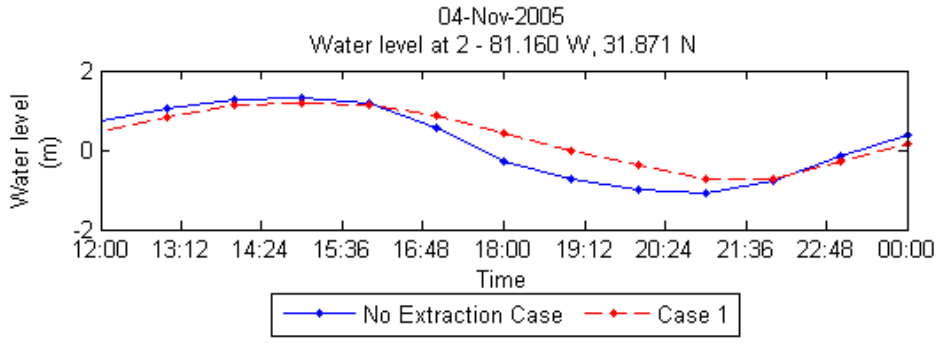

(c)

Figure 5.7. (a) Difference in the maximum water surface elevation between the case with no extraction and extraction across the entire cross-section. Time series for water surface elevations from points (b) upstream and (c) downstream of the extraction for the high tide on November 4th, 2005 are shown.

Similar plots for currents during maximum flood current and water levels during low tide are given for Case 1 in Figures 5.8 and 5.9, respectively. Flood currents in Canoochee River are reduced by 20 cm/s in average, and the maximum reduction is 70 cm/s, which occurs near the line of power extraction and further upstream in a meandering reach of the river. The magnitude of the currents at Point 1 and Point 2 are reduced by 34 cm/s and 4 cm/s. The current between Canoochee and Oggechee Rivers is ~20 cm/s weaker in Case 1 than the case with no extraction. The difference in the minimum water level during low tide between the no extraction case and the extraction across the entire channel is shown in Figure 5.9.a. It is seen that the water level is 25 to 35 cm higher than the baseline case upstream of the power extraction and is contained within the river channel during the low tide. The effect of power extraction from the entire cross-section of Canoochee River is felt upstream of the extraction location as a lag in the water level decrease during low tide (Figure 5.9.c). The difference in the water level at Point 1 negligible (< 1 cm) and 28 cm at Point 2 in this case.

The analysis of the results from Case 1 shows that there is a substantial impact from the power extraction on the hydrodynamics of the Canoochee River, especially during the maximum ebb current. The drop in the maximum and the increase in the minimum water level reduce the extent of the intertidal area while the lag affects the pattern of exposure to air and water. This should be investigated further for its effect on the intertidal ecosystem. There is some alteration in the current magnitudes at the Ossabaw Sound entrance (~40 cm/s drop on the southern half and a ~25 cm/s increase at the center of the entrance). No significant change is observed in the Ogeechee River.

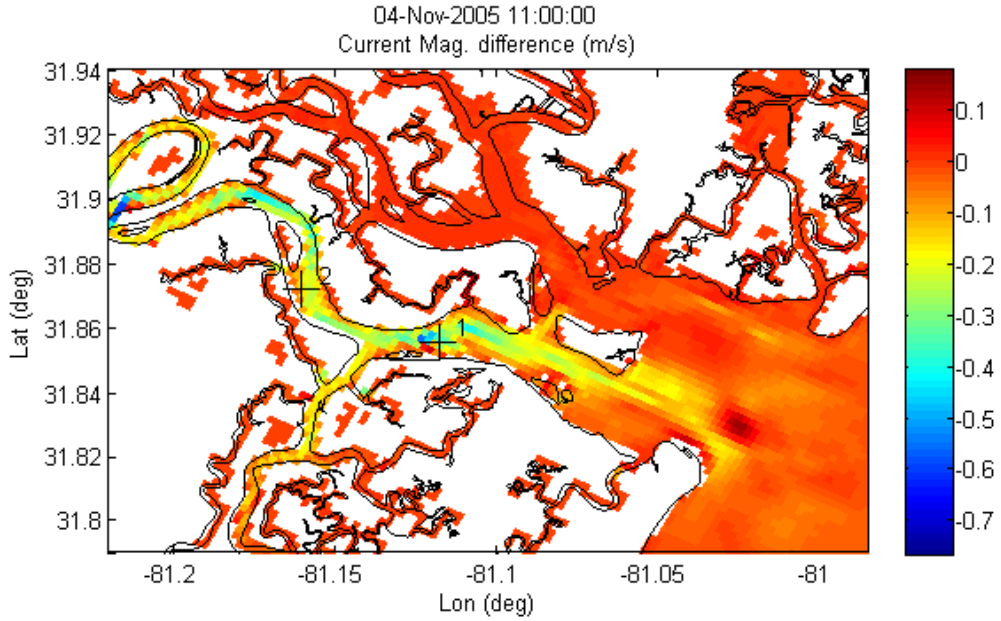

(a)

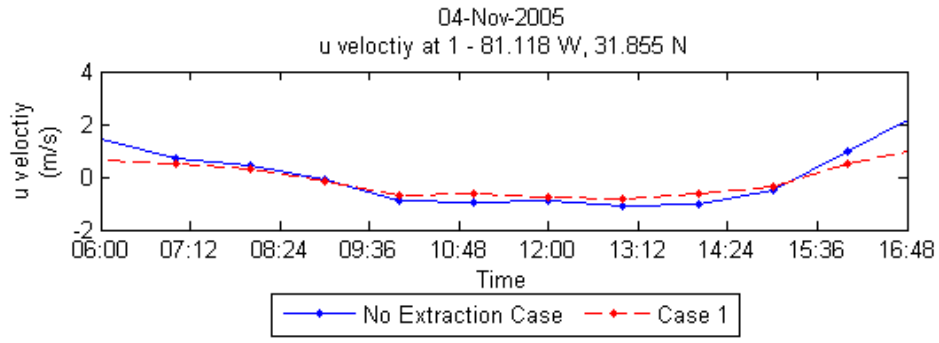

(b)

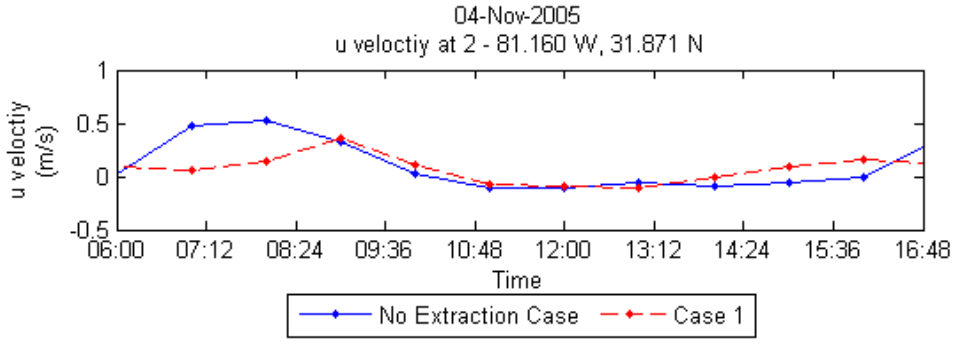

(c)

Figure 5.8. (a) Difference in the current magnitude in the computational domain between the case with no extraction and extraction across the entire cross-section, and time series for velocity from points (b) upstream and (c) downstream of the extraction for the flood tide on November 4th, 2005.

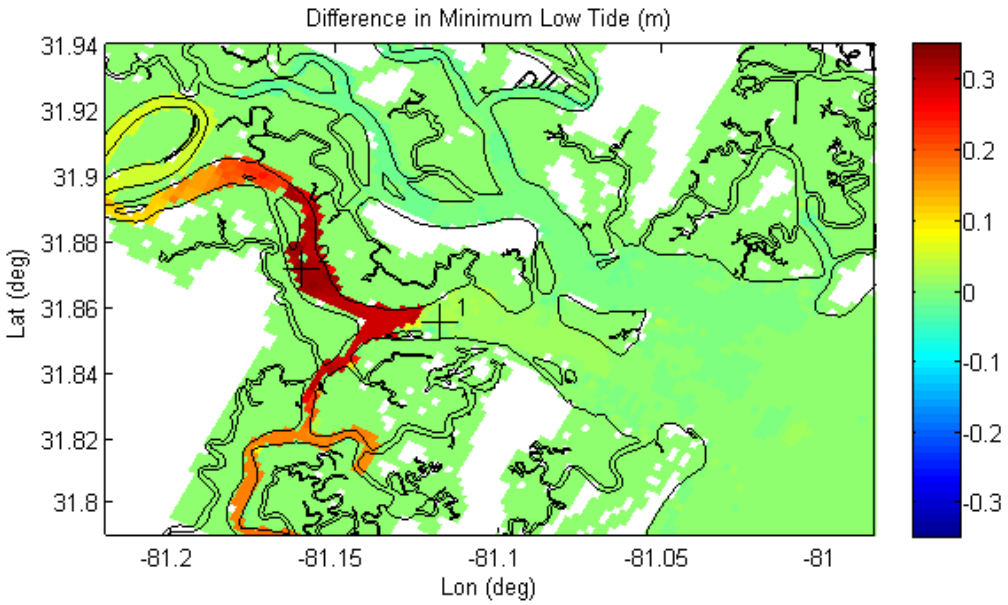

(a)

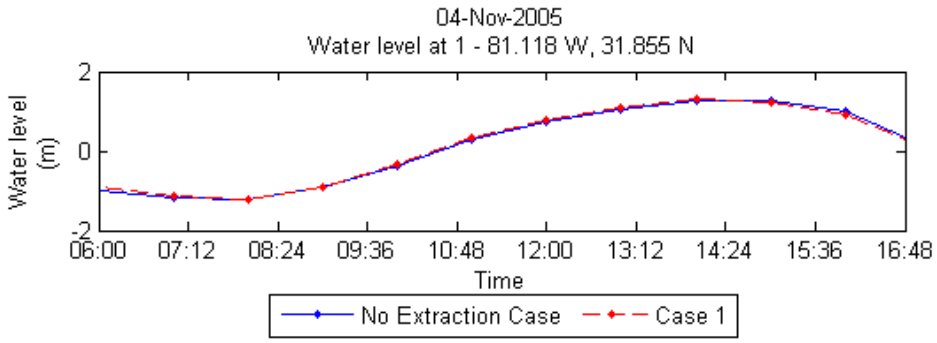

(b)

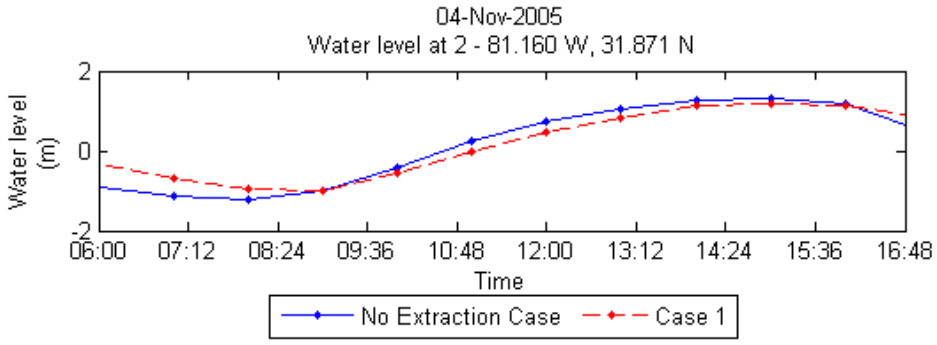

(c)

Figure 5.9. (a) Difference in the minimum water surface elevation between the case with no extraction and extraction across the entire cross-section. Time series for water surface elevations from points (b) upstream and (c) downstream of the extraction for the low tide on November 4th, 2005.

Because Case 2 has much more residual power than Case 1, it is expected to cause less alteration in the estuarine hydrodynamics. Snapshots of current magnitudes during the maximum ebb and flood currents are provided in Figures 5.10 and 5.11. The maximum decrease in the current magnitude, limited to an area near the extraction site, is on the order of 1.2 m/s. The average decrease (~0.60 cm/s) downstream of the obstructed half of the river is accompanied with a comparable amount of average increase (0.50 cm/s) in the other half. The current magnitude at Point 1 is 2.60 m/s, 78 cm/s less than the baseline case. There is minimal change at Point 2 through the complete ebb cycle. The velocity between the Ogeechee and Canoochee has increased by 25 cm/s, whereas there is no noticeable change at the sound entrance. Figure 5.11 demonstrates that there is no major difference in tidal currents between Case 2 and the baseline case during a flood tide. The maximum modifications in the current magnitudes occur at near the extraction location (±30 cm/s).

The distribution of the water level difference between Case 2 and the baseline case for maximum high tide and minimum low is given in Figure 5.12. A decrease in the water level less than 10 cm (4 cm at Point 2) is observed upstream of the extraction site during the maximum high tide. The minimum water level is only 3 cm higher upstream of extraction site during minimum low tide. The lag introduced at Points 1 and 2 in Case 2 is insignificant and provides identical water level time series with the no extraction case, therefore the time series are not provided here. The differences at Point 1 during high and low tide and for Point 2 during flood are found to be trivial (< 1cm). This case is anticipated to have less impact on the intertidal ecosystem since both the water level difference and the lag in are considerably smaller than Case 1.

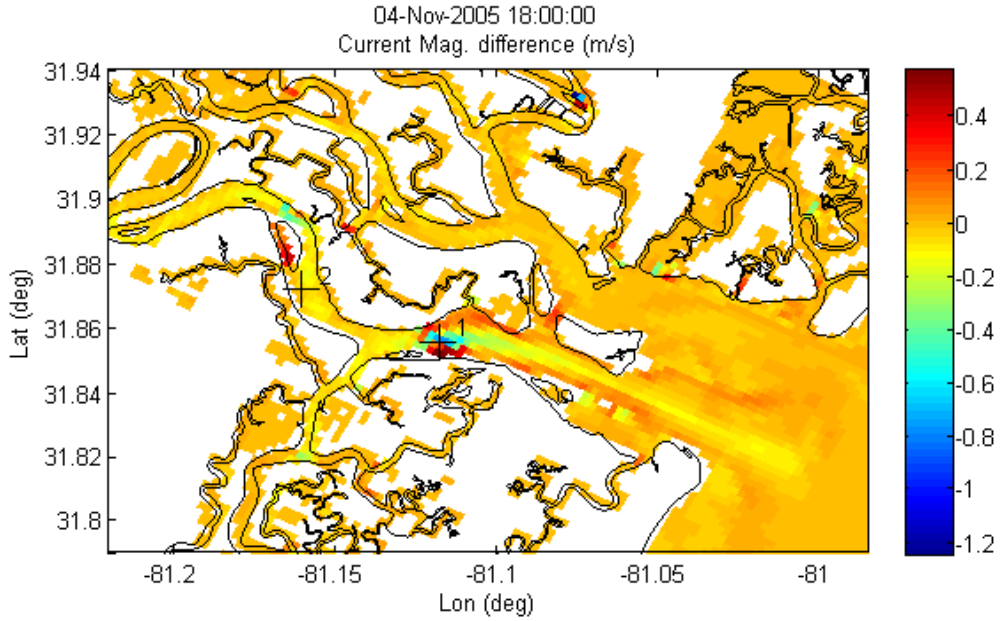

(a)

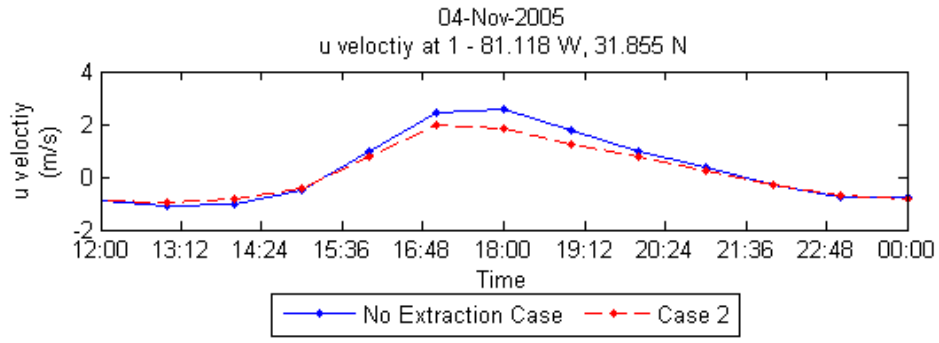

(b)

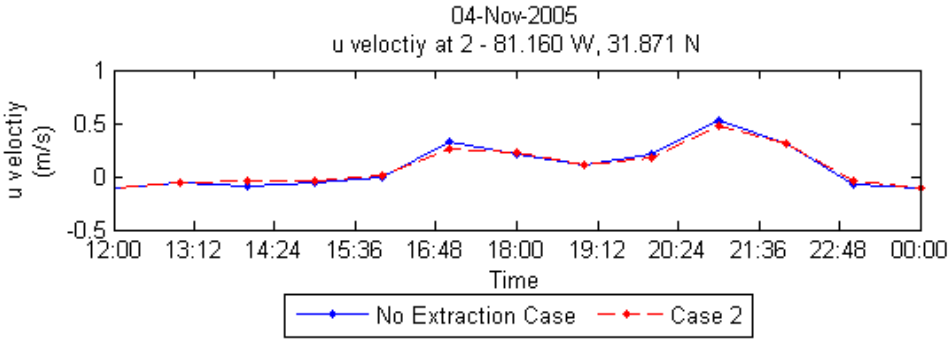

(c)

Figure 5.10. (a) Difference in the current magnitude in the computational domain between the case with no extraction and partial extraction, and time series for velocity from points (b) upstream and (c) downstream of the extraction for the ebb tide on November 4th, 2005.

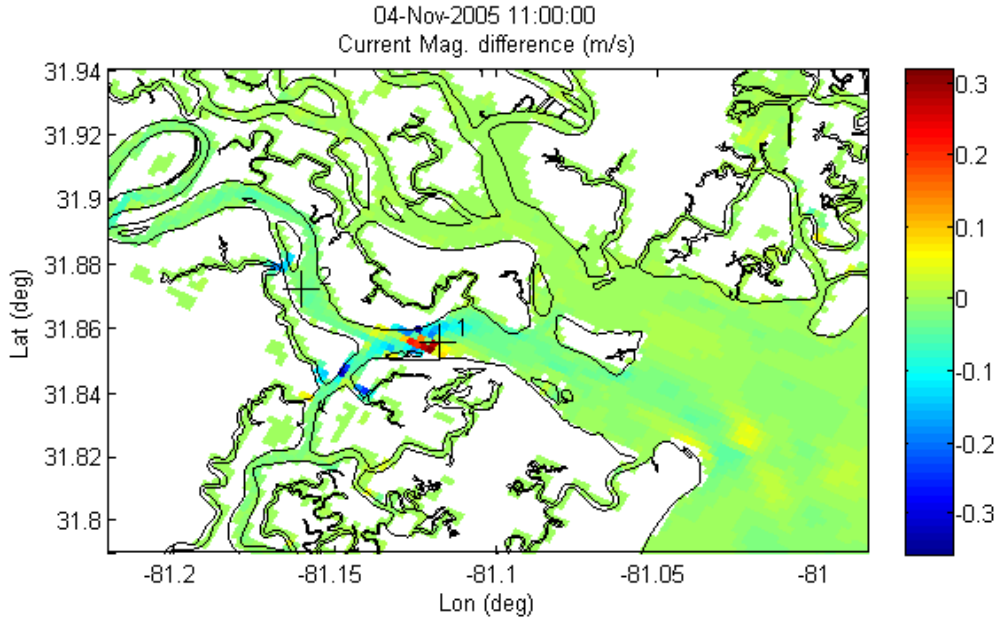

(a)

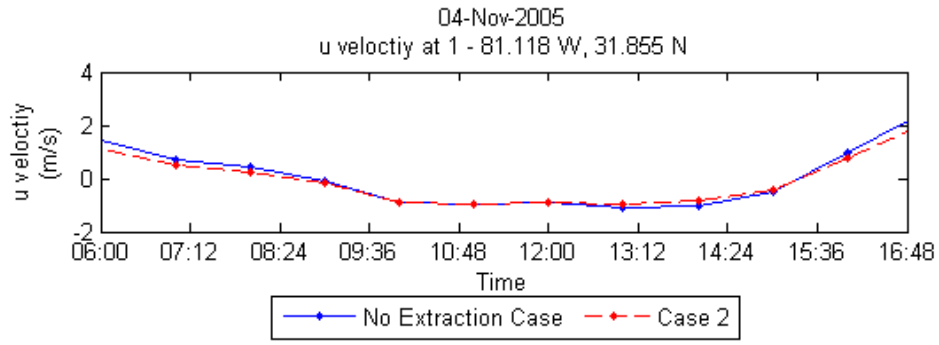

(b)

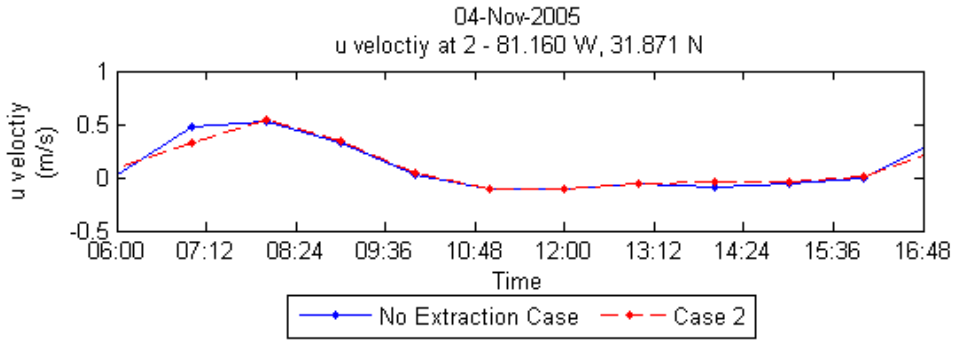

(c)

Figure 5.11. (a) Difference in the current magnitude in the computational domain between the case with no extraction and partial extraction, and time series for velocity from points (b) upstream and (c) downstream of the extraction for the flood tide on November 4th, 2005.

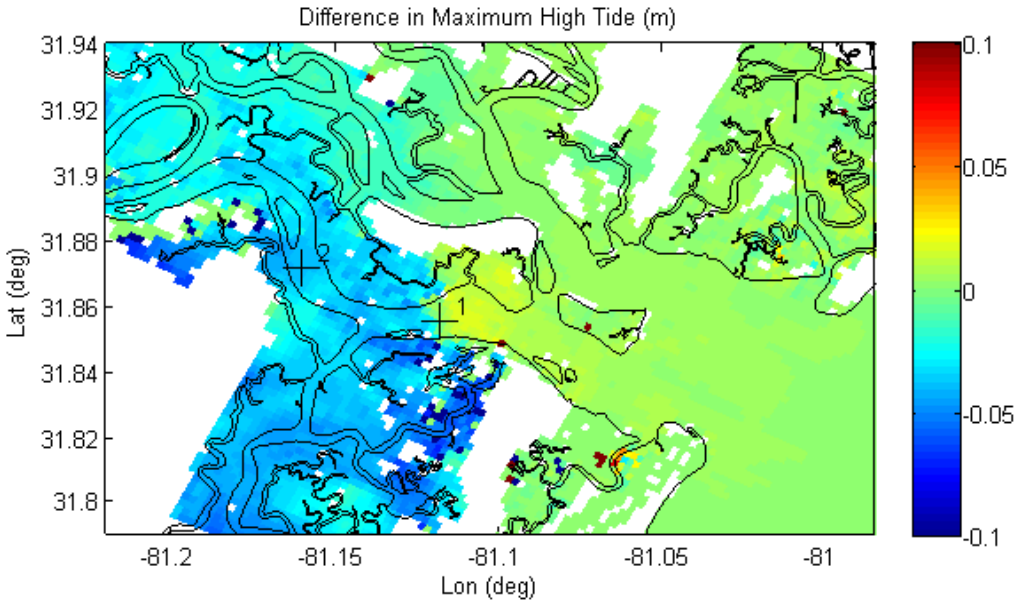

(a)

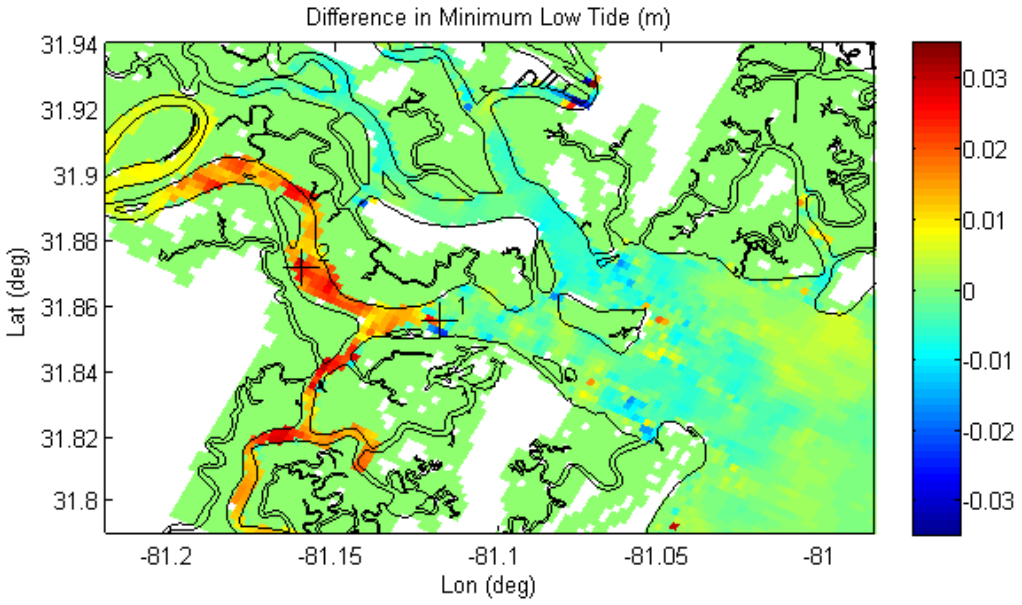

(b)

Figure 5.12. Difference in the (a) maximum and (b) minimum water surface elevation between the case with no extraction and Case 2.

The effect of power extraction is also evaluated in terms of the change in the constituents of the tidal currents upstream and downstream of the location of power extraction. Table 5.1 shows the difference in the magnitude and the phase of constituents with respect to the no extraction case using the validation parameters defined in Chapter 4. A considerable percent change is seen in the amplitude (*amdp*) of all constituents both downstream (Point 1) and upstream (Point 2) for this case. However, the amplitude difference (*amd*) is more significant for the M2, N2, M4 and M6, which are also the constituents with the largest magnitudes. The magnitude of M2 is reduced by 52 cm/s at Point 1 and by 16 cm/s at Point 2. The phase differences (*phd*) are positive at both locations indicating that the maximum currents lag the original maximum currents in the baselines case. In general, the amplitudes are reduced due to the power extraction and the phases are delayed due to the impediment of the entire cross-section in Case 1. The reduction in the amplitudes is higher at Point 1 since the power extraction removes more power from downstream. The phases, on the other hand, are larger upstream than downstream. There is a consistent and comparable delay in all of the constituents with 7 minutes delay in M2 constituent at Point 1, and 31 minutes at Point 2. A possible explanation for this is that the downstream location is on the side of the power extraction site with the tidal forcing at the open boundary, whereas the upstream location is on the other side, separated from the open boundary with the line of power extraction.

Table 5.1. Tidal change in the constituents of currents downstream (Point 1) and upstream (Point 2) of the power extraction site in Case 1 with respect to the no extraction case in terms of percent amplitude difference (*amdp*), amplitude difference (*amd*) and phase difference (*phd*).

		Point 1			Point 2		
Name	Period (hrs)	amdp (%)	amd (m/s)	phd (min)	amdp (%)	amd (m/s)	phd (min)
Q1	26.9	-23.8	-0.01	-8	24.9	0.00	27
O1	25.8	-38.1	-0.04	13	-13.1	-0.01	63
K1	23.9	-43.1	-0.05	2	-17.1	-0.02	45
N2	12.7	-44.7	-0.13	20	-11.6	-0.02	55
M2	12.4	-40.2	-0.52	7	-14.0	-0.16	31
S2	12.0	-31.7	-0.06	36	29.7	0.04	34
K2	12.0	-11.1	0.00	-60	18.8	0.01	-35
M4	6.2	-65.3	-0.23	8	-76.3	-0.20	34
M6	4.1	-35.9	-0.08	-21	-46.6	-0.07	-14

The difference in the tidal current constituent between Case 2 and the baseline case at Points 1 and 2 is presented in Table 5.2. The amplitude differences in Case 2 are smaller than Case 1, but similarly have significantly larger magnitudes at downstream than upstream. The largest changes are observed in the significant constituents M2, N2, M4, and M6 as well, with 23 cm/s drop at the downstream point and 3 cm/s. The phases at Point 1 for the significant constituents slightly lead the phases in the no extraction case. However, the difference between two cases is very small and not sufficient to generalize. Additionally, the phase of the next largest constituent, S2, is exceptionally lower than the baseline case and is not consistent with the results from other nearby points at this location. This may be related to a more complex system of currents at this location which sits in between the reduced currents on the obstructed side of the river and the increased currents on the open side. However, a consistent lag at the upstream point as in Case 1 is also observed in Case 2, only with smaller value this time. The extraction has a

considerable effect on the constituent magnitudes for the tidal currents in the accommodating river. Some lag in the phase of the tidal current constituents is observed especially upstream of the conversion location.

Table 5.2. Tidal change in the constituents of currents (a) downstream (Point 1) and (b) upstream (Point 2) of the power extraction site in Case 2 with respect to the no extraction case in terms of percent amplitude difference (*amdp*), amplitude difference (*amd*) and phase difference (*phd*).

		Point 1			Point 2		
Name	Period (hrs)	amdp (%)	amd (m/s)	phd (min)	amdp (%)	amd (m/s)	phd (min)
Q1	26.9	-22.3	-0.01	-30	-7.5	0.00	-19
O1	25.8	-14.8	-0.01	1	-3.0	0.00	7
K1	23.9	-18.7	-0.02	-11	-5.2	0.00	6
N2	12.7	-20.5	-0.06	-2	-3.3	-0.01	6
M2	12.4	-17.6	-0.23	-3	-2.3	-0.03	4
S2	12.0	-18.3	-0.03	-357	3.8	0.01	7
K2	12.0	-9.9	0.00	-12	3.6	0.00	-5
M4	6.2	-23.4	-0.08	-4	-10.7	-0.03	8
M6	4.1	-18.6	-0.04	-8	-18.9	-0.03	4

In summary, the power extraction causes a decrease in the magnitude of tidal currents at the extraction location downstream the ebb direction for an ebb dominant tidal regime. Extraction across the entire cross-section is found to reduce the current magnitudes excessively and cause significantly lower extraction than targeted. This scheme also causes a noticeable lag in high/low water times. On the other hand, extracting power by constricting only a part of the cross-section allows larger amount of power to be extracted with less impact on currents and on high/low water levels. Nevertheless, additional research is required to assess the effect of power extraction on the suspended sediment and redistribution of the bed load and on the intertidal ecosystem.

CHAPTER VI

SELECTION OF SUITABLE SITES FOR TIDAL STREAM POWER CONVERSION USING GIS

The purpose of this part is to provide a methodology to evaluate the quality of a location for tidal stream power conversion. A decision support system, which accounts for numerous constraints of the problem, was built to maximize the overall efficiency and economy, and to avoid or minimize the impacts on the environment. The site selection for converting tidal stream power is based on physical characteristics of the locations such as the mean tidal power density, environmental constraints and social impacts. While the economic analysis is another very important aspect of the evaluation and requires extensive analysis, it is beyond the scope of this study. The data from various GIS data repositories and user defined input are combined to analyze the results from modeling using a special GIS analysis package, and relevant thematic maps are created in the end (Defne et al., 2008).

6.1. Data Coverage

Geospatial data comes in many forms and formats, and its structure is more complicated than tabular or nongeographic geometric data. It is a subset of spatial data, with the difference that it is georeferenced by absolutely or relatively positioning on earth. There are many ways to define a terrestrial coordinate system and also to transform it to any number of local coordinate systems such as creating a map projection. In this

study the data are presented in geographical coordinates i.e. longitude and latitude without any map projection.

A large amount of GIS data is available online through governmental offices, science centers and the private sector. However, the information is scattered between these sources and requires significant amount of work to retrieve. Additionally, data providers sometimes provide the same data set through different addresses and user interfaces. Moreover, in the case of data from different sources there is a chance to end up with data with different datums, projections, scales and resolutions. Some of these data turn out to be formatted to be used with different software packages and at different platforms. In order to overcome this issue, the data is almost always provided with appropriate metadata information, which explains the properties and the quality of the data. Therefore, before combining information from different sources one has to make sure that the data formats and standards are compatible with each other. After an extensive investigation of online resources, the number of related sources is reduced down to a set of major data providers according to their coverage of information, data quality and accessibility. These major sources include National Oceanic and Atmospheric Administration (NOAA), United States Geological Survey (USGS), United States Census Bureau (CENSUS), Environmental Protection Agency (EPA). Geodata, which is maintained by USGS, is a one-stop source for obtaining state and country wide geographic data. Georgia GIS Data Clearing House also offers specific data, maps, images, and other geospatial data in the area of study. State and local environmental information can also be accessed at Georgia Department of Natural Resources (DNR).

The data gathered from various sources are categorized into three different layers as physical realization layer, environmental constraints layer and socioeconomic constraints layer. These layers include the information on the basic geometry and physics of the problem, areas that are of environmental concern, and areas of social and economical concern respectively. A summary of the sources of data and corresponding layers are shown in Figure 6.1. ESRI's ArcView package (ESRI, 2008) is used to construct and integrate the layers of geographically referenced information. The data in each layer come from the related governmental offices, science centers, and public databases in digital format and from the outputs of the user defined models. Due to the heterogeneity of the data sources and differences in the data types integrating all of the different information layers require careful assessment of the data formats and quality as well as merging of and conversion between vector and raster type data. For this purpose, the Spatial Analyst extension is used extensively. The Spatial Analyst extension offers tools for data type conversion, semantic map calculations and representations.

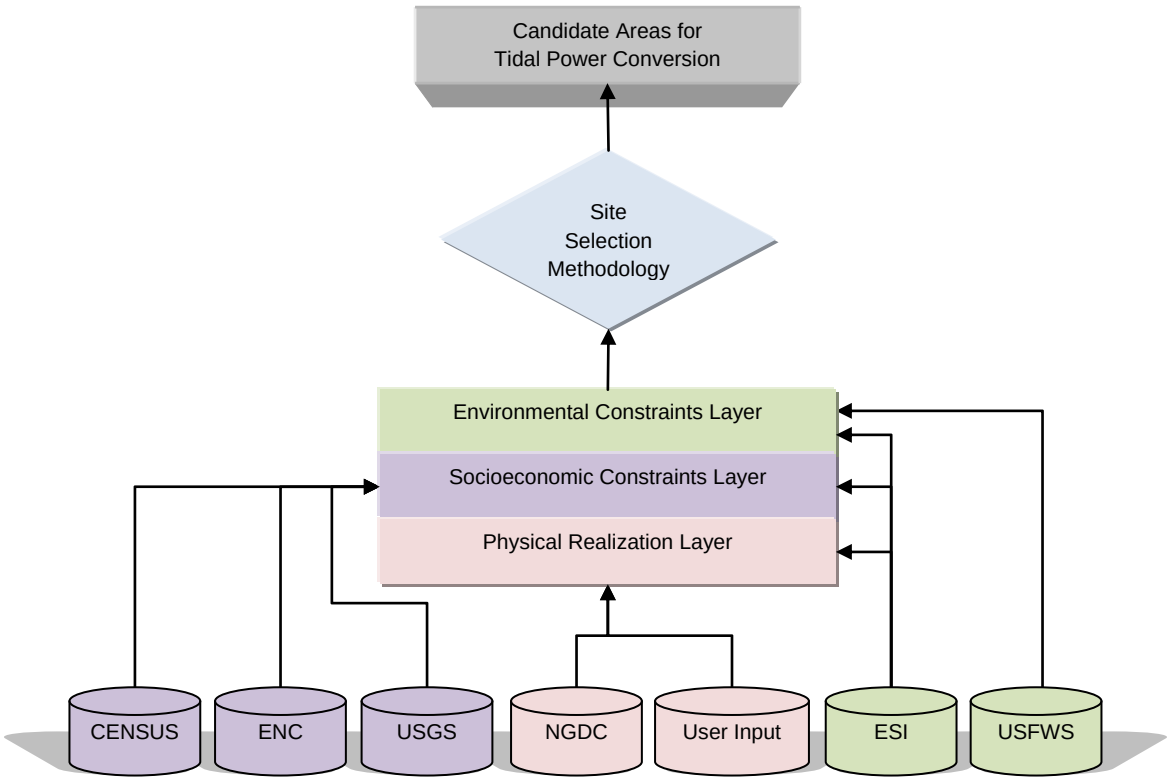

Figure 6.1. The structure of geographically referenced information and the underlying data sources used for selecting candidate areas for tidal power conversion.

6.1.1. Physical Realization Layer

The physical layer consists of the data used in creating the grids for model runs including the 1/70,000 scale, medium resolution shoreline from NOAA and the digital sounding data from NGD as the bathymetry input. The model results such as the velocity, available power and effective power outputs of the model at the computational grid locations are also defined as a part of this layer. The conversion from the NetCDF formatted results to a format accessible by the GIS system is performed with Matlab. This layer, defining the physical boundaries and the amount of power, contains the most essential data for the site selection scheme. One of the important parameters is the depth

of flow that is attached to the bathymetry data, which is used to verify the necessary vertical space to allocate the tidal power converters. While including the essential data, the physical layer itself is not enough to perform a full assessment. For instance, there should also be enough clearance from the surface of water for the boats and ships to travel safely if the site is located below marine traffic. There are also locations where dredging is required to allow enough clearance for large scale vessels, which need to be avoided. These are not included in the physical layer, thus the information from other layers is essential.

6.1.2. Environmental Constraints Layer

All plants, animals and microorganisms and the non-living physical factors of the environment in an area is called the ecosystem of that area. Tidal stream power converters with their very low rotation speeds and low noise levels are expected to have low impact on the ecosystem of an area while meeting a part of the energy demand from the surrounding areas. The blades can be avoided easily by fish and other sea animals (Devine Tarbell & Associates Inc., 2006). Nevertheless, it is still necessary to evaluate their possible interference with the ecosystem further, especially where endangered species are present. This study does not attempt to answer these questions but only use the available findings in the light of relevant studies in the literature. Environmental considerations require mapping of the habitat for the endangered species and avoiding these locations whenever possible.

An excellent source to be used in planning any large scale activities in the coastal zone is the Environmental Sensitivity Index (ESI) maps created by Office of Response

and Restoration of NOAA (NOAA, 2008c). These maps serve as quick references for oil and chemical spill responders and coastal zone managers in order to reduce the environmental consequences of both spills and cleanup efforts. However, the maps carry essential information that can be used at many other applications areas. They are available in digital format to be used in GIS applications and they contain information that can be integrated to each of the three data layers. Shorelines, which can also be used in physical realization layer, are ranked based on their physical and biological character, also their sensitivity to oiling hazard. Sensitive biological resources, such as seabird colonies and marine mammal hauling grounds, are depicted by shaded polygons and symbol icons to convey their location and extent on the maps. Detailed information on the threatened and endangered species in Georgia can be found at U.S. Fish & Wildlife Service's Endangered Species and Georgia Ecological Services Field Offices pages (USFWS, 2009a; b). The GIS data from this source is merged with ESI data for the environmental constraints layer. Supplementary data are provided from Georgia Environmental Resources Digital Data Atlas, which is served by USGS Center for Spatial Analysis Technologies (USGS, 2008a).

6.1.3. Socioeconomic Constraints Layer

Power from converters can be useful for many activities and developments that can take place in the coastal zone. Therefore the closeness to areas of human activity or social development is an important criterion. Additionally, the right of way for the transmission lines and for the roads to access the selected area is another important decisive factor. The right of way represents a big part of the cost of construction and it

may also disturb the immediate nature and habitat (Devine Tarbell & Associates Inc., 2006). It is desired to keep the right of way for the transmission and the access roads as short as possible. Therefore, the closeness of the power conversion projects to the transportation grid is important. Consequently, socioeconomic considerations favor the locations that are closer to the urbanized areas where most of the demand is located and also the locations that are closer to the main power grid for connection. Therefore, the socioeconomic constraints layer contains all levels and types of human activities in the region. Electronic Navigational Charts provided to public by the Office of Coast Survey of NOAA are vector-based digital files containing marine features suitable for marine navigation and usually used for route planning, and GIS applications (NOAA, 2008b). Therefore, they include the manmade structures and any other activities in the estuaries, bays and river reaches in the area of interest. The other input for the social layer is the census data which provides information about built-up areas, which are classified by their surface area and the amount of inhabiting population. Some of the supplemental data such as transportation and transmission lines can be found in Georgia Environmental Resources Digital Data Atlas, and are used after converting to the same format with the rest of the datasets. The location and orientation of transmission lines and the roads are some of the important parameters for power conversion projects. ESI maps also provide some socioeconomic information which includes but not limited to location of boat ramps, historical sites, and aquaculture and fishing sites. Sensitive human-use resources, such as water intakes, marinas, and swimming beaches are also shown in ESI maps.

6.2. Site Selection Methodology

Although the methodology is being applied to the entire Georgia coast, intermediate steps are going to be displayed on a on a large scale map for a smaller section of the coast for clarity. The area that covers the Savannah River, Wassaw and Ossabaw Sounds is selected for this purpose, since it allows for an overlap of information from different layers and areas with available tidal stream power density level sufficient for tidal stream power conversion. The compilation of GIS data for this pilot area from all constraint layers is displayed on a map in Figure 6.2, excluding the tidal power density data.

The areas managed by the U.S. Fish & Wildlife Service (USFWS) as National Wildlife Refuges or GA Department of Natural Resources (GA DNR) as State Wildlife Management Areas are shown as Wildlife Refuge on the map. National parks include national parks, seashores and monuments managed by the National Park Service. Marine sanctuaries denote the areas managed by the NOAA Sanctuary and Reserves Division as National Marine Sanctuaries and by NOAA and the state as National Estuarine Research Services. Endangered species (E), being at risk of becoming extinct, are usually under legal protection and human activities in the proximity of their habitat are limited. The species that are on the state and federal lists of endangered species are considered to be of concern for the tidal power conversion projects, therefore, the list of the sensitive biological resources acquired from the ESI maps are filtered to include only the species that are listed as endangered or threatened. The endangered marine mammals along the Georgia coast include whales and manatees. Given their size and offshore habitats, the whales are not as critical as manatees which can be found in estuaries, rivers and tidal

creeks for tidal power conversion projects in Georgia. High-use areas for the endangered West Indian Manatee species are Cumberland, St. Andrews, and St. Simons Sounds on the south and Savannah River on the north (Figure 6.2).

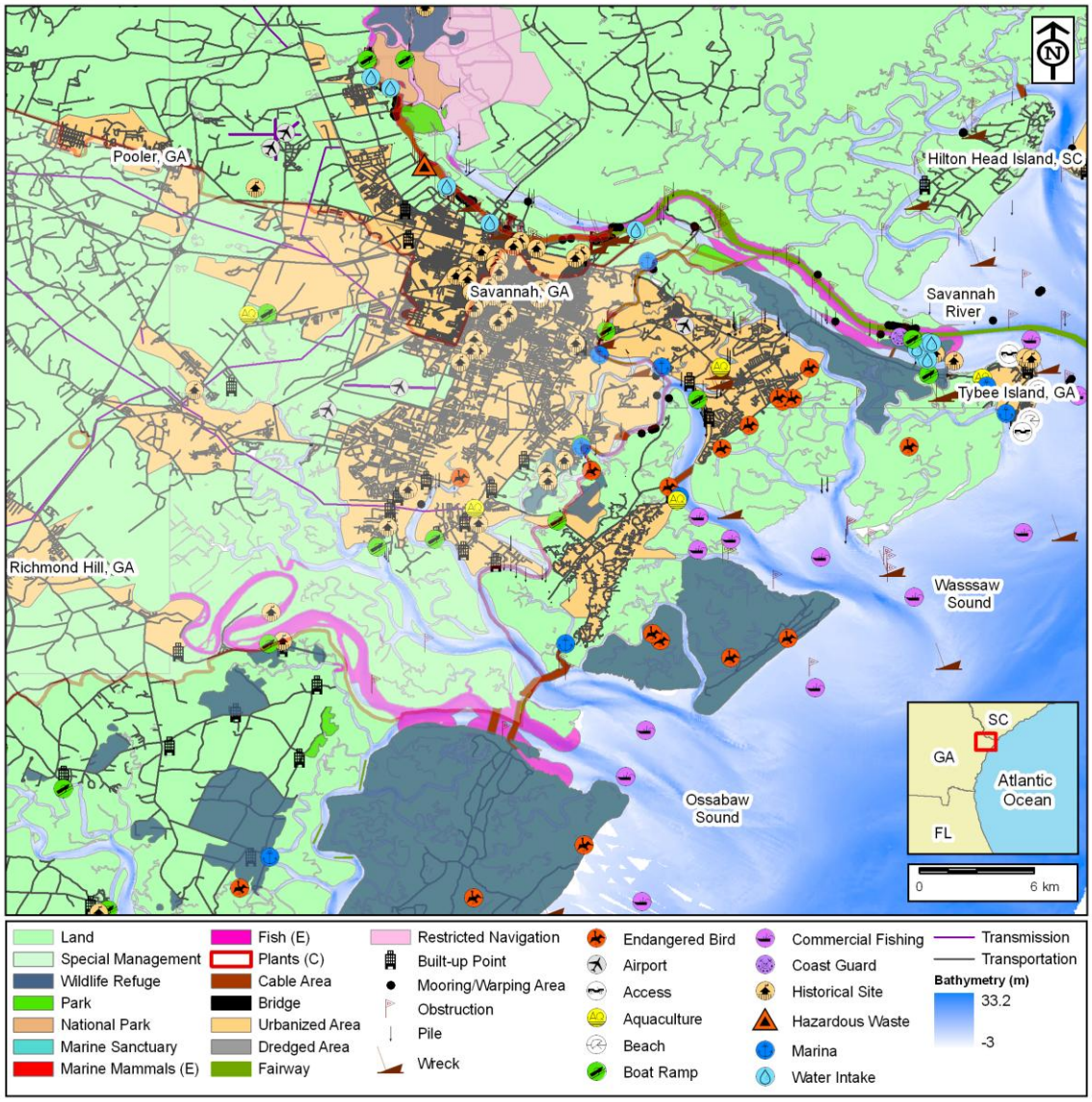

Figure 6.2. Demonstration of information from physical, socioeconomic and environmental constraints layers presented on the same map for Savannah River, Wassaw and Ossabaw Sounds.

The official state marine mammal of Georgia, the Northern Right Whale, is known to prefer areas offshore of Cumberland, St. Andrews, and St. Simons Sounds for breeding. The second-largest living animal and an endangered species, the Fin Whale, can be found at offshore of Georgia (Gray's Reef National Marine Sanctuary) at certain times of year. Though bottlenose dolphins are abundantly widespread in the Georgia waters, they are protected under the Marine Mammal Protection Act, as are all marine mammals. Endangered reptiles and endangered fish in Georgia include the Green Sea Turtle and the Shortnose Sturgeon, respectively. The Shortnose Sturgeon inhabits Savannah, Canoochee, and Altamaha Rivers, whereas the Green Sea Turtle is observed mostly at Gray's Reef. The Shortnose Sturgeon is depicted as Fish (E) in Figure 6.2. The endangered bird species in the coastal Georgia are limited to Wood Stork, which have their nests scattered across the coastal zone (Figure 6.2). Although Bald Eagles are listed as endangered in ESI maps, they were reclassified from endangered to threatened in 1995 by USFWS, and were removed from the USA federal government's list of endangered species in 2007 (USDOI, 2009).

The habitats of the threatened Indigo Snake and the endangered Frosted Flatwoods Salamander stretch from inland to the coastal zone along the southern coast and northern coast, respectively. Frosted Flatwoods Salamander adults migrate from surrounding upland habitats to their natal wetlands during rainfall events associated with passing cold fronts from September through December. Like the Indigo Snake, Frosted Flatwoods Salamanders are considered terrestrial animals. Pondspice, shown as Plants (C) in Figure 6.2, is a flowering plant species in Georgia with a listing status of Species of Concern. Being not endangered this terrestrial plant is not considered in the site

selection methodology, as are not the Indigo Snake and Frost Flatwoods Salamander (USFWS, 2009a).

Beaches, boat ramps, marinas, water intakes, U.S. Coast Guard facilities, and general areas where commercial fishing activities take place are marked with specific symbols on the map. Recreational fishing is abundant along the Georgia coast, hence not shown on the map. For historical sites, the generalized locations rather than the exact locations and extent are provided in the ESI data due to their sensitivity to disturbance. Most of the historical sites lie on the land, and contact information to acquire more information is available in the dataset if needed. Access marks designate the locations where it is possible to gain vehicular access to the shoreline or isolated coastal sites and islands. Farming of freshwater and saltwater organisms in Georgia waters includes mainly the Soft Shell Crab, Crawfish, Shrimp, and Clam. These locations are marked with as aquaculture sites on the map.

Based on the definition by the S-57 standard of the International Hydrographic Organization (IHO, 2009) for the ENC data , a fairway is a part of a river where the main navigable channel for vessels of larger size lies i.e. shipping channel. A dredged area is the bottom of a body of water which has been deepened by dredging, may sometimes overlap with the fairway. A pile is defined as a pole structure forced into the earth which may be free standing or may serve as a support for another marine structure. Similarly, an obstruction is anything that hinders or prevents movement, and poses an isolated danger to navigation. A mooring/warping facility is the structure used to secure a vessel, and a dumping site is a sea area where dredged material or other potentially more harmful material is deliberately deposited. A specified area designated by an appropriate authority

within which navigation is restricted in accordance with certain specified conditions is marked as restricted navigation in the compiled map for site selection. Pipeline areas consist of a string of interconnected submarine or overhead pipes used for transport of matter such as oil or gas. Built-up areas and locations are defined as a concentration of buildings and the supporting road or rail infrastructure by IHO. Airports are considered as a part of built-up areas in the compiled map. An urbanized area is defined as a densely settled territory that contains 50,000 or more people (USCB, 2009). The extent of the urbanized areas is based on the data by U.S. Census Bureau as of year 2000. Electric power transmission and all ground transportation are respectively indicated as transmission lines and transportation lines in Figure 6.2.

Each theme, its source and the constraint layer it belongs to within the created GIS database are shown Table 6.1. The themes in the physical realization layers are used to set the physical constraints of the problem. The remaining themes are color coded according to their roles in the site selection methodology. The themes that are highlighted with green are parts of the favorable areas, where it is socioeconomically more advantageous to have the power conversion projects closer. The red colored themes denote the restricted areas where the placement of a tidal power converter would not be allowed or should be avoided. These themes are entirely exclusive. The themes are shown in yellow are the critical areas, which correspond to sensitive biological resources and vulnerable living organisms in it. A flow diagram that shows the steps in the implementation of the site selection methodology is provided in Figure 6.3. The role of each group of themes is shown in the flow diagram and explained in the following paragraphs.

Table 6.1. List of layers, sources and themes categorized as favorable (green), restricted (red), and critical (yellow) areas.

Layer	Source	Theme
Physical realization	NGDC and User data	Coastline
		Bathymetry
	ESI, NOAA	Hydrology layer
	User data	Tidal power map
Socioeconomic constraints	CENSUS	Urbanized areas
	USGS, (DOE)	Transmission
	USGS, (DOT)	Transportation
	ENC, NOAA	Built-up areas
		Restricted areas
		Fairways and shipping lines
		Dumping sites
		Cable areas
		Pipeline areas
		Shoreline constructions
		Wreck points
		Mooring and warping points
	ESI, NOAA	Recreation areas and access locations
		· Boat ramps
		· Diving sites
		· Marinas
		Management areas
		· Marine sanctuary
		· National Parks
		· Wildlife refuges
		· Special Management areas
		Cultural heritage sites
		· Archeological sites
		· Historical sites
		Resource extraction sites
		· Aquaculture sites
		· Commercial fisheries
		· Recreational fishing
Environnemental contraints	ESI, NOAA and USFWS	Fish
		Invertebrates
		Reptiles
		Birds
		Mammals
		Plants and habitats

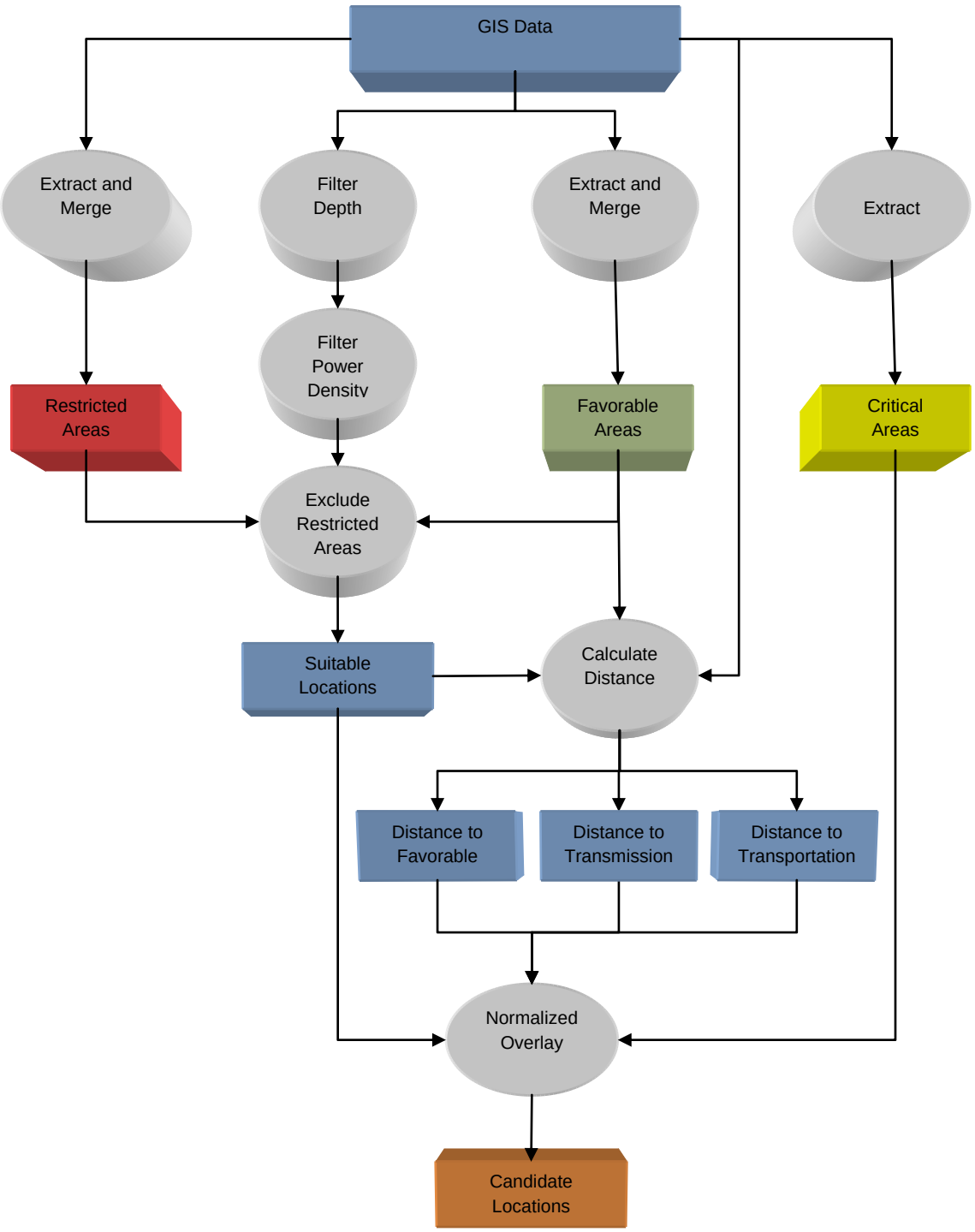

Figure 6.3. Flow diagram of the site selection methodology for tidal power conversion

In order to consider their impact on the environment, and on the existing use of sea space, some areas need to be excluded from tidal power conversion projects with a certain buffer area around them. The themes with restricted areas are merged in to a single theme of polygons after buffer zones are created around all of the polylines and locations. The size of the buffer is based on the related regulations whenever information is available, or a reasonable distance is determined by looking at the satellite images. All boat ramps, mooring /warping locations, marinas and coastguard are marked with a 400 m buffer. The locations indicated as hazardous in the original are applied 800 m buffer. Restricted navigation, pipelines, dumping ground, fairway, dredged area, cable locations and the special management areas are already defined as polygons in the original datasets and no buffer is required for these areas. Similar to the restricted areas, the themes that contain the favorable locations are also merged into a single polygon of called favorable areas. These include all airport and built-up locations, which are applied 100 m buffer, and the urbanized area polygons.

Since biological resources are in abundance, the information provided in the original datasets are filtered and minimized to a set of negative constraints based on their most critical subsets. This requires identifying the endangered and threatened species, which is done by querying the attribute tables of the shape files accordingly. Each of these resources is explicitly marked as sensitive against possible impacts on the environment. The spatial distribution of the endangered species other than the Wood Storks is provided as polygons in the original datasets and is used as is for the site selection methodology. Based on the environmental regulations the nest locations are applied a buffer zone of 800 m (USFWS, 2009a; b). Correspondingly, the same distance

is used for creating buffer zones around boundaries of the special management areas, such as wildlife refuges and national parks. Figure 6.4 shows this part of the methodology applied to the pilot region that consists of the Savannah River, Ossabaw and Wassaw Sounds. The merged favorable, restricted and critical areas are shown in green, red and yellow respectively. The circles with various sizes indicate the buffers created around the locations of interest. Some locations of interests such as aquaculture, commercial fishing, are not included in the site selection methodology at this stage. The benefits and the impact of tidal power conversion on these require special feasibility and design studies, and should include discussions and communications with all of the interested parties.

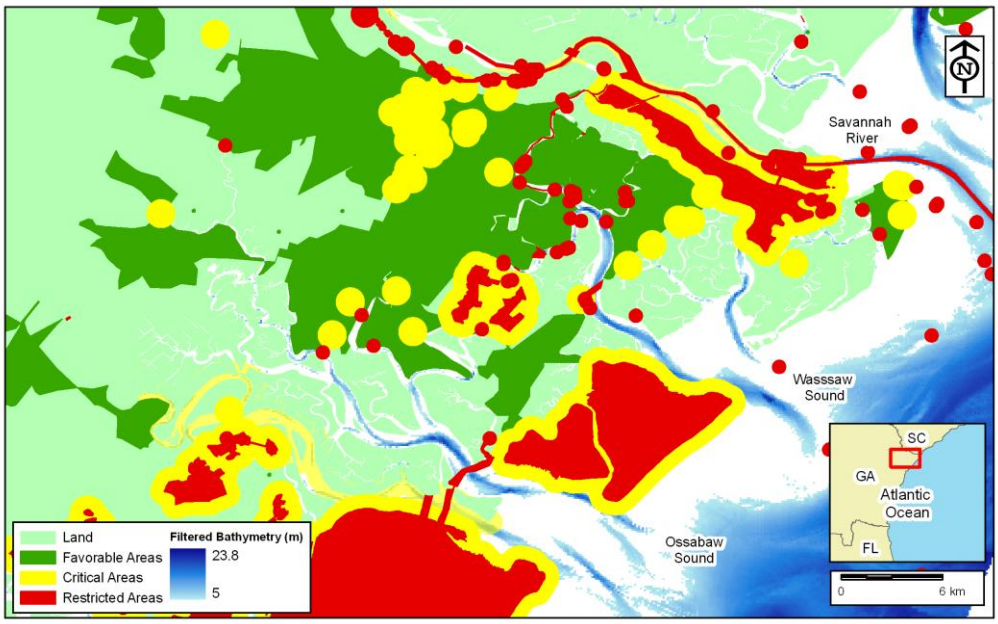

Figure 6.4. All exclusive (red), critical (yellow), and favorable (green) areas for tidal stream power conversion in Savannah River, Wassaw and Ossabaw Sounds.

Regardless of their design, most of the tidal stream power converters have a minimum depth requirement based on their dimensions. Additionally, there is usually a minimum flow speed (i.e. cut-in speed) that is required for the devices to start extracting power from the flow. The geospatial data for the power density and the bathymetry are filtered by minimum values to eliminate the locations that do not meet these criteria (Figure 6.3). There is no standard for the size of power conversion devices, and most of the existing devices and prototypes are built to meet the requirements of a certain project with the dimensions of the devices changing from several of meters to tens of meters (Bedard et al., 2006b; Froberg, 2006). Since the analysis in this study does not depend on a specific device and given the limited depth in Georgia coastal waters, the minimum depth is chosen to be 5 m, large enough to accommodate a small size conversion device with the existing technology. The bathymetry filtered by 5 m for the Savannah River, Wassaw and Ossabaw Sounds is shown as an example in Figure 6.5. It is seen in this figure that the 5 m filter removes a substantial amount of area from the whole domain, leaving only limited area along the main rivers and part of the sound entrances.

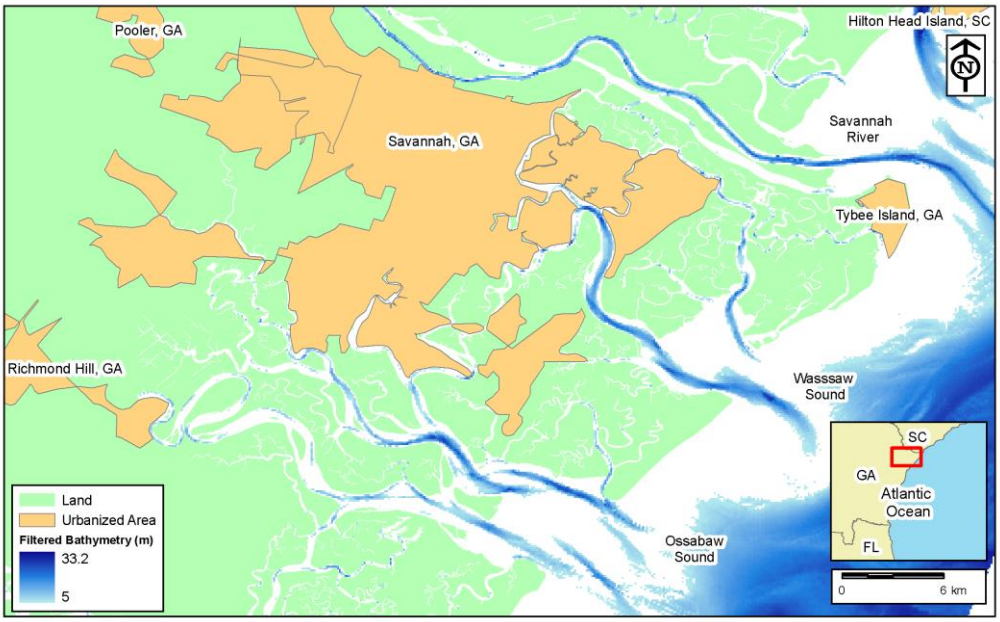

Figure 6.5. Bathymetry of the Savannah River, Wassaw and Ossabaw Sounds filtered by a minimum depth of 5 m.

The cut-in speeds for the tidal power conversion devices range from 0.5 m/s to 1 m/s depending on their design. Although some studies that simulate power extraction acknowledge cut-in speed values for the horizontal axis turbines as large as 1 m/s (Lim and Koh, 2009; Myers and Bahaj, 2005), there are many examples with cut-in speeds around 0.7 m/s and a vertical axis turbine with 0.5 m/s (Bedard et al., 2006b; Fraenkel, 2007; Lee et al., 2009). The minimum for the power density is selected as 250 W/m^2 which corresponds to a flow speed of 0.8. The filter removes all areas with lower power densities under the assumption that power levels less than this value are not extractable by the power converters. The example of the filtered power density for the pilot area is shown in Figure 6.6. The larger power density is observed to be constricted to the rivers and river mouths for this example.

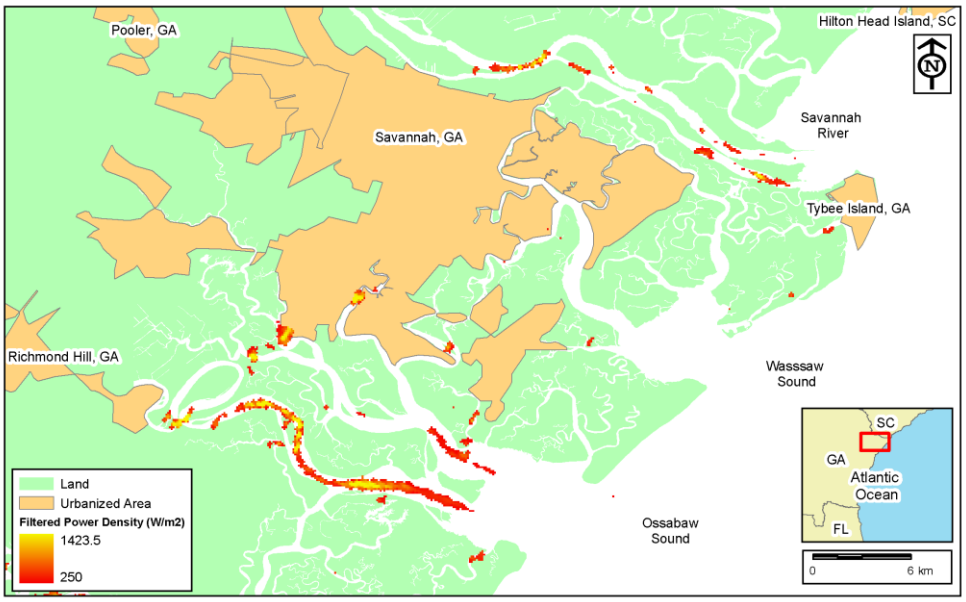

Figure 6.6. Tidal power density in the Savannah River, Wassaw and Ossabaw Sounds filtered by a minimum of 250W/m^2.

The restricted areas are excluded from the overlapping areas between the bathymetry and the power filter to determine the suitable locations for tidal power conversion (Figure 6.3). When applied together, these three constraints drastically reduce the potential areas for tidal power conversion (Figure 6.7).

At this stage of the site selection methodology before overlaying the themes, the map for each theme is normalized with its maximum value, so that the data values range between 0 and 1, 1 being the best score (Figure 6.3). The power density for every point is normalized with the maximum power density in the potential areas, so that the point with the highest power density scores 1. The critical area map includes the information on the conflict with the environmentally sensitive locations. Each distinct conflict is itemized and the values are normalized with the total possible number of conflicts at a point within the potential areas. For example if the maximum possible number of conflicts is 4, a point

in the buffer zone for the endangered bird species gets 0.75, whereas another point that lies on the intersection of the buffer zone of the endangered bird species and endangered fish gets 0.5. The point that has all possible conflicts gets a score of 0. For the transmission theme, the distances from every point on the potential areas are computed and normalized so that the closest point to the transmission lines gets a score of 1 and the most distant location gets 0. The normalization for the transportation lines and the favorable areas are performed the same way based on the distances to the points within the potential areas. The normalized distance to transportation lines from the suitable areas for the pilot region is shown in Figure 6.8 as an example. If solely the distance to the transportation was considered for example, the location with the largest power in the Canoochee River would not get a high score with regards to ease of access, which is likely to add up to the cost of a project at this location. At the final stage, all normalized maps are overlaid as shown in flow chart in Figure 6.3.

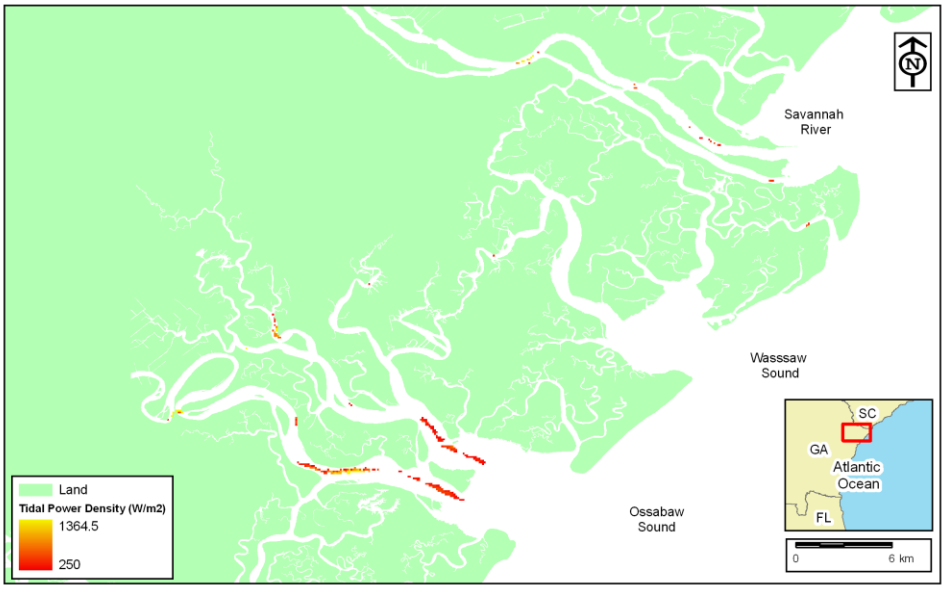

Figure 6.7. Tidal power density in the Savannah River, Wassaw and Ossabaw Sounds filtered by a minimum of 250W/m^2, 5 m depth and with restricted areas removed.

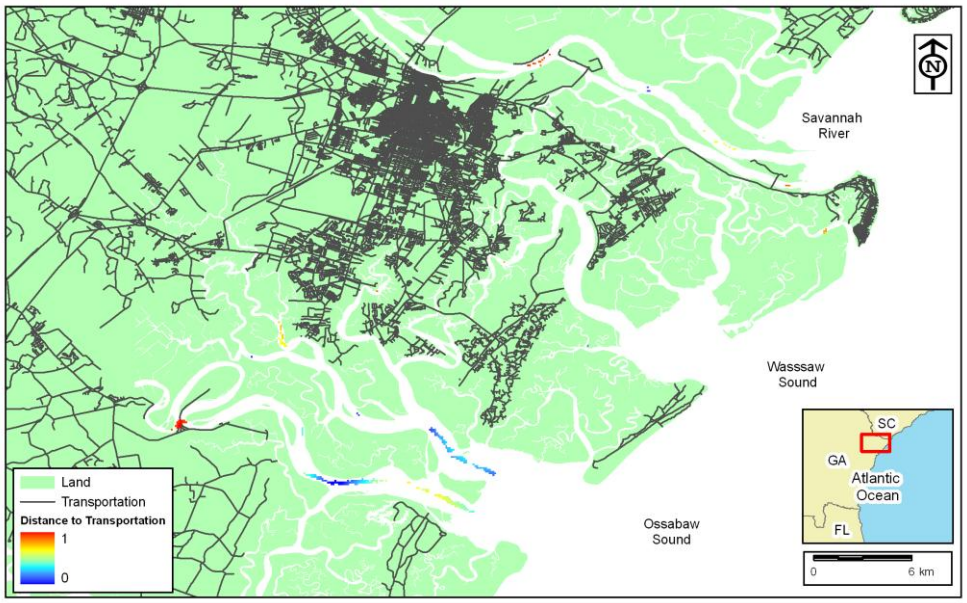

Figure 6.8. Normalized distance to transportation lines from the suitable locations for tidal stream power conversion in Savannah River, Wassaw and Ossabaw Sounds.

The candidate locations with tidal power conversion potential for the entire Georgia coast are determined by applying the created site selection methodology. The sites on the north and the south coast are shown in Figures 6.9 and 6.10, respectively. St. Catherines, Sapelo and Cumberland Sound entrances and the Ogeechee, Canoochee and Altamaha River mouths are found to have large areas of candidate sites for power conversion, with the Cumberland Sound having the largest power density amongst all. The Canooche and Medway rivers have considerably higher power density over a substantially large area that meets the criteria, and there are few isolated patches of very small areas such as Savannah River and upstream Altamaha River. Some of the areas with large power density presented in Chapter 4 are eliminated, and a more useful subset of suitable areas is obtained when the methodology developed here is applied to the Georgia coast.

Figure 6.9. The candidate locations with tidal power conversion potential on the northern Georgia coast that are determined by applying the site selection methodology.

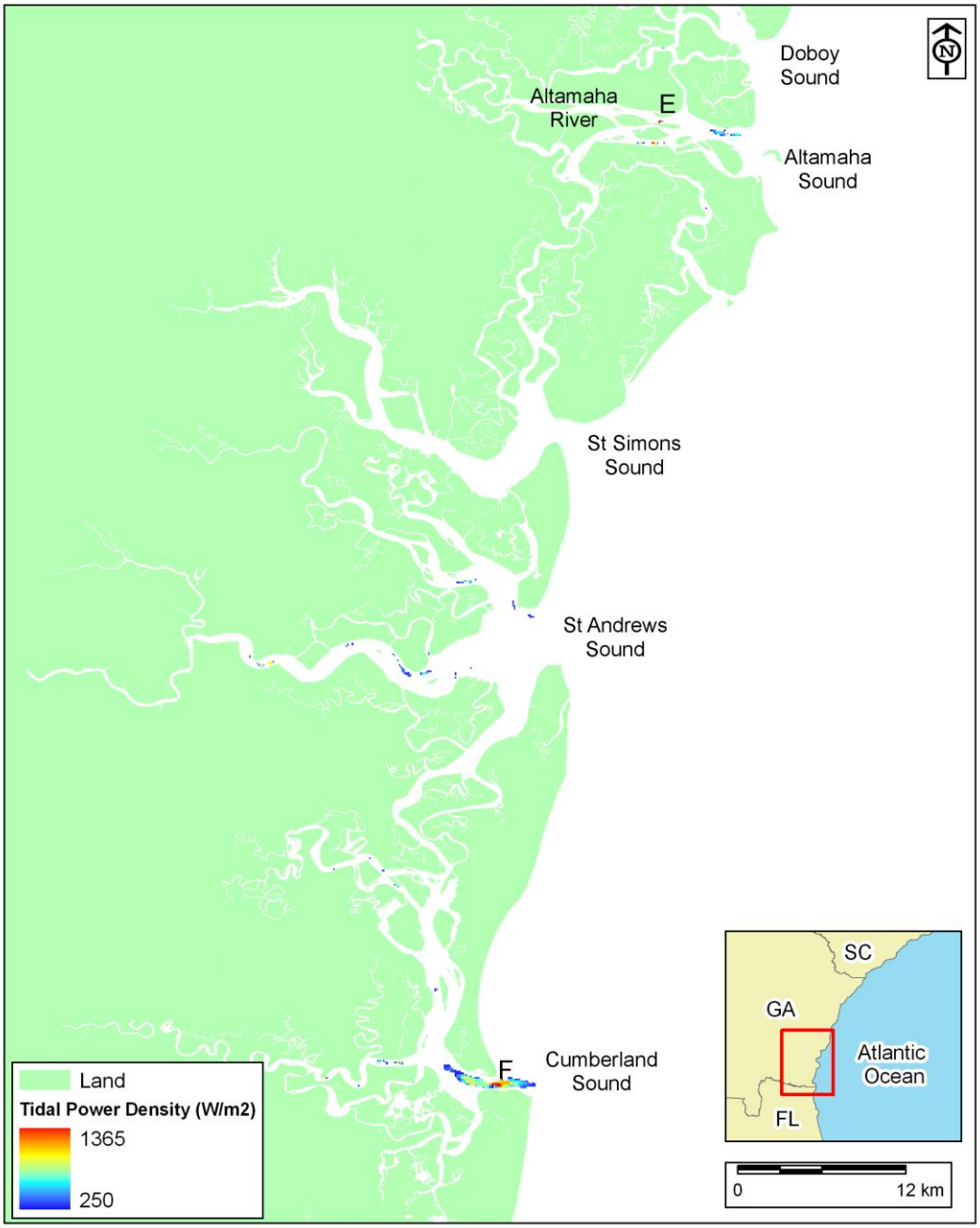

Figure 6.10. The candidate locations with tidal power conversion potential on the southern Georgia coast that are determined by applying the site selection methodology.

The site selection methodology can serve as a useful preliminary analysis tool for decision makers before allocating resources for a much more detailed evaluation. Consequently, the criteria for ranking the candidate sites can be simplified to three essential dimensions as the level of power density, accessibility of the site, and the environmental challenges. Normalized power density and the normalized environmental constraint are used to define two of the dimensions, whereas the normalized distances are combined into a single term to define the accessibility dimension. It is important to note that the accessibility dimension is related to economics, but the ranking algorithm used here does not include an economic dimension since an economic analysis is beyond the scope of this study. It is also assumed that all of the dimensions have the same importance. Therefore, no differential weighing is applied to any of the criteria. Additionally, preference is given to the locations with the least environmental conflict assuming that the associated rules and regulations are more binding.

Six locations that have larger power density relative to their surrounding area are selected from the candidate areas to demonstrate the use of site selection methodology as a decision support tool to rank the candidate areas according to the priorities that each project might have. For this purpose, these locations are further analyzed based on these essential dimensions using Kiviat diagrams (radar charts) as shown in Figure 6.11. Based on the aforementioned assumptions, the quality of each location for tidal power extraction is computed from the area under the triangle in the Kiviat diagrams using the formula

$$S = \frac{1}{2} \cdot sin\left(\frac{\pi}{6}\right) \cdot (P \cdot A + P \cdot E \cdot + A \cdot E) \qquad (6.1)$$

where *S* is the overall suitability score, *P* is the power density score, *A* is the accessibility score, *E* is the environmental score. The results are summarized in Table 1.2 and discussed bellow.

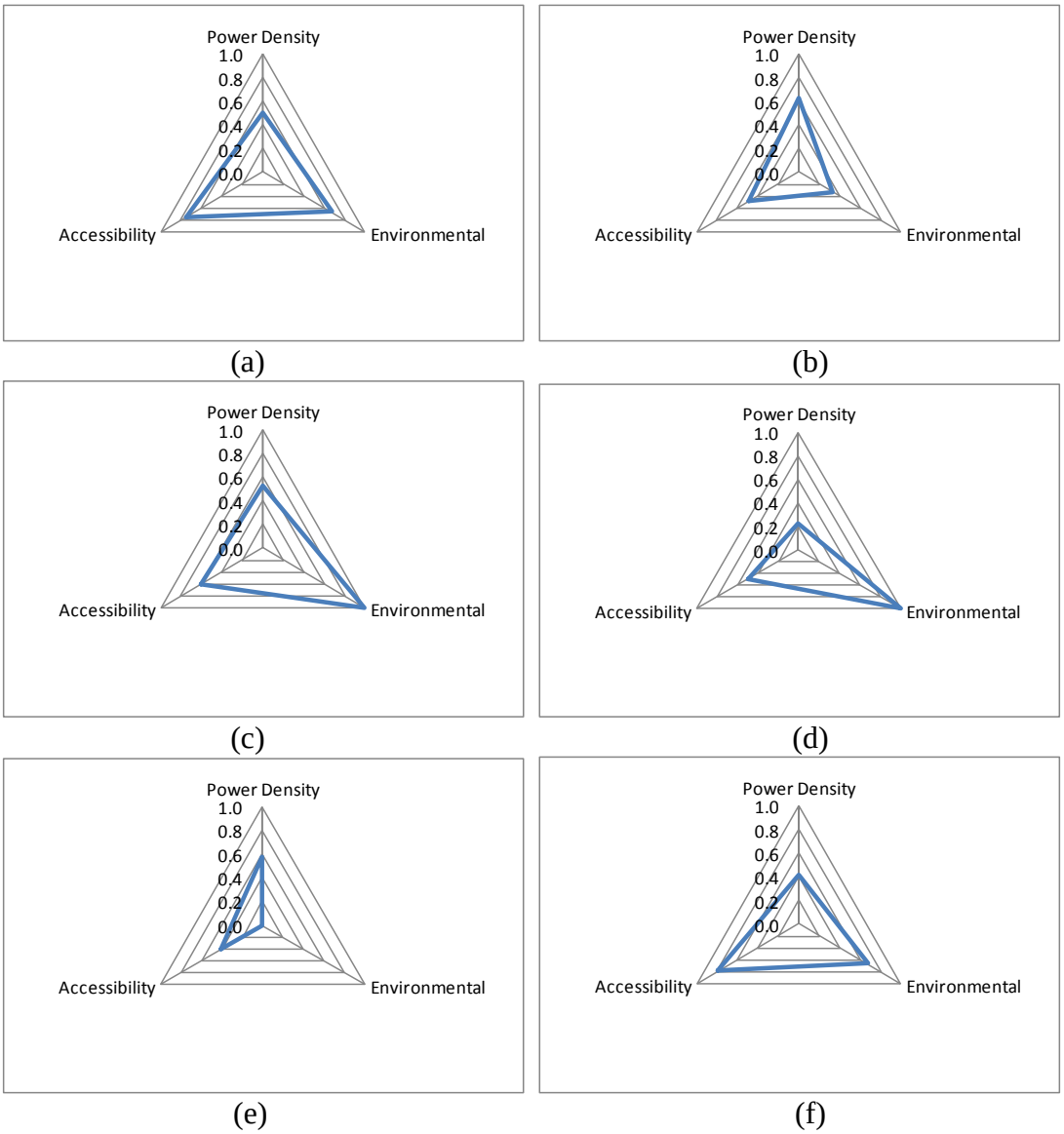

Figure 6.11. Kiviat diagrams showing the power, accessibility and environmental dimensions of tidal power conversion at selected locations shown in Figures 6.9 and 6.10 along the Georgia coast.

Table 6.2. Ranking results for tidal power conversion at selected locations shown in Figures 6.9 and 6.10 along the Georgia coast.

Point	Lon	Lat	Power Density Score (P)	Environmental Score (E)	Accessibility Score (A)	Overall Suitability Score (S)	Rank
A	-81.029	32.087	0.5	0.7	0.8	0.53	2
B	-81.127	31.857	0.6	0.3	0.5	0.30	5
C	-81.265	31.755	0.5	1.0	0.6	0.63	1
D	-81.182	31.539	0.2	1.0	0.5	0.36	4
E	-81.344	31.327	0.6	0.0	0.4	0.10	6
F	-81.448	30.708	0.4	0.7	0.8	0.50	3

Based on the ranking algorithm, Location E is ranked the worst of the six locations, since it has a conflict with all of the possible environmentally critical areas, and has low accessibility. Location B is also one of the environmentally disadvantageous locations, although it has a moderate power density. Location D and F are more preferable than these two locations. Location D has no environmental conflict, but considerably less power than all other locations while location F is more accessible and has a larger power density, but not as environmentally friendly as location D. Therefore, ranking between these two locations requires a more detailed analysis. On the other hand, location A has larger power density then location D, and may rank better than the two. The accessibility of location C is not the highest of all, which means the cost related to access roads and connection to the grid is expected to be higher. However, it has no environmental conflict, and a substantial tidal power density. Therefore, location C gets the highest rank based on the implemented algorithm.

A methodology is developed and is shown to be a useful tool to quantify the different parameters involved in selecting the most suitable locations for tidal power conversion. The algorithm implemented here can be used as a decision support tool in

preliminary analysis for feasibility of tidal power conversion projects. The algorithm is applied to the Georgia cost and a ranking process is demonstrated to select the most suitable location.

CHAPTER VII

CONCLUSIONS

The increasing demand for energy and the increased depletion rate of nonrenewable energy resources call for research on renewable alternatives. Mapping the availability of these resources is an important step for development of power conversion projects. For this purpose, the wave power potential along the Atlantic coast of the southeastern USA, and the tidal stream power potential along the coast of Georgia are investigated in this study. The effect of tidal stream power conversion on the tidal regime is studied at the estuary scale. A multi-criteria method for tidal power conversion schemes to select favorable locations and to rank them according to their suitability is developed and applied to the Georgia coast.

The offshore wave power along the Atlantic coast of the southeast USA, bounded by latitudes 27ºN and 38ºN and longitudes 82ºW and 72ºW, is assessed based on the data from the wave stations along the southeast coast. Wave power is calculated from hourly time series for the significant wave heights and average wave periods at every station. For a limited number of stations where spectral wave energy densities are also provided, the power is calculated using the spectral wave energy density, and compared to the power calculated based on the time series. A regression analysis of the two methods with 365,825 measurements show that the wave power calculated from the significant wave height and average period needs to be corrected with a factor of 0.61. The seasonal wave power variation at each wave station is provided, and annual average and maximum

power maps for the whole region are constructed. The estimated mean power is around 9 kW/m along the 500 m contour line and higher than 15 kW/m beyond the 3500 m contour line offshore. The wave energy converted with 20% efficiency 50 km offshore of Georgia coast is found to be on the order of the electricity consumption by 1800 residential units in Georgia.

The preliminary investigations show that the Atlantic coast of southeastern USA is a source of moderate wave power. For power conversion the power that can be extracted depends on the response curves and efficiencies of the power converters that can be used. For this purpose a higher resolution analysis to account for the response from the prototypes to be used and to give a more accurate estimate of the power and energy output is recommended. Although the available wave power is moderate, the accessible wave power off the southeast coast is still a considerable energy source. With advancing technological capabilities, increasing power conversion efficiencies and introducing new ways to harvest the wave power, the results may be better than expected today.

The tidal stream power along the coastline of the state of Georgia is evaluated using the tidal current predictions provided by NOAA, and with numerical modeling of tidal currents using ROMS. The NOAA tidal current predictions do not provide a full spatial coverage, therefore, are superseded with the numerical modeling of the currents. The Georgia coast is divided into three subdomains due to computational requirements, with the average computational cell size in the order of 250 m. The medium resolution coastline data and the digital sounding data are used to define the coastline and the bathymetry in the computational grids. A datum conversion between from MLLW to

MTL is applied to the bathymetry data. Wetting and drying of computational cells is permitted while doing the computational simulations. The simulations are forced at the open boundary of the computational grids with tidal forcing provided from larger scale modeling results (ADCIRC).

Validation of model results against the NOAA computed constituents shows that the error in the amplitude of the water level constituents is small, (on the order of centimeters). The phase differences for the constituents are usually under 30 minutes, except the overtide M4, which can be higher than 100 minutes. The model results are also validated against the available ADCP measurements. Comparisons with the two NOAA measurements and the two USACE measurements display ratios of within 1.0 and 1.1 between the current magnitudes form the model results and the measurements. The phase difference between the model and the measurements is on the order of 30 minutes for the currents in these cases. The standard deviation ratio of high/low tides computed by the model to the measurements is determined to be between 0.9 and 1 with the RMS differences in the order of 12 to 16 cm. The phase difference for the high/low tides between the model results and the measurements is also less than 30 minutes. Validation of model results with the ADCP measurements at Ogeechee and Satilla Rivers (Blanton et al., 1999; Seim et al., 2009; Seim et al., 2002) is satisfactory at most of the measurement locations. However, the currents in these rivers are fairly low which causes the error in the current magnitude ratios to be larger. The model results are also compared to the NOAA tidal current predictions for a one-month period (November, 2005), although the predictions are known to be less reliable(Rear, 2009). Generally, the model

results are found to agree with the predictions, but lower validation statistics are observed at some locations.

The sensitivity of the model to the change in the computational cell size, the offshore extent of the computational grid is tested. Reducing the computational cell size twofold results in a negligible change in the results, whereas this produces almost an eightfold increase in the computational time. Setting the offshore boundary at a distance not closer than 5 km to the shoreline introduces insignificant amount of differences in the current magnitudes and water surface elevations with respect to the simulations with boundaries further offshore. Wetlands constitute a big portion of the Georgia coast. They are implemented in the model simulations through wetting and drying of computational cells using the real topography. The effect of incorporating the wetlands into the simulations is observed as a noticeable increase in the overall tidal current magnitudes. Additionally, the asymmetry in the tidal cycle between the ebb and the current flows can be simulated with the model. The results from the model runs with wetlands agree better with the measurements than the model runs without wetlands.

Large variations in depth between neighboring computational cells may introduce model instabilities. In some cases decreasing the time is not a feasible solution for this problem due to limited computational power. The other option is to smooth the bathymetry without changing it significantly, but enough to increase the stability as occurred in the case of finer resolution grids in this study. The performances of different filtering schemes are tested during simulations, and Mellor-Ezer-Oey with the slope factor 0.8 is found to preserve the original bathymetry the best.

Based on the model results, the Canoochee River (1400 W/m^2) and the Intercoastal Waterway between the Altamaha and Doboy Sounds (1600 W/m^2) have the largest mean tidal power densities along the Georgia coast. The areas with large power densities are the Savannah River (1100 and 800 W/m^2); Ossabaw Sound, Ogeechee and Canoochee Rivers (800, 1050 and 1400 W/m^2); St. Catherines Sound and Medway River (800 W/m^2); Sapelo Sound (700 W/m^2); Altamaha River (800 W/m^2); St Andrews Sound (700 W/m^2); and Cumberland Sound (700 W/m^2). Wassaw, Doboy and St Simons Sounds do not have significant amount of tidal power density.

The results from the one-month simulations are used to generate one-year time series through a harmonic analysis of the computed hourly time series. Annual average power density for the high power density areas in the Savannah, Canoochee, and Altamaha Rivers are calculated from the one-year time series as 745, 880, and 1735 W/m^2. The amount of the total effective power that can be extracted from these areas of larger power density is evaluated based on a generic efficiency curve for a tidal power converter as 323, 405 and 870 W/m^2. The monthly energy that would be available from 20 converters with 5-m diameter deployed at the Canoochee River is estimated to be on the order of electricity consumption by 100 residential units in Georgia. These figures are based on the tidal currents only. Most of the rivers on the Georgia coast are tidal rivers with small upstream inflows. Savannah River has the largest inflow with an average of 500 m^3/s measured upstream of the tidal zone. Including this in the model, is found to increase the tidal power density at the river mouth by less than 3%. A constant maximum river discharge of 4000 m^3/s is found to increase the monthly average power density by

20%. However, this is a hypothetical extreme condition since the maximum flow conditions do not persist for a month, but occur very sporadically.

The effect of power extraction on estuarine hydrodynamics is simulated by implementing an additional retarding force in the governing momentum equations in the model and is evaluated in terms of the change in the mean tidal power, tidal current magnitudes and water levels of the original flow. Two different scenarios, one with the entire river cross-section obstructed with tidal power converters and another where only a part of the cross-section is constricted, are simulated on the Canoochee River. A reduction in current magnitudes is observed in both cases, especially drastically in the case of entire blockage, which is also discovered to reduce the efficiency of the extraction. Only 12.2% of the 1.865 GWh/month of total energy can be extracted by entirely blocking the cross-section. On the other hand, the power extraction with partial constriction is shown to have an extraction rate of 16.7 %, with a better flow recovery and less impact on the currents. The effect of the conversion on the water levels is noticed as a delay in recession of the water levels during the ebb flow. The delay is more noticeable upstream of the power extraction area in both cases, but it is negligibly small in the case of partial constriction. The high water elevation upstream of the conversion area is decreased and the low water elevation is increased considerably when the entire cross-section is blocked. The overall effect of these changes on the intertidal ecosystem as well as the sedimentation patterns needs to be addressed in a future study. The algorithm should be applied to other locations with large tidal current power and tested against measurements, if available.

A set of governing parameters that are necessary to evaluate suitability and classify the favorability of a site for power conversion is established using the analogy from site selection practices from other marine renewables, hydropower and wind energy projects. A methodology for selecting suitable sites for tidal power conversion is developed, and implemented using the available geospatial data and relevant GIS tools. It is applied to the Georgia coast to distinguish the areas with higher tidal power that meet the requirements of the multi-criteria selection methodology. The suitable sites for tidal power conversion are marked and evaluated for quality based on three essential dimensions; the level of power, the accessibility of the site and the number of environmental conflicts. Assuming equal weights on each dimension, it was found that a section of the Medway River proved to be the most promising location.

The Georgia coast has numerous locations with considerable tidal power density. The depth constraints, human activates in the coastal zone and the sensitive biological resources limit the amount of suitable location for tidal power conversion. Field measurements that are long enough to extract the tidal constituents are required at these locations to validate the model results. The design of tidal power conversion devices is a developing research area and the suitability of the various available technologies should be investigated for extracting tidal power on the Georgia coast.

REFERENCES

Amador, J, and Domínguez, J. (2005). "Application of geographical information systems to rural electrification with renewable energy sources". Renewable Energy. 30(12), 1897-1912.

Anaconda. <http://www.bulgewave.com/> (Accessed 2008).

Antheaume, S, Maître, T, and Achard, J-L. (2008). "Hydraulic Darrieus turbines efficiency for free fluid flow conditions versus power farms conditions". Renewable Energy. 33(10), 2186-2198.

Asif, M, and Muneer, T. (2007). "Energy supply, its demand and security issues for developed and emerging economies". Renewable and Sustainable Energy Reviews. 11(7), 1388-1413.

AWS. Archimedes Wave Swing. <http://www.waveswing.com/> (Accessed 2008).

Baba, M. (1987). "Wave power potential off the South-west Indian coast". Energy (Oxford). 12(6), 501-507.

Baban, SMJ, and Parry, T. (2001). "Developing and applying a GIS-assisted approach to locating wind farms in the UK". Renewable Energy. 24(1), 59-71.

Bedard, R, Hagerman, G, Previsic, M, Siddiqui, O, Thresher, R, and Ram, B. (2005). Offshore Wave Power Feasibility Demonstration Project Final Summary Report. WP 009 - US Rev 2. Electric Power Research Institute.

Bedard, R, Previsic, M, Polagye, B, Hagerman, G, and Casavant, A. (2006a). North American Tidal In Stream Energy Conversion Technology Feasibility Study. EPRI TP-008-NA. Electric Power Research Institute.

Bedard, R, Previsic, M, Siddiqui, O, Hagerman, G, and Robinson, M. (2006b). North American Tidal In Stream Energy Conversion Feasibility Demostration Project. EPRI TP-04-NA. Electric Power Research Institute.

Beels, C, De Rouck, J, Verhaeghe, H, Geeraerts, J, and Dumon, G. (2007). "Wave energy on the Belgian continental shelf". Institute of Electrical and Electronics Engineers Computer Society, Piscataway, NJ 08855-1331, United States, Aberdeen, Scotland, United Kingdom, 4302228.

Bergey, KH. (1979). "The Lanchester-Betz Limit". Journal of Energy. 3(6), 382-384.

Bernhoff, H, Sjostedt, E, and Leijon, M. (2006). "Wave energy resources in sheltered sea areas: A case study of the Baltic Sea". Renewable Energy. 31(13), 2164-2170.

Beserra, ER, Mendes, ALT, Estefen, SF, and Parente, CE. (2007). "Wave climate analysis for a wave energy conversion application in Brazil". Proceedings of the International Conference on Offshore Mechanics and Arctic Engineering - OMAE. American Society of Mechanical Engineers, New York, NY 10016-5990, United States, San Diego, CA, United States, 897-902.

Beyene, A, and Wilson, JH. (2007). "Digital mapping of California wave energy resource". International Journal of Energy Research. 31(12), 1156-1168.

Biberacher, M. (2008). "GIS-based modeling approach for energy systems". International Journal of Energy Sector Management. 2(3), 368-384.

Blanton, J, Alexander, C, Alber, M, and Kineke, G. (1999). "The mobilization and deposition of mud deposits in a coastal plain estuary". Limnologica - Ecology and Management of Inland Waters. 29(3), 293-300.

Blanton, JO, and Atkinson, LP. (1983). "Transport and Fate of River Discharge on the Continental Shelf of the Southeastern United States". J. Geophys. Res. 88.

Blanton, JO, Lin, G, and Elston, SA. (2002). "Tidal current asymmetry in shallow estuaries and tidal creeks". Continental Shelf Research. 22(11-13), 1731-1743.

Blanton, JO, Seim, H, Alexander, C, Amft, J, and Kineke, G. (2003). "Transport of salt and suspended sediments in a curving channel of a coastal plain estuary: Satilla River, GA". Estuarine, Coastal and Shelf Science. 57(5-6), 993-1006.

Blue Energy. <http://www.bluenergy.com/index.html> (Accessed 2008).

Boud, R. (2003). Wave and Marine Accessed Energy. UK DEpartment of Trade and Industry (DTI).

Bretschneider, CL, and Ertekin, CR. (1989). "Estimation of wave power as an energy resource for Hawaii". Publ by ASCE, Boston, MA, USA, Honolulu, HI, USA, 189-201.

Brody, SD, Grover, H, Bernhardt, S, Tang, ZH, Whitaker, B, and Spence, C. (2006). "Identifying potential conflict associated with oil and gas exploration in texas state coastal waters: A multicriteria spatial analysis". Environmental Management. 38(4), 597-617.

Brown, MA, Antes M, Franchunk, C, Koske, B H, Michaels, G, Pellegrino, J. (2006). Results of a Technical Review of the U.S. Climate Change Technology Program's R&D Portfolio. Oak Ridge National Laboratory, Oak Ridge, Tennessee.

Bryden, I, and Melville, G. (2004). "Choosing and evaluating sites for tidal current development". Proceedings of the Institution of Mechanical Engineers, Part A: Journal of Power and Energy. 218(8), 567-577.

Bryden, IG, and Couch, SJ. (2006). "ME1 - marine energy extraction: tidal resource analysis". Renewable Energy. 31(2), 133-139.

Bryden, IG, and Couch, SJ. (2007). How much energy can be extracted from moving water with a free surface: A question of importance in the field of tidal current energy? , 1961-1966.

Bryden, IG, Couch, SJ, Owen, A, and Melville, G. (2007). "Tidal current resource assessment". Proceedings of the Institution of Mechanical Engineers, Part A: Journal of Power and Energy. 221(2), 125-135.

Bryden, IG, Grinsted, T, and Melville, GT. (2004). "Assessing the potential of a simple tidal channel to deliver useful energy". Applied Ocean Research. 26(5), 198-204.

Carrion, AJ, Estrella, EA, Dols, AF, Toro, ZM, Rodriguez, M, and Ridao, RA. (2007). "Environmental decision-support systems for evaluating the carrying capacity of land areas: Optimal site selection for grid-connected photovoltaic power plants". Renewable and Sustainable Energy Reviews. In Press, Corrected Proof.

Charlier, RH. (2003). "A "sleeper" awakes: tidal current power". Renewable and Sustainable Energy Reviews. 7(6), 515-529.

Chen, C. (2000). "A Modeling Study of the Episodic Cross-Frontal Water Transport over the Inner Shelf of the South Atlantic Bight". Journal of Physical Oceanography. 30(7), 1722-1742.

Clean Current. Clean Current Power Systems Incorporated. <http://www.cleancurrent.com/> (Accessed 2008).

Clement, A, McCullen, P, Falcao, A, Fiorentino, A, Gardner, F, Hammarlund, K, Lemonis, G, Lewis, T, Nielsen, K, and Petroncini, S. (2002). "Wave energy in Europe: current status and perspectives". Renewable and Sustainable Energy Reviews. 6(5), 405-431.

Cornett, AM. (2006). "Inventory of Canada's offshore wave energy resources". American Society of Mechanical Engineers, New York, NY 10016-5990, United States, Hamburg, Germany, 10.

Couch, SJ, and Bryden, IG. (2006). "Tidal current energy extraction: hydrodynamic resource characteristics". Proceedings of the Institution of Mechanical Engineers, Part M: Journal of Engineering for the Maritime Environment. 220(4), 185-194.

Couch, SJ, and Bryden, IG. (2007). "Large-scale physical response of the tidal system to energy extraction and its significance for informing environmental and ecological impact assessment". OCEANS 2007 - Europe, 1-5.

Cowen, DJ, Jensen, JR, Bresnahan, PJ, Ehler, GB, Graves, D, Huang, XQ, Wiesner, C, and Mackey, HE. (1995). "The Design and Implementation of an Integrated Geographic Information-System for Environmental Applications". Photogrammetric Engineering and Remote Sensing. 61(11), 1393-1404.

Crisp, GN, and Scott, M. (1981). "The spatial distribution of wave power on the western UK coast". BHRA Fluid Eng, Cambridge, UK, 1-18.

CSE. Checkmate Sea Energy. <http://www.checkmateuk.com/seaenergy/system.html> (Accessed 2008).

CU. DIVAST. Hydro-environmental Research Centre, Cardiff University, <http://www.cardiff.ac.uk/engin/research/sustainabilityenergy/hydro/index.html> (Accessed 2008).

Defne, Z, Haas, KA, and Fritz, HM. (2009). "Wave Power Potential along the Atlantic Coast of the Southeastern USA". Rewable Energy. 34(10), 2197-2205.

Defne, Z, Haas, KA, Fritz, HM, and Cambazoglu, MK. (2008). "Assessment of Tidal Currents along the Atlantic Coast of the Southeast USA for Energy Conversion: Case Study for Georgia". International Conference on Ocean Energy (ICOE) 2008, Brest, France, In Press.

Del Rosario, JJA, Perez, JMV, Serrano, JP, and Sanchez, JCM. (2006). "Exploitation of tidal power in the Bay of Cadiz: ancient tidal mills". Scientia Marina. 70(1), 21-30.

Devine Tarbell & Associates Inc. (2006). Tidal power in North America Environmental and Permitting Issues. EPRI-TP-007-NA.

DHI. MIKE21. DHI, <http://www.dhigroup.com/Software/Marine/MIKE21.aspx> (Accessed 2008).

Domínguez, J, and Amador, J. (2007). "Geographical information systems applied in the field of renewable energy sources". Computers & Industrial Engineering. 52(3), 322-326.

Elghali, SEB, Benbouzid, MEH, and Charpentier, JF. (2007). "Marine tidal current electric power generation technology: State of the art and current status". IEEE International Electric Machines and Drives Conference 2007. Institute of Electrical and Electronics Engineers Computer Society, Piscataway, NJ 08855-1331, United States, Antalya, Turkey, 1407-1412.

EMEC. European Marine Energy Centre. <http://www.emec.org.uk/index.asp> (Accessed 2008).

EPA. State CO_2 Emissions from Fossil Fuel Combustion. Environmental Protection Agency, <http://epa.gov/climatechange/emissions/state_energyco2inv.html> (Accessed 2005).

EPRI. Wave Energy Conversion (WEC) Project. <http://oceanenergy.epri.com/waveenergy.html> (Accessed 2008).

EPRI. Tidal In Stream Energy Conversion (TISEC) Project. <http://oceanenergy.epri.com/streamenergy.html> (Accessed 2008).

ESRI. GIS Mapping Software, ArcView. <http://www.esri.com/software/arcgis/arcview/about/features.html> (Accessed 2008).

Fagerburg, T, Knowles, S, Fisackerly, G, Parman, J, Benson, H, and VICKSBURG, A. (1992). Hydrodynamic Data Collection in Cumberland Sound, Georgia. U.S. Army Engineer Waterways Experiment Station; Available from National Technical Information Service.

Finavera. <http://finavera.com/en/wave> (Accessed 2008).

Fraenkel, P. (2007). "Marine current turbines: pioneering the development of marine kinetic energy converters". Proceedings of the Institution of Mechanical Engineers, Part A: Journal of Power and Energy. 221(2), 159-169.

Fraenkel, PL. (2006). "Tidal current energy technologies". Ibis. 148, 145-151.

Froberg, E. (2006). Current Power Resource Assessment. Uppsala University, Uppsala.

GCK. GCK Technology Inc., <http://www.gcktechnology.com/GCK/index.html> (Accessed 2008).

Gorban, AN, Gorlov, AM, and Silantyev, VM. (2001). "Limits of the Turbine Efficiency for Free Fluid Flow". Journal of Energy Resources Technology. 123, 311-317.

Hagerman, G, and Bedard, R. (2006a). Maine Tidal In-Stream Energy Conversion (TISEC): Survey and Charaterization of Potential Project Sites. EPRI -TP-003 ME Rev 1. Electric Power Research Institute.

Hagerman, G, and Bedard, R. (2006b). Massachusetts Tidal In-Stream Energy Conversion (TISEC): Survey and Characterization of Potential Project Sites. EPRI -TP-003 MA Rev 1. Electric Power Research Institute.

Hagerman, G, Fader, G, and Bedard, R. (2006a). New Brunswick Tidal-In Stream Energy Conversion (TISEC): Survey and Characterization of Potential Project Sites. EPRI -TP-003 NB Rev 1. Electrical Power Research Institute.

Hagerman, G, Fader, G, Carlin, G, and Bedard, R. (2006b). Nova Scotia Tidal In-Stream Energy Conversion (TISEC): Survey and Characterization of Potential Project Sites. EPRI - TP- 003 NS Rev 2. Electric Power Research Institute.

Hagerman, G, Polagye, B, Bedard, R, and Previsic, M. (2006c). Methodology for Estimating Tidal Current Energy Resources and Power Production by Tidal In-Stream Energy Conversion (TISEC) Devices. EPRI-TP-001 NA Rev 3. Electric Power Research Institute.

Hagerman, G, Zickefoose, B, and Heller, T. (1989). "Wave energy resource and technology assessment for coastal North Carolina". Energy Conversion Engineering Conference, 755-760 vol.752.

Haidvogel, DB, Arango, H, Budgell, WP, Cornuelle, BD, Curchitser, E, Di Lorenzo, E, Fennel, K, Geyer, WR, Hermann, AJ, Lanerolle, L, Levin, J, McWilliams, JC, Miller, AJ, Moore, AM, Powell, TM, Shchepetkin, AF, Sherwood, CR, Signell, RP, Warner, JC, and Wilkin, J. (2008). "Ocean forecasting in terrain-following coordinates: Formulation and skill assessment of the Regional Ocean Modeling System". Journal of Computational Physics. 227(7), 3595-3624.

Hammerfest Strom. <http://www.hammerfeststrom.com/> (Accessed 2008).

Hammons, TJ. (1993). "Tidal power". Proceedings of the IEEE. 81(3), 419-433.

Harries, D, McHenry, M, Jennings, P, and Thomas, C. (2006). "Hydro, tidal and wave energy in Australia". International Journal of Environmental Studies. 63(6), 803-814.

Henfridsson, U, Neimane, V, Strand, K, Kapper, R, Bernhoff, H, Danielsson, O, Leijon, M, Sundberg, J, Thorburn, K, Ericsson, E, and Bergman, K. (2007). "Wave energy potential in the Baltic Sea and the Danish part of the North Sea, with reflections on the Skagerrak". Renewable Energy. 32(12), 2069-2084.

Herbert, JGM, Iniyan, S, Sreevalsan, E, and Rajapandian, S. (2007). "A review of wind energy technologies". Renewable and Sustainable Energy Reviews. 11(6), 1117-1145.

HydroHelix. <http://www.hydrohelix.fr/> (Accessed 2008).

HydroVolts. Hydrokinetic Turbines. <http://www.hydrovolts.com/Main%20Pages/Hydrokinetic%20Turbines.htm> (Accessed 2008).

IEA-OES. International Energy Association - Ocean Energy Systems, <http://www.iea-oceans.org/about/background/index.htm> (Accessed 2008).

IEC. Riding the waves at the helm. International Electrotechnical Commission, <http://www.iec.ch/online_news/etech/arch_2008/etech_0908/industry_1.htm> (Accessed 2008).

IHO. ENC Information International Hydrographic Organization, <http://www.iho-ohi.net/english/about-encs/> (Accessed 2009).

Independent Natural Resources Inc. World-wide Wave Market Research - Updated June 2007. Independent Natural Resources Inc., <http://www.inri.us/WECstudy/> (Accessed 2008).

JAMSTEC. (2003). The project for Research & Development of an offshore wave power device "Mighty Whale". In: IEA Ocean Energy Systems Newsletter.

JAMSTEC. JAMSTEC. <http://www.jamstec.go.jp/jamstec/MTD/Whale/> (Accessed 2008).

Kaijuka, E. (2007). "GIS and rural electricity planning in Uganda". Journal of Cleaner Production. 15(2), 203-217.

Kofoed, JP, Frigaard, P, Friis-Madsen, E, and Sorensen, HC. (2006). "Prototype testing of the wave energy converter wave dragon". Renewable Energy. 31(2), 181-189.

Kuik, GAMV. (2007). "The Lanchester-Betz-Joukowsky limit". Wind Energy. 10(3), 289-291.

Lanfredi, NW, Pousa, JL, Mazio, CA, and Dragani, WC. (1992). "Wave-power potential along the coast of the province of Buenos Aires, Argentina". Energy. 17(11), 997-1006.

Larsen, JK, and Madsen, J. (2000). "Effects of wind turbines and other physical elements on field utilization by pink-footed geese (Anser brachyrhynchus): A landscape perspective". Landscape Ecology. 15(8), 755-764.

Lebarbier, CH. (1975). "Power from Tides - The rance Tidal Power Station". Naval Engineers Journal. 87(2), 57-71.

Lee, MQ, Lu, CN, and Huang, HS. (2009). "Reliability and cost analyses of electricity collection systems of a marine current farm--A Taiwanese case study". Renewable and Sustainable Energy Reviews. 13(8), 2012-2021.

Leijon, M, and Nilsson, K. (2007). "Direct electric energy conversion system for energy conversion from marine currents". Proceedings of the Institution of Mechanical Engineers Part a-Journal of Power and Energy. 221(A2), 201-205.

Lim, YS, and Koh, SL. (2009). "Analytical assessments on the potential of harnessing tidal currents for electricity generation in Malaysia". Renewable Energy. In Press, Corrected Proof.

Lunar Energy. <http://www.lunarenergy.co.uk/index.htm> (Accessed 2008).

Martinho, AS, and Batteen, ML. (2006). "On reducing the slope parameter in terrain-following numerical ocean models". Ocean Modelling. 13(2), 166-175.

Mellor, GL, Ezer, T, and Oey, L-Y. (1994). "The Pressure Gradient Conundrum of Sigma Coordinate Ocean Models". Journal of Atmospheric and Oceanic Technology. 11(4), 1126-1134.

Michel, J, Dunagan, H, Boring, C, Healy, E, Evans, W, Dean, JM, McGillis, A, and Hain, J. (2007). Worldwide Synthesis and Analysis of Existing Information Regarding Environmental Effects of Alternative Energy Uses on the Outer Continental Shelf. MMS OCS Report 2007-038. U.S. Department of the Interior, Minerals Management Service, Herndon, VA.

MMS. (2006a). Technology White Paper on Ocean Current Energy Potential on the U.S. Outer Continental Shelf. Minerals Management Service Renewable Energy and Alternate Use Program, U.S. Department of the Interior.

MMS. (2006b). Technology White Paper on Wave Energy Potential on the U.S. Outer Continental Shelf. Minerals Management Service Renewable Energy and Alternate Use Program, U.S. Department of the Interior.

Moller, B. (2006). "Changing wind-power landscapes: regional assessment of visual impact on land use and population in Northern Jutland, Denmark". Applied Energy. 83(5), 477-494.

Mollison, D. (1982). Ireland's wave power resource. PB-84-109016. National Board for Science and Technology, Dublin, Ireland.

Mukai, AY, Westerink, JJ, and Luettich, RA. (2002). Guidelines for Using Eastcoast 2001 Database of Tidal Constituents within Western North Atlantic Ocean, Gulf of Mexico and Caribbean Sea. US Army Corps of Engineers.

Muselli, M, Notton, G, Poggi, P, and Louche, A. (1999). "Computer-aided analysis of the integration of renewable-energy systems in remote areas using a geographical-information system". Applied Energy. 63(3), 141-160.

Myers, L, and Bahaj, AS. (2005). "Simulated electrical power potential harnessed by marine current turbine arrays in the Alderney Race". Renewable Energy. 30(11), 1713-1731.

NDBC. Measurement Descriptions and Units. National Oceanic and Atmospheric Administration, <http://www.ndbc.noaa.gov/measdes.shtml#stdmet> (Accessed 2008).

NOAA. File Type 291 - Meteorology Oceanography and Wave Spectra. National Oceanic and Atmospheric Administration, <http://www.nodc.noaa.gov/General/NODC-Archive/f291.html> (Accessed.

NOAA. Office of Coast Survey Electronic Navigational Charts (ENC). National Oceanic and Atmospheric Administration, <http://nauticalcharts.noaa.gov/mcd/enc/download.htm> (Accessed 2008).

NOAA. Office of Response and Restoration, Environmental Sensitivity Index (ESI) Maps. National Oceanic and Atmospheric Administration, <http://response.restoration.noaa.gov/> (Accessed 2008).

NOAA. Tides and Currents. National Oceanic and Atmospheric Administration, <http://tidesandcurrents.noaa.gov/index.shtml> (Accessed 2008).

NOS. Vertical Datum Transformation NOAA's National Geodetic Survey (NGS), Office of Coast Survey (OCS), and Center for Operational Oceanographic Products and Services (CO-OPS), <http://vdatum.noaa.gov> (Accessed 2008).

Oceanlinx. <http://www.oceanlinx.com/> (Accessed 2008).

ON. Ocean Navitas Ltd., <http://oceannavitas.com/technology.html> (Accessed 2008).

OpenHydro. <http://www.openhydro.com/home.html> (Accessed 2008).

OPT. Ocean Power Technologies. <http://www.oceanpowertechnologies.com/> (Accessed 2008).

Otawa, T. (1980). "Wind Energy Planning: Development and Application of a site selection Method for Wind Energy Conversion Systems (WECS)". Energy Research. 4, 283-306.

Ozger, M, Altunkaynak, A, and Sen, Z. (2004). "Stochastic wave energy calculation formulation". Renewable Energy. 29(10), 1747-1756.

Pawlowicz, R, Beardsley, B, and Lentz, S. (2002). "Classical tidal harmonic analysis including error estimates in MATLAB using T_TIDE". Computers & Geosciences. 28(8), 929-937.

Pearce, N. (2005). "Worldwide tidal current energy developments and opportunities for Canada's Pacific coast". International Journal of Green Energy. 2(4), 365-386.

Pelamis Wave Power. <http://www.pelamiswave.com/> (Accessed 2008).

Polagye, B, and Bedard, R. (2006). Tidal In-Stream Energy Resource Assessment for Southeast Alaska. EPRI-TP-003 AK. Electric Power Research Institute.

Polagye, B, Malte, P, Kawasel, M, and Durran, D. (2008). "Effect of large-scale kinetic power extraction on time-dependent estuaries". Proceedings of the Institution of Mechanical Engineers Part a-Journal of Power and Energy. 222(A5), 471-484.

Ponte Di Archimede International <http://www.pontediarchimede.it/language_us/index.mvd> (Accessed 2008).

Pontes, MT, Rebelo, L, Silva, P, and Pata, C. (2005). "Database of wave energy potential in Portugal". American Society of Mechanical Engineers, New York, NY 10016-5990, United States, Halkidiki, Greece, 803-809.

Prest, R, Daniell, T, and Ostendorf, B. (2007). "Using GIS to evaluate the impact of exclusion zones on the connection cost of wave energy to the electricity grid". Energy Policy. 35(9), 4516-4528.

Ramachandra, TV, and Shruthi, BV. (2007). "Spatial mapping of renewable energy potential". Renewable and Sustainable Energy Reviews. 11(7), 1460-1480.

Ramirez-Rosado, IJ, Garcia-Garridoa, E, Fernandez-Jimenez, LA, Zorzano-Santamaria, PJ, Monteiro, C, and Miranda, V. (2008). "Promotion of new wind farms based on a decision support system". Renewable Energy. 33(4), 558-566.

Rear, L. (2009). NOAA. Personal Communication.

Robertson, R. (2006). "Modeling internal tides over Fieberling Guyot: resolution, parameterization, performance". Ocean Dynamics. 56(5-6), 430-444.

Rodman, LC, and Meentemeyer, RK. (2006). "A geographic analysis of wind turbine placement in Northern California". Energy Policy. 34(15), 2137-2149.

Salter, SH. (1974). "Wave power". Nature. 249(5459), 720-724.

Sanford, L. (2003). "Winning the tidal race". Modern Power Systems. 23(7), 11-12.

SARA. MHD Wave Energy Conversion (MWEC), Scientific Applications & Research Associates Inc., <http://www.sara.com/RAE/ocean_wave.html> (Accessed 2008).

Schwartz, SS. (2006). Proceedings of the Hydrokinetic and Wave Energy Technologies Technical and Environmental Issues Workshop. Workshop. Washington, DC. October 26-28, 2005. RESOLVE Inc., Washington, DC.

Scott, BE. (2007). "A renewable engineer's essential guide to marine ecology". Institute of Electrical and Electronics Engineers Computer Society, Piscataway, NJ 08855-1331, United States, Aberdeen, Scotland, United Kingdom, 4302218.

SEACOOS. Data Access and Mapping. SouthEast U.S. Atlantic Coastal Ocean Observing System, <http://seacoos.org/Data%20Access%20and%20Mapping> (Accessed 2008).

Seim, HE, Blanton, JO, and Elston, SA. (2009). "The effect of secondary circulation on the salt distribution in a sinuous coastal plain estuary: Satilla River, GA, USA". Continental Shelf Research. 29(1), 15-28.

Seim, HE, Blanton, JO, and Gross, T. (2002). "Direct stress measurements in a shallow, sinuous estuary". Continental Shelf Research. 22(11-13), 1565-1578.

Shchepetkin, AF, and McWilliams, JC. (2005). "The Regional Ocean Modeling System (ROMS): A split-explicit, free-surface, topography-following coordinates ocean model". Ocean Modelling. 9, 347-404.

Shepherd, W, Shepherd, DW. (1999). Energy Studies. Imperial College Press, London.

Sikiric, MD, Janekovic, I, and Kuzmic, M. (2009). "A new approach to bathymetry smoothing in sigma-coordinate ocean models". Ocean Modelling. 29(2), 128-136.

Sivaramakrishnan, TR. (1992). "Wave power over the indian seas during the southwest monsoon season". Energy. 17(6), 625-627.

Smith, GH, Venugopal, V, and Wolfram, J. (2006). "Wave period group statistics for real sea waves and wave energy extraction". Proceedings of the Institution of Mechanical Engineers Part M: Journal of Engineering for the Maritime Environment. 220(3), 99-115.

Smith, M, Stevens, C, and Gorman, R. (2004). Wave Energy Coastal Waves Primer. National Institute of Water & Atmospheric Research Ltd Wellington.

Spain, R. A possible Roman Tide Mill. The Kent Archeological Society, <http://www.kentarchaeology.ac/authors/rspain.html> (Accessed 2008).

Sperboy. <http://www.sperboy.com/> (Accessed 2008).

Stewart, S, Hunt MH, Shelton S, Webb R. (2007). Southern Winds: A study of wind power generation potential off the coast of Georgia coast. Georgia Institute of Technology and Southern Company.

Sutherland, G, Foreman, M, and Garrett, C. (2007). "Tidal current energy assessment for Johnstone Strait, Vancouver Island". Proceedings of the Institution of Mechanical Engineers Part a-Journal of Power and Energy. 221(A2), 147-157.

TELEMAC. TELEMAC System. <http://www.telemacsystem.com/gb/default.html> (Accessed 2008).

The National Commission on Energy Policy. (2004). Ending the Energy Stalemate: A Bipartisan Strategy to Meet America's Energy Challenges. The National Commission on Energy Policy, Washington DC.

Thorburn, K, Bernhoff, H, and Leijon, M. (2004). "Wave energy transmission system concepts for linear generator arrays". Ocean Engineering. 31(11-12), 1339-1349.

Thorpton Energy Services. <http://ourworld.compuserve.com/homepages/throptonenergy/homepage.htm> (Accessed 2008).

Tidal Stream. <http://www.tidalstream.co.uk/index.html> (Accessed 2008).

Triton Consultants Ltd. (2002). Green Energy Study for British Columbia. Phase 2: Mainland.Tidal Current Energy. Chapter 6: Technology Review. Prepared for BC Hydro, Engineering.

Tsenga, R, Wua R, Huangh C. (2000). "Model study of a shoreline wave-power system". Ocean Engineering. 27, 801–821.

Tucker, MJ, Pitt EG. (2001). Waves in Ocean Engineering. Elsevier Science Ltd, Oxford.

Turner, NE, and Owen, A. (2007). "The development of a tidal turbine for deployment in areas with slow moving tidal flows". Institute of Electrical and Electronics Engineers Computer Society, Piscataway, NJ 08855-1331, United States, Aberdeen, Scotland, United Kingdom, 4302428.

UEK Systems. <http://uekus.com/index.html> (Accessed 2008).

USCB. Decennial Management Division Glossar. U.S. Census Bureau, <http://www.census.gov/dmd/www/glossary.html> (Accessed 2009).

USDOI. Bald Eagle Soars Off Endangered Species List. U.S. Department of the Interior, <http://www.doi.gov/news/07_News_Releases/070628.html> (Accessed 2009).

USEIA. Electric Sales, Revenue, and Average Price 2007. U.S. Energy Information Administration, <http://www.eia.doe.gov/cneaf/electricity/esr/table5.html> (Accessed 2009).

USFWS. Endangered Species Program. U.S. Fish & Wildlife Service, <http://www.fws.gov/Endangered/> (Accessed 2009).

USFWS. Georgia Ecological Services Field Offices. U.S. Fish & Wildlife Service (Accessed 2009).

USGS. Georgia Environmental Resources Digital Data Atlas. U.S. Geological Survey, <http://csat.er.usgs.gov/statewide/downloads.html> (Accessed 2008).

USGS. Water Data for the Nation: National Water Information System. <http://waterdata.usgs.gov/usa/nwis/sw> (Accessed 2008).

Verdant Power. <http://verdantpower.com/> (Accessed 2008).

Voivontas, D, Assimacopoulos, D, Mourelatos, A, and Corominas, J. (1998). "Evaluation of Renewable Energy potential using a GIS decision support system". Renewable Energy. 13(3), 333-344.

Voss, A. (1979). "Waves, currents, tides - Problems and prospects". Energy. 4(5), 823-831.

Walker, A, Kandt, A, and Heimiller, D. (2005). "Wave power for U.S. coast guard first district lighthouses". American Society of Mechanical Engineers, New York, NY 10016-5990, United States, Orlando, FL, United States, 573-580.

Wave Dragon. (2003). Wave Energy Converter Wave Dragon Ready for Deployment. In: IEA Ocean Energy Systems Newsletter.

Wave Dragon. Wave Dragon. <http://www.wavedragon.net/> (Accessed 2008).

Wavebob. <http://www.wavebob.com/home/> (Accessed 2008).

WEC. (2004). 2004 Survey of Energy Resources. World Energy Council.

WEC. (2007). 2007 Survey of Energy Resources. World Energy Council.

Winter, AJB. (1980). "The UK wave energy resource". Nature. 287(5785), 826-828.

Xiaochun, W, Yi, C, Changming, D, Farrara, J, Zhijin, L, Matsumoto, K, McWilliams, JC, Paduan, JD, Rosenfeld, LK, Shum, CK, and Yu, W. (2006). "Tidal simulation using Regional Ocean Modeling System (ROMS)". European Space Agency, Noordwijk, 2200 AG, Netherlands, 6.

Yapa, LS. (1991). "Is GIS appropriate technology quest?". International Journal of Geographical Information Science. 5(1), 41 - 58.

Young, RM. (1995). "Requirements for a Tidal Power Demonstration Scheme". Proceedings of the Institution of Mechanical Engineers Part a-Journal of Power and Energy. 209(3), 215-220.

Yue, C-D, and Yang, GG-L. (2007). "Decision support system for exploiting local renewable energy sources: A case study of the Chigu area of southwestern Taiwan". Energy Policy. 35(1), 383-394.

Yue, CD, and Wang, SS. (2006). "GIS-based evaluation of multifarious local renewable energy sources: a case study of the Chigu area of southwestern Taiwan". Energy Policy. 34(6), 730-742.

Zevenbergen, LW, Lagasse, PF, and Edge, BL. (2004). Tidal Hydrology, Hydraulics, and Scour at Bridges. FHWA NHI-05-077. Ayres Associates.